DEVELOPMENT AND TESTING OF AN IMPLANTABLE PERFUSION AND OXYGENATION SENSOR FOR LIVER TRANSPLANT MONITORING

A Dissertation

by

TONY JOSEPH AKL

Submitted to the Office of Graduate and Professional Studies of
Texas A&M University
in partial fulfillment of the requirements for the degree of

DOCTOR OF PHILOSOPHY

Chair of Committee,	Gerard L. Coté
Committee Members,	Michael J. McShane
	Kenith E. Meissner
	Jim X. Ji
Head of Department,	Gerard L. Coté

December 2013

Major Subject: Biomedical Engineering

ABSTRACT

Since the first successful liver transplant in 1968 the surgery has become very common and 6,291 patients received liver transplants in 2010 in the United States. However, the monitoring methods used post-surgery, in the recovery phase, are still very basic and rely mainly on blood tests and looking for unusual symptoms. Complications are usually detected after the organ is substantially damaged which poses a risk to the patients' life. This dissertation presents the development and testing of an implantable sensor that can potentially be used to monitor the transplant continuously and transmit the information wirelessly to the medical staff for timely intervention. Such a sensor could have a great effect on survival and reduction of retransplantation rates.

The presented sensor employs near infrared spectroscopy to measure perfusion changes, arterial oxygenation and venous oxygenation in the parenchyma of the liver tissue and the supplying vessels. Light at three different wavelengths (735-, 805- and 940-nm) is shined on the tissue and the diffuse reflectance is collected via a photodetector. The collected signals can be transmitted wirelessly to an external unit for processing and display. In this dissertation, different perfusion and oxygenation monitoring techniques are reviewed and the instrumentation of an NIRS based wireless sensor is introduced. A phantom that mimics the anatomy of the liver and its optical and mechanical properties is presented. The processing methods to extract the information of interest from the diffuse reflectance are described in details. Finally, results from *in vitro* phantom experiments, *ex vivo* perfused livers and *in vivo* porcine studies are presented.

The first *in vivo* wireless monitoring of hepatic perfusion and oxygenation levels is reported. The studies show that the sensor can track perfusion changes with a resolution of 0.1 mL/min/g of tissue. The possibility of tracking oxygen saturation changes is also shown as well as the ability to separate them from perfusion changes. Combining results from the pulsatile wave and DC levels, venous and arterial oxygen saturation changes were tracked with a resolution of 1.39% and 2.19% respectively. In conclusion, optical spectroscopy is shown to track perfusion, and arterial and venous oxygenation in tissue. In particular, the method was tested on hepatic and intestinal tissue.

DEDICATION

To my mom, Laure Saad Akl, and my dad, Joseph Akl, for all the sacrifices they had to make for me to get here.

ACKNOWLEDGEMENTS

This dissertation and the work described herein could not have been possible without the contributions and help of a large group of individuals. First and foremost, I would like to thank my advisor, Dr. Gerard Coté, for his guidance throughout my doctoral studies. Dr. Coté has supported me in every step of my Ph.D. through advice, mentoring, encouragement, and opening doors of opportunities to widen my knowledge and explore a variety of projects in the rich biomedical sensing field. I would also like to thank each of my committee members for their helpful discussions and their expertise. Specifically, I would like to thank Dr. McShane for his help in the microfluidics portion of the work, Dr. Meissner for his expertise in understanding and modeling light interaction with tissue, and Dr. Jim Ji for the helpful discussions about signal processing techniques.

Throughout the course of this research, I was blessed to work with a great set of collaborators. In particular, Dr. Mark Wilson from the University of Pittsburgh, who helped me learn and better understand the physiology and the medical applications and who made himself available to discuss any ideas I have. Dr. Nance Ericson, from Oak Ridge National Laboratory, who, in addition to his scientific contributions, always supported and encouraged me. I always felt that I had the full support of my advisor and all of our collaborators which gave me the confidence to venture into new ideas and for that I am very thankful.

I would like to thank my friends in the Optical Biosensing Laboratory and the Biomedical Engineering Department. They made my time at Texas A&M a great experience. I would also like to thank the faculty and staff in the Biomedical Engineering Department; they create a great work environment that made me want to come to work every morning.

My parents have always been my number one supporters in everything I do and have always encouraged me to pursue my education. I am really thankful to them and all the sacrifices they made to make this possible. I would also like to thank my brother, Charbel, who encouraged me to pursue my doctoral studies. Finally, I am very thankful to my fiancée, Joey Jabbour, for her patience and support throughout my studies.

NOMENCLATURE

AC	Alternating Current
BPM	Beat Per Minute
DC	Direct Current
DCS	Diffuse Correlation Spectroscopy
EAGF	Early Acute Graft Failure
ESLD	End Stage Liver Disease
ε	Extinction coefficient
HA	Hepatic Artery
Hb	Reduced or deoxy- hemoglobin
HbO_2	Oxy- hemoglobin
HbT	Total hemoglobin
HV	Hepatic Vein
IR	Infrared
LDF	Laser Doppler Flowmetry
LED	Light Emitting Diode
λ	Wavelength
MC	Monte Carlo
NA	Numerical Aperture
NIR	Near-Infrared
NIRS	Near-Infrared Spectroscopy

PDMS	Polydimethylsiloxane
PPG	Photo-Plethysmogram or Photoplethysmography
PV	Portal Vein
RF	Radio Frequency
SaO_2	Arterial oxygen saturation
SO_2	Oxygen Saturation
SpO_2	Peripheral Oxygen Saturation
SvO_2	Venous oxygen saturation
UV	Ultraviolet
VGA	Variable Gain Amplifier
Vis	Visible
YM	Young's Modulus

TABLE OF CONTENTS

Page

LIST OF FIGURES

LIST OF TABLES

CHAPTER I

INTRODUCTION

Liver Transplant: Past, Present, and Future

The liver is the largest internal organ in the human body (2% of the total body weight) and has many essential functions to the human life [1]. Terminal liver failure is life threatening and currently the only treatment for end stage liver disease (ESLD) is transplant. ESLD can be inherited or caused by a wide variety of factors including viral infections, drugs, and alcohol abuse. The first successful liver transplant was performed by Dr. Thomas Starzl in 1967 [2]. Since then, this operation has become a standard of care for patients with ESLD. A timeline of the progress of liver transplantation has been recently reviewed by Zarrinpar *et al.* [3]. The increase in the number of performed liver transplants has been exponential in the 1980s and 1990s and it plateaued in the early 2000s, due to the shortage of organs [4]. Currently, around 6,400 and 4,200 liver transplants are performed yearly in the United States [5] and Europe [4]. The 1-, 3-, and 5-year survival rates in the United States (1997-2004) for liver transplant recipients are 86, 78, and 72% respectively [5].

Liver transplant is a complex procedure and often patients suffer from life threatening early acute graft failure (EAGF) complications such as hepatic artery thrombosis, portal vein thrombosis, primary graft non-function, hemorrhage, and others [6]. The majority of complications take place in the first two weeks following the surgery [7]. The current standard of care relies on biweekly blood work and needle

biopsies for suspicious cases [8]. These procedures are expensive, time consuming, and do not provide real-time assessment of the graft leading to delayed detection in many cases increasing the risk on the patient's life and reducing the success rate of the intervention. Our group is working on developing an implantable sensor to monitor graft health in real-time and provide the care providers with frequent quantitative measurements to help detect any acute complications in the first two weeks post-transplant in a timely manner [9, 10]. Figure 1 shows a schematic of the envisioned system.

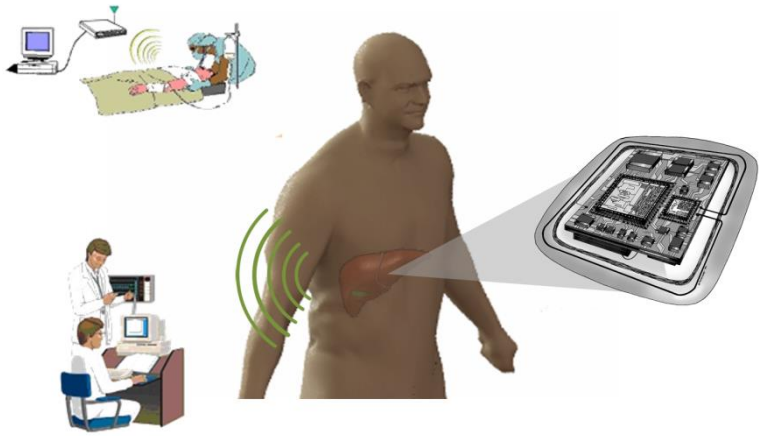

Fig. 1. Schematic of the envisioned system [9].

Most EAGFs are associated with a disturbance in the hepatic perfusion pattern or tissue oxygenation. Vascular complications are typically associated with a decrease in hepatic tissue perfusion levels due to a decrease in supply (HA and PV complications) or a downstream blockage (Hepatic Vein complications). Klar *et al.* found in two different

clinical studies that liver transplant failures were associated with decreased perfusion levels under 60 mL/min/100 g of tissue during [11] or after transplant [12]. These perfusion changes are accompanied with changes in the tissue oxygen supply and consumption. Normal perfusion levels vary between subjects and to assess the adequacy of perfusion, measurements should be coupled with an oxygen consumption measure. Takaya *et al.* found in a clinical study (88 patients) that oxygen consumption can be used as a "predictive indicator for liver allograft function after transplantation" [13]. A sensor tracking perfusion and oxygenation changes in real-time can detect graft failures at an early stage and allow for timely medical intervention.

Perfusion and Flow Monitoring Techniques

There is a wide variety of blood flow and perfusion monitoring techniques. Perhaps the most common techniques used clinically are Doppler based techniques [14]. The Doppler principle relies on measuring the change in the frequency of a wave after bouncing off a scatterer, in this case red blood cell. This change, namely Doppler shift, is proportional to the velocity of the moving scatterers. Doppler measurements are not quantitative and track patterns of flow changes. This principle is used in Laser Doppler Flowmetry (LDF) that employs optical waves to measure the Doppler shift caused by blood flow. This measure of flow is often related to perfusion by assuming the probed blood volume (vessels and capillaries) is constant. If the volume of the blood vessels or capillaries is constant, this quantity can be related to tissue perfusion. This assumption should be used very carefully since many physiologic conditions can trigger changes in the probed blood volume such as vasoconstriction.

Another widely used technique is Transit-Time Ultrasound (US) flowmetry [15]. In this technique, the time it takes for an US wave to propagate across a blood vessel and back is measured and is proportional to the flow in that vessel. The main advantage of that technique over LDF is the quantitative measurements it provides. However, a major drawback is the inability to use the technique for tissue perfusion measurements since it requires an US reflector placed at a known distance from the source.

Blood perfusion controls the tissue thermal properties. Bowman *et al.* showed that by using thermistor probes to measure the thermal properties of tissue, one can monitor its perfusion levels [16]. Since then, this technique became widely used for numerous applications ranging from skin grafts to brain tissue [17, 18]. This technique has shown success in monitoring hepatic microcirculation [12, 19]. The probes used in these monitors employ two thermistors. The proximal thermistor is passive and is used to measure the baseline temperature of the surrounding tissue. The second thermistor is active and is placed on the distal side of the probe. When this thermistor is powered, it causes an increase of about 2°C in the local temperature. The power needed to cause that change is used to measure perfusion levels.

Another technique that is widely used in hemodynamics research is laser speckle flowmetry. When coherent light is shined on tissue, the reflected light forms an interference pattern known as speckle. This pattern is blurred when the scatterers in the medium start moving. Many variations of this principle have been developed to study tissue perfusion in a variety of biomedical applications [20]. In its current form, laser

speckle perfusion monitoring does not provide quantitative measurements which is one of the main drawbacks of this technique [21].

A technique that has emerged recently in blood flow monitoring is Diffuse Correlation Spectroscopy (DCS) [22, 23]. This technique typically employs NIR coherent light sources and operates in reflectance mode using long source to detector separations which gives the technique the advantage of probing deeper tissue compared to LDF [24]. This technique can be combined with Near Infrared Spectroscopy (NIRS) to get oxygenation information [25, 26].

These techniques are the most used in the clinic and research for flow and/or perfusion monitoring. There are other imaging techniques that are mainly used in diagnostic and are not suitable for long term monitoring mainly due to their cost and size and in some cases the use of ionizing radiation [27, 28].

A common problem with these techniques is the difficulty to miniaturize the instrumentation to a level where the sensor can be implanted with the organ and monitor the perfusion in the first two weeks post-surgery. In addition, all these techniques except the combined DCS-NIRS systems, do not provide any oxygenation information which is essential to assess the adequacy of perfusion and the oxidative stress levels on tissue.

Oxygenation Monitoring Techniques

Oxygen is not very soluble in water and hemoglobin is used as the carrier of oxygen in our blood to transport it from our lungs to the different organs of the body. Each hemoglobin molecule has four oxygen binding sites. When one of the binding sites is bound to oxygen, it increases the affinity of the other binding sites to oxygen so the

free oxygen will preferably bind to the hemoglobin molecule that has more binding sites occupied by oxygen. This leads to having the majority of hemoglobin molecules in one of two states: oxygenated (HbO_2) or reduced (Hb). The ratio of HbO_2 to the total amount of hemoglobin (HbT) is known as the hemoglobin oxygen saturation (SO_2).

Optical techniques are still the gold standard for non-invasive blood oxygen monitoring. Hemoglobin's extinction coefficient depends on its oxygenation state [29-31] and this property has been used in multiple optical techniques to quantify oxygenation levels [32-35]. Figure 2 shows hemoglobin's extinction coefficient in its two oxygenation states.

Oximetry using light first started in the 1930s-1940s [36, 37]. However, the idea of employing the pulsatile signal to isolate the contribution of the arterial blood to the collected signal wasn't discovered until the 1970s by Takuo Aoyagi [34, 36]. This marked the first realization of pulse oximetry in its current basic form. Today, pulse oximetry is the standard for monitoring peripheral oxygen saturation (SpO_2) and is used in nearly every surgical procedure that involves anesthetia or sedation in the developed world. Its concept relies on comparing the absorbance of light by the arterial blood on two different wavelengths. The details of the theory will be described later in this thesis. Since its invention, there have been many variations on pulse oximetry to enhance its signal and optimize it for use in different applications but the principle remains the same [38-40]. The instrumentation used in this technique is simple and multiple groups have shown the possibility to miniaturize it to the level of implantable and/or wearable

sensors [9, 10, 41, 42]. In addition, multiple reports have shown the possibility of using the photoplethysmogram (the pulsatile signal) to track perfusion changes [35, 42-45].

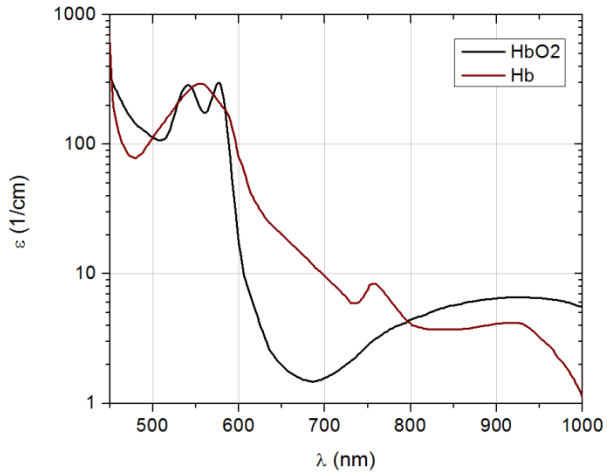

Fig. 2. Hemoglobin extinction coefficient in the VIS-NIR range (data from [31]) [43].

Another technique that has shown a success in monitoring oxygenation changes is Near Infrared Spectroscopy (NIRS) [46]. Similar to pulse oximetry, NIRS uses two or more wavelengths of light in the red to NIR range and the difference in absorbance at the two wavelengths can be used to track changes in the concentration of HbO_2 and Hb. An absolute measure of these concentrations is dependent on the optical pathlength. Different techniques have been used to accomplish that such as NIRS in frequency domain (FD-NIRS) and in time domain (TD-NIRS) [33, 47]. FD-NIRS employs modulated light sources and uses the phase of the collected wave to measure the optical pathlength. In TD-NIRS, pulses of light are used to illuminate the tissue and the delay

and shape of the collected pulse is used to determine the optical pathlength. The information in pulse oximetry is contained mainly in the pulsatile signal that constitutes around 0.2 to 5.2 % of the collected signal [48]. NIRS uses the full signal which allows it to use long source to detector separations with NIR wavelengths to probe deeper in tissue. That gave NIRS an advantage in some applications such as functional brain imaging (fNIRS) [33]. Note that NIRS measures tissue oxygenation levels which include arterial, capillary, and venous contribution. Pulse oximetry measures pulsatile oxygen saturation which, in most cases, follows the arterial oxygenation closely.

Pulse oximetry and NIRS are very similar. The main difference is the method each of the techniques uses to separate the contribution of blood from that of tissue. In the sensor described herein, both of these techniques were used as complementary measurements to get arterial and tissue oxygenation measurements.

Proposed Approach

The sensor described herein is based on photoplethysmography (PPG). That type of sensors can operate in reflectance and transmittance modes [41, 42, 44, 45]. In transmittance mode, the photodetector is on the opposite side of the light source and light goes through the full thickness of tissue before it is collected. This mode is used in applications such as finger and ear pulse oximeters [49]. However, it can not be used on large organs due to the limited penetration depth of light. The sensor presented in this thesis operates in reflectance mode where the light source and photodetector are on the same side. This mode can be used to monitor hemodynamics in thick organs [9, 10, 42, 45]. To obtain perfusion and oxygenation information, we employ three Light Emitting

Diodes (LEDs) emitting in the Red-NIR region (735, 805, and 940 nm). Figure 3 shows a schematic of the sensor probe with the three LEDs and the photodetector.

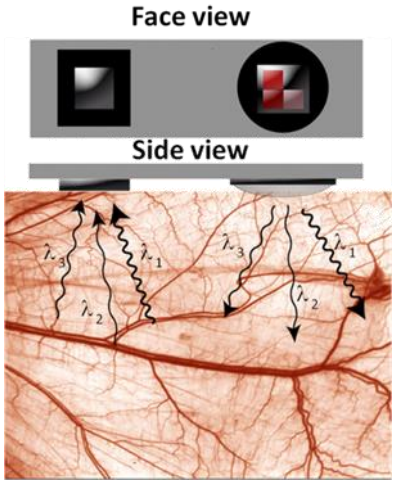

Fig. 3. Probe schematic : (top) face view and (bottom) side view when placed on tissue. The different lines (λ1, λ2, and λ3) refer to different wavelengths of light [9].

When light is shined on tissue, part of it is absorbed by various chromophores in tissue (hemoglobin, melanin, water, etc.). The remainder of the light exits the tissue scattered in various directions and locations. A photodetector placed on the surface of the tissue detects any fluctuations in the signals due to changes in the concentration/volume of the chromophores. The collected signal has multiple frequency components caused by different periodic processes (respiration, blood flow/pressure, vasomotion, etc.). Changes at the heart rate are due to the arterial pulsatile blood flow and can be used to separate the blood signal from the tissue contribution. This signal is measured as an alternating current (AC) signal and is referred to as the

photoplethysmogram (PPG). PPG can be used to monitor heart rate and perfusion levels [35, 44]. The amplitude of the PPG is a function of wavelengths. By using two or more wavelengths, blood oxygen saturation can be quantified and separated from perfusion changes [50]. The photodetector also measures a direct current (DC) that maps the absorbance of chromophores that are not time variant during the collection/integration period. These chromophores include non-pulsatile arterial blood, venous blood, and surrounding tissue (Figure 4). Although this part constitutes the majority of the reflectance and is rich in information about the hemodynamics of the tissue, PPG sensors commonly employ the DC level for the sole purpose of normalizing the AC signal to account for tissue absorbance, light-source intensity and coupling, and other undesired background signals. In our system, the DC levels are used to measure venous oxygenation changes.

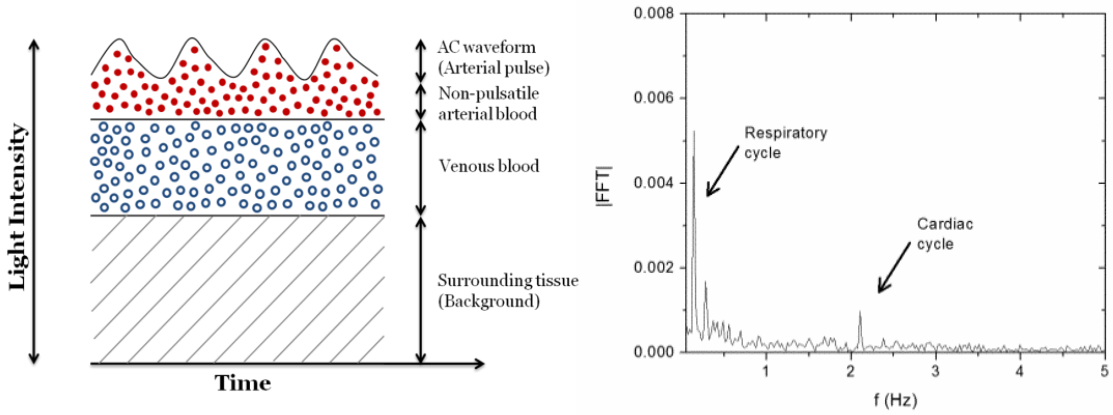

Fig. 4. Diagram of the different parts of the collected light signal (left) and a typical frequency spectrum of the collected intensity (right) prior to any amplification. Note that the signals are not to scale in the diagram and the DC signal is omitted from the spectrum to be able to visualize the pulsatile signal peaks.

Traditional PPG systems use hemoglobin as the chromophore of interest to detect blood pulsation. However, some variations of PPG systems are used to monitor exogenous chromophores such as Indocyanine Green (ICG) [51] and gold nanoshells [52] in the blood stream. These systems are typically used to study the clearance of introduced exogenous chromophores from the blood stream for a variety of applications ranging from studying liver function [51] to measuring cardiac output [53].

Although PPG is most known for the aforementioned applications, there are many variations of this technique that are currently being explored to suit various biomedical applications. One of the growing areas of interest with PPG is contactless monitoring [54-57]. Similar to regular PPG, these systems have the potential to be used to monitor heart rate [54] perfusion [56] and oxygenation [57]; however, more studies are needed to validate and assess their performance.

As mentioned earlier, the PPG signal is relatively weak and the instrumentation design requires optimization of multiple parameters (probe geometry, filtration and amplification, wavelength selection, etc.) to maximize the collected signal. These parameters have been studied by various groups and have shown to have substantial effect on the performance of the PPG sensors [39, 40, 58-61]. Most of these parameters depend on the application of interest. In the following chapter, the optimization of the instrumentation is discussed for an implantable PPG sensor for continuous monitoring of perfusion and oxygenation changes in liver tissue.

CHAPTER II

INSTRUMENTATION DESIGN[*]

Instrumentation Overview

The essential parts of a typical multiwavelength PPG sensor are: light sources multiplexed to avoid cross-talk between the channels, one or multiple photodetectors, and filters and amplifiers to extract and amplify the weak pulsatile signal (Figure 5). The system described herein utilizes three wavelengths to measure and separate perfusion and oxygenation signals and correct for motion artifacts [50, 62]. The three light sources are multiplexed which allows the use of a single photodetector. In our system we use time-division multiplexing (TDM) which reduces power consumption in comparison with frequency-division multiplexing (FDM) [10]. Figure 5 shows a block diagram of the sensor. The left side shows the three light sources with the corresponding drive units. Light Emitting Diodes (LEDs) were used as light sources because of their availability in small sizes, low prices, and low power consumption. The signal detection and separation diagram is shown in the right part of figure 5. The light measured by the photodetector is first amplified by a low noise preamplifier. The signal is then demultiplexed into four channels: one for each wavelength and one that is measured when all LEDs are off to quantify the dark current. The signal then goes through a differential amplifier for dark

[*] Part of this chapter is reprinted from T. J. Akl, R. Long, M. J. McShane *et al.*, "Optimizing probe design for an implantable perfusion and oxygenation sensor," Biomed Opt Express, 2(8), 2096-109 (2011)., with kind permission of OSA, Copyright 2013 by The Optical Society.

current subtraction. The resultant signal on each of the wavelength channels is split into a DC channel with a low pass filter and an AC channel with a bandpass filter and a variable gain amplifier (VGA) that is set by the user to amplify the AC signal [9, 10, 63]. Each sensor results in 6 channels (AC and DC channels for each of the 3 wavelengths) which are digitized and saved into a data acquisition computer.

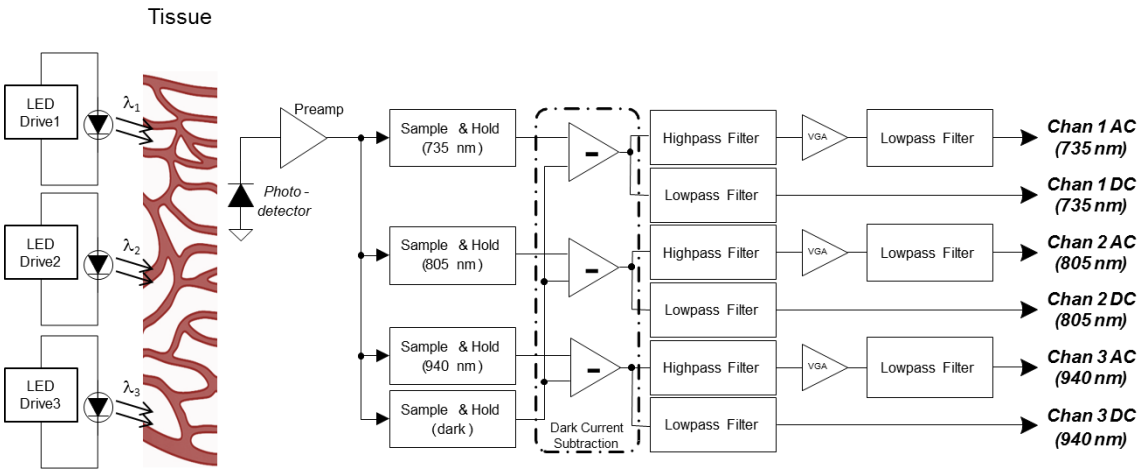

Fig. 5. Block diagram of illumination and signal processing electronics for a 3 wavelengths sensor.

The PPG sensor performance depends on multiple parameters that will be discussed in details in this chapter. These parameters include the probe geometry, illumination wavelength(s), filter cutoff frequencies, and amplification. First we discuss the probe design and fabrication (source to detector separation, illumination wavelengths, etc.) followed by a description of the filtering and amplification parameters.

Probe Design

The separation of the illumination and collection points in a reflectance based sensor is essential in determining the probing volume and probing depth which are directly related to the signal to background ratio [64, 65]. In addition, by varying the probing volume, the optical pathlength is altered leading to a change in absorbance and the collected light intensity. For these reasons, the source to detector separation should be optimized, especially in the case of an implantable sensor where power is limited and artifacts are relatively high. Similarly, the optical properties of chromophores are wavelength dependent and the performance of an optical sensor depends largely on the wavelengths used. In this section, we investigate the effect of source to detector separation and other source-detector characteristics to optimize the sensor's signal to background ratio using Monte Carlo (MC) based simulations and *in vitro* phantom studies. In summary, separations in the range 0.45 to 1.25 mm were found to be optimal in the case of a point source. The numerical aperture (NA) of the source had no effect on the collected signal while the widening of the source spatial profile caused a shift in the optimal source-detector separation. Specifically, for a 4.5 mm flat beam and a 2.4 mm × 2.5 mm photodetector, the optimal performance was found to be when the source and detector are adjacent to each other. These modeling results were confirmed by data collected from *in vitro* experiments on a liver phantom perfused with dye solutions mimicking the absorption properties of hemoglobin for different oxygenation states.

Materials and Methods

Monte Carlo Simulations

A multilayer photon propagation Monte Carlo simulation program based on the algorithm developed by Wang *et al.* [66] was developed in MATLAB (Appendix A). The placement of the sensor on the portal vein, the main blood supplier to the liver [67], and the hepatic artery were modeled as three layer structures (Fig. 6). The first and third layer have the optical properties of liver tissue [68] and the middle layer has the optical properties of whole blood and the dimensions of the vessel under investigation (Table 1). The optical properties of blood were changed to mimic different oxygenation states [30, 31]. Table 2 shows the optical properties of the two oxygenation states of blood at three wavelengths of interest [29, 31].

Table 1. Diameter and wall thickness of the portal vein and hepatic artery ([69, 70] & [69, 71])

	Portal Vein (PV)	**Hepatic Artery (HA)**
Vessel wall thickness (mm)	0.61	0.49
Vessel lumen diameter (mm)	7.8	3.8

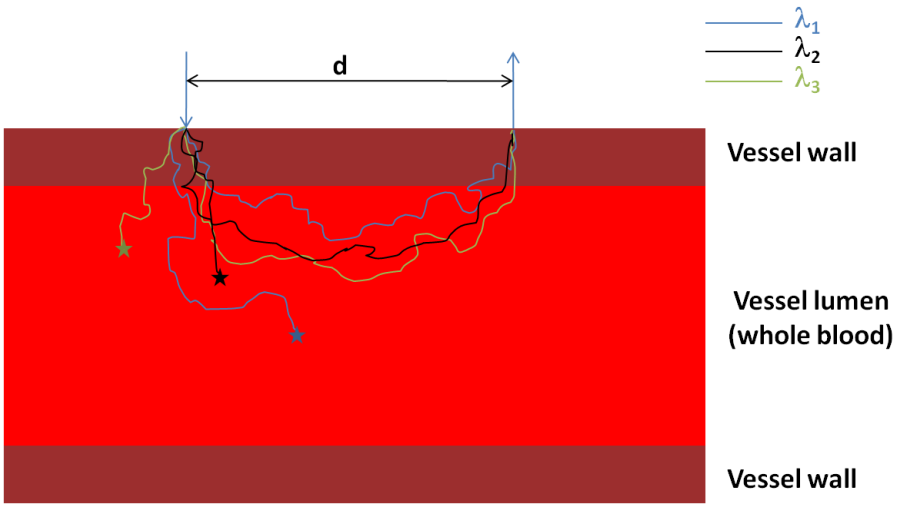

Fig. 6. Schematic of the multilayer MC model mimicking a blood vessel.

For each run, 1 million photon packets were launched in different directions, with equal probability, within the Numerical Aperture (NA) of the source. The program recorded the collected intensity at the tissue surface and the corresponding penetration depth of each photon collected, producing a photon distribution map indicating at every point of the surface how many photons were collected and the penetration depth of each photon. This feature was used to find the probing depth for every source to detector separation and to separate the background intensity collected from photons that are probing the blood.

Table 2. Blood optical properties for two oxygenation states[29, 31]

λ (nm)	Oxygenated			Deoxygenated		
	μ_a (1/mm)	μ_s (1/mm)	g	μ_a (1/mm)	μ_s (1/mm)	g
735 nm	0.2408	80.5	0.9790	0.6025	80.5	0.9790
805 nm	0.4557	76.7	0.9786	0.3943	76.7	0.9786
940 nm	0.6555	67.7	0.9760	0.3744	67.7	0.9760

To study the effect of the source spatial distribution, the collected intensity was convoluted with the source spatial profile as discussed by Wang *et al.* [72]. All the modeling results were verified by comparison to MCML and CONV developed by Wang *et al.* [66, 72].

The performance of various wavelengths was studied by changing the optical properties of the layers to match those of the corresponding chromophore (tissue or blood) for that specific wavelength.

In Vitro Setup

To verify the modeling results, an *in vitro* system was constructed to measure perfusion and oxygenation in a liver phantom at different source - detector separations. Polydimethylsiloxane (PDMS) based phantoms were designed and fabricated to mimic the optical properties of liver tissue as described in details in Chapter IV. In summary, a mixture of PDMS, Al_2O_3 powder, Black India Ink, and blue food coloring was poured into a petri-dish containing a plastic tube (8 mm in outer diameter for the PV or 3 mm

for HA) fixed at 1 mm above the petri-dish bottom surface and cured at 65°C to completely crosslink the PDMS. The plastic tube was removed, and the resulting phantom is a slab with the optical properties of liver tissue containing a hollow cylindrical structure with similar dimensions to the vessel under investigation (PV or HA). Slabs of the same material were also fabricated for use in case extra-thickness above or below the initial design is needed. Fig. 7 shows a schematic of the phantom with the optical probe placed on top of it.

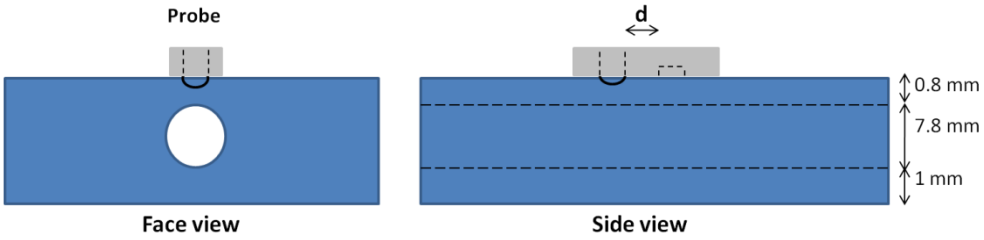

Fig. 7. Schematic of the PDMS based portal vein phantom showing the placement of the probe on top. The Light Emitting Diode is protruding out of the probe surface to provide better light coupling to the interrogation medium. The source to detector separation is referred to as d.

The phantoms used in this study mimicked the case where the sensor is placed on a blood vessel (PV or HA) at the entrance of the liver to monitor the blood supply. The phantoms were perfused with dye mixtures that simulate the optical properties of blood in its different oxygenation states. These mixtures are described in details and characterized in Chapter IV.

Two peristaltic pumps (Gilson, Minipuls 3) driven using LabVIEW via a data acquisition board (National Instruments, USB 6009) were used to pump the dye

solutions through the phantom. Extra care was taken to ensure no air bubbles were circulated. The driver signal used to control the pumps was a square wave. The frequency and the pulse width were set to the desired values that mimic the cardiac pulsatile flow pattern. Each pump can be used to pump a different dye solution corresponding to different oxygenation states and the mixture can mimic any oxygenation state by changing the ratio of the pump speeds.

The probes used are circular (1 inch in diameter) and contain a single can package with four light emitting diodes (epitex, L660/735/805/940-40B42-C-I) and a silicon photodetector (Hamamatsu, S2833-01). Five different LED to photodetector spacings were used ranging from 2 mm to 10 mm (edge to edge separation) with a step of 2 mm. A mechanical arm was used to fix the probe on the surface of the phantom above the hollow cylinder (Fig. 7) with the LED and photodetector aligned along the tube. Fig. 8 shows the complete setup with the LabVIEW interface used for data collection and visualization.

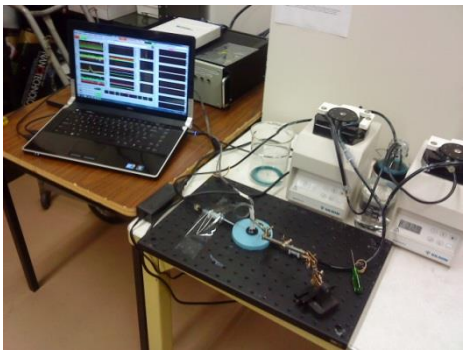

Fig. 8. In vitro *setup showing the two peristaltic pumps pushing a dye solution through the PV phantom with the optical probe held on top with a mechanical arm. Note the phantom appears light bluish in color to the eye but has the optical properties, in the 735-940 nm wavelength range, of liver.*

Results

Monte Carlo Modeling Results

The diffuse reflection intensity at the surface decayed rapidly with increasing source-detector separation for all three wavelengths, for both simulated oxygenated and de-oxygenated signals. However, these intensities (the case of oxygenated blood is shown in Fig. 9a) carry signal from the blood volume as well as background intensity from the surrounding tissue. To separate the signal from background intensity, we looked at the difference between the collected intensity in the cases of oxygenated and deoxygenated blood. This difference eliminates the constant background intensity and is a better indicator of the optimal spacing to collect the highest signal probing the blood volume. The difference showed a plateau phase followed by a quick decay for the 735 and 940 nm wavelengths. This plateau extends to 0.55 and 0.45 mm for the 735 and 940 nm wavelengths respectively (Fig. 9b). However, the 805 nm wavelength, since it is near

the isobestic point, carried little information about the oxygenation state. Note that the 805 nm wavelength does have a bias to the 940 nm side, since in our model 805 nm is on the IR side of the isobestic point. After the peak, the difference signal decayed rapidly to reach 10% of its maximal value at 2.4 and 2.2 mm for the 735 and 940 nm wavelengths respectively. Despite the rapid decay, there was still a relatively long range where the signal is strong enough to have a dynamic difference between the two oxygenation states.

In Fig. 9 the signal is presented in terms of its total reflectance at a specific distance (Fig. 9a for oxygenated simulation) and difference between oxygenated and de-oxygenated reflectance (Fig. 9b). However, the overall intensity decays with increasing separation. This implies that, although signal (*S*) is decaying, the signal to background ratio (*SBR*) might be constant or even increasing. To validate this hypothesis, we looked at the normalized intensity that we defined as the ratio of signal difference (*S*) to the total average intensity (I_t). Equation (II.1) shows the defined *SBR* ratio where R_{oxy} and R_{Deoxy} are the photon fluence at the surface in the oxygenated and deoxygenated state respectively.

$$SBR = \frac{R_{Oxy} - R_{Deoxy}}{0.5 \times (R_{Oxy} + R_{Deoxy})} = \frac{S}{I_t} \qquad \text{(II.1)}$$

S is the signal defined as the difference between the collected intensities in the oxygenated and deoxygenated states: $S = R_{Oxy} - R_{Deoxy}$

I_t is the average total intensity in the oxygenated and deoxygenated states: $I_t = (R_{Oxy} + R_{Deoxy}) \big/ 2$

Note that I_t is the average total intensity, thus it comprises both signal and background and the defined *SBR* is the ratio of the difference signal to the total collected intensity which gives an idea about the signal to background ratio.

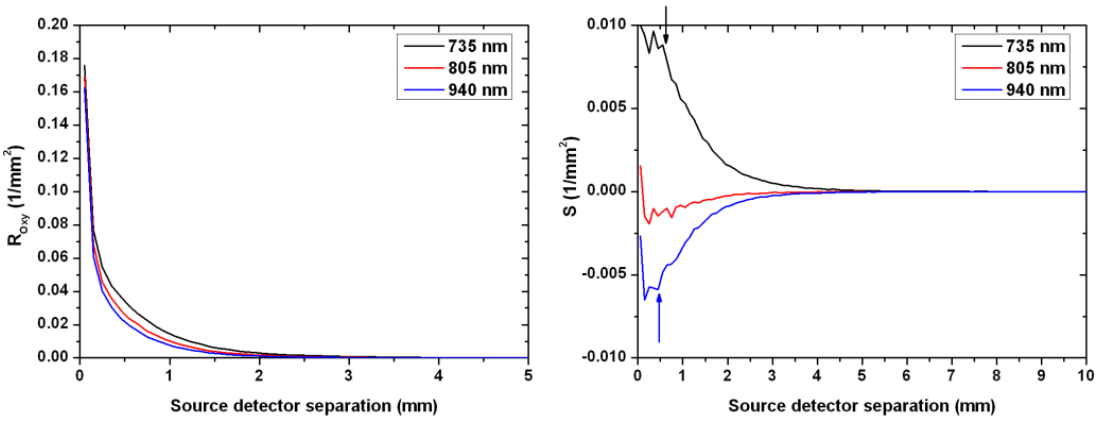

Fig. 9. Light fluence & oxygenation signal as a function of source to detector separation. (Left) Fluence decay curves for all three wavelengths as a function source to detector separation. These curves correspond to the case of oxygenated blood. The curves indicate a rapid decay in total collected fluence with increasing separation. (Right) The difference ($S=R_{OXY} - R_{DEOXY}$) as a function of source to detector separation. The signal S shows a plateau phase with a maximal value followed by a rapid decay for the 735 and 940 nm wavelengths. The 805 nm wavelength carries a low oxygenation signal since it was slightly on the IR side of the isobestic point. The arrows indicate the end of the plateau phase and the start of the rapid decay.

Fig. 10 shows the *SBR* calculated using (II.1) as a function of source-detector separation. In the source-detector separation range shown (0.05 to 10 mm) the absolute value of the *SBR* is monotonically increasing. Past this range, this ratio is very noisy due to the weakness of the collected intensity.

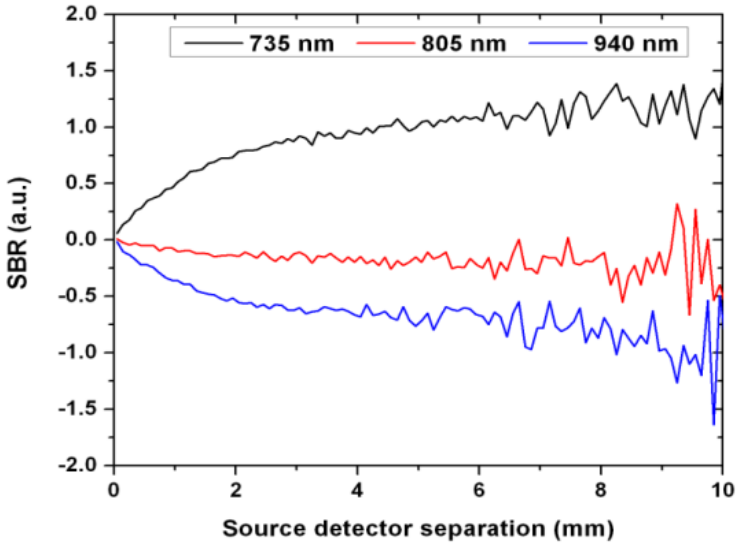

Fig. 10. SBR as a function of source to detector separation. SBR starts from 0 and absolute value increases monotonically (Note by definition this means at 735 nm the SBR is positively increasing and at 940 nm the SBR is negatively increasing with separation indicating a decrease in the background to signal ratio. For the 805 nm wavelength, SBR is close to zero with a little bias to the negatively increasing 940 nm side, since in our model 805 nm is on the IR side of the isobestic point.

To better understand this phenomenon, we added to our MC algorithm a feature to record the penetration depth of the collected photons on the tissue surface. As shown in Fig. 11(a) below, although the total intensity decreased, the ratio of photons collected from the vessel lumen (deeper than 0.5 mm which is the vessel upper limit) increased relatively to the photons probing the shallow tissue as we increased the source to detector separation. However, the total number of collected photons probing the blood layer decreased. This supports the data presented in Figures 9 and 10 and indicates that the total intensity and signal decrease with increasing source to detector separations but the signal to background ratio increases. These findings are very important to know

when designing probes for this type of sensor in order to optimize the use of the dynamic range of the photodetector as discussed in further details in the *Discussion* section.

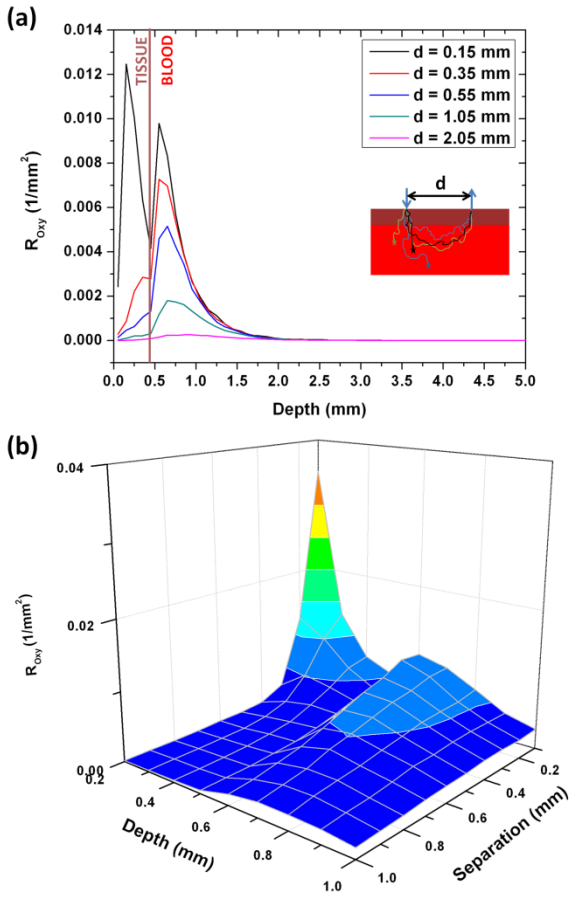

Fig. 11. The distribution of the collected photon fluence on the penetration depth for the 735 nm wavelength. Photons with a penetration depth higher than 0.5 mm are considered as signal while those that have a shallower penetration depth are considered as background since they do not probe the blood volume. Panel (a) shows the data for 5 selected source-detector separations. Panel (b) is a 3D representation of the data.

Fig. 11(b) shows the collected photon fluence as a function of separation and penetration depth of each photon. This figure shows two peaks before and after the vessel lumen boundary at 0.5 mm. The shallower peak corresponds to the background intensity and, although higher in intensity, decays (as a function of source to detector separation) faster than the second peak that corresponds to the signal collected from the vessel lumen. The axes on this graph start at 0.2 mm (depth) and 0.1 mm (source to detector separation) because before these points there is a high background peak (at 0.1 mm depth and 0.1 mm source to detector separation) that is difficult to visualize with the signal peak on the same scale.

One way to maximize both quantities, *SBR* and *S*, if weighted equally is to maximize their product (equation II.2). Fig. 12 shows the product as a function of source-detector separation.

$$S * SBR = \frac{\left(R_{Oxy} - R_{Deoxy}\right)^2}{0.5 * (R_{Oxy} + R_{Deoxy})} \qquad \text{(II.2)}$$

As expected, the 805 nm wavelength carries almost no oxygenation information and the product is stable at nearly zero for all spacings. However, for both the 735 and 940 nm wavelengths, the product starts as an increasing function with source to detector separation and plateaus at 0.35 and 0.45 mm respectively. This plateau ends and a rapid decay starts around 1.25 and 1.35 mm respectively.

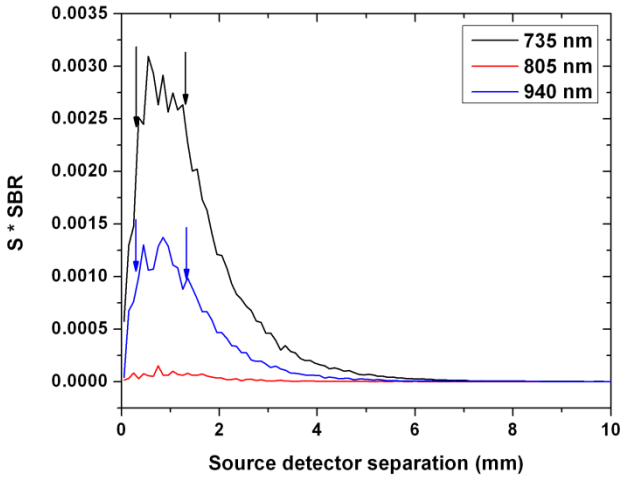

*Fig. 12. The product of signal (S) and SBR as a function of source to detector separation. The product shows a plateau phase with maximal S*SBR product for the 735 and 940 nm wavelengths. The 805 nm wavelength carries almost no oxygenation signal and the product is stable at nearly zero.*

All the previous results were based on a collimated point source. Other probe characteristics such as the source NA and spatial profile might have a significant influence on these findings. The NA effect was studied by launching the photons in different directions, with equal probability, within a cone corresponding to a numerical aperture specified by the user. As expected, the numerical aperture of the source had no significant effect on the results because of the highly scattering nature of tissue.

To investigate the effect of the source spatial profile, we compared the results of the point source to those of a 4.5 mm cylindrical flat beam mimicking the light emitting diodes used in our probes (Epitex, L660/735/805/940-40B42-C-I) and a photodetector with an active area of 2.4 mm x 2.5 mm (Hamamatsu, S2833-01). Fig. 13 shows the corresponding results.

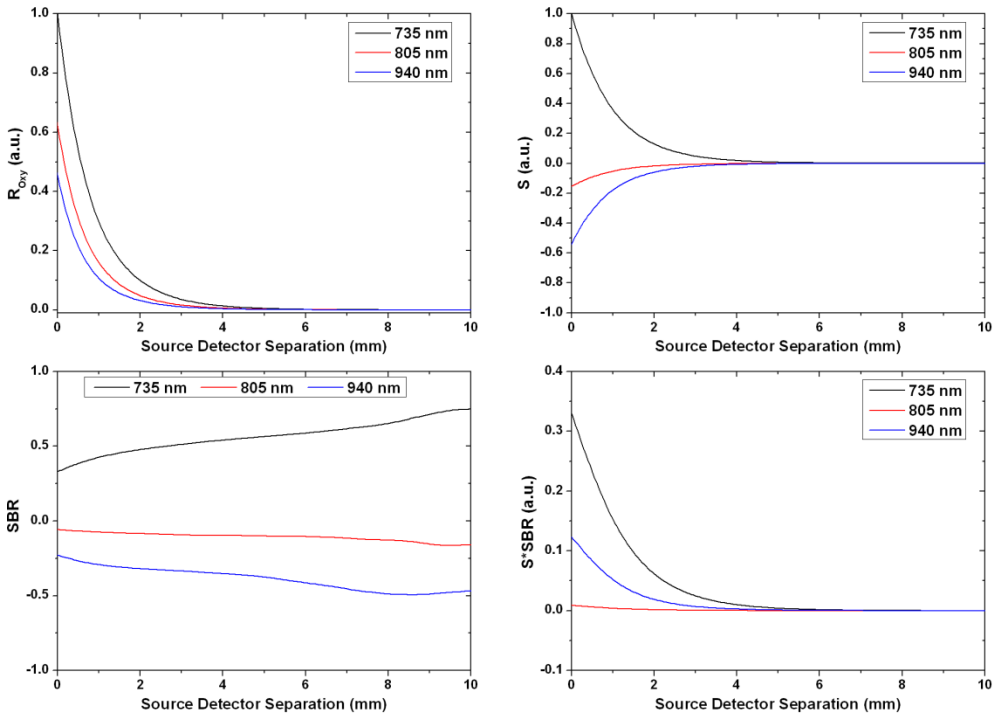

Fig. 13. MC modeling results for a 4.5 mm source and a 2.4 mm x 2.5 mm photodetector. The diffuse reflectance for all three wavelengths was normalized to the reflectance at the closest separation for the 735 nm wavelength. The signal S was normalized similarly.

Similar to the point source case, Fig. 13 shows a rapid decay in the intensity and signal as the detector is moved away from the source. The *SBR* ratio shows also a similar profile to the previous case with the main difference being the start point that is not equal to zero in that case. This is expected since the broad source can be considered as an assembly of point sources and even when the detector is placed right next to the source there will still be a point source at the other end that is far from the detector and is probing deep in the tissue collecting signal from the blood vessel lumen. Note that the results from the circular flat beam appear less noisy due to the convolution process, used

to account for the source spatial profile, which eliminates high frequency noise. This can be thought of as having multiple point sources, instead of one, launching photons leading to a less noisy diffuse reflectance signal. Table 3 summarizes these results.

Table 3. Summary of the MC modeling results[a]

		Point Source		4.5 mm beam	
		Maximum	**Plateau Phase**	**Maximum**	**Plateau Phase**
735 nm	**S**	0	0 – 0.55 mm	0	x
	SBR	↗	> 3.05 mm	↗	x
	S*SBR	0.55	0.35 – 1.25 mm	0	x
940 nm	**S**	0	0 – 0.45 mm	0	x
	SBR	↗	> 2.55mm	↗	x
	S*SBR	0.85	0.45 – 1.35 mm	0	x

[a]↗ refers to a monotonically increasing function with increasing source-detector separation. The plateau phase refers to ranges of source-detector separations where the corresponding function is changing relatively slow compared to the rest of the source-detector separations.

In Vitro Results

To verify the modeling results and apply them to our system, we used the setup described in the *in vitro setup section*. Five source-detector spacings were used and compared to the model. For each run, one of the two dye solutions corresponding to the two oxygenation states of blood, was passed through the phantom using the flow system previously described. We alternated between the dye solutions to calculate the quantities defined in the previous *section (MC results)* and the phantom was washed in between runs by flowing deionized (DI) water through the fluidics system. This experiment was repeated three times. For each set of experiments, data was collected with the shortest

spacing probe first and its position on the phantom was marked to guaranty similar coupling between all probes. Fig. 14 shows the signal *S*, previously defined in equation II.1, for the *in vitro* phantom studies compared to the MC modeling results. The data from 3 sets of experiments was averaged. In terms of calibration, the average of the shortest spacing probe was normalized to the model to account for the probe characteristics such as detector sensitivity and LED power, the same calibration factor was applied to the rest of the probes. Since the 805 nm wavelength carries minimal information about changes in the dye solution (i.e. simulated oxygenation), it was used as a baseline to account for any changes not related to varying the dye solution as shown in equation II.3. In the ideal case, where there are no changes in the background, the intensity on the 805 nm wavelength is the same for both dye solutions and equation II.3 reduces to (I_{Oxy} - I_{Deoxy}). In this case, I_{Oxy} and I_{Deoxy} are the collected intensity at the wavelength of interest when the phantom is perfused with the dye solution mimicking oxygenated and deoxygenated blood respectively.

$$\begin{aligned} S &= (I_{Oxy} - I_{Oxy805}) - (I_{Deoxy} - I_{Deoxy805}) \\ &= (I_{Oxy} - I_{Deoxy}) - \Delta I_{805} \end{aligned} \qquad \text{(II.3)}$$

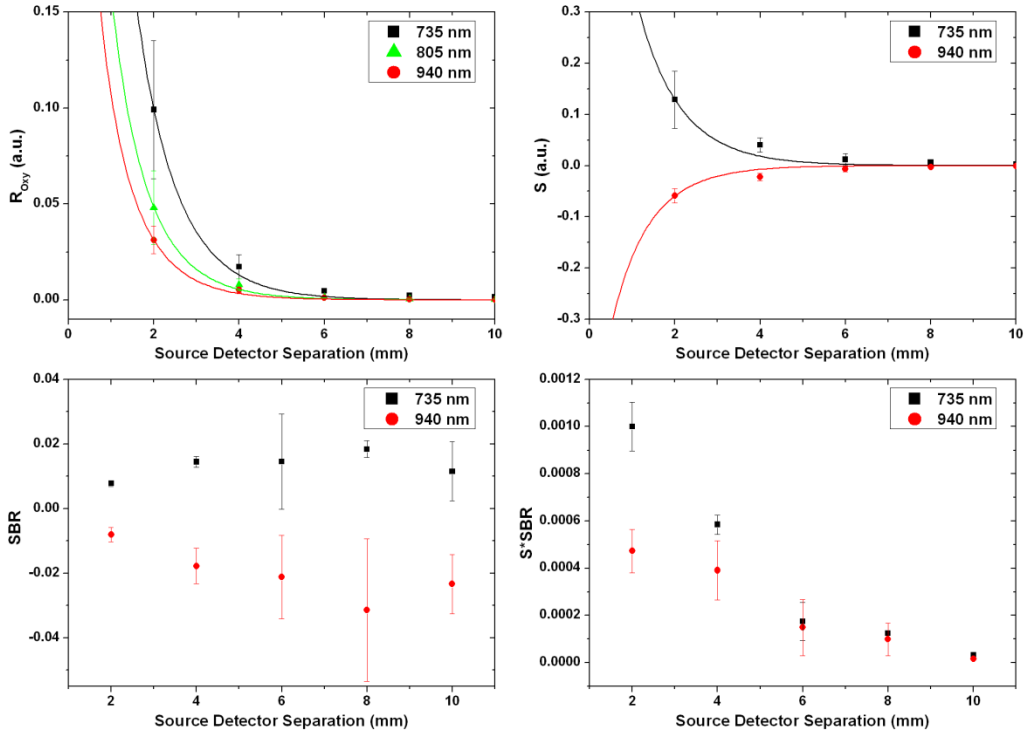

Fig. 14. In vitro *data collected from the PDMS based phantom perfused with the dye solutions. The solid lines show the data from the MC model while the squares and circles represent the average of the collected data from the phantom at the 735 and 940 nm wavelengths respectively. The error bars correspond to (+/-) one standard deviation.*

Wavelength Selection

Wavelength selection is an essential part in designing any optical system and in particular spectroscopy based sensors. The first step in selecting suitable wavelengths for a spectroscopy sensor is determining what wavelengths are sensitive to the analyte or property of interest. In the case of an oxygenation and perfusion sensor, the wavelengths have to be sensitive to the hemoglobin oxygenation state. To study that we looked at the change in the extinction coefficient with the oxygenation state (equation II.4). Figure 15 shows the normalized oxygenation signal as a function of wavelength. The highest

change in hemoglobin's extinction coefficient is around 660 nm which is commonly used in pulse oximeters. Note that the zero crossings correspond to isobestic points where the optical properties are independent of the oxygenation state.

$$S_\lambda = \left| \varepsilon_{Hb,\lambda} - \varepsilon_{HbO_2,\lambda} \right| \tag{II.4}$$

Figure 15 shows that there are various wavelengths bands that are sensitive to hemoglobin oxygenation state. However, many of these wavelengths have a limited penetration depth and are not suitable for sensing in tissue. Equation II.5 shows the theoretical mean penetration depth in a homogeneous medium as a function of its optical properties.

$$Z_{r,\lambda} = \frac{0.476 r^{1/2}}{\left(\mu_a \mu_s'\right)^{1/4}} \tag{II.5}$$

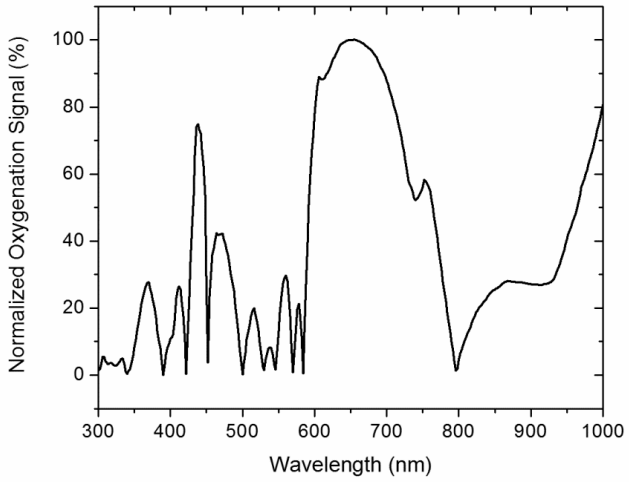

Fig. 15. Normalized oxygenation signal vs wavelength.

This equation was derived by Weiss *et al.* based on a random walk model [73]. It defines the mean penetration depth (Z) as a function of the source to detector separation (r), the absorption coefficient (μ_a), and the reduced scattering coefficient of the medium (μ'_s). The mean penetration depth vs. wavelength is shown in figure 16 for various source-to-detector separations. The mean penetration depth increases significantly for NIR wavelengths (700-1000nm) compared to their visible counterparts. That is why this region is referred to as the therapeutic window (also known as optical window) and most optical sensors and imaging systems operate in this wavelength range. In addition, since the measurements of the described sensor require the use of multiple wavelengths, and to avoid probing different tissue volumes on the different wavelength which can lead to erroneous reading, we wanted all three wavelengths to have a similar penetration depth and that is why we selected all three wavelengths in the 700-950nm band where the penetration depth is similar. Although this range is less sensitive to oxygenation changes compared to the 660 nm wavelength, but it does carry oxygenation information in wide bands that are suitable to use with LEDs.

The sensor requires the use of one isobestic point and in this range there is one isobestic point around 800 nm and LEDs are commercially available with emission wavelength in that range. In all the following studies, unless otherwise specified, 805 nm LEDs were used as one of the three wavelengths. It is preferable to have the other two wavelength on opposite sides of the isobestic point. This allows to have one wavelength more sensitive to HbO_2 and another more sensitive to Hb. We selected the 735 nm and

940 nm wavelengths. These wavelengths are commercially available, sensitive to oxygenation changes, and have similar penetration depth.

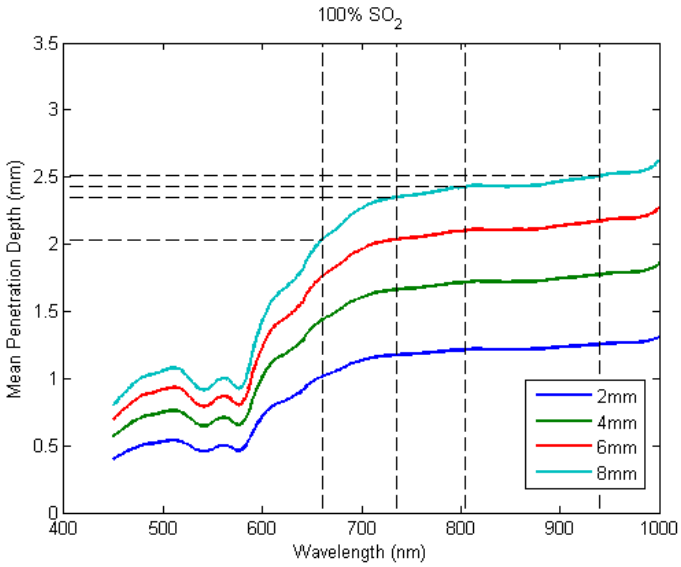

Fig. 16. Mean penetration depth in liver tissue perfused with oxygenated blood as a function of wavelength for various source to detector separations.

Another problem with the 660 nm wavelength that led us to avoid its use is the high extinction coefficient of deoxy-hemoglobin on that wavelength (figure 2). This leads to a limited penetration depth on this wavelength for low oxygen saturation states [58]. Using equation II.5 and assuming that the liver tissue is perfused with deoxygenated blood (SO_2=0%), we can calculate the mean penetration depth shown in figure 17. It can be seen that for low oxygenation states, the 660 nm is highly attenuated and has a lower penetration depth compared to the selected wavelengths (735, 805, and

940 nm). This is important to account for since the liver gets 75% of its blood supply from the portal vein which carries blood with low oxygen saturation levels [1].

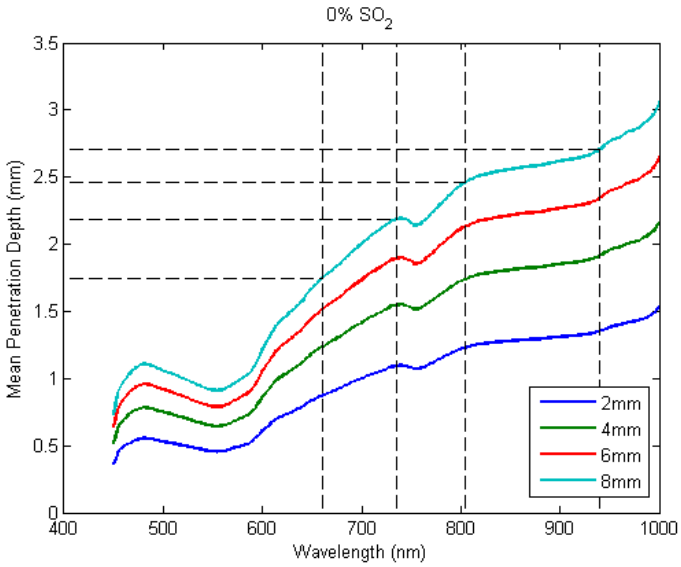

Fig. 17. Mean penetration depth in liver tissue perfused with deoxygenated blood as a function of wavelength for various source to detector separations.

Filter Design

The main signal in a PPG sensor is the cardiac modulation of the optical signal. As discussed earlier, this signal is relatively weak [48] and is typically filtered and amplified before any digitization. If not filtered and amplified, the signal will be buried by electronic and digitization noise. One of the main challenges in accomplishing that goal is the relatively high amplitude noise surrounding the cardiac cycle component. The normal resting heart rate for human adults ranges between 60 and 80 bpm (1 and 1.33 Hz) [74]. As discussed earlier, prior to filtering the PPG signal has many other

components one of which is the respiratory rate due to the pulsation of veins and motion artifacts in the measuring site. The normal resting respiratory rate ranges from 12 to 20 respirations per minute (0.2 – 0.33 Hz). The collected cardiac cycle component is much weaker than most other variables in the PPG, including the respiratory component, and requires high amplification. A successful filtering scheme has to separate these two components and attenuate the respiratory component on the AC channel to avoid saturating the high gain amplifiers.

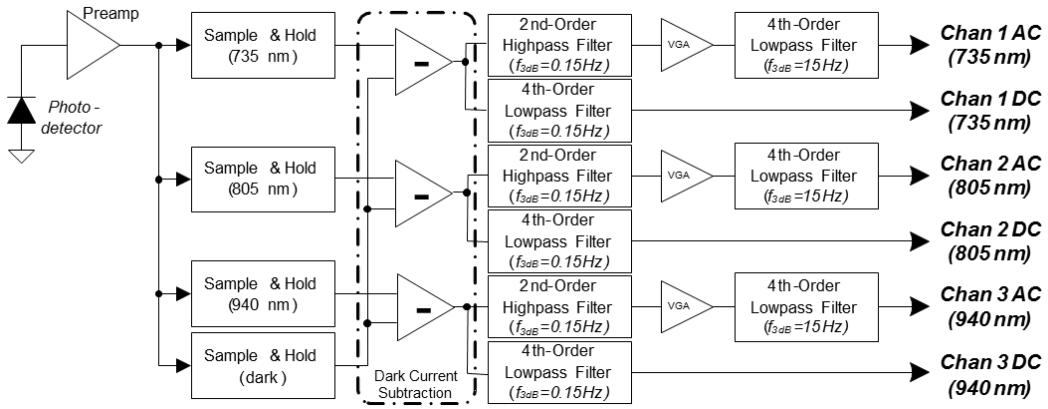

Fig. 18. Block diagram of the signal processing electronics in the bench-top system [63].

The first bench-top system that was used in the *in vitro*, *ex vivo*, and early *in vivo* studies used a 4th order Low Pass Filter (LPF) with Butterworth response characteristics and a 3 dB cutoff frequency of 0.15 Hz on each of the DC channels. The AC channel had a 4th order High Pass Filter (HPF) and a 4th order LPF both with Butterworth response characteristics and a 3 dB cutoff frequency of 0.15 and 15 Hz respectively.

Figure 18 shows the diagram of the signal processing electronics for the bench-top system [63]. All filters were partitioned using a cascade of 2^{nd} order filters implemented using Sallen-Key active filter topologies. The VGA allows the user for selecting the AC gain from a range of 1 V/V to 440 V/V using DIP switches.

The bench-top system was used for testing and optimizing the hardware design. The filters used in that system were not capable of blocking the low-frequency noise adequately and the AC channels were often saturated by the respiratory artifacts during *in vivo* porcine studies. The filters were modeled in custom LabVIEW software that was built to model the performance of various filters and their ability to block low-frequency noise. The simulation assumed a low frequency sinusoidal respiratory signal that has a ten times higher amplitude than the cardiac cycle signal. Its frequency was varied between 0.1 and 0.33 Hz to model the different rates of respiration. The frequency of the cardiac signal was changed between 1 Hz, mimicking the case of a human adult at rest, and 2.1 Hz, mimicking the case of porcine to assess the performance for animal studies. Figure 19 shows a snapshot of the simulated signal and its corresponding power spectrum as seen on the LABVIEW interface.

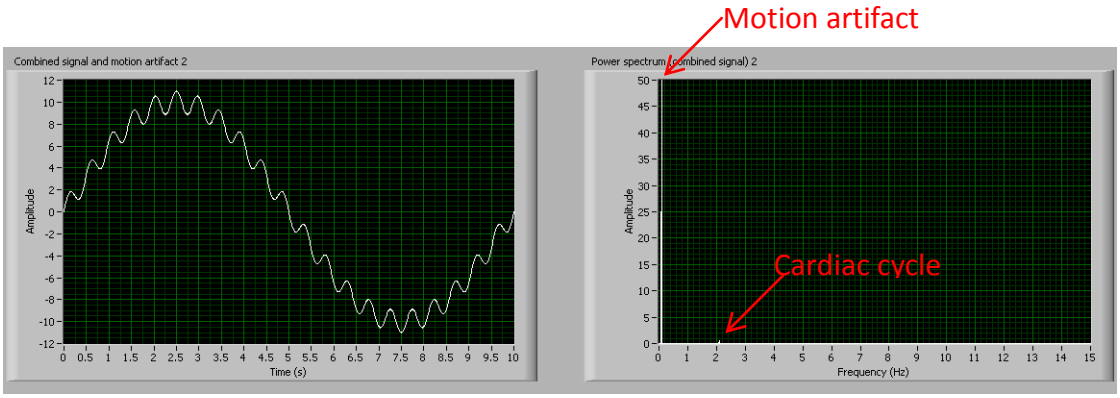

Fig. 19. The simulated signal used to test the performance of the designed filters showing the cardiac cycle component and a motion artifact at the respiratory rate.

To quantify the performance of the filters we looked at the power spectrum of the input and output signals and defined the following quantities:

Background : Amplitude of the low-frequency peak

Signal : Amplitude of the cardiac cycle peak

SBR : Signal to background ratio

When using the filter described above, the input SBR was calculated to be 1/100 (Signal = $(1/\sqrt{2})^2$ = 0.5 and background = $(10/\sqrt{2})^2$ =50) and the output SBR was approximately 1/17 (5.8 folds enhancement) which means the background signal is still more than 4 times larger in amplitude than the output signal. Figure 20 shows the characteristics of the filter and the output signal after filtering.

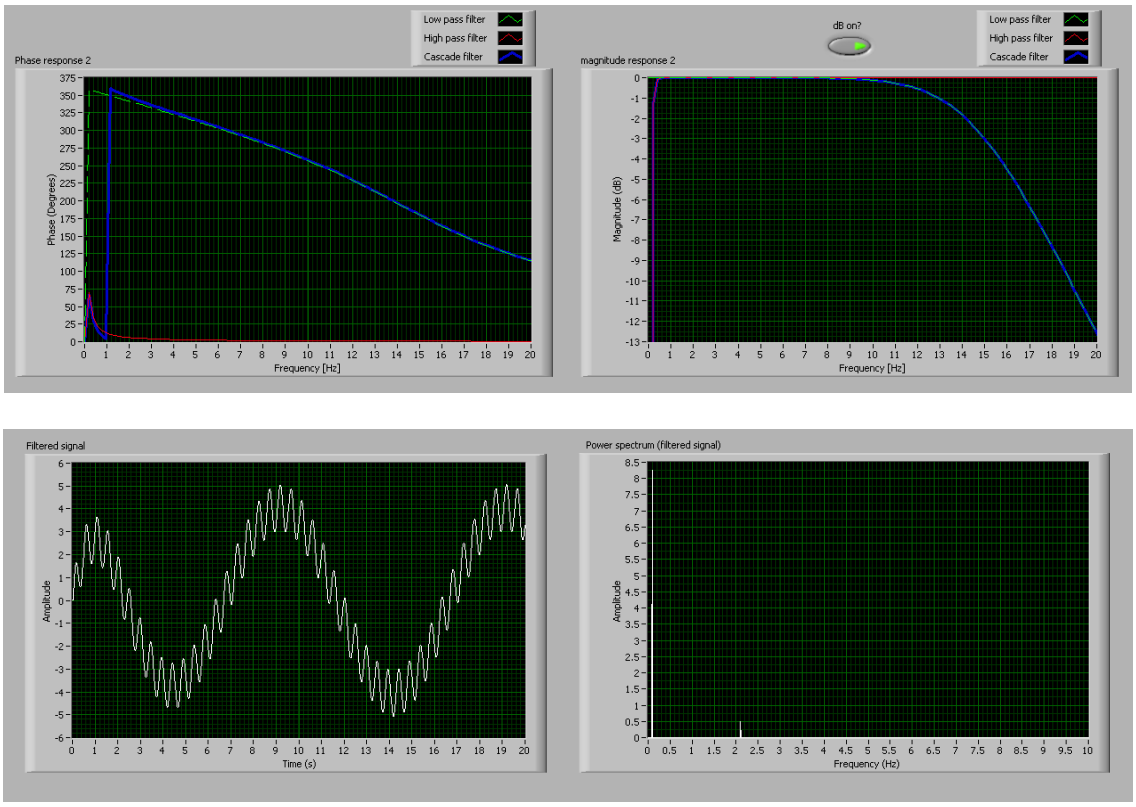

Fig. 20. Filter characteristics (upper panel) and response to the simulated signal (lower panel) of the bench-top system.

To enhance that, we tried various filters limiting them to the 4th order to limit the filters to a simple two stage implementation. We found that the LPF on the AC channel does not have a substantial effect since the majority of the background and noise are low frequency signals (respiration, motion artifact, etc.). For the high pass filter, we decided to use a 4th order Butterworth filter with a 3dB cutoff at 0.55 Hz. This filter leads to an output SBR of 1111 indicating that the background was highly attenuated (5 orders of magnitude) and the signal amplitude is more than 33 times higher than the background

on the output. Figure 21 shows the described results and the characteristics of the proposed filter.

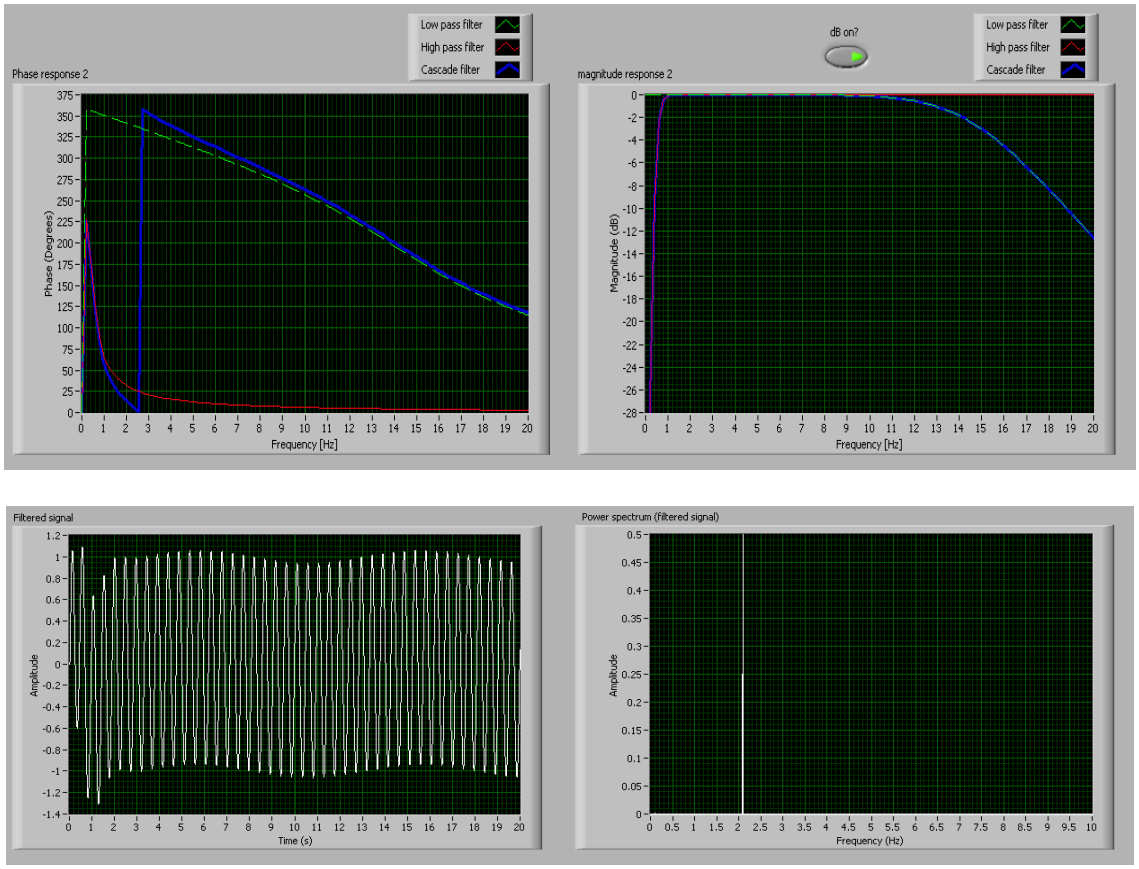

Fig. 21. Filter characteristics (upper panel) and response to the simulated signal (lower panel) of the redesigned band-pass filter.

Next we tested the worst case scenario when the heart rate is at 60 bpm (1 Hz) and the respiratory rate is at 20 breaths per minute (0.33 Hz). The cardiac signal used in this case simulated the shape of the pulse as reported by Millasseau *et al.* [75]. In this case the proposed filter resulted in a SBR of 0.625 (signal amplitude 1.26 times weaker

than background) which was a 2 orders of magnitude improvement over the filters in the original bench-top system (SBR of 1/100). Figure 22 shows the results of the proposed filter.

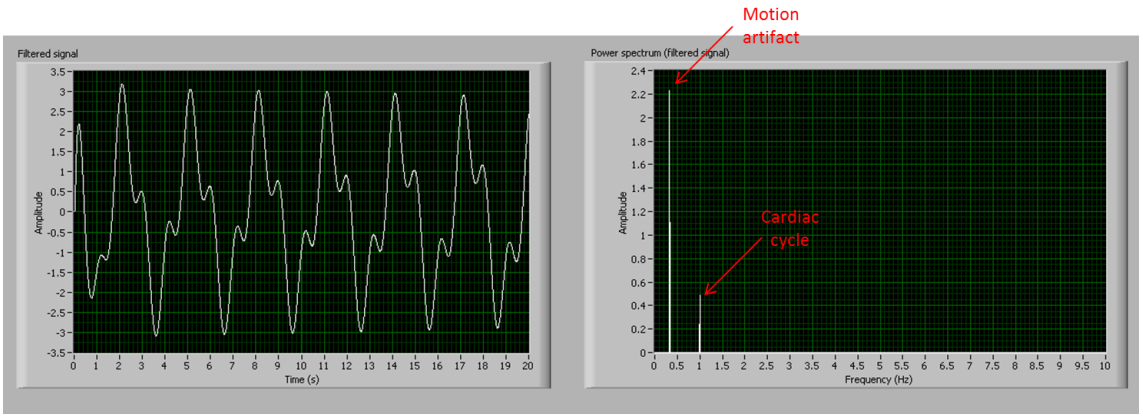

Fig. 22. The output signal of the redesigned band-pass filter in response to a cardiac signal at 1 Hz (60 bpm) and a respiratory signal at a rate of 0.33 Hz (20 bpm).

Discussion

The probing depth in diffuse reflection is highly dependent on the source to detector separation. Large separations lead to deeper probing which increases the blood signal carrying portion of the total intensity. However, this increases the optical path length and attenuates the total intensity causing lower levels of light to be collected which leads to higher system error. Photodetectors and electronic amplifiers have a limited dynamic range, and optimizing the separation is critical to increase the levels of the signal without saturating the detection electronics with background intensity. Using higher separations lead to better signal to background ratios (less sample noise) but at

the same time it decreases the intensity of the collected light leading to a decrease in the system signal to noise ratio assuming fixed electronics noise. A compromise has to be made between the signal to background ratio and the absolute values of the collected intensity and signal. Our model showed that, for a point source, there is an optimal range with high signal levels and high signal to background ratio for both wavelengths (735 and 940 nm) extending from 0.45 to 1.25 mm. These values change with the spatial profile of the source. For the case of a 4.5 mm LED, most of this plateau phase overlapped with the source and only a peak was seen right next to the source followed by a signal decay. Despite this decay, the collected signal is high enough to be detected millimeters away from the source. This was shown in our *in vitro* data (Fig. 14) where changes in oxygenation were still detected 10 mm away from the edge of the source. The previously defined *SBR* ratio showed a similar increasing trend for the *in vitro* data. However, past 6-8 mm edge to edge separation the ratio showed a decreasing trend that is due to the system noise since the total intensity at this point is close to the detection limit of our hardware. Note that the same amplification level was used for all separations to provide a fair comparison. The numbers for the *SBR* ratio from the *in vitro* data are much lower than those calculated by the model due to multiple reasons. The main reason for this discrepancy results from the use of a simplified 2D layered model with the blood vessel represented as a layer of blood. In the real case, the blood vessel is surrounded by tissue that contributes to the background intensity and not the oxygenation signal. Also, the dynamic range between the optical properties of the two dye mixtures mimicking the two oxygenation states is less than that of whole blood which causes a reduction in the

signal (*S*) intensity. However, this second factor is not as significant as the first since the optical properties of the dye mixtures at the 940 nm wavelength match those of whole blood very closely and the reduction in the *SBR* ratio can still be seen. As expected, similar to the modeling results, the product S*SBR also showed a decreasing trend for the *in vitro* data. This shows that the optimal performance of this source-detector pair is at the closest separation.

To better understand this tradeoff between signal levels and the signal to background ratio, we ran simulations for different oxygenation levels and observed the correlation between the photon fluence values and the oxygenation levels as shown in Fig. 23 (a-c). For very short separations, the coefficient of determination, R^2, started as an increasing function and peaked at 0.45 mm separation with a peak value of 0.9941. Past this point, R^2 showed a decreasing trend and reached 0.9795 (0.7022) at 1.05 mm (10.05 mm) separation. As for the slope of the linear fit, it showed a similar trend with increasing source-detector separation as the signal S which was expected (Fig. 23-d).

The coefficient R^2 shows that, although the slope representing the signal level is highest for the shortest separation (Fig. 23-d), the optimal spacing where the signal correlates best with changes in the vessel lumen is at 0.45 mm. This is shown in Fig. 23(a-c) where the slope and intensity values are the highest in panel (a) (d = 0.15 mm) while the photon fluence doesn't correlate with oxygenation as closely as in the top right panel (d = 0.45 mm).

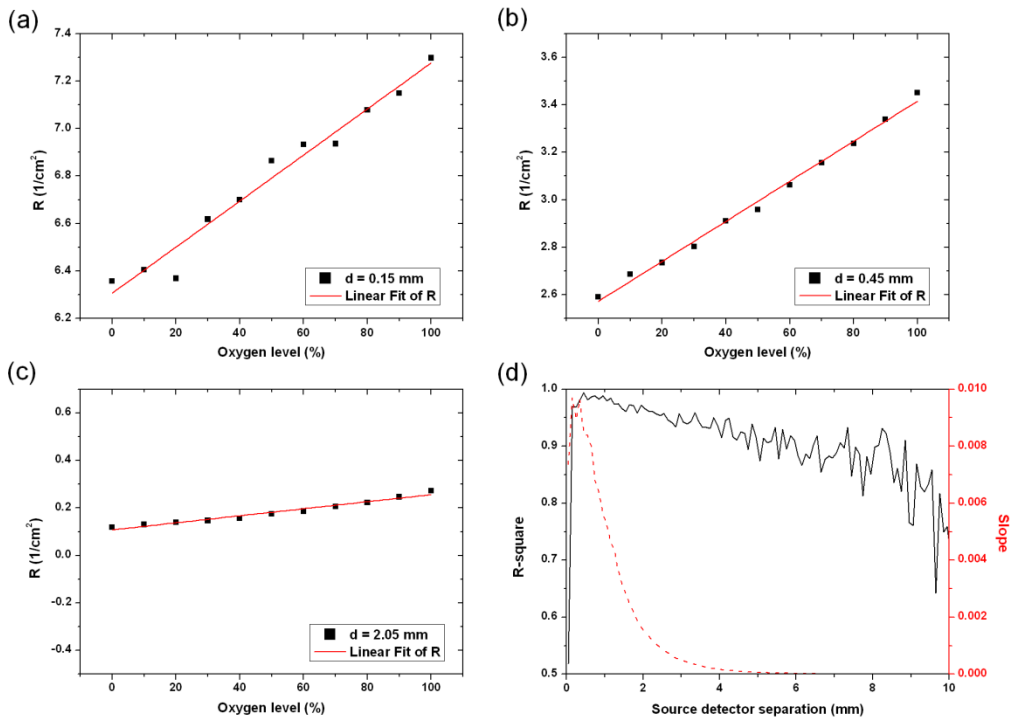

Fig. 23. Photon fluence vs. oxygenation level. The three panels (a-c) correspond to three different source-detector spacings indicated in the inset legends. At 0.45 mm separation, the change in diffuse reflection correlates well with the oxygenation changes (R^2 = 0.994) and the slope of the linear fit is high (0.00844) indicating a good sensitivity to oxygenation changes. Panel d shows the changes of the R^2 factor and the slope as a function of the source to detector separation.

Although the principle we used in optimizing the source-detector separation relies on changing the oxygen saturation of the blood and monitoring its effect on the collected diffuse reflectance, the results stand true for any change in the optical properties of the blood whether they were due to oxygenation, perfusion or hematocrit variations.

As mentioned earlier in the introduction, this sensor can be used to monitor perfusion and oxygenation in many other visceral organs. Since the optimal source-

detector separation is a function of the optical properties and the dimensions of the vessel under investigation, the results presented in this paper stand true only for the case of the portal vein. However, the same methods employed in this chapter can be used to define the optimal source-detector separation for similar applications.

Chapter Conclusions

Source to detector separation is a major factor in optimizing the performance of any diffuse reflectance based optical sensor. This becomes more important in the case of implantable biosensors where power consumption is of significant concern. In this work, we modeled the performance of an implantable perfusion and oxygenation sensor and found a source-detector separation of around 0.5 mm to be optimal in the case of a point source. Closer placement of the detector yields very high background intensity while moving the detector further than 1.2 mm shows a rapid decay in total intensity and signal levels. For the more realistic case of a 4.5 mm diameter LED package and a 2.4 mm x 2.5 mm photodetector, it was shown that the highest signal is collected with the source and detector placed right next to each other. However, similar to the point source case, it was shown that larger separations lead to higher *SBR*.

The results were compared to data collected from *in vitro* phantom studies. We reported a dye solution mimicking the absorption properties of the two oxygenation states of blood. These mixtures can be useful in characterizing and testing any optical sensor that probes blood. We used these mixtures to perfuse a phantom mimicking the optical and anatomical properties of the portal vein and the results were used to verify our modeling data. The *in vitro* data showed similar trends to those of the MC model

with some contribution from the system/hardware noise that caused the *SBR* ratio to show a decreasing trend past 6-8 mm source-detector separation. In the remainder of this dissertation, a 2 mm (edge to edge) separation was used in all experiment unless otherwise indicated.

In addition, the filter design for the high amplification AC channel was discussed. The results show that a 4^{th} order filter with a 3 dB cut-off frequency of 0.5 Hz enhances the signal to background ratio on the AC channel substantially. These findings were later tested *in vivo* as shown in Chapter V and lead to a significant enhancement in the performance of the system by avoiding amplifier saturation from background signals. Finally, the wavelength effects on the penetration depth and oxygenation signal were investigated and the penetration depth was found to be relatively constant throughout the 700 – 1000 nm range which has several bands that can be potentially used for oxygen saturation measurements.

CHAPTER III

THEORY AND SIGNAL PROCESSING

Light Propagation in Tissue

One of the challenges in the proposed sensor is the ability to separate the venous and arterial oxygenation signals. As described earlier in chapter I the collected light intensity from an NIRS sensor contains information about both arterial and venous oxygenation. The signal also contains very valuable information about the biomechanics of the tissue that is commonly ignored. In this chapter, we review some of the theory behind pulse oximetry and near infrared spectroscopy, the two main techniques used in this sensor.

When light is shined on tissue, it is scattered and absorbed by the various chromophores present in the medium. This process is described by the Beer-Lambert Law highlighted in equation III.1.

$$I = I_0 . \exp\left(-\varepsilon . c . l\right) \qquad \text{(III.1)}$$

This equation explains that the collected light intensity (I) is a function of: the source intensity (I_0), the extinction coefficient of the chromophore (ε), the chromophore concentration (c), and the optical pathlength (l). Any change in these parameters is reflected as a variation in the collected light intensity.

In tissue, there are many chromophores and equation III.1 is expanded to include the contribution of all chromophores. The resulting absorbance is the sum of all individual absorbances as shown in equation III.2.

$$I = I_0 . \exp\left(- \sum_i \varepsilon_i . c_i . l_i \right) \qquad \text{(III.2)}$$

The source intensity term is usually known and kept constant. The extinction coefficients of chromophores of interest are known and do not change. The pathlength term can be estimated using theoretical formulas [76], or measured [33, 47]. This leaves the chromophores concentration unknown. Measuring the collected light intensity at multiple wavelengths can be used to quantify each chromophore concentration. The number of wavelengths needed depends on the number of chromophores of interest. An oximetry sensor has to measure two chromophores at least, oxygenated hemoglobin and deoxygenated (reduced) hemoglobin. This requires a minimum of two wavelengths.

Temporal Frequency Analysis

Because of changes in the propagation medium, the optical pathlength, described above, is a function of time (equation III.3). Different phenomena cause this factor to change which results in a modulation of the chromophore concentration signal. This property can be used to isolate different components of the signal. This concept is the basis of pulse oximetry [36, 77]. The absorbance signal has many frequency components that correspond to a variety of physiologic processes, noise, and background changes. Some of these frequencies are: heart rate, respiratory rate, low frequency vascular autoregulation, and motion artifacts as shown in equation III.4.

$$I_{PD}(\lambda,t) = I_{LED}(\lambda,t).\exp\left(-\sum_i \varepsilon_i(\lambda).C_i.l_i(t)\right) = I_{LED}.\exp\left(-A(\lambda,t)\right) \quad \text{(III.3)}$$

$$A(\lambda,t) = \sum_i \varepsilon_i(\lambda).C_i.l_i(t) = \underbrace{\sum_a \varepsilon_a(\lambda).C_a.l_a(t)}_{\textit{Heart rate}} + \underbrace{\sum_j \varepsilon_j(\lambda).C_j.l_j(t)}_{\textit{Other frequencies}} + \underbrace{\sum_k \varepsilon_k(\lambda).C_k.l_k}_{\textit{DC component}} \quad \text{(III.4)}$$

The first two components shown in equation III.4 are the AC signal while the last one is the DC level. Notice that the DC component is not a function of time. The chromophores in the DC component include: arterial blood, venous blood, and surrounding tissue. Changes in the signal at the heart rate (component 1 in equation III.4) are due to changes in the arterial blood volume between the systolic and diastolic phase. This component is isolated and used to extract information about arterial blood.

The system described in this thesis utilizes the first and third component of equation III.4. The first component is extracted from the AC signal to measure arterial changes. The DC component is used to measure tissue oxygenation levels. Knowing the arterial oxygenation, the venous component can be extracted from the tissue oxygenation levels. The AC and DC components are also used to measure the perfusion index (PI), that tracks the pulse volume, and the tissue total hemoglobin concentration respectively. The following sections in this chapter describe the origins of the AC and DC signals and the flow of the signal processing used in the described sensor.

AC Signal

The assumption used in pulse oximetry is that the signal at the heart rate is solely due to changes in arterial blood. When other frequencies are filtered out, the only chromophores contributing to the resulting signal are those present in the blood, which are dominated by the various forms of hemoglobin. Assuming that the only forms of hemoglobin present are oxygenated and deoxygenated hemoglobin for simplicity, the heart rate component of equation III.4 can be reduced to the form below:

$$A(\lambda,t) = \varepsilon_{HbO2}(\lambda).C_{HbO2}.\Delta l + \varepsilon_{Hb}(\lambda).C_{Hb}.\Delta l = (\varepsilon_{HbO2}(\lambda).C_{HbO2} + \varepsilon_{Hb}(\lambda).C_{Hb}).\Delta l \quad \text{(III.5)}$$

The change in optical pathlength between systole and diastole is represented by Δl. This change is due to the varying blood volume in the interrogated tissue during the cardiac pulse and can be used to track pulsatile perfusion changes.

As mentioned earlier, multiple wavelengths are needed to obtain oxygenation information. Using a pair of wavelengths (R and IR), and taking the ratio of the two as shown below (equation III.6), we get the modulation ratio (R) that is used in pulse oximetry to track arterial oxygenation changes.

$$R = \frac{A(\lambda_R,t)}{A(\lambda_{IR},t)} = \frac{(\varepsilon_{HbO2}(\lambda_R).C_{HbO2} + \varepsilon_{Hb}(\lambda_R).C_{Hb}).\Delta l}{(\varepsilon_{HbO2}(\lambda_{IR}).C_{HbO2} + \varepsilon_{Hb}(\lambda_{IR}).C_{Hb}).\Delta l} \quad \text{(III.6)}$$

Rearranging the equation above, R can be written as a function of arterial oxygen saturation (SaO_2):

$$R = \frac{\varepsilon_{Hb}(\lambda_R) + (\varepsilon_{HbO2}(\lambda_R) - \varepsilon_{Hb}(\lambda_R)).SaO_2}{\varepsilon_{Hb}(\lambda_{IR}) + (\varepsilon_{HbO2}(\lambda_{IR}) - \varepsilon_{Hb}(\lambda_{IR})).SaO_2} \quad \text{(III.7)}$$

DC Signal

In addition to the background, the DC signal carries information about hemoglobin oxygenation changes that is typically not used in pulse oximetry. Figure 24 shows the change in the DC levels on three wavelengths (735, 805, and 940 nm) collected *in vivo* during a breath hold that causes the oxygenation levels to drop. Note that the 805 nm wavelength is at an isobestic point and does not change significantly during oxygenation changes. Although the absolute change in the DC levels are small (left panel), the normalized signals show a significant change over a 50 seconds period.

The processing methods used with the AC signal do not need to quantify the optical pathlength to get a measure of oxygenation changes. However, to get quantitative oxygenation measurements using the DC component, the optical pathlength has to be measured or estimated. The optical pathlength is a function of the optical properties of the propagation medium and the optodes separation. The Beer-Lambert law is typically modified when studying highly scattering media [78]. The modified Beer-Lambert law (MBLL) incorporates an additive term describing the scattering losses and a multiplier to account for the increase in optical pathlength caused by scattering of light. The pathlength correction factor is referred to as the Differential Pathlength Factor (DPF). MBLL can be written as:

$$A_\lambda = \log_{10}\left(\frac{I_0}{I}\right) \approx \varepsilon_\lambda .C.d.DPF + G \qquad \text{(III.8)}$$

Where d is the optode separation (source to detector separation) and G is the additive term describing scattering losses. Although G is unknown, it does not change

over time and by measuring the change in attenuation (A) between two different time points, we can rewrite equation III.8 to eliminate the additive term. The change in attenuation is commonly referred to as differential attenuation.

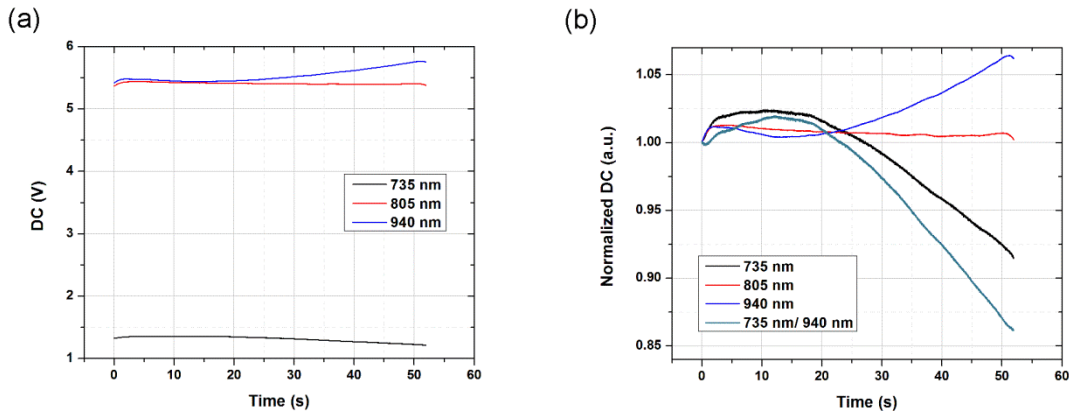

Fig. 24. Absolute (a) and relative (b) DC changes during a breath hold porcine experiment.

$$\Delta A_\lambda = \varepsilon_\lambda . \Delta C . d . DPF \qquad \text{(III.9)}$$

This equation can be expanded to account for the two chromophores of interest (i.e. oxygenated and reduced hemoglobin):

$$\Delta A_\lambda = \left(\sum_{i=1}^{2} \varepsilon_{\lambda,i} . \Delta C_i \right) . d . DPF \qquad \text{(III.10)}$$

Combining measurements from two wavelengths, we get a system of two equations with two unknowns that can be written in matrix form as shown in equation III.11. Solving these equations gives the relative changes in oxygenated and deoxygenated hemoglobin concentrations (ΔHbO_2 and ΔHb respectively). The sum of

the two is the relative change in total hemoglobin concentration (III.11-a) while the difference is the hemoglobin oxygenation index (III.11-b) commonly used to track tissue oxygenation changes [79].

$$\begin{bmatrix} \Delta A_{\lambda 1} \\ \Delta A_{\lambda 2} \end{bmatrix} = \frac{1}{d} \begin{bmatrix} \varepsilon_{HbO_2}^{\lambda 1} / DPF_{\lambda 1} & \varepsilon_{Hb}^{\lambda 1} / DPF_{\lambda 1} \\ \varepsilon_{HbO_2}^{\lambda 2} / DPF_{\lambda 2} & \varepsilon_{Hb}^{\lambda 2} / DPF_{\lambda 2} \end{bmatrix} \begin{bmatrix} \Delta HbO_2 \\ \Delta Hb \end{bmatrix} \quad \text{(III.11)}$$

$$\Delta HbT = \Delta HbO_2 + \Delta Hb \text{ (III.11-a)} \quad \& \quad \Delta HbD = \Delta HbO_2 - \Delta Hb \text{ (III.11-b)}$$

Processing Flow

The pulsatile signal tracks arterial changes and can be used, as described earlier, to track pulsatile perfusion and the arterial oxygen saturation (SaO_2). The trends in pulsatile perfusion are tracked using the perfusion index (PI=AC/DC). The arterial saturation can be computed using the modulation ratio (equation III.7) and a calibration algorithm. The hemoglobin oxygenation index described earlier is a function of arterial and venous oxygenation as shown in equation III.12. Knowing SaO_2 and having the calibration factors, we can compute SvO_2 from the measured ΔHbD. In addition, the total hemoglobin concentration can be measured as shown earlier to track perfusion changes. Figure 25 shows a flow diagram of the processing method.

$$\Delta HbD = \Delta HbO_2 - \Delta Hb = a.SaO_2 + v.SvO_2 + c \quad \text{(III.12)}$$

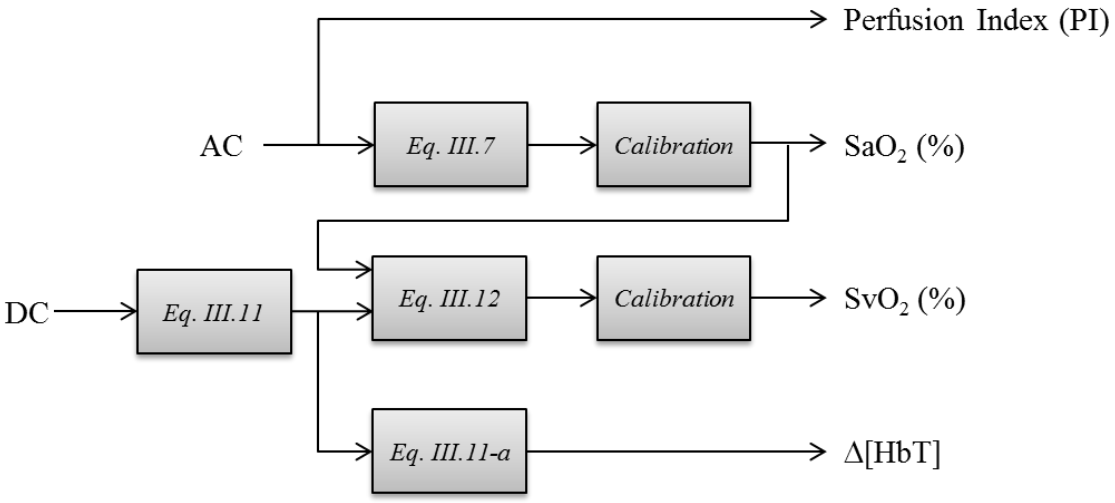

Fig. 25. Signal processing flow diagram

Chapter Conclusions

When light is shined on tissue, the collected optical signal has an AC and a DC component. Both components carry information about the tissue hemodynamics and can be used to assess perfusion and oxygenation changes. The AC signal carries information about the pulsatile blood which is typically the arterial blood. Note that in the case of hepatic tissue, the pulsatile blood is not completely arterial and it has a venous component since this tissue is supplied by an artery (hepatic artery) and a vein (portal vein). However, this pulsatile signal is still considered the supply blood and it carries information about oxygen supply to the tissue. This issue will be discussed in further details in chapter V.

To get oxygenation information, a minimum of two wavelengths is needed since oxygenation is controlled by the concentration of two chromophores (oxygenated and

deoxygenated hemoglobin). In addition, at least one of the two wavelengths has to be sensitive to hemoglobin oxygenation changes. Figure 26 shows an example on how the signal changes during hypoxia and decreased perfusion on three wavelengths that have different sensitivity to hemoglobin oxygenation. The 805 nm is an isobestic wavelength and is not affected by oxygenation changes. The 735 nm has a higher absorption coefficient for deoxygenated hemoglobin while the 940 nm is absorbed more by oxygenated hemoglobin. Note how during hypoxia the amplitude of the 735 and 940 nm signals are flipped relative to the unchanged 805nm signal (relative to baseline).

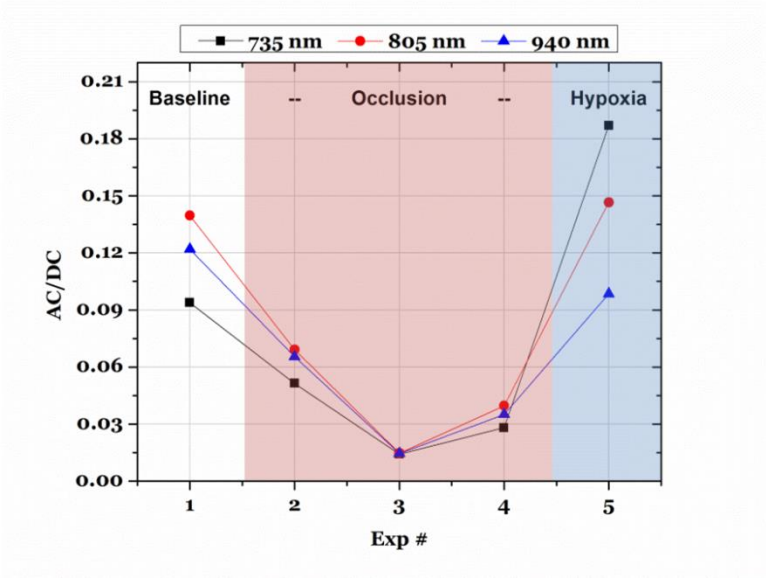

Fig. 26. Changes in the AC signal during vascular occlusions (red) and hypoxia (blue) at three different wavelengths (735, 805, and 940 nm).

In the following chapter, we will test the performance of the sensor and the processing techniques described in this chapter in a series of *ex vivo* and *in vitro* studies.

CHAPTER IV

IN VITRO AND *EX VIVO* TESTING[*]

Introduction

To minimize the need for animal studies during the optimization and testing of the sensor, phantoms mimicking the optical, mechanical, and anatomical properties of hepatic tissue were developed and tested. This is a common practice used to evaluate and optimize optical techniques, and compare performance of various systems [80]. There are numerous liver phantoms for non-optical techniques such as CT and MRI [81-90]. In addition, some optical phantoms have been reported to mimic optical properties of hepatic tissue for specific wavelengths and most of them are in the aqueous phase which is not suitable for perfusion studies required to evaluate a perfusion sensor [91, 92]. However, no functional fluidic phantoms have been reported in the literature to mimic optical, anatomical, and mechanical properties of liver tissue. In this chapter, we will describe a new set of phantoms that mimic these properties along with the fluidic circuit

[*] Part of this chapter is reprinted from T. J. Akl, R. Long, M. J. McShane *et al.*, "Optimizing probe design for an implantable perfusion and oxygenation sensor," Biomed Opt Express, 2(8), 2096-109 (2011), with kind permission of OSA, Copyright 2013 by The Optical Society; and from R. Long, T. King, T. Akl *et al.*, "Optofluidic phantom mimicking optical properties of porcine livers," Biomed Opt Express, 2(7), 1877-92 (2011), with kind permission of OSA, Copyright 2013 by The Optical Society; and from T. J. Akl, T. J. King, R. Long *et al.*, "Performance assessment of an opto-fluidic phantom mimicking porcine liver parenchyma," J Biomed Opt, 17(7), 077008 (2012), with kind permission of SPIE, Copyright 2012 by Society of Photo Optical Instrumentation Engineers; and from T. J. Akl, T. J. King, R. Long *et al.*, "*In vitro* performance of a perfusion and oxygenation optical sensor using a unique liver phantom," Proc. SPIE, 8229, (2012), with kind permission of SPIE, Copyright 2012 by Society of Photo Optical Instrumentation Engineers.

used to mimic blood perfusion and the dye mixtures used to mimic the different oxygenation states of blood. These phantoms and dye mixtures were used in a series of *in vitro* and *ex vivo* studies to assess the performance of the reported sensor. But first, we start by describing the anatomy of the liver and the properties that the phantoms were designed to mimic.

Liver Anatomy

The liver is a highly vascularized organ. It stores around 450 milliliters of blood (almost 10% of the total blood volume) and around 1450 mL of blood flow into the liver every minute which amounts to 29% of the resting cardiac output [1]. It is supplied with blood by two major vessels: the hepatic artery (HA), and the portal vein (PV). The HA supplies around 25% of the total hepatic blood flow (350 mL/min) while the PV is responsible for the remainder 75% (1100 mL/min). Although the PV is supplying blood and takes the role of an artery, it is a vein and the blood it carries has been deoxygenated in the spleen and gastrointestinal tract. The PV supplies around 25% of the total hepatic oxygen while the rest is supplied by the HA. The dimensions of the HA and PV are shown in Table 1 (Chapter II). The hepatic parenchyma is made of hexagonal structures known as lobules. Each lobule is several millimeters in length and 0.8 to 2 millimeters in diameter. The lobule is constructed of small microchannels, known as sinusoids, transporting blood from the corners of the hexagon to the center point where a central vein is located that transports blood into the hepatic vein and thence into the vena cava. Each corner of the hexagon has an arrangement named the portal triad. This arrangement consists of a portal vein, a hepatic artery, a common bile duct, lymphatic vessels, and a

branch of the vagus nerve. The diameter of the sinusoids connecting the portal triad to the central vein is around 8.8 μm [93]. Figure 27 shows a schematic of a hepatic lobule [94]. The liver is made of 50,000 to 100,000 lobules stacked next to each other to form the parenchyma [1].

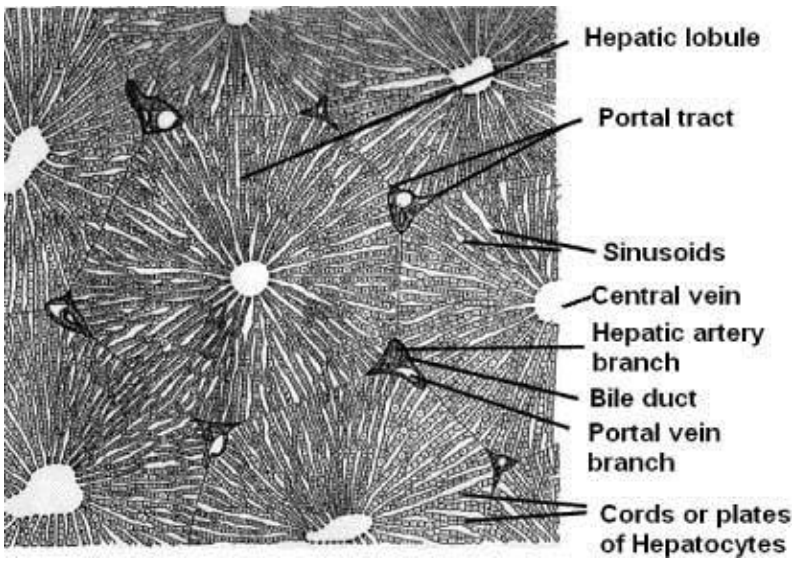

Fig. 27. Schematic of liver lobules showing the structure of the sinusoids, the portal triad, and the central vein [94].

Three types of phantoms are desired for the testing of the perfusion and oxygenation sensor: PV & HA phantoms for testing of vascular sensors and a parenchymal phantom mimicking a slab of 10 mm x 10 mm x 2 mm of liver tissue for testing of parenchymal sensors. All phantoms had to meet the following criteria: 1) match the optical properties of hepatic tissue in the range that covers all the wavelengths of interest (630 – 1000 nm); 2) mimic the anatomical properties of the HA, PV, and the

hepatic parenchyma; 3) allow for adjustment of flow/perfusion state in the physiological ranges of the liver; 4) provide good thermal stability and low chemical reactivity for possible use with blood and other perfusate at various temperatures; and 5) possess elastic properties that allows the phantoms to deform and regain native shape when perfused with low frequency (0.5-5 Hz) pulsatile flow.

Soft lithography was used to produce silicone-based phantoms with various geometries to match the hepatic vasculature. Dyes and scatterers were added to the mixture to match the desired optical properties. The curing parameters were adjusted to control the mechanical properties. In the following sections of this chapter, the materials and methods used to fabricate these phantoms are explained in details followed by testing results to verify compliance of the phantoms with the aforementioned criteria.

Materials and Methods

Phantoms Materials and Recipe

Polydimethylsiloxane (PDMS) was chosen as the main constituent in the designed phantoms (SYLGARD® USA). PDMS is easy to handle, stable once cured, chemically inert, and has a low viscosity making it suitable for surface preparation and soft lithography applications [95]. In addition, its optical properties are suitable for soft tissue phantoms. It is optically clear and has a refractive index (~1.4) similar to that of soft tissue (1.33-1.50) [96]. To mimic the optical properties of tissue, a combination of various scatterers and absorbers were mixed with PDMS. This recipe was developed and tested by Long *et al.*[97]. The recipe was prepared by mixing 437.4 mg of 0.5-1 μm

Al_2O_3 powder (99.99% purity, average particle size: 0.5-1μm, Inframat® Advanced MaterialsTM), 120 mg of 100 nm Al_2O_3 powder, 4.02μL of black India ink (Higgins, Black India 4415), 120 μL of blue food coloring (Wilton®), and 60mL PDMS resin. Long *et al.* showed that this formula has similar optical properties to liver tissue [97]. Figure 28 shows the effective attenuation coefficient of hepatic tissue and the PDMS recipe [97]. The mixture was sonicated and stirred until homogeneously distributed. Then, curing agent was added to the mixture and stirred until uniform. The amount of curing agent added was differs depending on the desired mechanical properties as described later in this chapter. Vacuum was applied to degas bubbles in the mixture. Finally, the mixture was cast into a petri-dish containing a mold that mirrors the anatomy of either the HA, PV, or hepatic parenchyma and placed in an oven for curing. The following section presents the details of the various molds used and the curing process.

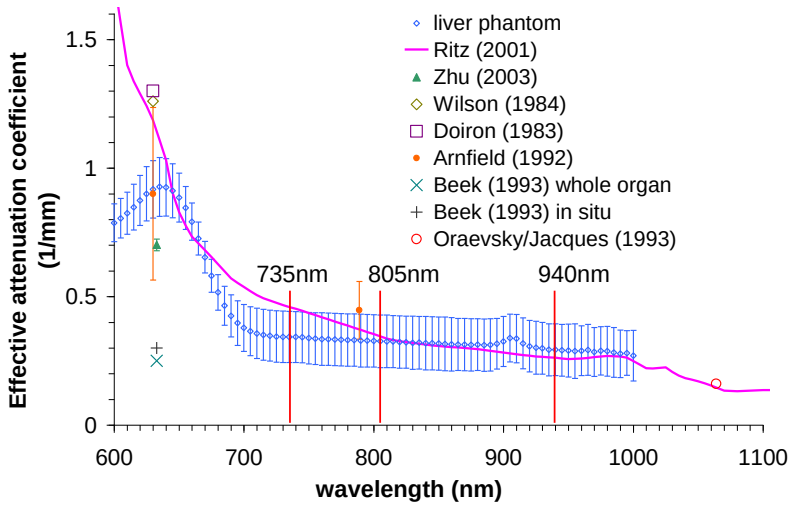

Fig. 28. Effective attenuation coefficient of the prepared liver phantom compared to hepatic tissue [97].

Molds & Phantoms Fabrication Process

Vascular Phantoms

To mirror the anatomy of a blood vessel embedded in tissue, a plastic tube (8 mm in outer diameter for the PV or 3 mm for the HA) was fixed in a petri-dish (40 mm in diameter) at 1 mm above the bottom surface as shown in Figure 29-a. The PDMS was poured into the petri-dish until the tube is completely covered and then placed in the oven to corss-link the PDMS. Different curing parameters (temperature and time) were used depending on the desired mechanical properties as described in the following section. Once the PDMS was completely cross-linked, the phantom was left at room temperature for a minimum of 2-3 hours before being removed from the petri-dish and the tube taken out of the PDMS. Two small tubes were placed on the sides of the hollow structure and were sealed with silicone to make the connection to a flow circuit simple. This resulted in a hollow structure that resembles a vessel embedded in tissue as seen in Figure 29-b. Slabs from the same recipe were also fabricated for use in case extra thickness above or below the initial design is needed.

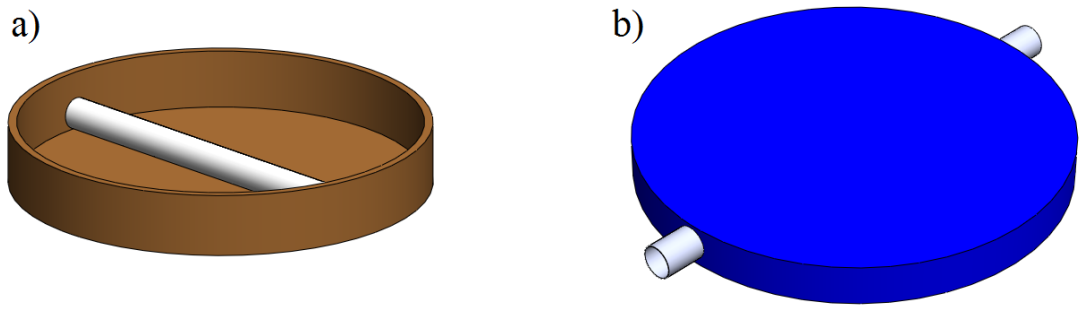

Fig. 29. Drawings of the portal vein phantom (b) and the mold used to prepare it (a).

Parenchymal Phantoms

Blood flow in the hepatic parenchyma goes through the sinusoids that range in diameter between 5.9 and 7.1 μm [98]. SU-8 molds were fabricated to mirror a cross-section of an arrangement of lobules.

A pattern of a cross-section of lobules was designed with computer aided design (CAD) software (Rhinoceros 4.0). The pattern consists of adjacent hexagons with 0.5 mm vertices. At each intercept of vertices, a cylinder of 0.06 mm diameter was placed to mimic the hepatic artery and portal vein branches in the portal triad. In the center of the hexagon lies a cylinder of 0.1 mm diameter mimicking the central vein. A series of 10 μm wide micro-channels radiate outward from the center of the hexagon to the sides as shown in Figure 30 mimicking the liver sinusoids. All these structures are 50 μm high.

To supply all channels with flow, the sides of adjacent hexagons were interconnected. The design included two inlets that can be connected to a flow circuit mimicking the portal vein and hepatic artery supplying the liver and one outlet that takes the function of the hepatic vein draining the effluent solution from the microchannels. A pattern of 20x20 hexagons was printed onto a transparent film with a black background and clear features to be used as the mask for photolithography.

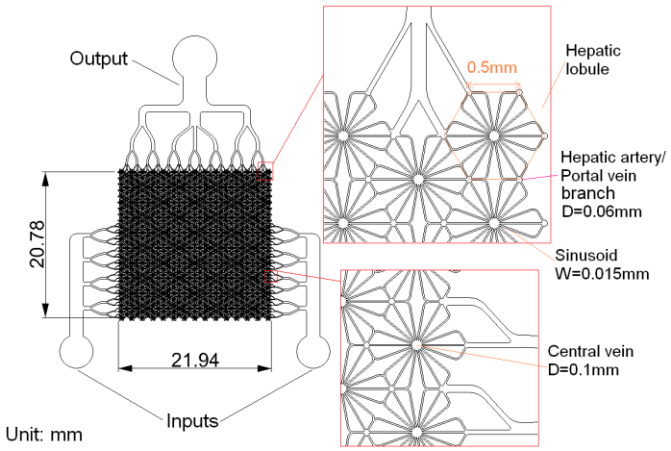

Fig. 30. Designed microfluidic pattern to mimic the parenchymal microcirculation.

These masks were used to create the molds of the parecnchymal microcirculation on silicon wafers. The silicon wafers (4 inch in diameter) were cleaned first in hydrochloric acid at 80˚C for 20 min and then rinsed with acetone, isopropyl alcohol (IPA) and deionized (DI) water. The wafers were then dried on a hot plate set at 130˚C for 30 minutes. The wafers were left at room temperature to cool down and then 4 mL of degassed SU8-50 photo-resist (MicroChem) were dispensed on the center of the wafer placed in a spin coater. The wafer was spun at 500 RPM (acceleration rate of 100 RPM/s). Once that speed was reached, it was held constant for 10 seconds which allowed the photo-resist to cover the full surface of the wafer. The speed was then increased to 2000 RPM with an acceleration rate of 300 RPM/s and held constant at that level for 30 seconds. This results in a 50 µm thick layer of SU8-50 on top of the wafer. The photo-resist was then placed on a hot plate and baked on two steps: 1) 65˚C for 10 min (pre-bake); 2) 95˚C for 20 min (soft bake). After the wafer cooled down, the mask

described above was placed on top of the photo-resist in a closed collimated UV lamp for 32 seconds. This was followed by another two step bake: 1min at 65˚C followed by 5min at 95˚C. After cooling down, the wafer was placed in a 7 inch glass dish containing the SU8 developer solution and left there for 6 min. The dish was shaken gently multiple times during the development process to ensure that the uncross-linked portion of the photoresist was dissolved completely. The wafer was then removed from the solution and rinsed with IPA then dried with a gentle stream of air. Finally the wafer was baked at 135˚C for 2 hours to ensure complete crosslinking of the SU-8 mold.

Similar to the vascular phantoms, degassed PDMS was poured onto the micropatterned mold and left on a level surface till it stabilize and covers the entire wafer. The volume of the PDMS used for each layer was calculated according to the desired thickness of the layer (~0.5 mm). The PDMS on the micropatterned mold was degassed again to remove any air bubbles trapped between channels. Depending on the number of the desired layers of microfluidics, multiple of these molds were used. In addition, an empty petri-dish without any mold in it was used to make the base layer (~5 mm thick) that is required to seal the other side of the microchannels. The PDMS covered molds and the petri-dish were placed in a preheated oven at 65˚C for 50 min to pre-cure the PDMS. Holes that align with the inlets and outlet of the microfluidic pattern were made in the base layer using 20-gauge needles. The PDMS layer was then carefully peeled from the micropatterned mold. The microfluidic PDMS layer and the base layer were corona treated and attached to one another making sure that the access ports align with the holes in the base layer. Flat tipped needles were inserted in the holes to allow

for connecting the channels to the flow circuit when needed. When extra layers of microfluidic channels were desired, the bonding process was repeated by using the obtained phantom (base layer + channels) as the base layer for the following layer and making sure that the access ports on the following layer do not overlap with any channels in the previous layer(s). Finally, the bonded PDMS layers were baked at 65˚C for an extra 70 min to completely cure the PDMS. In the studies described in this dissertation, two types of parenchymal phantoms were used: 1) Single layer phantoms consisting of one layer of microfluidic channels and 2) Multilayer phantoms consisting of three layers of microfluidic channels. Figure 31 shows a schematic of the multilayer phantom. Note that the different layers of the phantom are not interconnected in the phantom. However, the flow circuit can be adjusted to get the same supply to all layers.

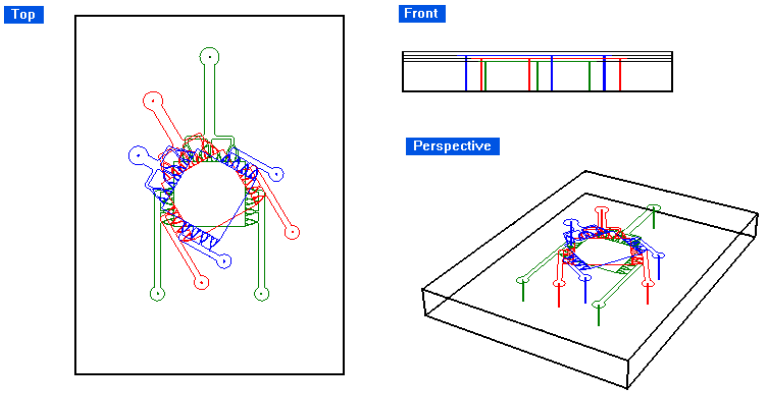

Fig. 31. Schematic of a three-layer phantom showing the various layers and the corresponding access ports with different colors.

The phantoms were left a room temperature over night with the layers compressed before being connected to the flow circuit. In addition, prior to any flow studies, the phantoms were perfused with either DI water or a dye solution to test for leakage. Figure 32 shows pictures of clear phantoms (PDMS without the dyes and scatterers) perfused with a red dye to highlight the channels.

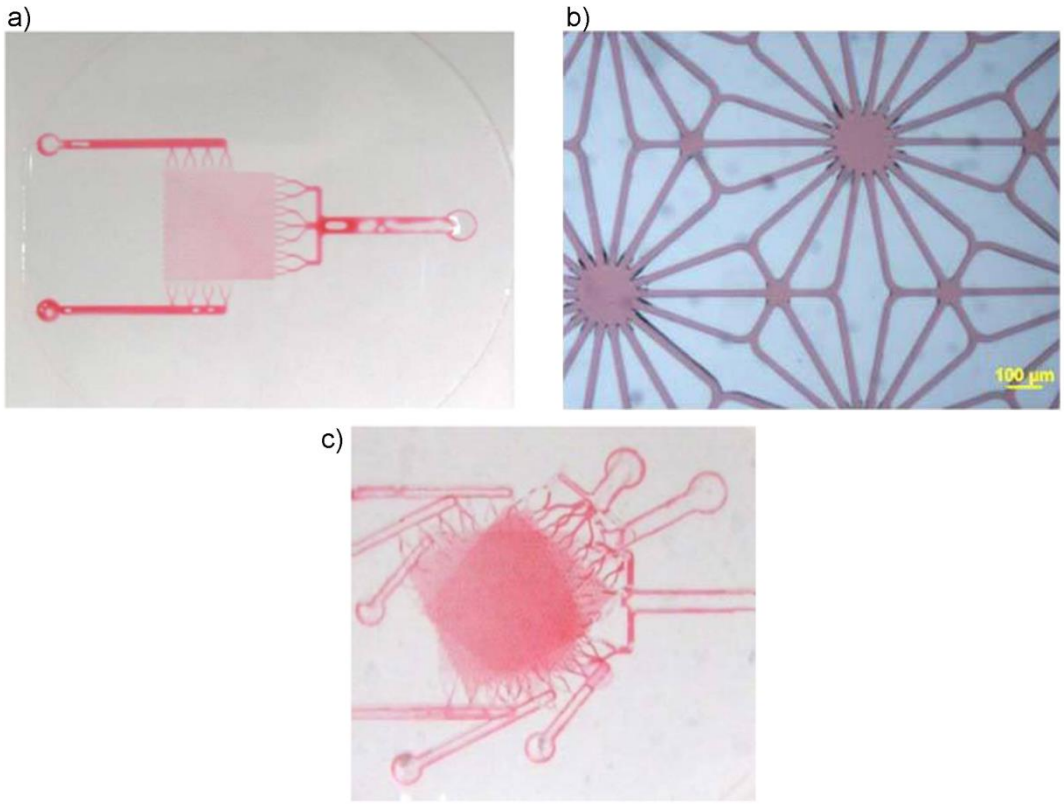

Fig. 32. Images of clear phantoms perfused with a red dye to visualize the channels: (a) single layer phantom, (b) close up look at the microchannels in a single layer phantom, and (c) three layers phantom.

Phantoms' Mechanical Properties

The PDMS curing process determines its mechanical properties. Various parameters can be adjusted to vary the elasticity of the PDMS phantoms including the concentration of the curing agent, the curing temperature, and the curing time [99]. These parameters were varied to build phantoms with different mechanical properties that mimic those of normal liver tissue and different disease states that lead to loss of tissue elasticity [70, 95, 100]. For most perfusion and oxygenation studies described in this dissertation, the PDMS was mixed with the curing agent at a volumetric ratio of 10:1 and cured at 65ºC for 120 min, unless otherwise indicated.

When preparing the phantoms, a portion of the recipe used in each phantom was put in a separate petri-dish (40 mm in diameter) and cured with the phantom (same oven, curing time, and curing temperature). This slab (1-3 mm in thickness) provided 2-3 specimens of PDMS for testing the mechanical properties of the phantom. Tensile tests were performed on the specimens using an Instron 3345 Universal tester configured for tensile testing as shown in Figure 33. MATLAB (Mathworks, Inc., MA, USA) software was implemented to quantify the Young's Modulus of each specimen from the collected data (Appendix D).

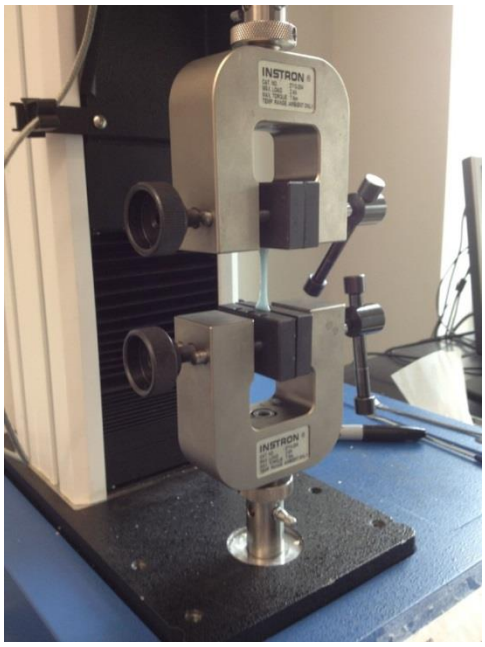

Fig. 33. Image of the Instron 3345 system used for testing the YM of the phantoms' PDMS recipe.

Hemoglobin Mimicking Dye Solutions

To avoid handling whole blood that needs to be in a pH and temperature controlled medium, and requires oxygenators and blood analyzers to change and test oxygen levels, we formulated two dye solutions that have optical properties similar to circulating blood in its oxygenated and deoxygenated states [29, 31]. To mimic the absorption spectrum of whole blood in its deoxygenated state, we used a mixture of 0.226% v/v India ink (Speedball Art, product number 3338) and 4.17% v/v inkjet photo cyan (Macro Enter, cat.# FPB085) dissolved in Phosphate Buffered Solution (PBS 0.1M, pH 7.4). The India ink has an extinction coefficient that covers all the wavelength bands of interest [101, 102] and it was used to create a baseline in the extinction coefficient

spectrum that matches the absorption in the near infrared wavelength range. The inkjet photo cyan was used to increase the absorption on the red side of the spectrum, a characteristic of the deoxygenated state of blood. On the other hand, the oxygenated state has a higher absorption in the NIR region and 358.8 mg/L of Epolight 2735 (Epolin, Inc.) was used to increase the absorption in the NIR region along with 0.068% v/v of India ink in a PBS (0.01M, pH 7.4). The extinction coefficient of the two dye solutions compared to that of whole blood is shown in Figure 34. The absorption of the NIR dye (Epolight 2717) was found to be pH sensitive. Because the Inkjet Photo Cyan is highly acidic (low pH), when the HbO_2 mimicking dye was mixed with the Hb mimicking mixture to mimic various oxygenation levels the HbO_2 dye mixture changed its absorption profile (See data in Appendix B). In addition, the mixture was not very stable, changed its profile over time, and formed large aggregates that fell out of solution (Appendix B). To overcome that problem, a stronger buffer (PBS 0.1 M pH 7.4) was used with the Hb dye mixture to maintain its pH at 7.4 which resolved the problem.

The dyes that were used with the microfluidic phantoms went through additional steps to make sure that they don't contain any large aggregates that can clog the channels. First, the India Ink dye that was used was first diluted in PBS to 10 times the concentration needed for the final mixture. The diluted mixture was then filtered through 0.45 µm syringe filters (VWR, cat. # 28145-481). The filter was changed multiple times during the filtration depending on the volume filtered solution due to clogging. The extinction coefficient of the filtered dye was measured to estimate the dye concentration in the filtered solution. The dye was then diluted to the desired concentration and mixed

with the other components as described above. Once the mixture was made, the final solution was sonicated and filtered through a 0.45 µm syringe filter. The sonication was performed prior to every phantom study if the dyes have not been sonicated on that day.

Mixtures of the two dye solutions in various proportions were made to mimic different oxygenation states. The right panel of Figure 34 shows the extinction coefficient of these mixtures at the three wavelengths of interest. All extinction spectra were measured using a spectrometer (Ocean Optics USB-2000), a UV-VIS fiber coupled light source (Hamamatsu, part # L10290) and a fiber coupled cuvette holder. Mixtures were placed in a 1 mm glass cuvette (Starna cells, part # 1/G/1) for spectrum measurements.

The extinction coefficient of the dye solutions matches closely to that of whole blood at the three wavelengths of interest (735, 805 and 940 nm). The isobestic point is red shifted when compared to the data reported by Prahl [31], however, there are inconsistencies in the reported isobestic point between different groups and it ranges between 797 nm [31] and 815 nm [103]. Our dye mixtures have an isobestic point, at 807 nm, in between these two extremes. At 735 nm the extinction coefficient of the dye solution M1 does not match exactly that of the oxygenated state of circulating blood. This causes the dynamic range between the two dye solutions at 735 nm to decrease causing the resolution in detecting oxygenation changes to decrease. For the purpose of this paper, this is not problematic since the main goal is to determine the optimal probe design and the same dye solution will be used to compare all of the different designs. At 940 nm, the two solutions match the desired extinction coefficients exactly.

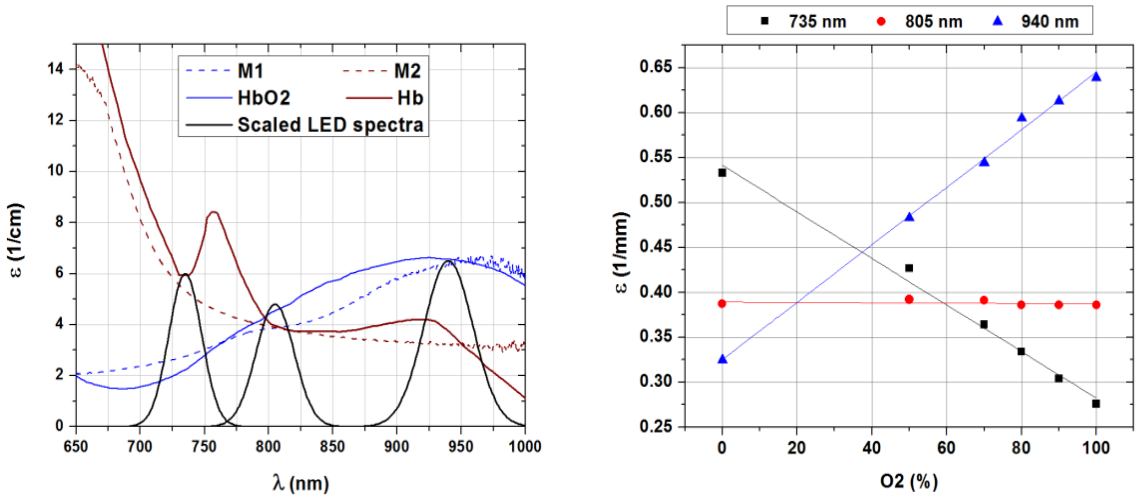

Fig. 34. Absorption spectra of whole blood and the two dye solutions used in the in vitro *setup. (Left panel) Extinction spectra of the dye mixtures (M1: HbO_2 mixture, M2: Hb mixture) compared to hemoglobin's spectra [31]. The LEDs emission spectra (shown in black) were scaled to match the scale of the extinction spectra. (Right panel) Extinction coefficient at the three wavelength of interest as a function of the simulated oxygen saturation [104].*

Flow System Setup

To create the desired flow patterns, the phantoms were connected to two peristaltic pumps (MINIPULS 3, Gilson) driven by a LabVIEW virtual instrument (VI) via a data acquisition board (USB-6009, National Instruments). Two pumps were used only with the PV phantom to be able to reach the high levels of flow that mimic the normal physiologic flow (1100 mL/min). In the case of the microfluidic phantoms one pump was sufficient to get the desired flow levels; however the phantoms had to be preloaded with the desired dye solution prior to starting the pulsatile flow, as described in the following paragraph, to avoid bursting the connections at the input and output ports. The VI used generated a square wave with a variable amplitude, frequency and

duty cycle (Appendix C). The VI allows the user to adjust the flow level, the pulse frequency to mimic the heart rate, and the pulse width. In addition, the VI also read data from a thermistor that was used to give the user feedback on the fluid temperature. This last feature was added for the *ex vivo* studies described later in this chapter. The tubing size was varied depending on the phantom used, the type of the experiment, and the desired flow rates. Prior to any data collection, the phantoms were perfused with the desired dye solution until no air bubbles were seen in the circuit. Figure 35 shows a schematic of the pumping circuit along with the electronics of the bench-top system (left panel) and a picture of the flow circuit with the single layer parenchymal phantom.

The microfluidic phantoms were preloaded with the desired dye solution prior to the start of the pulsatile flow experiments to avoid bursting the phantom inlets and outlets due to the high levels of flow and the resistance of the microfluidic channels. Two syringe pumps were used to accomplish that: the first syringe pump (cat. # 70-2208, Harvard Apparatus) was connected to the input ports and set to pump at a volumetric flow rate of 0.3 mL/min and 0.9 mL/min for the single and multilayer phantom, respectively, and the second syringe pump (New Era Pump Systems, Inc., NE-4000) was connected to the output ports and set to withdraw at a rate of 0.35 mL/min and 0.95 mL/min for the single and multilayer phantom, respectively, creating a negative pressure gradient to help perfuse the phantoms without bursting the connections at the input and output ports [105].

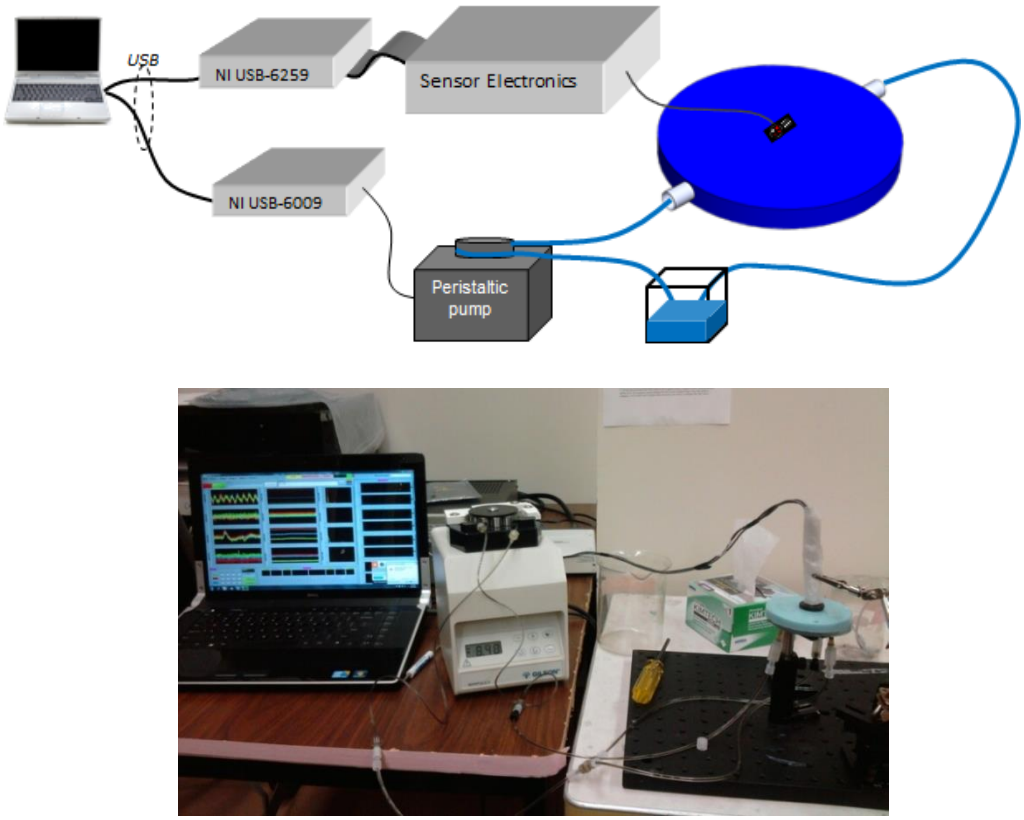

Fig. 35. Schematic (top) and image (bottom) of the in vitro *pumping system, phantom, and bench-top sensor electronics [104] and [97].*

Ex Vivo Liver Perfusion

The phantom experiments were designed to minimize the use of animal studies and *ex vivo* tissue studies. However, these studies were still performed in much smaller numbers to test verify the *in vitro* results. The *ex vivo* studies were performed by perfusing freshly harvested livers (rats and rabbits) with the aforementioned dye mixtures. Blood perfusion was tested first but many complications were encountered

especially with blood clotting and getting enough blood for the perfusion circuit. The following sections describe the organ harvesting procedure and the perfusion circuit used in these studies.

Harvesting of the Liver

Male Sprague-Dawley rats (250 – 300 g) were anesthetized by Isoflurane (3%) induction via a vaporizer in an anesthesia chamber. The animal was then placed on a water circulated heating pad, abdominal fur was clipped and chlorhexidine (an antiseptic antibacterial agent) was applied to the abdomen. After confirming adequate depth of anesthesia, a right subcostal incision was made to get access to the liver. The portal vein was dissected and ligated on the proximal side to avoid excessive bleeding. Tubing (PE 200) was inserted into the portal vein and 1 mL of heparinized saline (20 units/mL) was injected. Next, the hepatic artery was ligated and dissected. The inferior vena cava was ligated and cut on the proximal side of the ligation. The liver was re-irrigated with heparinized saline until the effluent became clear. The liver was removed to an iced buffer container and moved to the perfusion system. The portal vein cannula was connected to the pump output in the perfusion chamber. Figure 36 shows a liver placed in the perfusion chamber prior to the start of the experiment. The animal was then euthanized via administration of pentobarbital intracardially. These experiments were performed at the University of Pittsburgh, Pennsylvania, and all procedures followed the local animal regulations.

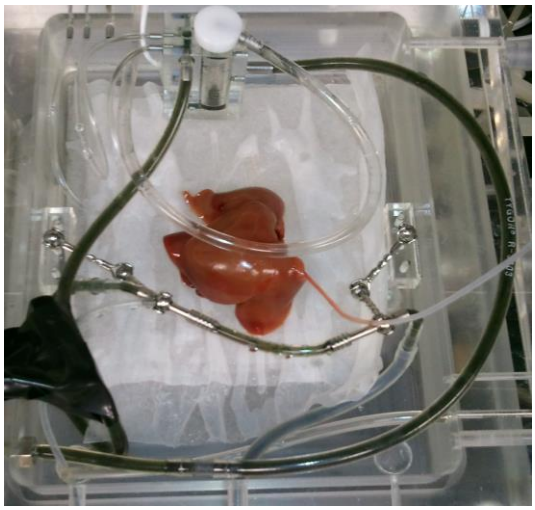

Fig. 36. Ex vivo *perfusion chamber.*

Perfusion System

After the liver was harvested, it was weighted and then placed in a flow circuit that allowed the adjustment of flow/perfusion levels. All flow levels were normalized by the tissue weight to get an average perfusion level. The main component of the flow circuit consisted of a Harvard apparatus perfusion system (Harvard Apparatus, Item # 739909) that allowed for temperature control of the tissue and the solution used to perfuse it. In addition, it controlled the pressure levels at the input of the liver. The harvested liver was placed in the perfusion chamber and the cannula in the portal vein was connected to a pulsatile blood pump (Harvard Apparatus, Item # 529552). Flow levels were recorded using a Transit Time Flowmeter (Transonic systems). In these studies, the bench-top system was used with one probe placed on the hepatic tissue and another placed on the tubing upstream from the organ. Figure 37 shows the *ex vivo* flow

circuit. Note that the flow circuit was ran for a minimum of 1 hour prior to the placement of the organ to make sure that the temperature of the chamber and the fluid are stable at the desired levels (37-38ºC). Once the organ was ready to be connected to the circuit, the flow was paused and the cannula was connected then flow was initiated at 0.25 ml/min/g of liver tissue with a "pulse rate" of 100 cycles per minute. Flow was then maintained at this level for 10 minutes to get to assure stable temperature and flow rate. Data was then collected with the bench-top system and the flow was increased to 5-6 levels in the range of 0.1 – 1.5 mL/min/g tissue. Each level was maintained for a duration of 5 minutes or more during which data was collected for 2 min intervals.

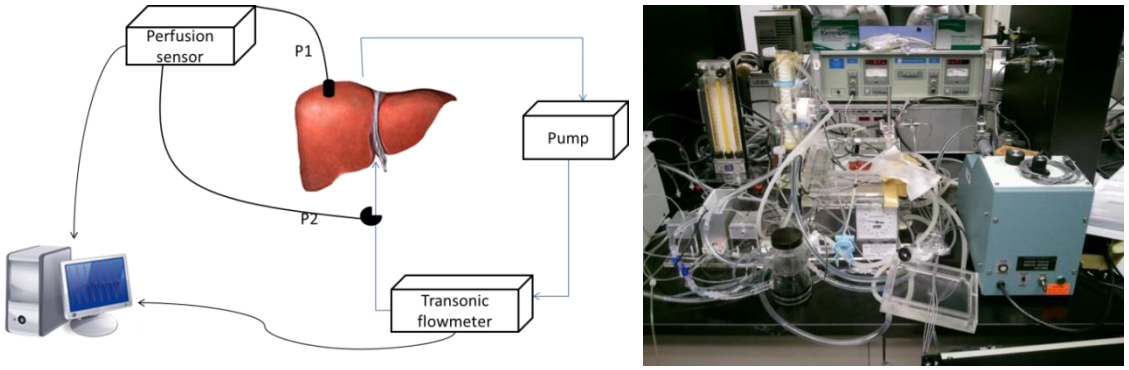

Fig. 37. Schematic (left) and image (right) of the ex vivo *flow circuit.*

Results

In Vitro Phantom Studies

Perfusion Studies

The performance of the sensor in detecting changes in flow/perfusion was assessed in three types of phantoms: Portal Vein (PV) phantoms, Single Layer (SL) parenchymal phantoms, and Multi-Layer (ML) parenchymal phantoms. The PV phantom studies model the case of a sensor placed above a major vessel buried in hepatic tissue. For these studies, flow levels in the range of 0-500 mL/min were used. This range is lower than physiologic flow levels seen in the PV (~1100 mL/min). Our pumping system does not have the capability of covering the full range of flow with fine resolution; therefore the flow circuit was designed to get flow levels that mimic low physiologic levels that are seen during liver transplant complications and are more challenging for the sensor to pick up. During these studies, each flow level was maintained constant for at least 1 minute to let everything in the circuit stabilize then data was collected using the bench-top system described in Chapter II for a duration of 1 to 2 minutes. The collected data was processed using an automated processing software implemented in MATLAB (Mathworks, Inc.) shown in Appendix E. The software computes the FFT spectrum on each of the wavelengths and detects the peak of the pulsatile flow which is then normalized by the DC level to calculate the perfusion index (PI) commonly used in PPG sensors to track pulsatile perfusion/flow [106].

$$PI=AC/DC$$

Figure 38 (left panel) shows a typical waveform collected with the bench-top system from one of the PV phantom studies. The right panel shows the FFT spectra corresponding to three flow levels (50, 150, and 250 mL/min). The flow pulse rate in this experiment was set to 70 bpm (1.167 Hz). The frequency peak corresponding to the pulsatile flow and multiple harmonics can be seen at all three flow levels. The amplitude of the peak, which was used to measure the AC amplitude, changes with the flow level. Note that the DC levels are not shown in this graph.

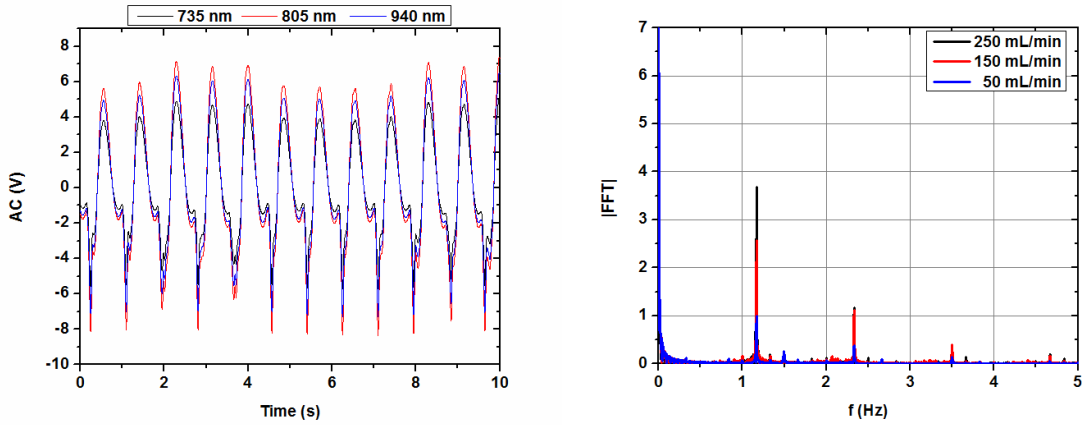

Fig. 38. A typical waveform measured from the portal vein phantom and the corresponding FFT spectrum for multiple flow levels (left and right panel respectively) [104]. Note the change in the FFT peak amplitude with flow and the multiple harmonics measured.

Figure 39 below shows the perfusion index (PI) as a function of the flow level on three separate experiments. The error bars represent the standard deviation. The flow was changed in different directions for the separate runs (increased, decreased, and then increased again). During these studies the phantoms were perfused with the same dye

mixture, mimicking oxy-hemoglobin, for all flow levels. The perfusion index shows a non-linear trend with flow. This is due to the mechanical properties of the phantom and is similar to the non-linearity seen in the stress-strain curves. If we limit the data to flow levels between 0 and 250 mL/min, the root mean squared error for predicting flow using a linear model is 13.48, 16.55, and 19.19 for the 940, 805, and 735 wavelengths respectively.

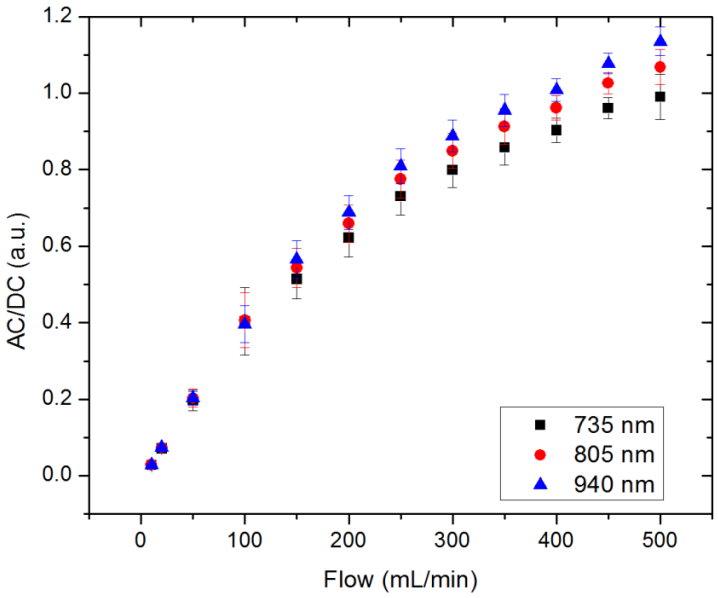

Fig. 39. Perfusion index as a function of flow measured from the portal vein phantom experiments.

Similar experiments were used to assess the performance of the bench-top system in detecting perfusion levels in the microfluidic phantoms. Prior to starting the pulsatile flow, the phantoms were preloaded with the desired dye solution using two peristaltic pumps as described earlier in the "Materials and Methods" section of this chapter. A

similar setup was used to perfuse the phantoms with the dye mixtures. In these experiments, a single peristaltic pump was used with smaller tubing sizes compared to the PV experiments. The pump frequency was set at 100 bpm (1.67 Hz) to approximate the cardiac pulsatile rate seen during the *in vivo* porcine data. Figure 40 shows 10 second intervals of the pulsatile wave measured from the SL phantom, ML phantom, and *in vivo* porcine studies and the corresponding FFT spectra. The FFT spectra show that the pulsatile flow peak can be seen in the FFT spectra of the microfluidic phantoms and multiple harmonics can be seen as well. In addition there are some low frequency components that we will discuss later in this section.

The average physiologic flow to the liver is 1450 mL/min [1]; however, this flow is divided to between the approximately 1 million lobules that constitute the 1.5 Kg of liver tissue (~0.967 mL/min/g tissue) [1]. Our phantoms mimic a small section of the liver that contains 20*20 lobules in each layer. This means that each layer of the phantoms should receive around 0.58 mL/min (1450*400/1,000,000) to mimic the physiologic rate of 0.967mL/min/g of tissue. In these studies, each layer was perfused with 0.6 mL/min when mimicking the physiologic conditions. This corresponds to 1 mL/min/g of tissue. All other flow levels are reported in terms of hepatic perfusion levels in mL/min/g of tissue using this same reasoning.

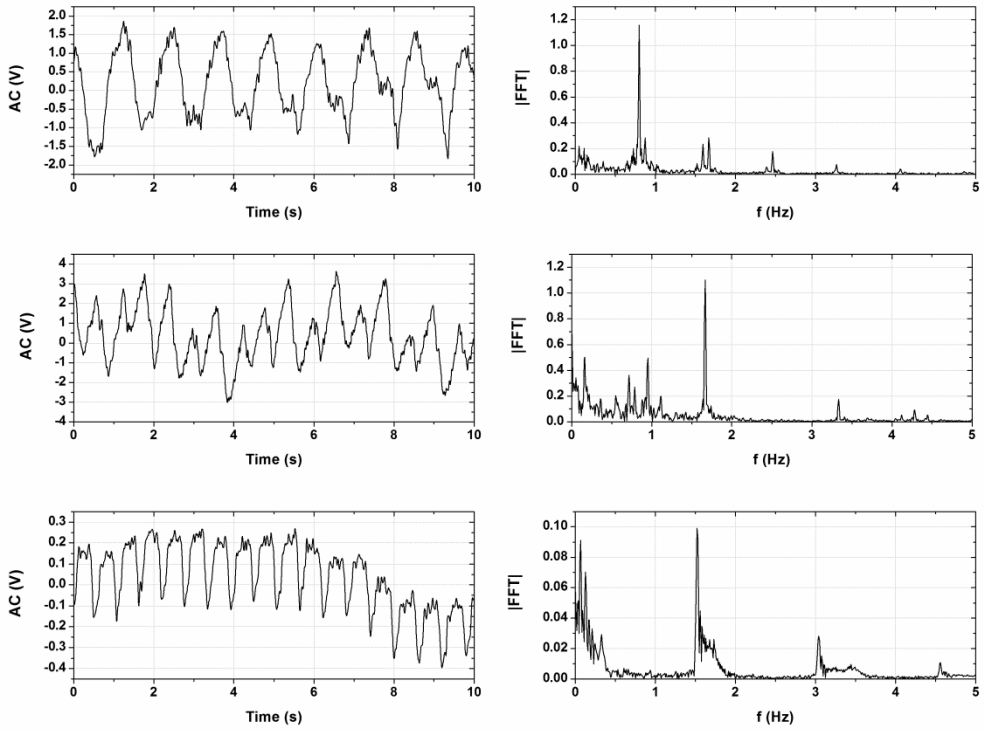

Fig. 40. Pulsatile wave (left) and the corresponding FFT spectrum (right) from the single layer phantom, multilayer phantom, and in vivo *porcine studies (top to bottom respectively).*

For the SL phantom, the flow was varied between 0.2 and 0.6 mL/min in 0.1 mL/min steps which is equivalent to perfusion levels in the range of 0.33 to 1 mL/min/g. The FFT peak changed linearly with perfusion changes. The root mean squared error of prediction (RMSE) is 0.077, 0.078 and 0.071 mL/min/g of tissue for the 735, 805, and 940 nm wavelengths respectively. Figure 41 shows the average FFT peak of 4 experiments on each of the wavelengths as a function of perfusion level. The error bars correspond to the standard deviation.

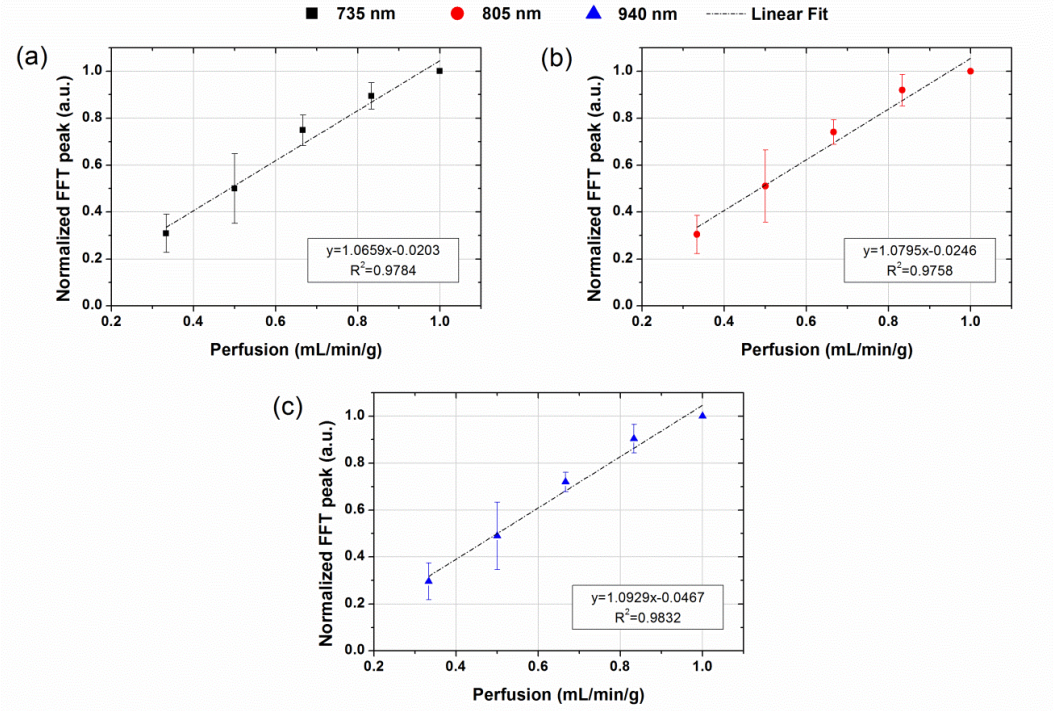

Fig. 41. Results of the single layer phantom perfusion experiments [105].

For the ML phantom, the flow was varied between 0.76 and 1.8 mL/min which corresponds to perfusion levels in the range 0.42 to 1 mL/min/g of tissue. Using the normalized FFT peak, we were able to predict the perfusion level with an RMSE of 0.0718, 0.066, and 0.062 mL/min/g for the 735, 805, and 940 nm wavelengths respectively. Note that in both SL and ML phantom studies, the results were normalized to the FFT peak at the 1 mL/min/g perfusion level. This is required because this method is not quantitative and monitors trends in perfusion. Figure 42 summarizes the results of the ML phantom studies.

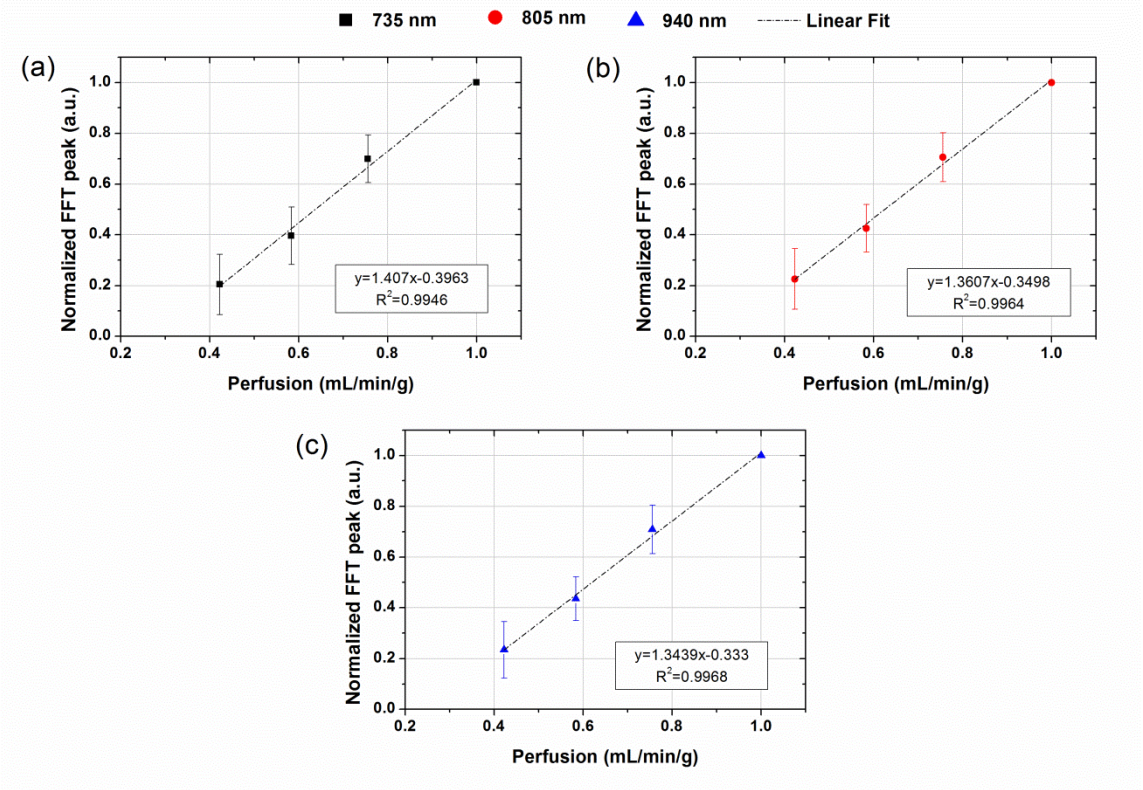

Fig. 42. Results of the three layers phantom perfusion experiments [105].

The measured signal from the microfluidic phantoms had a low frequency component (around 0.833 Hz). We believe this frequency component corresponds to back flow due to pressure build up in the circulation system. To verify this hypothesis, since our measurements are not sensitive to flow direction, air bubbles were introduced in the circulation and the flow pattern monitored visually. In this experiment, back flow was depicted at the corresponding frequency. To better understand this phenomenon, the flow levels were varied in the SL phantom experiment which resulted in a linear shift of the peak (R^2=0.9997) as shown in Figure 43. This was expected since for higher flow levels the pressure builds up faster and the frequency of the back flow was higher.

Further, the amplitude of the peak did not correlate to the changes in flow level. This peak could be varied by adjusting the mechanical properties of the fluidic system either by changing the curing method of the PDMS as described earlier, or modifying the tubing (material or size) used in the system. Preliminary studies were conducted to verify this hypothesis and we were able to shift the low frequency peak from 0.833 Hz to 0.55 Hz at a constant perfusion level of 1 ml/min/g by using a more compliant phantom. This peak can be adjusted to mimic different noise artifacts seen *in vivo* such as the back pressure seen *in vivo* in the venous system due to respiration.

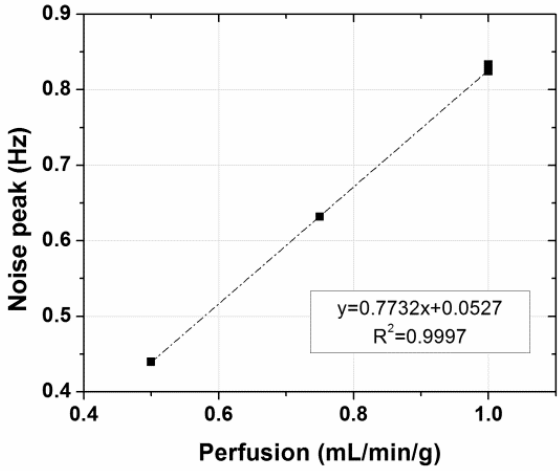

Fig. 43. Back pressure peak frequency as a function of perfusion levels for the single layer phantom. Note that the plot has 16 data points at three different flow levels but most of these points are overlapping.

Oxygenation Studies

After preparing the two dye mixtures mimicking oxy- and deoxy-hemoglobin, the two solutions were mixed in different ratios to model oxygen saturations between 50 and 100% in steps of 5% as shown previously in Figure 34. The PV phantom was perfused with these mixtures at a rate of 500 mL/min and the collected data was used to measure the modulation ratio (R) used in pulse oximetry to measure oxygen saturation. The modulation ratio as a function of oxygen saturation is shown in Figure 44. The error bars correspond to +/- one standard deviation that was computed from three runs. After collecting data for 1-2 minutes on every oxygenation level in every run, the dye solution was pumped out of the dye and collected for later studies. The phantom was then perfused with the new dye solution and the mixture was left to circulate through the circuit for 1-2 minutes prior to collecting any data. This allowed time to eliminate air bubbles from the circuit and make sure there are no residues of the previous mixture in the circuit. The optical probes were not moved during this experiment to minimize changes in light coupling.

$$R = \frac{AC_{735} / DC_{735}}{AC_{940} / DC_{940}}$$

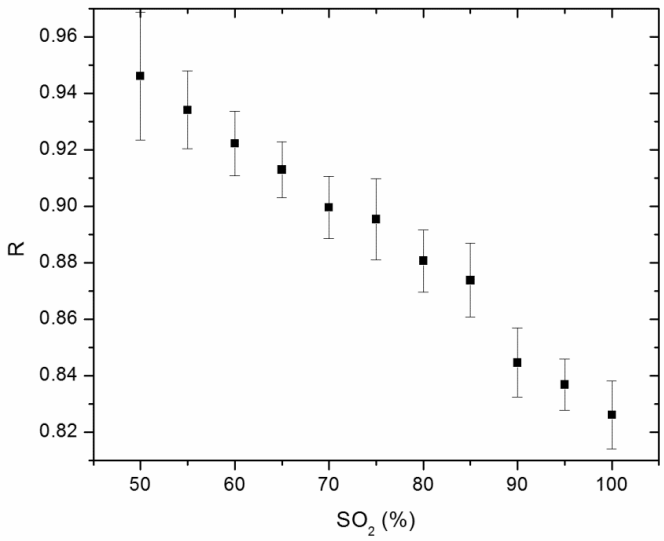

Fig. 44. Modulation ratio measured from the PV as a function of oxygen saturation. The error bars correspond to the standard deviation on three runs. Note that every SO2 value corresponds to a dye mixture that mimics the optical properties of hemoglobin for that saturation level.

The error of prediction of oxygen saturation using the modulation ratio shown above was around 1.3 % when using data from a single run and 4.6% when using the averages shown in the figure above. This is on the order of the prediction error using the extinction coefficient of the prepared dye mixtures which is 3.7% and 2.4% for the 735 and the 940 nm wavelength respectively.

Waveform Analysis

The PPG contains information in its amplitude, frequency, phase, and waveform [35]. Most common PPG sensors utilize only the amplitude and frequency of one or multiple wavelengths to measure perfusion [42, 45, 106], oxygenation [41, 107], and heart and respiratory rates [54, 108]. The phase and waveform of the measured pulse

contain information about blood pressure [109], and cardiovascular health and mechanical properties [35, 75, 110-112]. In this section, we will present some preliminary results on analyzing the pulse shape to get information about hepatic tissue and assess the origin of vascular complications when they take place.

The measured pulse in PPG is affected by the mechanical properties of the cardiovascular system. In this chapter, we start by studying the effect of tissue compliance on the measured PPG signal. A device that can quantify the mechanical properties of hepatic tissue non-invasively would be of interest for many applications including staging liver fibrosis. As liver fibrosis progresses, the elastin to collagen ratio increases [113] and the crosslinking is increased [114]. These changes lead to an increase in tissue stiffness [95] which affects the response of tissue to flow and governs the shape of the pulse. To mimic these changes, we used different curing methods in building the vascular PDMS phantoms as described earlier. The Young's Modulus (YM) was varied between 15 KPa and 61 KPa which mimics the change seen from normal hepatic tissue (stage F0) to fibrotic tissue (stage F4) [95]. Figure 45 shows the tensile test data from two different curing methods of the PDMS phantoms. Note that the YM of the PDMS phantom mixture differ from that of PDMS alone.

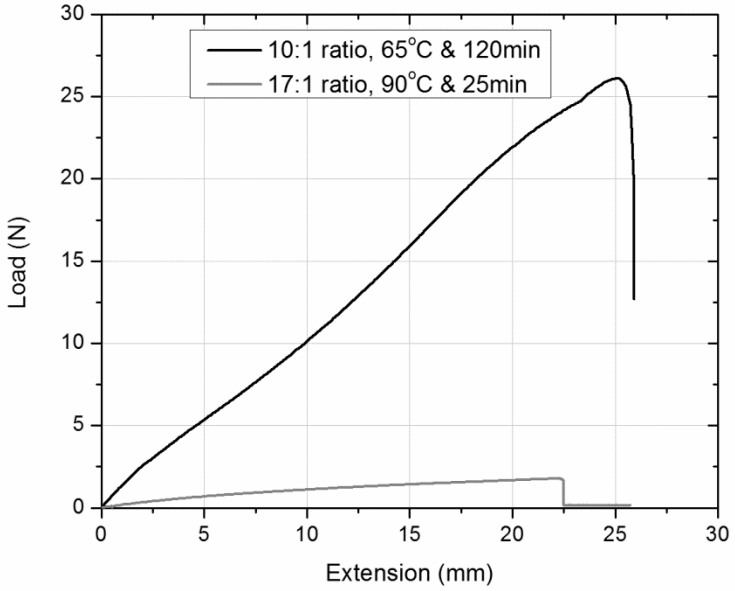

Fig. 45. Tensile test data of the PDMS phantoms' mixture with two different sets of curing parameters.

Multiple parameters were computed and compared between the two cases. One of these parameters is the emptying time for each pulse. The emptying time correspond to the time it takes for the fluid to exit the vasculature during diastole. During this period the PPG is increasing in amplitude due to the decrease in absorbance. To quantify that, an algorithm was developed that automatically detects the point that is 10% above the valley of the PPG pulse (start of diastole) and the point that is at 90% of the peak of the PPG pulse (end of diastole). The time between these two points was defined as the emptying time. The algorithm was implemented in MATLAB (Mathworks, Inc.) and is shown in Appendix F. The emptying time decreased from 305 ms for phantoms with YM of 15 KPa to 195 ms for phantoms with YM of 100 KPa. As shown in Figure 46.

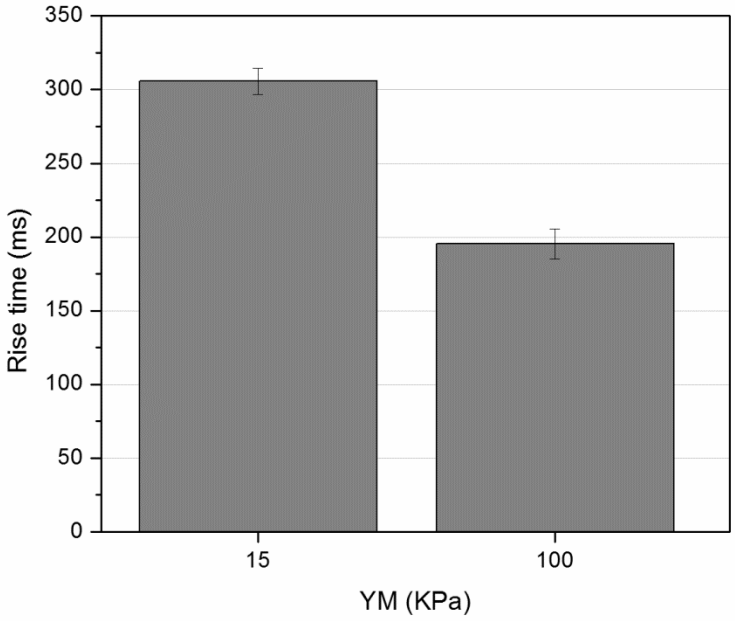

Fig. 46. Vessel emptying time for a Young's modulus of 100 and 15 KPa.

Note that these absolute numbers depend on the flow circuit as well as the phantom's mechanical properties. This means that, when applied *in vivo*, these measurements will be affected by systemic changes as well and a reference measurement should be made to account for systemic variables. This can be done by analyzing the peripheral pulse. This experiment was repeated with another flow circuit and this time using three different phantoms with Young's moduli of 11.7, 15.1, and 61 KPa. The same trend was observed as shown in Figure 47. Note that 11.7 and 15.1 are both in the normal range. The change in the absolute numbers is due to the change in the flow circuit as discussed earlier.

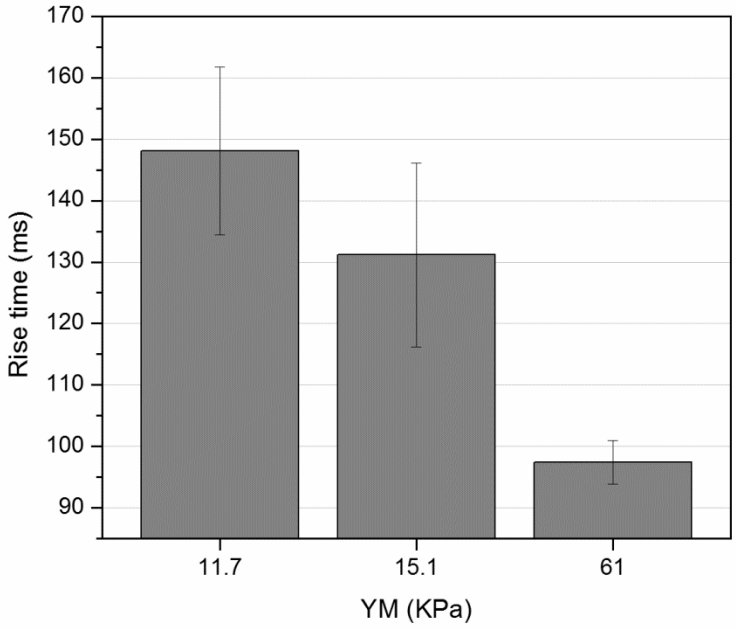

Fig. 47. Vessel emptying time as a function of YM (11.7 – 61 KPa).

In addition, when a vascular complication is detected from the perfusion data, PPG waveform analysis can provide insight into the type of complication. More specifically, a reduced level of perfusion can be caused by an obstruction of flow either downstream or upstream from the organ (measurement site). Downstream occlusion are expected to increase downstream pressure which would increase the resistance in the diastole phase leading to longer emptying times which are expressed as rise times in the PPG signal. To test that theory, a flow circuit was built with a peristaltic pump and the vascular phantom. Clamps were placed downstream and upstream from the phantom as shown in Figure 48.

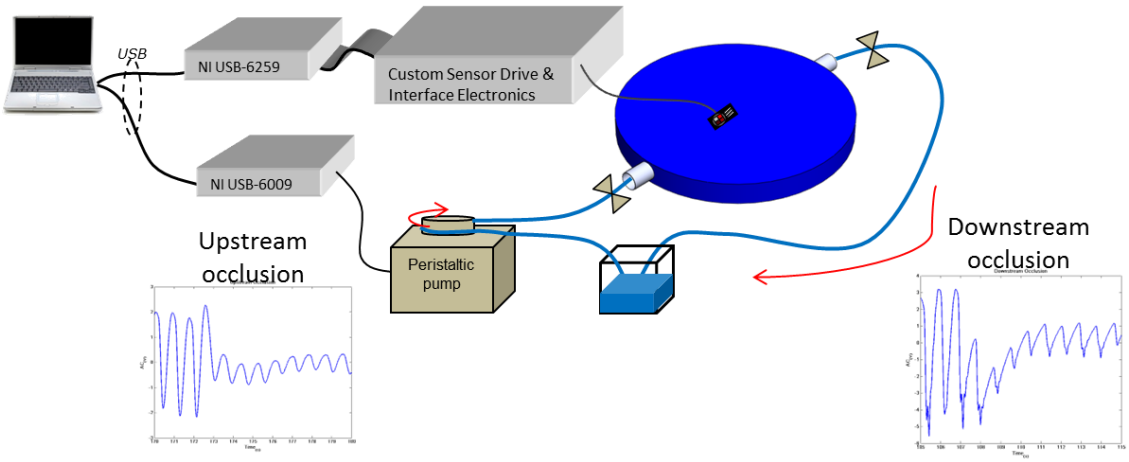

Fig. 48. Schematic of the in vitro *clamping study showing the change in the PPG waveform in the case of upstream and downstream occlusions.*

Baseline data were collected and then one of the clamps was tightened while recording the PPG waveform. As seen in Figure 48, the downstream occlusions show a decrease in the slope of the diastole phase which is not seen in the upstream occlusions. This was quantified by measuring the vessel emptying time as described earlier. Figure 49 shows the PPG rise time changes during an upstream and a downstream occlusion.

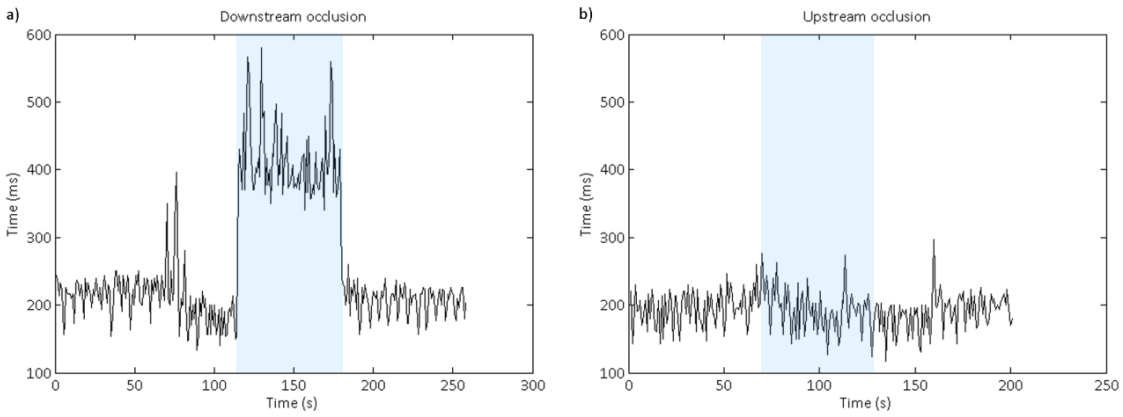

Fig. 49. Changes in PPG rise time during upstream (a) and downstream (b) occlusions. The shaded areas correspond to the occlusion time.

These experiments were repeated three times and the averages and standard deviations are shown in Figure 50.

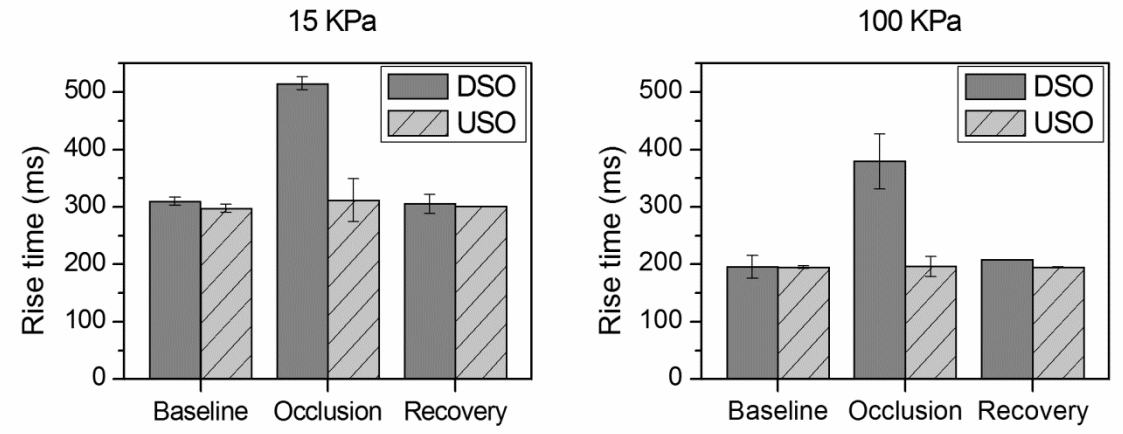

Fig. 50. Changes in PPG rise time during occlusions for the 15 KPa (a) and 100 KPa (b) phantoms.

Ex Vivo Studies

To verify the results obtained *in vitro*, we conducted a limited number of *ex vivo* rat liver perfusion studies. During these studies, only perfusion changes were monitored. Figure 51 shows the perfusion data measured from one of the livers. Note that the Transit-Time flow monitoring system was measuring flow in the supplying tube of the flow circuit and not the tissue microcirculation which could have added error to our measurements in the case of any perfusion inhomogeneity in the liver microcirculation. The collected pulsatile signal was processed in the time domain by measuring the amplitude of each pulse (difference between local maxima and minima) using the automated MATLAB code (Appendix F). The perfusion index (PI=AC/DC) was used to track perfusion changes. The DC level was computed for each pulse by taking the average of the DC channel between two consecutive pulses. All three wavelengths tracked perfusion changes with similar accuracy. Perfusion levels were varied between 0.01 and 1 mL/min/g of tissue. The PI was averaged for 5 seconds intervals to eliminate pulse to pulse variation. The root mean squared error (RMSE) in the study shown below was 0.0874 mL/min/g of tissue.

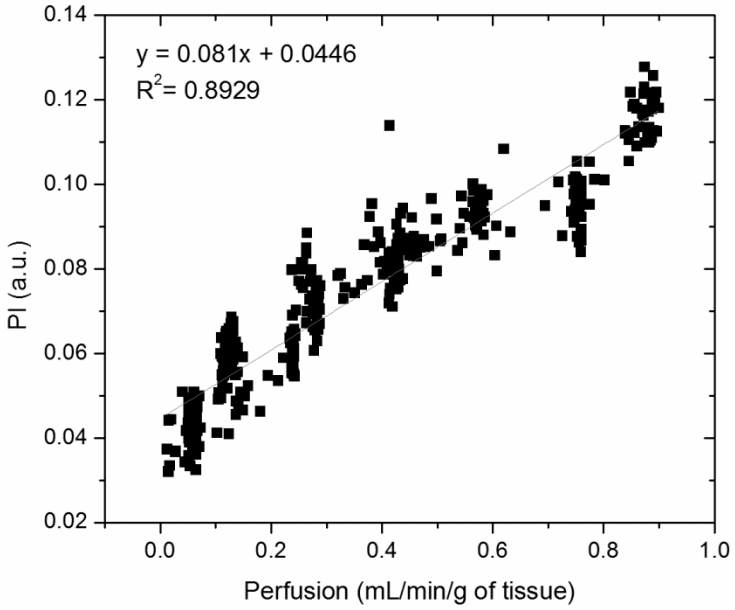

Fig. 51. Perfusion index as a function of liver perfusion measured from excised rat livers perfused with hemoglobin mimicking dyes mixture.

Chapter Conclusions

In this chapter, a phantom that simulates the optical, mechanical, and anatomical properties of the liver and its vasculature was presented. This phantom can be used to evaluate the performance of a variety of optical sensing and imaging systems that operate in the 650 to 1000 nm wavelength range. The designed phantoms were used with different dye mixtures that mimic the optical properties of blood in its various oxygenation states in a flow system to test the performance of the perfusion and oxygenation sensor. The sensor tracked perfusion changes with an RMSE of 0.077 mL/min/g for the single layer phantoms and 0.071 mL/min/g for the three layers phantom. These results were verified in *ex vivo* rat liver perfusion studies and perfusion

was tracked with an RMSE of 0.0874 mL/min/g of tissue. This resolution is similar to that of thermal diffusion perfusion monitoring systems that have an error of around 10% caused by the tissue temperature variation (0.025°C). The 10% error translates to a variation of 0.0367 mL/min/g of tissue in the perfusion range used in the *ex vivo* studies reported in this chapter. The sensor was also tested for sensitivity to oxygenation changes *in vitro*. The sensor was able to track oxygenation changes with a prediction error of 1.3% within a study and 4.6% across studies. These numbers are on the same order as the prediction error on the extinction coefficients of the dye mixtures due to preparation errors.

CHAPTER V

IN VIVO TESTING

Introduction

While the studies presented in the previous chapters show the ability of the sensor to track perfusion and oxygenation changes, *in vivo* studies present additional sources of noise and challenges that are not present in the controlled environment of *in vitro* and *ex vivo* testing. In order to evaluate the performance of the sensor in a more realistic environment, we conducted a series of *in vivo* porcine studies. Various techniques have been validated *in vivo* for monitoring liver perfusion and/or oxygenation such as NIRS [115], thermal diffusion [12, 19], Laser Doppler Flowmetry [116], and others. Several animal models have been used in these studies; however, since the ultimate goal of the sensor presented herein is to be implanted, we chose the porcine model due to the body size and since the mechanical properties of porcine livers have been shown to be similar to those of human livers [70, 100]. In this chapter, we will describe the porcine studies and the data collected using the bench-top and the telemetry system. The data show the ability of the proposed system to measure and separate perfusion, arterial oxygenation, and venous oxygenation. In addition, we investigate the homogeneity of perfusion across the liver.

Materials and Methods

Animal Study Protocol

The studies were performed on eight swine. Four studies were performed with each of the systems (bench-top and telemetry). The animal body weights from the early bench-top experiments were not recorded. The animal body weights form the telemetry studies ranged between 21 and 29.5 kg. Prior to anesthesia, the animals were premedicated with Telazol (5-10 mg/kg) and the analgesic Buprenorphine (0.01-0.05 mg/kg). Both drugs were introduced via intramuscular injections. To induce anesthesia, the animals were given 3-4% Isoflurane in Oxygen at 3 L/min via a face mask. An endotracheal tube was inserted into the trachea, secured in place and connected to a mechanical ventilator (8-12 BPM and tidal volume of 5-10 mL/lb). Isoflurane (0.5-4%) was introduced in Oxygen to maintain anesthesia. A laparotomy was performed to expose the liver. Transit-Time Ultrasound probes were placed on the Hepatic Artery (Transonic Systems, cat# MA4PSB) and the Portal Vein (Transonic Systems, cat# MA10PSB) to monitor flow changes. During the last two hypoxia studies with the telemetry system two oxygenation catheters were used to monitor oxygen saturation changes. The first oxygenation catheter was placed in the aorta via the iliac artery (Edwards Lifesciences, cat# XA3820HKCDC) and connected to a Vigilance Monitor (Edwards Lifesciences). Another oxygenation catheter was placed in the inferior vena cava at the level of the hepatic veins to monitor venous oxygenation changes. Two laser Doppler flowmeter probes were placed on the parenchyma to monitor tissue perfusion changes. A catheter was placed in the femoral artery to monitor arterial pressure.

Throughout the experiments, the vital signs (body temperature, SpO_2, heart rate, blood pressure, etc.) were monitored closely and recorded. All reference equipment were connected to a custom built data acquisition system and saved for further processing. The probes from the sensing system were placed on the HA, PV, and the liver parenchyma. For the studies with the bench-top system, at least two parenchymal probes were used to verify that there are no significant heterogeneities in the hepatic tissue perfusion. This resulted in four total probes (1 HA, 1 PV, and 2 parenchymal) compared to only three used with the telemetry system. All probes were secured using 5/0 Prolene sutures. Note that the HA and PV probes were placed for reference; however, no vascular probes will be used in the final application. Vascular occluders were placed on the HA and PV to be able to alter hepatic flow and perfusion. Hypoxia was induced by inhalation of low oxygen content mixtures. The electronic unit was placed outside the body next to the animal on the surgical table and tethered to the probes. The relay unit was connected to a laptop placed around 4 feet from the surgical table. Data were collected intermittently prior, during, and after any flow or oxygenation perturbation. At the end of the experiment, while still anesthetized, the animal was euthanized with a barbiturate derivative solution administered intravenously (80-120 mg/kg). Finally, livers were extracted and weighted (465 and 525 g for the 21 and 27 kg animals respectively) to convert the flow measurements (mL/min) into an average tissue perfusion measure (mL/min/g of tissue). All studies were performed under an animal use protocol (AUP #2010-257) approved by the Institutional Animal Care and Use Committee at Texas A&M University.

Instrumentation

The initial studies were conducted using a bench-top system. The system consisted of four sensor interface boards driving four different probes. The AC channels on this system have band-pass filters with cut-off frequencies (f_{3dB}) at 0.15 and 15 Hz for the high- and low-pass filters respectively. These filters were originally designed to block the DC light from the high gain AC channel to avoid saturation. Because of this design, the bench-top system allows part of the respiratory signal to pass through the high amplification AC channels. This signal is usually much higher than the measured cardiac cycle and causes saturation of the channel. For that reason, the animals' breath was held for short durations to collect data with this system and avoid saturation. The left panel of Figure 52 shows a pulsatile signal collected *in vivo* using the bench-top system while the animal is on a mechanical ventilator. The supply voltages for the amplifiers in this system are -10 V and 10 V and the figure below shows the saturation periods when the gains are adjusted to get an AC amplitude of around 10 V (half of the dynamic range of the system).

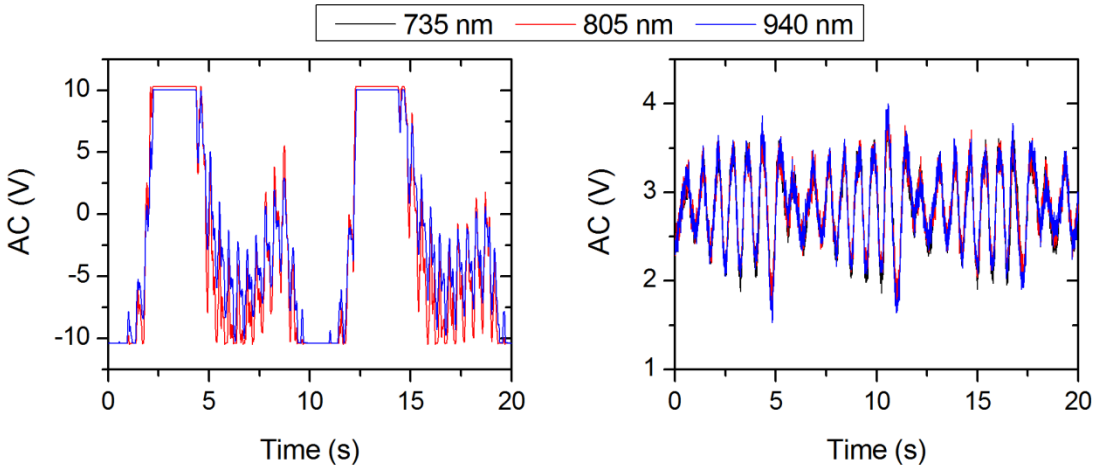

Fig. 52. Pulsatile waveform collected in vivo *from the hepatic parenchyma using the bench-top system (left) and the telemetry system (right) during respiration. The bench-top system's AC signal saturates due to respiration which is not seen with the telemetry signal.*

As discussed in chapter II, these filters were redesigned for the telemetry system to avoid that problem. The redesigned filters block the majority of the respiratory signal and do not show any saturation problems. The right panel of Figure 52 shows a pulsatile waveform collected with the telemetry system *in vivo* from the hepatic parenchyma while the animal was on a mechanical ventilator. Note that the dynamic range of the amplifiers in the telemetry system is 0-5 V and that is why the gain on this system is adjusted to get an AC amplitude around 2 V. Both systems are shown in the figure below.

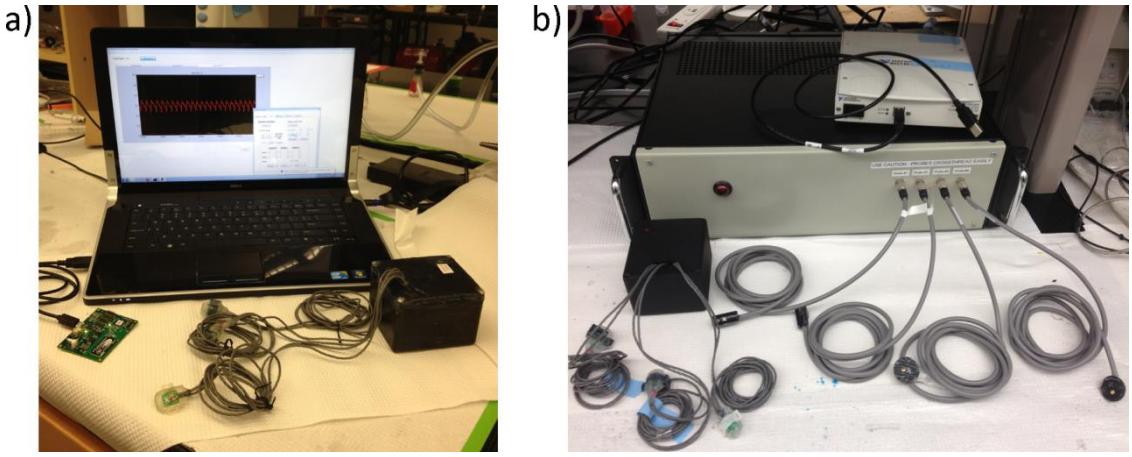

Fig. 53. (a) Picture of the telemetry system showing the sensors, probes, relay unit, and computer interface. (b) Bench-top and telemetry system next to each other.

Data Processing

Each of the sensors extracts an AC signal from the collected diffuse reflectance and amplifies it by a gain specified by the user (1 to 96 X for the telemetry system and 1 to 470 X for the bench-top). Both the DC and AC signals are transmitted to a data acquisition and saved on a computer for further processing.

AC Processing

Fourier processing was used to measure the amplitude of the pulsatile wave. The Fast Fourier Transform (FFT) was calculated for 25 s data intervals using software developed in MATLAB (MathWorks, Inc.). The software detects the peak that corresponds to the cardiac cycle and uses it as the amplitude of the AC signal. The frequency of that peak was used to measure the heart rate in beats per minute ($60*f_{peak}$).

Using the AC amplitude at the 735 and 940 nm wavelengths, we calculated the modulation ratio R that is typically used in pulse oximeters to assess oxygen saturation. This quantity requires a calibration curve to produce quantitative oxygen saturation results. To calibrate our sensor we fit the data to a calibration model in the form shown in equation V.1-b. Although the fitting parameters (a, b, c, and d) can be estimated theoretically, previous work has shown that the practical calibration curve is different from the theory that is simplified and does not account for the effects of scattering [117]. However, the general form of the equation still holds.

$$R = \frac{AC_{735} / DC_{735}}{AC_{940} / DC_{940}} \qquad \text{(V.1-a)}$$

$$SO_2 = \frac{a.R + b}{c.R + d} \qquad \text{(V.1-b)}$$

The quantity (R) is a measure of the ratio of absorbance at the red and NIR wavelengths of the pulsatile perfusion. Due to the compliance of the tissue, blood flow loses its pulsation on the venous side. Thus R is used to follow the changes in the oxygen supply (i.e. arteries and the arterial side of the capillary network).

DC Processing

The DC signals were processed using the typical equations employed for NIRS signals described in details in Chapter 3 [76]. The pathlength factor was estimated using the theoretical equation reported by Boas *et al.* [76]. These equations are used to derive the change in concentration of oxyhemoglobin, deoxyhemoglobin, and total hemoglobin

(ΔHbO_2, ΔHb, and ΔHbT respectively). The change in total hemoglobin concentration (ΔHbT) tracks perfusion. To obtain a measure of the change in oxygenation, we used the hemoglobin oxygenation index ($\Delta HbD = \Delta HbO_2 - \Delta Hb$) [79]. During perfusion changes, ΔHbO_2 and ΔHb vary similarly and the difference (ΔHbD) remains unaltered. However, for oxygenation changes, ΔHbO_2 and ΔHb vary in opposite directions leading to a change in the hemoglobin oxygenation index (ΔHbD).

The values calculated using the DC levels as described above represent tissue oxygenation which may be affected by either changes in oxygen supply (arterial side) or in oxygen consumption (venous side). It is of paramount importance to separate the two contributions to be able to possibly diagnose the cause of complications when they occur. Most previous reports employing NIRS measured, or assumed a constant percent contribution of, venous and arterial components to the collected signal [118, 119]. This ratio is different for various types of tissue and probe geometries. If this ratio is determined it can be used to extract the venous signal contribution to the DC levels. To accomplish that we used Multiple Linear Regression (MLR), and the measured venous oxygenation was fit to the linear combination of the DC measured changes (ΔHbD) and the oxygen saturation of the supply (equation V.2).

$$SvO2 = a.DC + b.SO2 + c \qquad (V.2)$$

Reference Measurements

The liver has a complex vasculature that is supplied by two different vessels: the hepatic artery (HA) and the portal vein (PV). The HA supplies approximately 25% of

nutrient and total blood flow but it is rich in oxygen and delivers approximately 75% of the total liver oxygen supply. The PV is part of the venous system but supplies blood to the liver. The portal venous blood is rich in nutrients but relatively poor in oxygen, and it supplies roughly 75% of liver nutrients along with 25% of its oxygen. Thus, the supply oxygenation in the liver tissue is not that of the artery alone, but it is the addition of the contribution of the PV and the HA. In the remainder of this chapter we will refer to this quantity as the mixed oxygen saturation (MOS) as defined in equation 3. Due to the limited exposed space on the PV (few centimeters) and the required flow probes and vascular occluders placed on that vessel, we could not insert a catheter into the PV to monitor its oxygenation. We assumed it to be equal to the non-hepatic venous oxygenation for the purpose of our calculations.

$$MOS(\%) = \frac{Flow_{HA}.SaO_2 + Flow_{PV}.SvO_2}{Flow_{total}} \qquad \text{(V.3)}$$

In addition to the Laser Doppler Perfusion monitor, we used the total flow as measured by two Transit-Time vascular flow monitors to track tissue perfusion as described by equation (V.4) below:

$$Flow_{total} = Flow_{HA} + Flow_{PV} \ \alpha \ Tissue\ Perfusion \qquad \text{(V.4)}$$

Results

Figure 54 shows a typical pulsatile waveform collected using the bench-top system during *in vivo* porcine studies. The corresponding FFT spectrum shows multiple harmonics of the cardiac cycle peak that can be measured with this system.

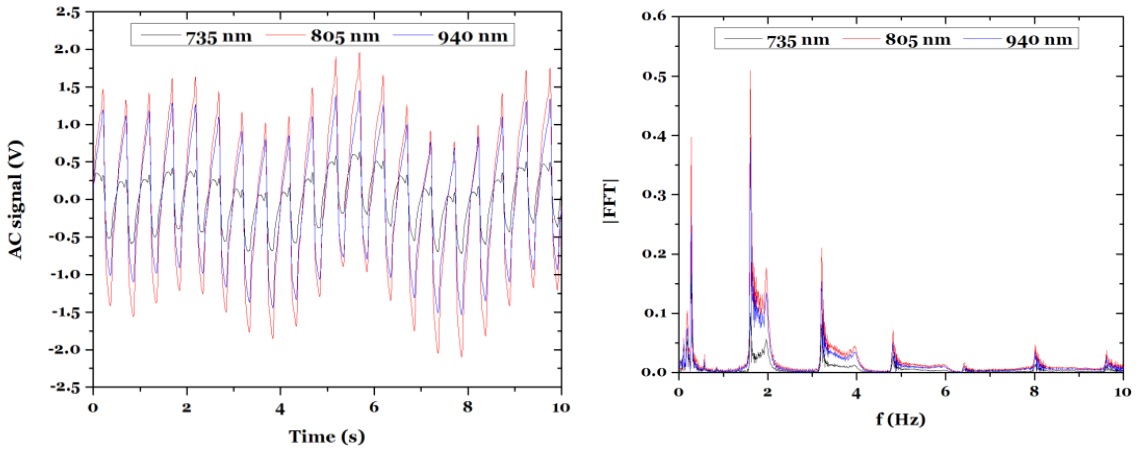

Fig. 54. Pulsatile waveform (left) collected in vivo *from the hepatic artery using the bench-top system and its corresponding FFT spectrum [63].© 2011 IEEE.*

Similarly, AC waveforms collected with the telemetry system and their corresponding FFT spectra are shown in Figure 55 below.

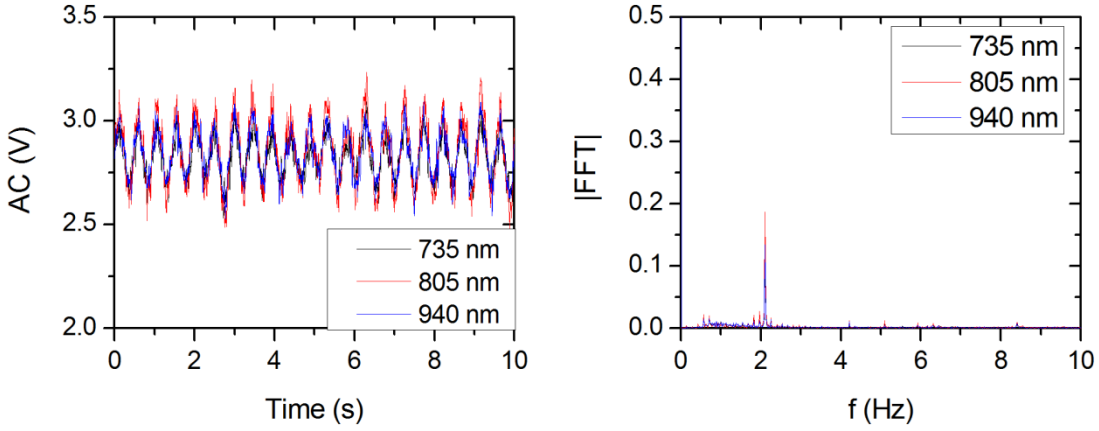

Fig. 55. Pulsatile waveform (left) collected in vivo *from the hepatic parenchyma using the telemetry system and its corresponding FFT spectrum.*

Bench-Top System

Perfusion

In the early studies conducted with the bench-top system, we were not able to get readings from the reference equipment used to monitor hepatic flow and perfusion. This prevented us from performing a quantitative analysis of the performance of our sensor in monitoring perfusion *in vivo*. Figure 56 shows the measured perfusion index (PI=AC/DC) from a parenchymal probe on all three wavelengths from data collected during an occlusion study to the hepatic artery. Each data point represents the average of 60 seconds of data. Note that after a duration of occluding the HA, the perfusion index goes back up on the parenchymal tissue which is likely due to an increase in portal vein flow as a response to the decreased HA flow.

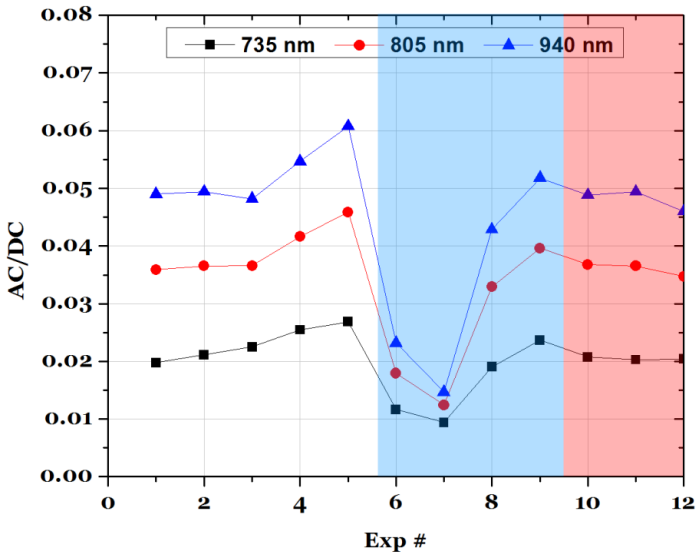

Fig. 56. Perfusion index changes during an HA occlusion. The blue shaded area represent the full HA occlusion while the red area corresponds to a 50% HA occlusion.

The perfusion index measures the pulse volume (pressure) which tracks pulsatile perfusion changes. However, there are many other confounding factors that affect the PI such as pressure. Thereby, the total hemoglobin concentration changes (ΔHbT) was used to track perfusion changes. This quantity measures changes in tissue hemoglobin content by using the DC levels on two or more wavelengths. In our case, three wavelengths were used. Figure 57 shows the changes in total hemoglobin concentration during an HA occlusion and the corresponding signal measured by a Hemedex thermal diffusion perfusion monitor.

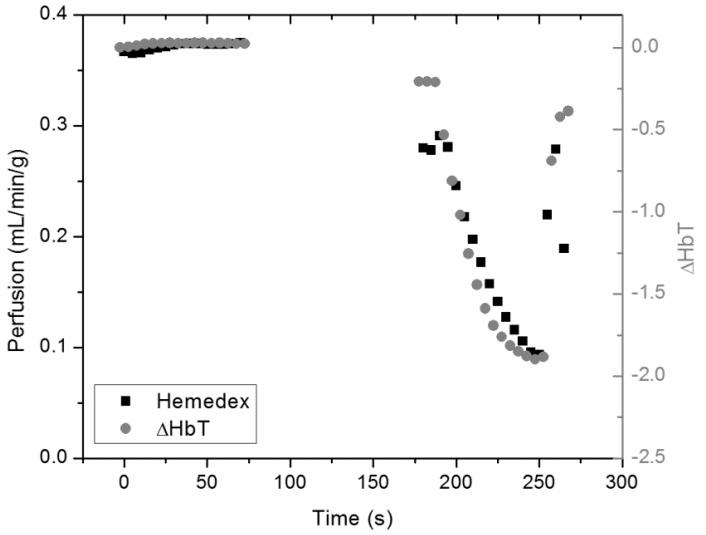

Fig. 57. Perfusion changes during an HA occlusion as measured by the total hemoglobin concentration and the Hemedex perfusion monitor.

Heterogeneity of Liver Perfusion

All sensors discussed herein measure local tissue perfusion. Often, it is assumed that hepatic perfusion is homogeneous and these point measurements are used as

indicators of total hepatic perfusion. To study this assumption, we used two bench-top systems (8 probes total) and placed the probes on various locations of the liver. Two probes were placed on the HA and PV. The remaining 6 were placed on different parts of the liver. Different source to detector separations were used to probe different depths in tissue. The separations ranged between 2 and 6 mm edge to edge separation which corresponds to 7 to 11 mm center to center separation. The signal on one of the parenchymal probes was lost after the start of the study and data from that probe were not used in the analysis. Figure 58 shows the data from the 5 parenchymal probes during two consecutive occlusions of both the HA and PV. This should result in a complete blockage of hepatic flow if the occlusions are successful. Each data point in the graph corresponds to a 5 s average of the change in total hemoglobin concentration.

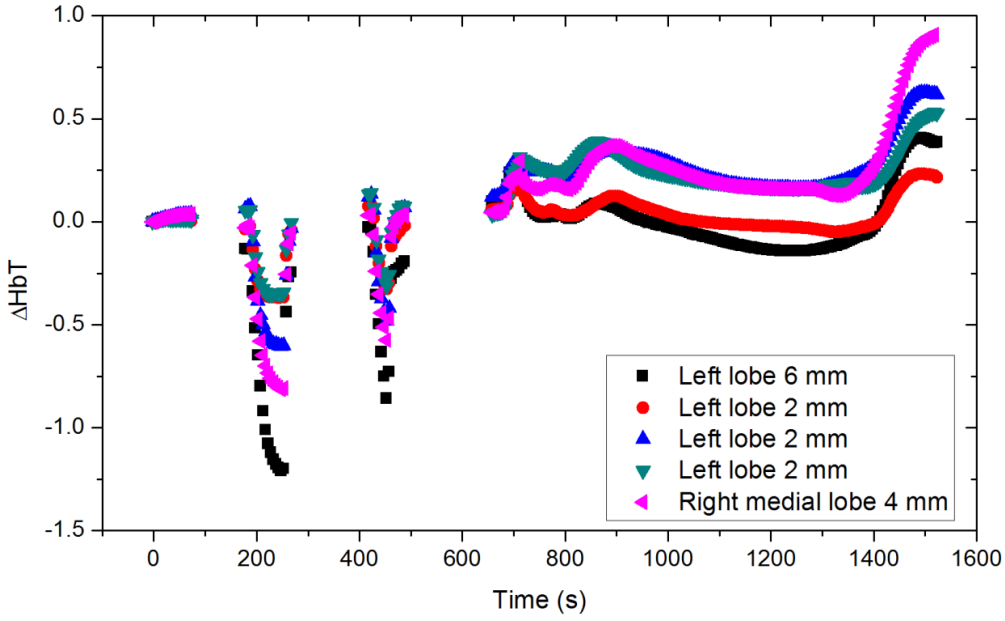

Fig. 58. Change in total hemoglobin concentration during HA and PV occlusions measured on 5 different sites of the liver.

The data show that all 5 parenchymal probes detected a decrease in perfusion during the HA occlusions. The changes in perfusion seem to be independent of the location on the liver. However, differences in the trends can be seen for the various optodes' separations. This indicates that the perfusion trends, when hepatic flow is restricted, vary with depth in the tissue. Figure 59 shows various scatter plots of the detected hemoglobin concentration changes measured by various probes with different optodes' separation. The scatter plots show that the low optodes' separation probes reach the minimum perfusion levels prior to their long separation counterparts. The left panel shows data from all probes plotted against the 4 mm separation probe placed on the right lobe. Note how all lower separations (2 mm) show a horizontal asymptotic behavior for low perfusion levels while higher separations (6 mm) shows a vertical asymptotic behavior. This suggests that for low perfusion levels, low separation probes stop detecting changes while the higher separation probes are still detecting perfusion changes. Similarly, the right panel of Figure 59 shows all probes data plotted against the 6 mm probe (highest optode separation). Note that this was only seen during very low perfusion levels when both HA and PV were occluded. This indicates that ischemia affects shallow tissue first. This can also be seen in Figure 58 above during the first occlusion. The short separation probes reach a minimum first and the signal flattens at one low level until reperfusion.

Despite the differences for very low perfusion levels, data from all probes correlated with each other with coefficients of determination (R^2) mostly above 0.9 (6 combinations above 0.9 and 4 above 0.8). This suggests that there are no significant

differences in the perfusion levels observed among different sites of the liver. Note that this might be different in the case of a transplant and this study only investigated normal, healthy livers.

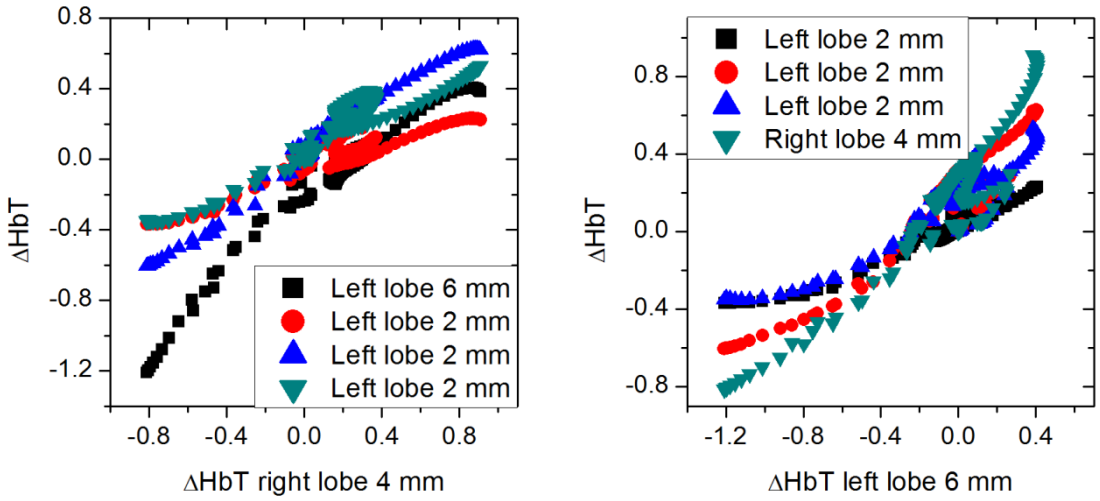

Fig. 59. Scatter plots showing the performance of different probes with different separations placed on various parts of the liver.

Oxygenation

The hemoglobin oxygenation index (ΔHbD) tracks hemoglobin oxygen saturation. In the early studies with the bench-top system, we did not have a continuous oxygenation monitoring system and blood gas analysis was used as the gold standard to verify oxygenation measurements. Data from the bench top system was still collected in intervals of at least one minute length and averaged to be compared to the blood gas analysis data. Since the filters of that system could not block the respiratory signal that

caused saturation of the AC channels, data were collected during breath hold intervals with intermittent intervals of mechanical ventilation. Thereby we were not able to maintain the oxygenation levels constant during data collection and quick drops in oxygen saturation levels were seen during data collection on the peripheral pulse oximeters used for monitoring the animals. The data in panel (a) of Figure 60 shows the hemoglobin oxygenation index measured by the HA probe and the blood gas analysis of the arterial blood samples. Panel (b) is a close up look at the data of one of the experiments showing the drop in ΔHbD.

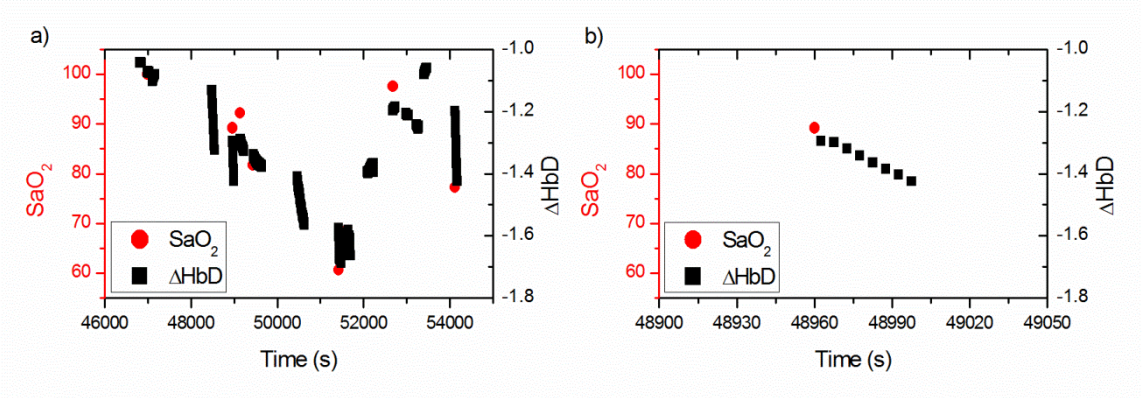

Fig. 60. Hemoglobin oxygenation index and blood gas analysis results during a hypoxia study using the bench-top system. The full duration of the study is shown in panel (a) and a zoom in on one segment during a breath hold is shown in panel (b).

To perform the quantitative analysis, the data from each interval (60-120 s) were averaged to one data point. The resulting hemoglobin oxygenation index is shown in Figure 61 below. Panel (b) shows the scatter plot of the blood gas analysis data (SaO_2) versus the hemoglobin oxygenation index ΔHbD. The resultant coefficient of

determination (R^2) is 0.886 and the root mean square error (RMSE) is 5.1%. Part of this error is due to the point measurements for the blood gas analysis used as a reference and the comparison to the average measured by the bench-top system. This adds a significant error especially since the oxygenation levels are not stable during data collection as described earlier. Note that in this study, the venous catheter was clogged and we could not get venous oxygenation measurements.

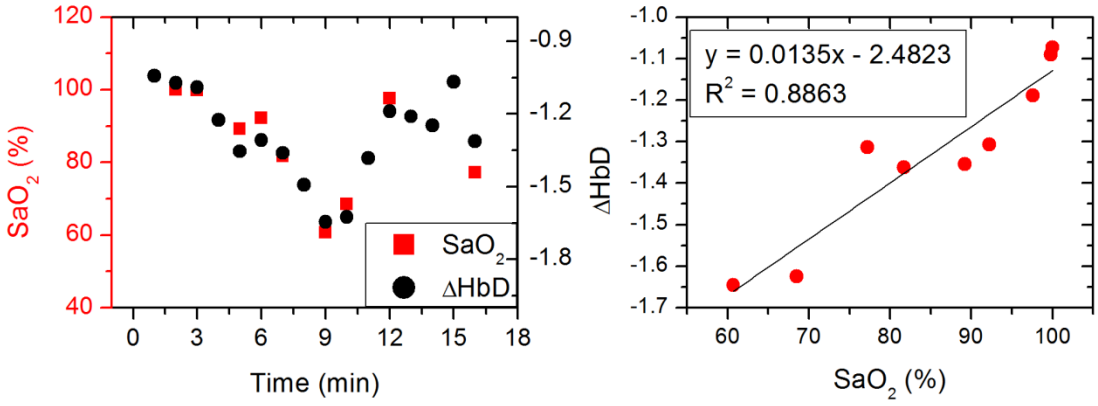

Fig. 61. Hemoglobin oxygenation index during hypoxia after 1 minute data averaging.

In the following experiment, venous and arterial samples were collected and analyzed for blood gases. The bench-top system had 2 vascular probes (HA and PV) and two parenchymal probes on the left and right lobes of the liver. The data shown in the graphs below correspond to the parenchymal probes. The modulation ratio was computed as described earlier and used to predict the arterial oxygen saturation. The same data was used for calibration and prediction. No significant differences were seen between the left and right lobe. Data from both probes and the blood gas analysis are

shown in panel (a) of Figure 62. The predicted arterial oxygen saturation correlated with the blood gas analysis data with a coefficient of determination (R^2) of 0.74. As discussed earlier, part of this error is due to comparing a minute average data to a single time point. In addition, the modulation ratio, computed from the parenchymal probes, measures the oxygenation of the pulsatile blood that is supplying the liver. The hepatic supply comprises blood from the HA and PV. Thereby, the hepatic oxygen supply can not be measured by the saturation of the arterial blood but instead it is the weighted average of the hepatic artery oxygen saturation and portal vein oxygen saturation. The weighting coefficients in measuring the hepatic oxygen supply are proportional to the flow levels of each vessel (HA and PV). The hepatic oxygen supply can be computed as defined by the mixed oxygen saturation (MOS) formula described in the Materials and Methods section of this chapter (equation V.3). For this study, we could not get vascular flow data from the ultrasonic transit time flowmeters to compute the MOS.

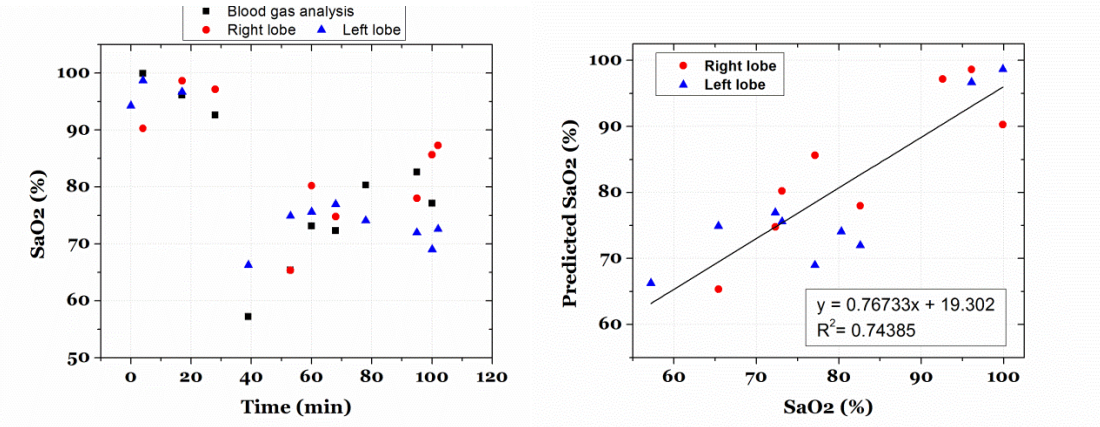

Fig. 62. (Left) Arterial hemoglobin oxygen saturation as measured by the parenchymal probes and the blood gas analysis on arterial blood samples. (Right) Scatter plot of parenchymal probes vs. blood gas analysis.

The venous oxygen saturation was computed from the DC data as described in the Materials and Methods section. Data were obtained from both parenchymal probes and displayed in Figure 63. The coefficient of determination for the venous oxygen saturation is 0.98. The RMSE for the arterial and venous oxygen saturation for this study was found to be 6.73% and 3.47% respectively.

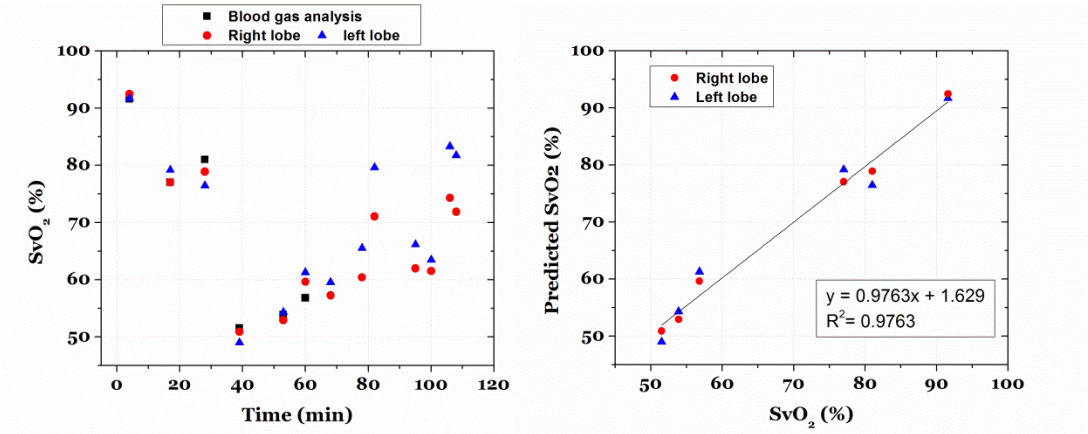

Fig. 63. (Left) Venous oxygen saturation as measured by the parenchymal probes and blood gas analysis. (Right) Scatter plot comparing the predicted SvO_2 to the blood gas analysis results.

Telemetry

The telemetry system was tested in two porcine studies. Two different data collection procedures were used on the two animals. For the first study, we induced hypoxia without imposing any change to the hepatic flow to test the ability of the sensor to track oxygenation changes. The second study began with four consecutive hepatic artery occlusions, followed by three portal vein occlusions. These occlusions were

performed at normal systemic oxygenation levels. Hypoxia was induced afterwards, and vascular occlusions (HA and PV) were performed again at low systemic oxygenation levels. All occlusions were brief (less than 1 minute for full occlusion) and were performed in gradual steps. Although the inhaled oxygen level was not changed during occlusions, the hepatic oxygen saturation is expected to be altered due to an increased hepatic oxygen extraction ratio and a change in the relative flow (see the MOS equation above V.3) of the HA (high oxygen content) and PV (low oxygen content). In the following figures, hypoxia periods are indicated by a dark grey box on the upper horizontal axis. Note that the recovery period from hypoxia is also included in the grey boxed region. Vertical white lines indicate segments where one or more hepatic artery occlusions were performed while horizontal white lines indicate where one or more portal vein occlusions were performed. The occlusion periods include multiple occlusions and baseline readings in between.

To verify that the pulsatile signal collected with the wireless sensor is tracking the cardiac cycle, we looked at the cardiac cycle peak detected by our system and compared it to the heart rate measured by the arterial pressure catheter. This was performed on data from two animals and the detected heart rate was accurate with an RMSE of 3.9 bpm (0.065Hz). Some of this error is due to the difference in the integration time between the telemetry sensor (25 s) and the pressure catheter (2 s). Figure 64 shows the heart rate throughout the study as measured from the arterial pressure catheter and the FFT of the PPG signal measured with the telemetry sensor.

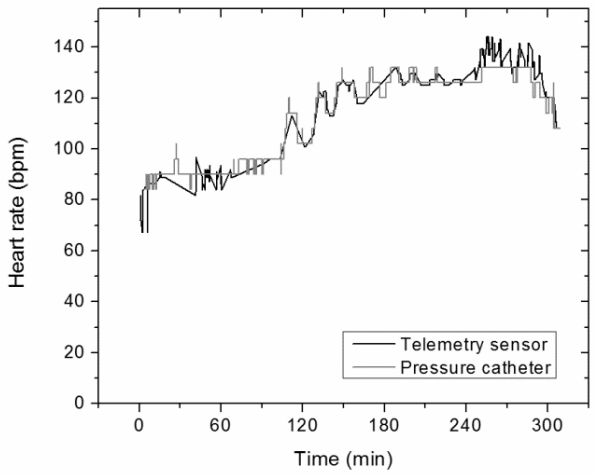

Fig. 64. Heart rate changes as measured by the arterial pressure catheter (grey) and the telemetry sensor (black).

Perfusion

One of the important features of the presented sensor is the ability to track perfusion and oxygenation changes simultaneously. To track perfusion changes, we measured the change in tissue total hemoglobin concentration (ΔHbT) as described in the Materials and Methods section. After analyzing the laser Doppler flowmetry (LDF) data from the commercial system, we found that the LDF signal correlated with changes in HA flow but not PV nor total flow (R-square= 0.8, 0.1, and 0.5 respectively) measured by vascular transit-time ultrasonic flowmeters. These data are shown in detail in Appendix G (Figures S3 & S4). We believe that the LDF was probing a branch of the HA and was not tracking tissue perfusion. Because the LDF measurements reflected the HA flow and not tissue perfusion, they were not used as a reference for parenchymal perfusion. Instead, the total hepatic flow measured by the addition of the signal from two

transit-time ultrasound flowmeters (HA & PV) was used as the reference for parenchymal perfusion measurements.

Figure 65 (left panel) shows the changes in hemoglobin concentration measured by the optical telemetry sensor and the total hepatic flow measured by the transit-time ultrasonic flowmeters. The two quantities correlate with high accuracy in the first 70 minutes of the study (t= 150-220 min) during which four HA occlusions were performed. After the first PV occlusion (t=220 min), the signal from the optical telemetry sensor showed a slow decreasing trend in perfusion while the transit-time flowmeter showed an increase. This is due to the fact that the telemetry sensor is measuring tissue perfusion directly by looking at the tissue hemoglobin content while the ultrasonic transit-time flowmeter is measuring vascular flow changes. This discrepancy between the two can be due to a systemic response causing vasoconstriction that results in a decrease in microvasculature perfusion while increasing the blood flow in the central vasculature. Such a response can be triggered by a decrease in blood pressure. To verify this theory, we looked at the change in the Mean Arterial Pressure (MAP) shown in the right panel of Figure 65. During the period of increase in the Transit-Time flowmeter signal, the MAP increased from 52 mmHg to more than 70 mmHg. We believe this event was triggered by the first portal venous occlusion that caused a decrease in venous return to the heart thereby causing a decrease in blood pressure to around 30 mmHg. This decrease in pressure is not seen during the first four occlusion events (HA occlusions) since the HA flow (350 mL/min in humans) is much lower than the PV flow (1100 mL/min, ~22% of total cardiac output) [67]. In general,

vasoconstriction is associated with an increase in MAP which supports our proposed explanation [67]. In addition, we looked at the telemetry sensor data from the hepatic artery probe, and they showed a similar increasing trend as measured by the transit-time flowmeter. This is an advantage of the employed technique since perfusion measurements are desired. Flow readings are usually used as an estimate of perfusion trends; however, in addition to perfusion, these measurements are affected by changes in blood pressure. Spectroscopy based techniques measure the real hemoglobin content in tissue which is essential to know the availability of nutrients and oxygen to cells.

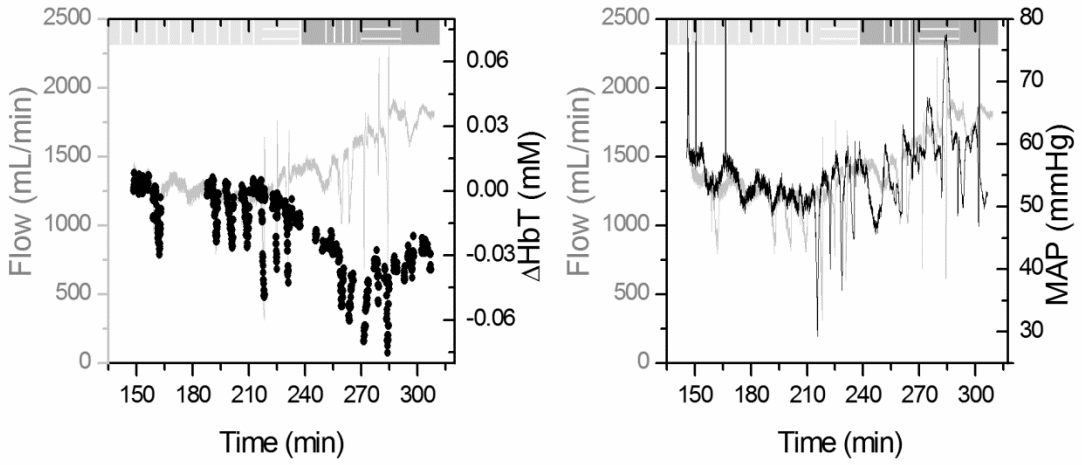

Fig. 65. (Left) Total hemoglobin concentration (ΔHbT, black dots) in hepatic tissue versus total hepatic flow measured by the addition of the HA and PV transit-time flowmeters' measurements (grey line). (Right) Total hepatic flow (grey) and mean arterial pressure (black) trends show that the increase in flow after t=200 min is accompanied by an increase in the arterial pressure suggesting that a systemic response is responsible for that increase.

To assess the accuracy of the perfusion measurements, we compared the readings from the telemetry sensor and the transit-time flowmeter prior to the increase in blood

pressure (first 4 occlusions). The telemetry sensor was able to resolve perfusion changes with a RMSE of 0.135 mL/min/g of tissue (70.87 mL/min) as shown in Figure 66. Note that the standard deviation of the transit-time flowmeter measurements (0.09 mL/min/g of tissue ⇔ 47.6 mL/min) during the first baseline collection (t=148 - 155 min) is on the same order as the RMSE of the telemetry sensor.

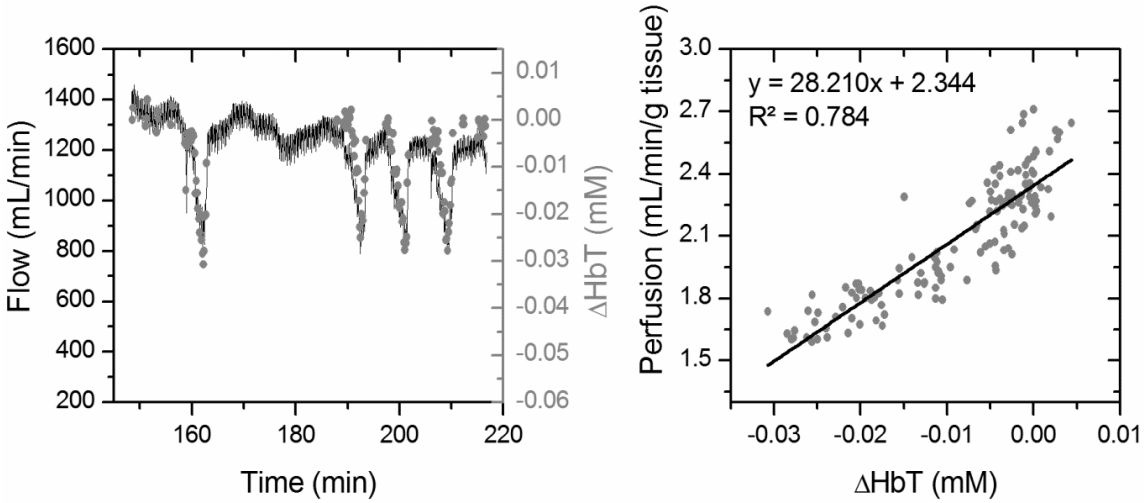

Fig. 66. (Left) Total hemoglobin concentration (ΔHbT) and flow changes. (Right) Scatter plot of measured hemoglobin concentration change (ΔHbT) vs. tissue perfusion (flow normalized by liver weight).

Oxygenation

To track oxygenation changes, the hemoglobin oxygenation index (ΔHbD) was computed, as obtained from the measured DC levels, which, as discussed in the Materials and Methods section, is a measure of tissue oxygenation affected by both arterial and venous oxygen saturation levels. This level is compared to both oxygen

supply (MOS) and venous oxygenation (SvO_2) from the two different studies as shown in Figure 67. As described earlier, for the first study (Figure 67-a) we induced hypoxia and we did not alter perfusion. However, in the second study (Figure 67-b) we had multiple occlusions of the HA and PV at various levels of oxygen saturation during hypoxia. Vascular occlusions have been shown to alter tissue perfusion and oxygenation in liver tissue [115].

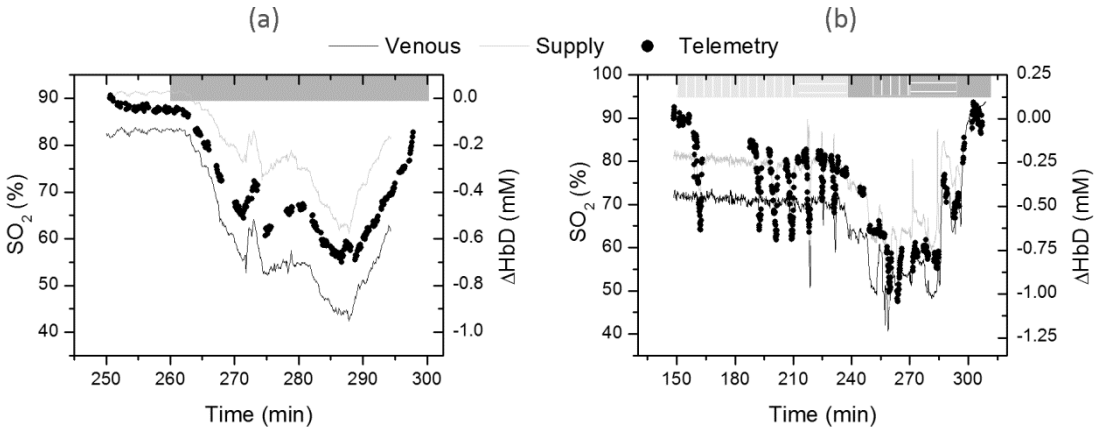

Fig. 67. Hemoglobin oxygenation index (right axis) measured by the optical telemetry system versus venous and mixed oxygen saturation (left axis) for study 1 (a) and 2 (b). Venous oxygenation is measured by the oximetry catheter placed in the vena cava while the supply oxygenation is the weighted average of the HA and PV oxygenation described by equation V.3.

Figure 67 indicates that the measured hemoglobin oxygenation index is tracking oxygenation changes. This measure was obtained from the collected DC signal that is probing both the HA/PV supply and the post-hepatic venous components. To verify that this measure contains oxygenation information about both supply and hepatic venous blood we correlated the measurements to the reference data obtained from the

oxygenation catheters and flow meters. Although ΔHbD correlated well with both supply and venous oxygenation (data shown in supplementary information), it correlated best with a combination of the two using multiple linear regression (MLR) analysis described by equation V.5. The coefficient of determination (R^2) was 0.99 for study 1 (no vascular occlusions) and 0.80 for study 2 (vascular occlusions at multiple levels of oxygenation) respectively. This corresponds to a root mean square error (RMSE) of 1.39% and 3.93% respectively.

$$\Delta HbD = a.MOS + b.SvO_2 + c \qquad (V.5)$$

Having the calibration coefficients (a, b, and c) from the MLR, the mixed oxygen saturation (MOS) measured by the gold standards, and the hemoglobin oxygenation index (ΔHbD) measured by the telemetry system, equation V.5 was used to compute venous oxygen saturation (SvO_2). Figure 68 shows the predicted venous oxygenation and the measured oxygenation by the venous catheter as a function of time. Note that in study 2, occlusions are performed on the hepatic artery and are always seen as a decrease in the measured venous oxygenation by our probe. However, this decrease is not detected by the venous catheter during the first three occlusions because the catheter was measuring hemoglobin oxygen saturation in the vena cava rather than the hepatic veins. Thus, the first three occlusions performed on the hepatic artery caused a decrease in the hepatic venous oxygen saturation as shown by our probe but did not have a substantial effect on the systemic venous oxygenation, where the venous catheter is measuring, since the HA flow is relatively low (7% of total cardiac output) compared to the portal vein flow (22% of total cardiac output).

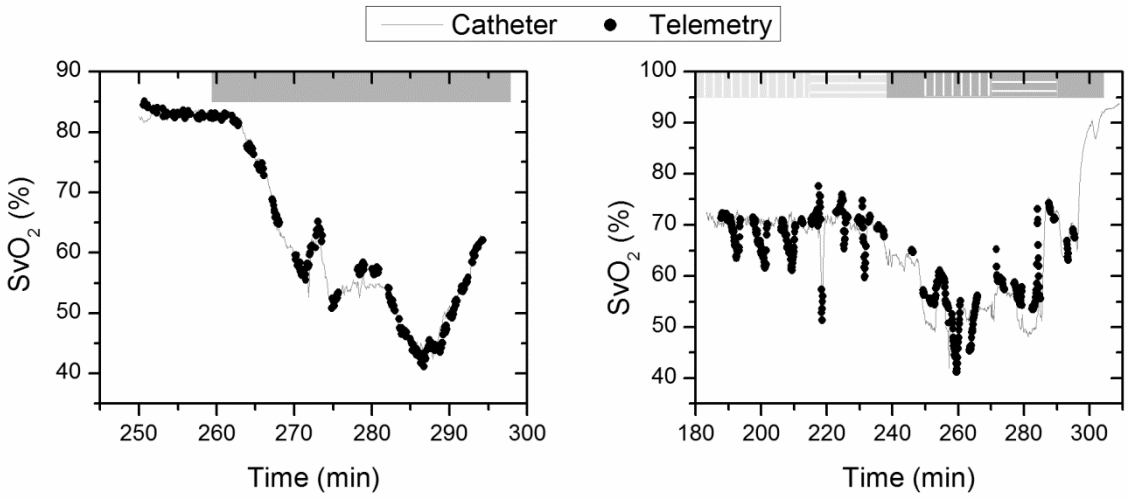

Fig. 68. Venous oxygen saturation as measured by the telemetry sensor (black dots) and the central venous catheter (grey line) for study 1 (left) and 2 (right).

The data from both experiments are shown on the scatter plot of Figure 69. Note that the data from study 2 have a higher RMSE (3.93%) compared to study 1 (1.39%). This increase is mainly due to the occlusions performed in that study, and part of this perceived error is from the reference measurements, and not our system, because it was probing central venous oxygenation and not the hepatic vein.

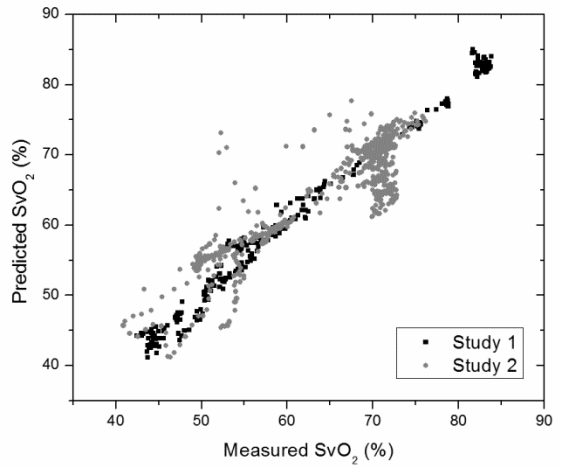

Fig. 69. Scatter plot of the predicted (telemetry) versus measured (catheter) venous oxygen saturation for both studies (1: black & 2: grey).

The data shown in Figures 68 and 69 use the supply oxygen saturation levels obtained from the catheters to extract the venous oxygenation from the DC levels. However, as described earlier, we wanted to determine the supply oxygenation levels from the pulsatile signal and avoid using any additional reference measurements. To do so, the modulation ratio (R) was calculated, and measurements were calibrated as discussed in the Materials and Methods section. The data from each experiment were calibrated separately. These measurements were compared to the Mixed Oxygen Saturation (MOS) described earlier. Figure 70 shows the measured MOS and the reference data from the catheters and the flowmeters computed using equation V.3. The modulation ratio was able to predict the MOS except when the oxygen saturation dropped below 75%. This is a known problem of pulse oximeters and is mainly due to the high attenuation of the red wavelength (735 nm) for low oxygenation levels. If needed, this issue can be resolved by optimizing the sensor design (illumination

wavelength, amplification, etc.) to operate for low oxygen saturation levels [58]. During study 2, the oxygen saturation during vascular occlusions dropped to as low as 56%, and the sensor was still able to measure it accurately. We believe this is due to the decreased absorbance as a result of the perfusion decrease that allowed the red wavelength (735 nm) to still be measured accurately.

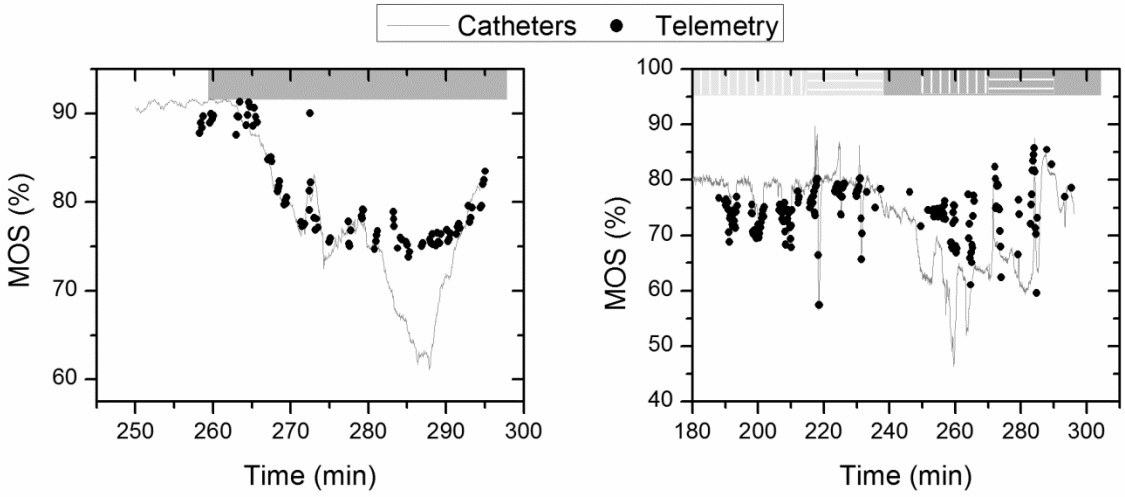

Fig. 70. Mixed oxygen supply (MOS) measured by the telemetry sensor (black dots) and the reference equipment (grey line) for both studies (1: left, & 2: right).

For oxygenation levels above 72% (for normal perfusion levels) and 55% (for low perfusion levels) the calculated modulation ratio from the pulsatile signal was able to predict oxygenation changes with an RMSE of 2.19% and 2.82% for study 1 and 2 respectively. Figure 71 shows the corresponding scatter plot.

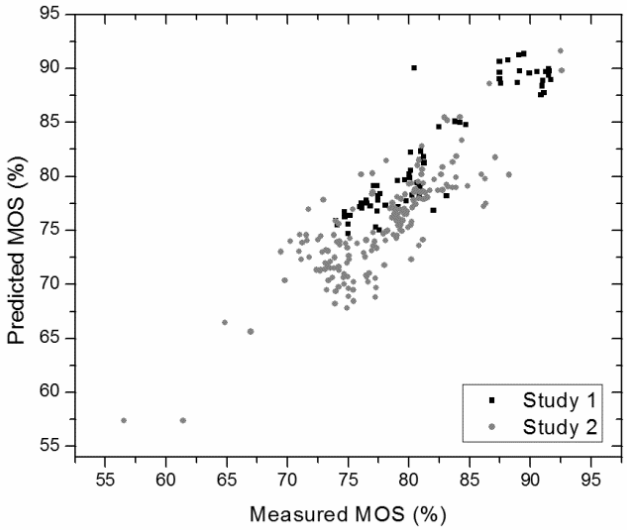

Fig. 71. Scatter plot of the predicted vs. measured MOS for study 1 (black) and 2 (grey).

These predicted MOS levels can be used with equation V.5 to predict venous oxygenation SvO_2 without the need for a reference measurement. Because the pulsatile signal could not predict data for very low oxygen saturations, we tested this concept on all other parts of the data, and we obtained the measurements shown in Figure 72. For study 1, we were able to measure venous oxygen saturation with an RMSE of 1.17% (R^2=0.986) while for study 2 the RMSE was higher at 3.44% (R^2=0.1). This increased prediction error is mainly due to the changes measured during HA occlusions that are not reflected in the central venous oximetry catheter measurements. However, we believe that these changes likely reflect variations in the hepatic venous oxygenation.

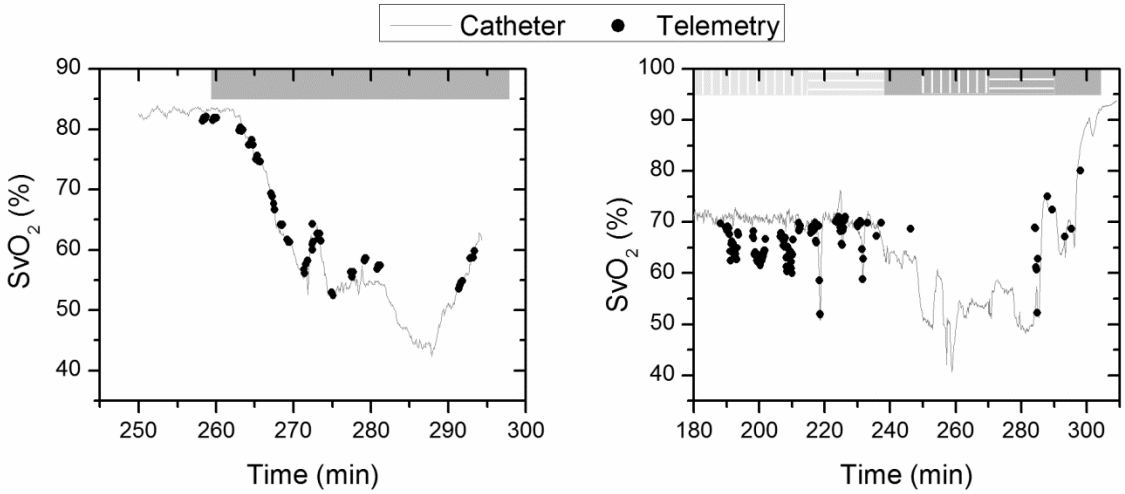

Fig. 72. Predicted venous oxygen saturation by combining the DC NIRS measurements with the AC pulse oximetry measurements. Note that the missing values correspond to the periods where MOS dropped below 72% and, because of the previously reported problem with signal from the red wavelength, could not get reliable pulse oximetry measurements. Study 1 & 2 are shown in left & right panel respectively.

Discussion

The oxygenation measurements obtained by the telemetry sensor agreed for the most part with the reference oxygen saturation measurements acquired by the vascular catheters. Specifically, the pulse oximetry signal was shown to track the defined quantity MOS which is a function of the flow and oxygenation of the HA and PV. The hepatic tissue supply oxygenation was measured with an RMSE of 2.82% for the range 72-100%. We were able to resolve venous oxygenation changes with an RMSE of 1.39%. This resolution went up to 3.93% when vascular occlusions were performed simultaneously with the hypoxia. Finally, we were able to measure perfusion changes with a resolution of 0.135 mL/min/g of tissue in the range of 1.5 to 3.0 mL/min/g. This

resolution was similar to the variation of the baseline measurements by the reference flowmeters.

The main discrepancy between the oxygenation measurements obtained by the telemetry sensor and the reference oxygen saturation measurements acquired by the vascular catheters occurred during HA occlusions where the telemetry sensor showed a decrease in the venous oxygen saturation while the central venous catheter did not show any change. We believe that the short duration of occlusions on the HA caused a local drop in the intrahepatic venous oxygenation which was not reflected in the systemic data measured by the oximetry catheters.

During vascular occlusions, the measured hemoglobin concentration changes correlated with the hepatic flow (R^2~0.78). During these occlusions, HbO_2 levels decreased while Hb levels increased, thereby resulting in a net decrease of total hemoglobin concentration (HbT). This agrees with previously reported findings by El-Desoky *et al.* that measured hemoglobin changes in porcine hepatic tissue using a commercial NIRS system [115]. The RMSE in tracking tissue perfusion was found to be 0.13 mL/min/g. We believe that part of this error is caused by the comparison of direct perfusion measurements from the telemetry system to flow levels measured by the reference vascular flowmeters. Soft tissue acts as a capacitor and quick changes seen in the vascular flow can sometimes be delayed and filtered by the tissue.

Chapter Conclusions

In this chapter, a bench-top and a wireless sensor were tested in a series of *in vivo* porcine studies. Perfusion heterogeneity studies showed that there are no significant

differences in perfusion changes among the different parts of the hepatic parenchyma. Five different locations were tested and all probes detected similar trends of perfusion during vascular occlusions.

In addition, the resolution of the sensors was tested and the bench-top system was able to resolve arterial and venous oxygenation changes with an RMSE of be 6.73% and 3.47% respectively. In this study, reference vascular flowmeters were not able to detect flow signals. Thus, we were not able to correct the supply oxygenation to include the contribution of the portal vein. This contributed partially to the high error in measuring arterial oxygenation. In addition, reference perfusion measurements were not available to quantify the performance of the sensor; however, the measured perfusion trends detected all induced vascular occlusions.

The wireless system resolved perfusion changes with an RMSE of 0.13 mL/min/g of tissue. This was on the same order as the fluctuations measured from the baseline data collected with the reference flow meters. Oxygen supply changes were detected with a resolution (RMSE) of 2.19 %, when perfusion levels were not altered, and 2.82 % when vascular occlusions were induced. The sensor could not detect changes in supply oxygenation when oxygen saturation went below 72% for normal perfusion levels. Similarly, venous oxygen saturation was measured with an RMSE of 1.39%. This resolution went up to 3.93% when vascular occlusions were induced.

As mentioned earlier, the described sensor can be applied to a wide variety of applications that can benefit from continuous monitoring of perfusion and oxygenation. In the following chapter, we demonstrate the use of this sensor to monitor intestinal

perfusion for abdominal trauma patients and the required modification to the sensor design.

CHAPTER VI

OTHER APPLICATIONS: MONITORING INTESTINAL PERFUSION[*]

Introduction

The sensor described in this dissertation is designed to measure perfusion and oxygenation in tissue. Although the focus of the work described herein is hepatic tissue, the same principle can be applied to any type of tissue where vasculature can be probed by light. Depending on the properties of the tissue under investigation, some of the sensor parameters might need to be adjusted. In this chapter, we demonstrate the possibility of applying the same sensing principle for monitoring severe trauma patients during resuscitation. Monitoring intestinal perfusion and oxygen consumption in abdominal trauma patients is essential during the resuscitation period. Photoplethysmography is capable of monitoring these changes in real-time to provide the medical staff with a timely and quantitative measure of the adequacy of resuscitation. In this chapter, the challenges of using optical techniques in monitoring hemodynamics in intestinal tissue are discussed and solutions to these challenges are presented using a combination of Monte Carlo modeling and theoretical analysis of light propagation in tissue. In particular, it is shown that by using visible wavelengths (i.e. 470 and 525 nm) the perfusion signal is enhanced and the background contribution is decreased compared

[*] Part of this chapter is reprinted from T. J. Akl, M. A. Wilson, M. N. Ericson *et al.*, "Intestinal perfusion monitoring using photoplethysmography," J Biomed Opt, 18(8), 87005 (2013), with kind permission of SPIE, Copyright 2013 by Society of Photo Optical Instrumentation Engineers.

to using traditional near infrared wavelengths leading to an order of magnitude enhancement in the signal to background ratio. It was further shown that, using the visible wavelengths, similar sensitivity to oxygenation changes could be obtained (over 50% compared to that of NIR wavelengths). This is mainly due to the increased contrast between tissue and blood in that spectral region and the confinement of the photons to the thickness of the small intestine. Moreover, the modeling results show that the source to detector separation should be limited to roughly 6 mm while using traditional near infrared light, with a few centimeters source to detector separation, leads to poor signal to background ratio. Finally, a visible wavelength system was tested in an *in vivo* porcine study and showed the possibility of monitoring intestinal perfusion changes.

Injury is the leading cause of death for people aged 1-44 year(s) in the United States. It results in 31 million Emergency Department (ED) visits each year and accounts for approximately a third of all ED visits and 8% of all hospital stays [120]. Injury is a worldwide problem, and it results in 5.8 million deaths annually, many of which can be prevented [121]. When a patient loses a large volume of blood due to an injury, their blood pressure drops causing poor perfusion and oxygen delivery to tissue. This lack in perfusion results in anaerobic metabolism that causes tissue acidosis which can lead to the failure of multiple vital organs, known as multiple organ dysfunction syndrome (MODS). To avoid MODS, treatment usually starts by controlling the bleeding and volume resuscitation before operating on any of the primary injuries [122, 123]. The oxygen deprivation period is commonly known as shock. Longer shock periods result in a higher tissue oxygen debt, which usually requires longer resuscitation time even after

some of the vital signals (i.e. heart rate, blood pressure, etc.) of the patient are back to normal levels. During that period, the tissue oxygen uptake/consumption and perfusion are elevated to accommodate for tissue needs. Consequently, normal oxygen consumption has been proposed as the safe end-point of resuscitation [124]. The current standard of care for the resuscitation end-point relies on systemic indicators such as blood pressure, urine output and heart rate. After these parameters are normalized, up to 85% of patients are still in "compensated shock" and still have tissue acidosis [122]. Monitoring tissue perfusion and oxygen consumption in real time can provide clinicians with a more clear and safe end-point of resuscitation [124].

Some functional imaging modalities, such as magnetic resonance imaging (MRI), can provide information about perfusion and oxygen consumption; however they are not cost-efficient and have a low throughput, thus they are not appropriate for continuous monitoring [125]. Optical techniques can potentially provide a real-time, cost-efficient and minimally invasive way for monitoring perfusion and oxygenation changes in tissue [9, 14, 22, 38, 77, 107, 126]. Currently, the gold standards for tissue perfusion and flow monitoring in operating rooms are thermal diffusion, laser Doppler and transit-time ultrasound flowmetry [14-17]. Although these techniques can provide continuous, real-time reading of microcirculation perfusion changes and/or vascular flow levels, they do not provide any data on the oxygen uptake which is critical to assess the adequacy of perfusion and tissue stress.

Traditional oxygenation measurement techniques, such as catheterization and blood draws, are invasive and not suitable for long-term, continuous monitoring of

oxygenation changes. Optical techniques remain the gold standard for non-invasive monitoring of tissue oxygen saturation because of hemoglobin's optical properties that change depending on its oxygenation state [30, 31]. Near Infrared Spectroscopy (NIRS) is perhaps the most common of these techniques [32, 126, 127].

Optical oximetry sensors commonly employ long visible and NIR wavelengths (660 nm to 940 nm) due to the relative transparency of biological tissue in that range [58, 59]. Compared to visible light, this allows a higher penetration depth (several millimeters) and a larger probing volume that is typically desired to increase the hemoglobin signal. For that same reason, large source to detector separations (~10 - 50 mm) are typically used to probe deep tissue and avoid superficial poorly vascularized regions [60, 128-130]. However, in the case of monitoring trauma patients during resuscitation, particularly abdominal trauma, it is of paramount importance to monitor perfusion and oxygen uptake in the intestines which are relatively thin and transparent to light [131, 132]. The human jejunum is 3.5 to 4 mm in thickness and probing it with conventional NIR probes leads to high background signals and causes strong motion artifact from the lumen of the intestine and/or other tissue surrounding it [133]. This is problematic for any optical technique and in particular to PPG sensors that measure the inherently weak arterial pulsatile signal (0.2-5.2%), which can sometimes be overridden by these motion artifacts [48]. In addition, because of the small volume of probed tissue, the hemoglobin signal is usually weak. Previous studies by Hickey *et al.* showed that using shorter source to detector separations can lead to better PPG signals from the splanchnic organs such as the bowel and stomach [39, 134]. However, wavelength

selection was not discussed which is essential to maximize the signal to background ratio from the small probed volume. Moving to the visible wavelengths range where hemoglobin absorption is an order of magnitude higher than its NIR counterpart, increases the sensitivity to hemoglobin changes. In this paper, a thorough theoretical analysis of the problems of monitoring perfusion and oxygenation using NIR light in the intestine are presented. Monte Carlo simulations to support the findings as well as potential solutions are also proposed and tested. Finally, the results are verified with preliminary *in vivo* porcine studies with a sensor based on the PPG technique.

Materials and Methods

In order for an optical sensor to succeed in monitoring perfusion and oxygenation changes in the intestine it has to satisfy a few conditions: 1- High sensitivity to hemoglobin concentration changes, 2- Optical contrast between the two oxygenation states of hemoglobin at the selected wavelength(s) and 3- Penetration depth that is sufficient to satisfy conditions 1 and 2 but that does not exceed the thickness of the probed tissue (< 3 mm). In the following paragraphs of this section, the methods used to adjust these parameters to conform to the proposed criteria are presented. The two main independent variables are: illumination wavelengths and source to detector separation.

Perfusion and Oxygenation Signal

Hemoglobin absorption is the main source of contrast in monitoring perfusion and oxygenation changes. To study the strength of the signal at different wavelengths, we look at the absorption coefficient dynamic range due to perfusion and oxygenation

changes. This is followed by Monte Carlo simulations that consider the contribution of both the absorption and scattering of light in tissue.

The oxygenation signal is mainly a result of the change in the absorption properties of hemoglobin when it switches between its oxygenated and deoxygenated state (HbO_2 and Hb respectively). A typical pulse oximeter would operate two Red-NIR wavelengths of light: one that is more sensitive to oxy-hemoglobin and the other more sensitive to deoxy-hemoglobin. Most sensors employ a third wavelength at an isobestic point that has optical properties independent of the oxygenation state. This wavelength is typically used to measure and/or separate the contribution of other hemoglobin forms (met-hemoglobin and carboxy-hemoglobin) as well as other confounder chromophores and dyes in the selected spectral region [34, 135]. A common method of studying the oxygenation signal as a function of wavelength is to look at the differences between the optical properties of oxy- and deoxy-hemoglobin. These differences are mainly due to the absorption coefficient since the scattering properties of blood have been shown to be relatively independent of its oxygen content [30]. Equation (VI.1) was used to look at the oxygenation signal at each wavelength. Note that the zero crossings of that equation correspond to isobestic points.

$$S_\lambda = \left| \varepsilon_{Hb,\lambda} - \varepsilon_{HbO_2,\lambda} \right| \qquad \text{(VI.1)}$$

In equation (VI.1) S_λ is the difference signal and $\varepsilon_{Hb,\lambda}$ and $\varepsilon_{HbO2,\lambda}$ are the absorption coefficient of deoxy- and oxy-hemoglobin respectively.

The perfusion signal is a result of the change in blood volume in the tissue. To simulate that signal, the full dynamic range due to changes in blood volume is examined.

This is quantified by the difference in absorption coefficient between normally perfused tissue and unperfused (ischemic) tissue (eq. (VI.2)). This quantity, designated SBR_λ, has the same trend as the signal to background ratio (blood to total signal). Further details on equations VI.1 and VI.2 are described in the supplementary information.

$$SBR_\lambda = \left| \varepsilon_{perfused,\lambda} - \varepsilon_{tissue,\lambda} \right| \Big/ \left(\varepsilon_{perfused,\lambda} + \varepsilon_{tissue,\lambda} \right) \quad \text{(VI.2)}$$

These simplified equations served as a guide for the simulations. Specifically, they provided information regarding which wavelengths are viable candidates for determining appropriate oxygenation and perfusion signals and which ones are less sensitive to hemodynamic changes. The performance of the wavelengths of interest guided by the above 2 equations was modeled using Monte Carlo simulations as described in a later section (*Monte Carlo Model*).

Penetration Depth

The penetration depth properties were assessed using the equations derived by Weiss *et al.* based on a random walk model [73]. The first quantity of interest is the mean penetration depth (Z). This symbolizes the average penetration depth of a group of photons launched into a medium. This quantity is a function of the optical properties (μ_a and μ_s') of the medium, which in turn depend on the wavelength of light and the distance from the source to detector (r) used to collect these photons (eq. (VI.3)).

$$Z_{r,\lambda} = \frac{0.476 r^{1/2}}{\left(\mu_a \mu_s'\right)^{1/4}} \quad \text{(VI.3)}$$

In equation (VI.3), μ_a and μ'_s are the absorption coefficient and the reduced scattering coefficient of the medium (perfused tissue) respectively. In addition, r is the source to detector separation. Although important in describing how deep photons propagate in the medium, the mean penetration depth (*Z*) described above does not provide the full picture needed to understand the probing volume nor what percentage of photons are probing the intestine lumen and/or surrounding tissue. To obtain that information, the probability density function (*p*) of the penetration depth is calculated as described in equation (VI.4) [73]. The equation describes the distribution of the collected photons over depth for which *z* represents the depth in tissue which is different from the mean penetration depth *Z*.

$$p_{z,r} = 8\left(3\mu_a\mu_s'\right)^{1/2}.\frac{z}{r}.\exp\left(-\left(48\mu_a\mu_s'\right)^{1/2}.\frac{z^2}{r}\right) \qquad \text{(VI.4)}$$

Note that equations 3 and 4 assume a homogeneous infinite medium of perfused tissue. The optical properties are also considered to be the weighted average of tissue and fully oxygenated blood (SO_2=100%) and all of these equations (VI.1 – VI.4) are evaluated in MATLAB (Mathworks inc, MA).

Monte Carlo Model

For the Monte Carlo (MC) simulations, the MCML program developed by Wang *et al.* was employed [66]. The medium was considered a single layer of homogeneous tissue. The optical properties were varied to model changes in the perfusion and oxygenation state as shown in Table 4. Eight commercially available LED wavelengths were selected for the simulations. The optical properties used for the intestine tissue

were reported by Chan *et al.* [132]. The tissue refractive index and anisotropy factor were assumed to be 1.4 and 0.9 respectively. There are numerous references for the optical properties of blood but the ones used in this work were based on the data reported by Scott Prahl [31] and Friebel *et al.* [30]. The refractive index of blood was assumed to be constant at 1.4. Previous work has shown that changes in whole blood refractive index are minimal and that the refractive index ranges between 1.375 and 1.4 for the wavelength range of interest [136]. Every MC simulation consisted of 10 million photon packets.

Table 4. Optical properties of the human jejunum and oxygenated & deoxygenated blood. The absorption and scattering coefficients in the table are all in cm^{-1}.

Wavelength (nm)	Tissue			Oxygenated Blood			Deoxygenated blood		
	μ_a	μ_s	g	μ_a	μ_s	g	μ_a	μ_s	g
470	3.98	129.2	0.9	177.8	400.8	0.996	86.5	400.8	0.996
525	2.65	107.5	0.9	165.4	392.0	0.995	188.3	392.0	0.995
590	3.08	129.2	0.9	77.12	329.5	0.992	151.7	329.5	0.992
630	1.5	81.6	0.9	3.26	316.0	0.992	27.57	316.0	0.992
660	1.32	76.8	0.9	1.71	315.0	0.991	17.28	315.0	0.991
735	1.47	69.2	0.9	2.21	304.2	0.992	5.90	304.2	0.992
805	1.73	65.8	0.9	4.49	292.5	0.991	3.93	292.5	0.991
850	2	64	0.9	5.67	282.5	0.991	3.70	282.5	0.991

In the case of perfused tissue, the medium was considered homogeneous and the optical properties were set to the weighted average of the two (tissue and blood). Skinner

et al. reported that the percentage of vasculature within the mucosa of the colon tissue varies between 7.7 and 13.4 %v/v depending on the exact location (proximal, mid and distal colon) [137]. This number should be a fair estimate of the percentage of vasculature in the small intestine. In the model 12% was used as the percentage of vasculature.

Instrumentation

To verify the results of the model, data was collected using a PPG sensor system developed by our group. The instrumentation has been previously described in detail and the performance of the system has been validated on phantoms and liver tissue [38, 63, 104, 105, 138]. In brief, the sensor system interface board has four channels each that can drive a three wavelength PPG probe. The wavelengths are time multiplexed and the reflected light is collected using a single photodetector. The collected signal from each sensor, after passing through a pre-amp, is split into two channels. The first channel, the AC channel, has a band-pass filter with cutoff frequencies (f_{3dB}) at 0.15 and 15 Hz. It should be noted that the high-pass cutoff frequency in the band-pass filter was set at 0.15 Hz to separate the DC level from the AC signal. The pulsatile AC signal is known to be around 0.2 to 5.2% of the total collected signal [48] and requires high gain amplification; however, it is essential that the DC signal be eliminated from the amplification channel to avoid saturation and that is the role of the 0.15 Hz cutoff filters. In the new generation of this device, the cutoff frequency is set at 0.55 Hz to also eliminate the respiratory motion. The filtered AC signal passes through a variable gain amplifier that allows for 8 gain settings in the range of 1- to 400-V/V. In the second channel, the DC channel, the

signal passes through a low pass filter with a 3 dB cutoff frequency at 0.15Hz. The same process is applied to all three wavelengths of each sensor resulting in a total of 24 channels (4 sensors, 3 wavelengths each, AC and DC signals). All channels are digitized and sent to a computer for processing via a USB-6529 (National Instruments Corporation, TX).

Two types of probes were used in the *in vivo* porcine study. The NIR probes, which our group has used in the past to measure perfusion and oxygenation in liver tissue, consist of three wavelengths 735, 805 and 940 nm (L660/735/805/940-40B42, Epitex Inc., Japan) [38, 104, 105]. All three wavelengths are packaged in the same lens to probe the same location and avoid problems associated with tissue perfusion heterogeneity. The second set of probes was fabricated for the sole purpose of this study and consists of visible wavelengths bands centered at 465, 525 and 639 nm (part number LED528EHP, LED465E, LED630E respectively, Thorlabs Inc., MD, USA). Each of the wavelengths is a separate LED with a separate lens. The three LEDs were placed at three of the corners of the photodetector to insure the source to detector spacing is the same for all wavelengths. Both probes used the same silicon photodetector (S2833-01, Hamamatsu, Japan). The edge to edge separation on all probes used in this work was approximately 2 mm (equivalent to 6-7 mm center to center separation). The visible probes were coated with polydimethylsiloxane (PDMS) to protect the circuitry from the wet tissue. Figure 73 shows the sensor interface and the probes.

Fig. 73. The benchtop PPG sensor (on left) including the laptop, data acquisition card and sensor interface electronics (from left to right). The right panels show the visible (upper) and NIR LEDs (lower) used in this study.

In Vivo Porcine Study

All animal studies were performed under an animal use protocol (AUP #2010-257) approved by the Institutional Animal Care and Use Committee at Texas A&M University. The study was performed on a pig (body weight 27.5 kg). The pig was premedicated with Telazol 5-10 mg/kg. Buprenorphine 0.01-0.05 mg/kg was used as an analgesic. Both drugs were introduced intramuscularly 10 to 15 minutes prior to anesthesia induction. Initial anesthesia was induced via inhalation of 3-4% Isoflurane in Oxygen at 3 L/min. An endotracheal tube was placed and connected to a breathing circuit. Anesthesia was maintained by inhalation of Isoflurane (0.5-4%) in Oxygen (15 mL/lb). Once the animal was anesthetized, a laparotomy was performed to get access to the intestine. The two PPG probes (NIR and VIS) were placed in adjacent spots on the serosal surface of the jejunum and sutured in place. Throughout the operation, the animal's vital signals (SpO_2, pressure, heart rate, temperature and respiratory rate) were monitored and recorded. To alter the perfusion levels, the intestine was clamped for short durations (<1min) throughout the study. The PPG signals on both probes were

recorded continuously before, during and after the occlusions. At the end of the data collection, while still anesthetized, the animal was euthanized with a barbiturate derivative solution administered intravenously (80-120 mg/kg).

Results and Discussion

Perfusion and Oxygenation Signals

Using equation (VI.2), the changes in signal to background ratio as a function of wavelength (*Fig. 74*) were investigated. The visible wavelengths were shown to carry a higher signal from blood relative to tissue. The results of this equation (solid line in Fig. 74) were compared to the ratio of reflectance from the perfused and unperfused cases from a MC simulation (dots in Fig. 74). The two methods show the same trend indicating a higher perfusion signal from the visible wavelengths. The signal (reflectance ratio) is over an order of magnitude higher at 470 nm compared to the NIR wavelengths (735, 805 and 940 nm). Note that the three wavelengths of 470, 525 and 590 nm have similar levels of perfusion signal. This quantity was calculated for the case of oxygenated and deoxygenated blood and the results are similar in both cases (data shown in the supplementary information). In summary, at 470 nm the signal is higher in the oxygenated case while for the 590 nm wavelength the signals are flipped and the deoxygenated case shows a higher level of signal. The 525 nm showed the same levels of signal independent from the oxygenation level and can be used as an isobestic wavelength.

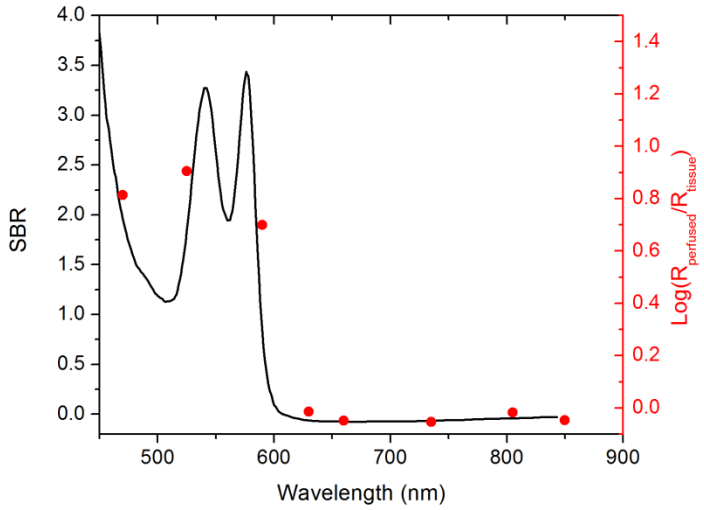

Fig. 74. Perfusion signal as a function of wavelength when the intestine is perfused with oxygenated blood. The solid lines show the SBR calculated from the change in the optical properties between perfused and ischemic tissue (eqn. VI.2). The dots are the Monte Carlo simulation results at the wavelengths of interest. The data show over an order of magnitude enhancement when moving from the NIR to VIS wavelengths.

Equation (VI.1) was used to better quantify the oxygenation signal. The zero crossings in that equation indicate isobestic points in the hemoglobin spectrum (*Fig. 75 – solid line*). Since this equation is simplified and does not take into account the effects of scattering, tissue optical properties and geometry, we compared the results to the change in reflectance measured from MC simulations ($|R_{Oxy} - R_{Deoxy}|$) as reflected by the red dots in Fig. 75. The results show that the level of the oxygenation signal is similar for both the visible and NIR wavelengths. Moreover, there are multiple wavelengths in the visible range that can be used as isobestic points. Note that the oxygenation signal defined in equation VI.1 and shown in Figure 75, describes the sensitivity of the sensor

to oxygenation changes since it measures the total change in signal over the full range of oxygenation (from 0 to 100% saturation).

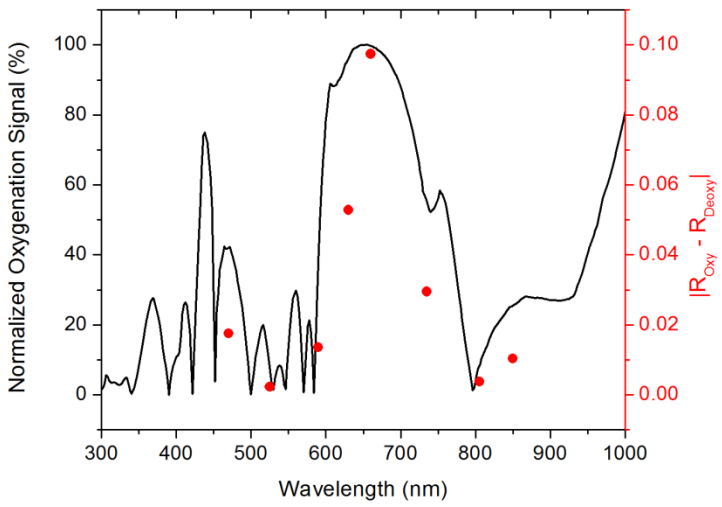

Fig. 75. Oxygenation signal as calculated by equation VI.1 (solid line) and through Monte Carlo simulations (red dots). Note the multiple isobestic points in the visible range and the bands of oxygenation sensitive wavelengths.

One possible issue in using the visible wavelengths is the narrowness of the oxygen sensitive bands which might pose a problem when using LEDs. To test for that, the extinction coefficient of hemoglobin over the wavelength band of commercially available LEDs was integrated and the ratio of extinction coefficient of oxy- and deoxy-hemoglobin over these bands for both the NIR and visible wavelengths were explored. This ratio shows the change in hemoglobin absorption coefficient with the change in its oxygenation state indicating whether or not a wavelength is sensitive to hemoglobin's oxygen saturation levels. The specifications of the LEDs are based on the datasheets of

Epitex LEDs (part # L470-30M32, L525-30T52, L590-35D32 and L660/735/805/940-40B42) and the full width half max ranged between 14 and 45 nm. The results shown in Figure 76 indicate that the 525 and 805 nm LEDs can both be considered as isobestic points and their absorption coefficients are independent of the oxygenation level (ratio close to 1). The other wavelengths showed similar levels of change (40 to 80% change in optical properties) depending on the oxygenation state. The 470 and 940 nm wavelength bands are more sensitive to oxy-hemoglobin while the 590 and 735 nm wavelength bands are more absorbed by deoxy-hemoglobin.

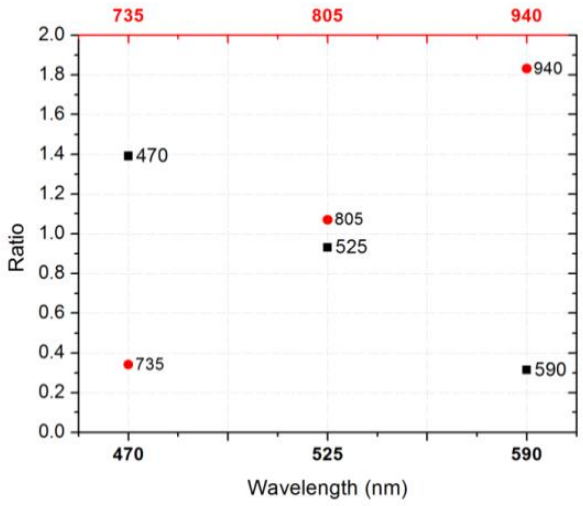

Fig. 76. Ratio of the average absorption coefficient of oxy- to deoxy-hemoglobin over the band of commercially available LEDs in the visible and NIR range. The data show that the change in the hemoglobin absorption coefficient with oxygenation changes is similar for NIR and VIS wavelengths.

Penetration Depth

The simulation results presented in the previous section show that some visible wavelength bands (i.e. 470, 525 and 590 nm) carry enough perfusion and oxygenation information to be used in a PPG sensor. However, the simulation results do not answer the concerns about motion artifacts from the lumen of the intestine and adjacent tissue. To study the effects of motion, the mean penetration depth described in equation (VI.3) was explored. As shown in Figure 77, the mean penetration depth depends on the illumination wavelength and the source to detector separation (A plot of mean penetration depth vs. source to detector separation is provided in the supplementary information). There is a clear increase in the penetration depth when moving from visible to NIR wavelengths and that is why this region of NIR is sometimes referred to as the therapeutic window. Note that even for a 16 mm separation, the mean penetration depth of NIR wavelength is still under 3 mm. However, different photons penetrate to different depths in tissue and the mean penetration depth is only the average and does not represent the maximum penetration of photons.

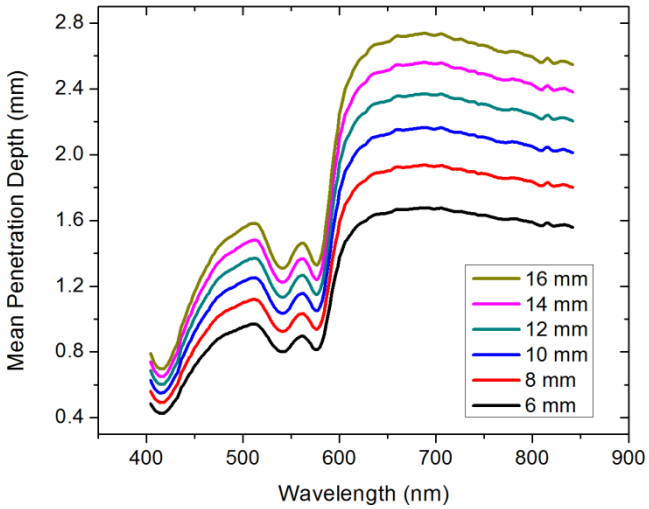

Fig. 77. Mean penetration depth for different source to detector separations as a function of wavelength. The legend shows the corresponding source to detector separation for each line (In case colors are not available, note that the legend is in the same order as the lines appear on the graph).

Although the mean penetration depth provides insight into the relationship between the penetration depth and the wavelengths and source to detector separation, it does not tell the full story. To assess the amount of light probing the background, the probability distribution of the penetration depth given by equation (VI.4) is investigated. Below is an example of the probability distribution for the two studied isobestic points (525 and 805 nm). The mean wall-thickness used for the human small intestine is 4 mm [133]. This number varies across patients and even across different areas of the intestine of the same patient, however, the serosal side of the intestine is where perfusion should be monitored and the penetration depth there should be limited to around 3 mm. Anything past that limit is assumed to contribute to the background signal. The data in Figure 78 show that approximately 25.25% of photons probe the background when using

NIR wavelengths and a 16 mm separation. This can be reduced by either limiting the source to detector separation to less than 6 mm for the NIR wavelengths or using visible wavelengths with separations up to 20 mm. As mentioned earlier, most NIR based sensors utilize separations that are greater than 10 mm. Furthermore, if the sensor is utilizing regular LEDs and photodiodes, the average diameter of each is approximately 5 mm which constrains the source to detector separation, measured from center to center, to 5 mm or more. Moving to the visible wavelengths gives more flexibility in the geometry of the probe.

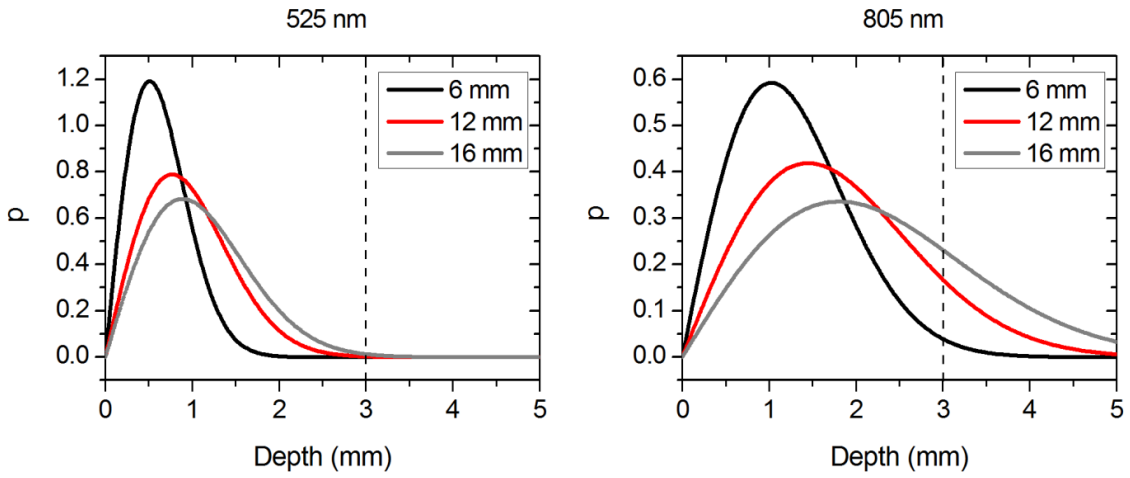

Fig. 78. Probability density function of the photon penetration depth for the visible and NIR isobestic wavelengths (525 and 805 nm) for multiple source to detector separations.

Figure 79 shows the transmittance and reflectance data from the MC simulation. Transmittance is the amount of light that was transmitted through the wall relative to the light that was incident on the tissue. It is three to seven orders of magnitude lower for

visible wavelengths compared to their NIR counterparts. Furthermore, this decrease in the transmittance does not reduce the reflectance substantially. The reflectance is the light intensity collected at the surface of the tissue relative to the intensity coming from the source.

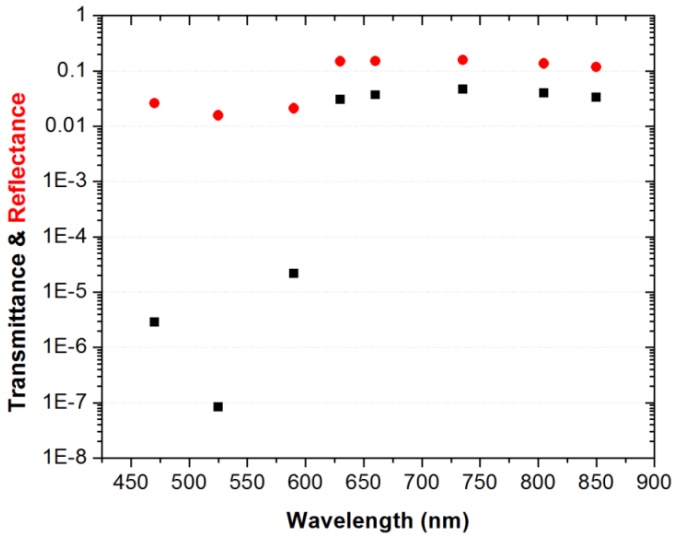

Fig. 79. Transmittance (squares) and reflectance (dots) as a function of wavelength as calculated by MC simulations. Note that the y-data is shown on a log scale.

In summary, the modeling indicates that the visible wavelengths (470, 525 and 590 nm) have a better perfusion signal with similar oxygenation signal compared to their NIR counterparts. The green (525 nm) wavelength can be used as an isobestic point if needed. Moreover, all three visible wavelengths have similar perfusion signal levels and similar penetration depths. This is imperative to insure similar probing volumes and avoid problems associated with perfusion heterogeneity that can lead to erroneous

oxygenation results [58]. In addition, at typical separation distances, NIR wavelengths penetrate through the wall of the intestine to probe its lumen, and sometimes neighboring tissue. This results in high background signals that can vary tremendously with motion artifact. In the following section, preliminary *in vivo* results are presented that validate and fortify these theoretical findings.

In Vivo Porcine Study

Data was collected from the jejunum using two probes simultaneously. One of the probes had three NIR wavelengths (735, 805 and 940 nm) while the second probe had three visible wavelengths (470, 525 and 630 nm). As shown in the modeling results in the previous section, the red LED (630 nm) used in the visible probe for these experimental results was not optimal since it would pick up a strong background. However, at the time of the study the 590 nm LED was not available so the 630 nm LED was used as a reference since it uses the same photodetector as the other visible wavelengths and is probing the same tissue. Figure 80 shows the time domain PPG waveform collected on each of the wavelengths (on right) and the corresponding Fast Fourier Transform (on left). Three peaks can be seen in the spectra: 1) 0.25 Hz which corresponds to the respiratory rate (15 breaths/min); 2) 2.18 Hz corresponding to the cardiac cycle peak (130.8 beats/min); and 3) 3.95 Hz that corresponds to a non-thermoregulatory shivering motion. Note that the body temperature was closely monitored and controlled throughout the study. Multiple reports discuss the non-thermoregulatory shivering that is common in an anesthetized animal but still not completely understood [139, 140]. This high frequency motion peak was slightly shifted

on the NIR probe (4.61 Hz) compared to the VIS probe (3.95 Hz) which might be due to the different wavelengths probing different locations or different depths.

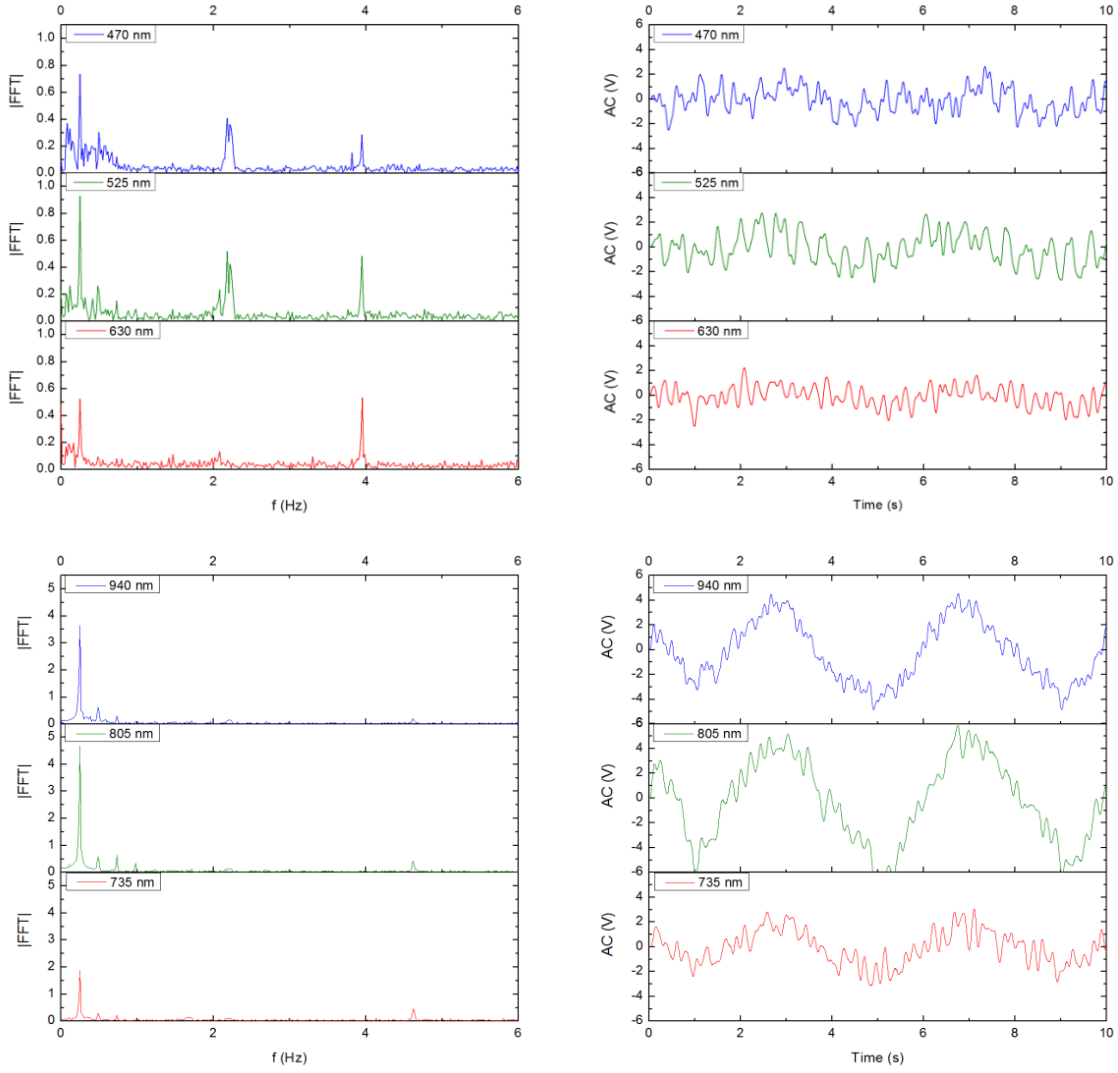

Fig. 80. The time domain (right column) PPG signal collected in vivo *and the corresponding FFT spectrum (left column) for VIS and NIR wavelengths. In Figure 96 in Appendix H the 1-5 Hz region is zoomed in showing the cardiac cycle and high frequency motion peaks.*

In Figure 80 it was shown that the NIR wavelengths have a much greater background at low-frequency. In addition, the cardiac cycle peak, which carries information about arterial blood, is higher for the visible wavelengths (see zoomed in 1 to 5 Hz range in Figure 96 in Appendix H). These findings indicate that the visible wavelengths have higher blood signal and lower background levels and verify the modeling from the previous section. To quantify the signal to background enhancement, the ratio from these spectra is plotted as shown in Figure 81. The signal to background ratio is defined as the ratio of the cardiac cycle peak to the highest background frequency component above 0.15 Hz (DC excluded). Compared to the signal to background ratio from the Monte Carlo simulations (red dots) it can be seen that both quantities follow the same trend and show a better performance for the visible wavelength range compared to the traditional NIR wavelength range. Note that the Monte Carlo simulations assumed monochromatic sources while the *in vivo* data were collected with LEDs that had a bandwidth (FWHM~14-45 nm). This accounts for some of the discrepancy in the results for the 630 nm wavelength that falls on the tail of the decaying SBR graph. The LED data show a higher SBR for that wavelength compared to the model in part, because it is integrating over that tail.

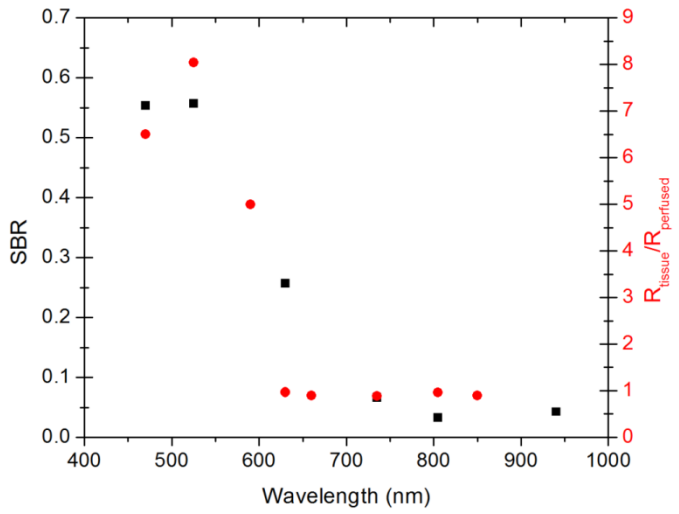

Fig. 81. The signal to background ratio from the in vivo *porcine data (black squares) compared to the Monte Carlo simulations results (red dots).*

To verify that the cardiac cycle peak is not motion artifact and is in fact probing the microvasculature, the part of the small intestine that had the optical probes was occluded for short periods of time (~30s). The probes recorded data continuously throughout the process (4 occlusions and 4 baselines). The Fast Fourier Transform (FFT) was applied to a sliding window (25 seconds in width and shifted 10 seconds for every data point) and the cardiac cycle peak was detected using an automated program implemented in MATLAB (Mathworks, Inc.). The cardiac cycle peak was monitored during baseline and occlusion periods (Figure 95, Appendix H). Figure 82 shows the change in the peak amplitude due to the drop in perfusion during occlusions at the two visible wavelengths (470 and 525 nm). The data show that the peaks correlate well with perfusion changes and can discriminate the baseline and occlusion state ($p<0.05$, two pair student t-test). The goal of these studies was to assure that the detected signal was

due to the microvasculature perfusion. In the future, the sensor will be optimized and quantitative studies comparing its performance to other monitors (i.e. Laser Doppler) will be conducted to assess the accuracy, sensitivity and resolution of the sensor to perfusion and oxygenation changes. The inspired oxygen level was maintained constant during these studies. The modulation ratio (R) was calculated using the data from the two visible wavelengths (470 and 525 nm) as shown in figure 95 in the Appendix H.

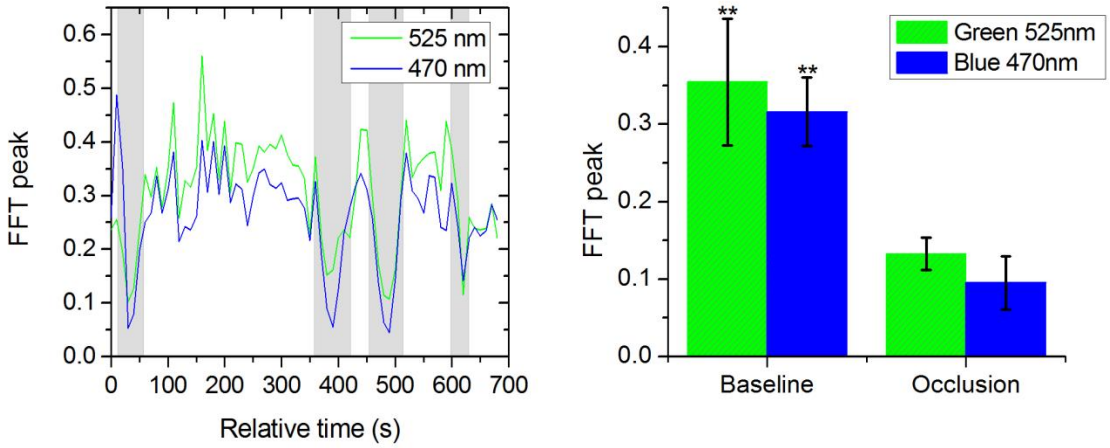

Fig. 82. In vivo *porcine occlusion study data. The left panel shows the change in time of the FFT peak on the two wavelengths of interest. The grey areas correspond to the occlusion periods. The right panel shows the average of the FFT peaks during baseline and occlusion periods.*

The findings presented in this chapter can be applied to other cases where limited penetration depth is desired. One example is monitoring skin oxygenation and perfusion which is of interest in cases such as wound healing and critical limb ischemia [141, 142]. As discussed earlier, current perfusion and oxygenation systems are optimized to probe

relatively deep tissue and when sensors are applied to the skin, the collected signal is mainly probing muscle vasculature and reflects muscle rather than skin hemodynamics which is a desired property when studying muscle physiology [128, 143, 144]. The reported findings can be applied to measure skin perfusion and oxygenation changes for the aforementioned applications or coupled with NIRS measurements of muscle hemodynamics to correct for small variations in the muscle signal due to skin perfusion.

Chapter Conclusions

In this chapter, we investigated the use of the sensor described in this thesis for other applications provided some minor changes. In particular, we investigated the challenging application of monitoring intestinal tissue that presents challenges in high background signals and low hemoglobin signature due to weak perfusion. The use of the bench-top photoplethysmography sensing system with visible and NIR wavelengths was modeled and tested *in vivo* for use as an intestinal perfusion and oxygenation sensor. This type of sensing system, once optimized and reduced in size, could be a critical improvement for monitoring trauma patients during resuscitation. By modeling the signal in the visible wavelength range (i.e. 470, 525 and 590 nm), it was shown that the perfusion signal could be increased and the background signal reduced while keeping the same levels of oxygenation sensitivity as traditional NIR sensors. In addition, it was shown that by using small source to detector separations (6 mm or less) the background signals collected from the lumen of the intestine and/or surrounding tissue can be decreased by limiting the probing depth. These findings were confirmed in an *in vivo* porcine study by comparing NIR and VIS LED based probes. VIS wavelengths had a

higher signal to background ratio than NIR wavelengths. In addition, we used the sensor to monitor perfusion changes during *in vivo* occlusion studies and showed that the signal correlates with the perfusion state.

These results show the possibility of employing the technology described in this dissertation in a variety of applications provided minor adjustments.

CHAPTER VII

CONCLUSIONS AND FUTURE WORK

Every year, over 6,000 patients receive a liver transplant in the United States alone [5] and we still don't have a continuous sensor to monitor the graft in real-time and alert the medical staff of any complications. Such a device could have a great impact on patient survival and retransplantation rates. In this thesis, a perfusion and oxygenation sensor is described. The sensor is designed to operate on batteries and transmit data wirelessly with the goal of building an implantable sensor that can monitor hepatic hemodynamics in the first two weeks post-surgery. Nearly 60% of graft failures take place during that period [7].

The first part of this thesis (Chapters I-III) focused on describing the theory of the used optical techniques and the instrumentation of the sensor. The sensor combines the principles of pulse oximetry and near infrared spectroscopy. This allows for measuring and separating the hemoglobin oxygen saturation of the supply and venous vasculature and subsequently providing a measure of oxygen consumption to assess oxidative stress. In addition, the sensor tracks perfusion changes. The relative measure of perfusion, coupled with the oxygenation readings gives an assessment of the sufficiency of nutrients supply to the tissue. The sensor uses three wavelengths of light in the tissue optical window (also known as therapeutic window) where light can penetrate deeper in tissue. The three light emitting diodes are time multiplexed allowing for the use of a single photo-detector to collect the signal from the three sources. Band-pass filters were

designed to separate the DC component from the weak pulsatile signal for amplification. The separation between the source and the detector is an important factor in determining the performance of an optical sensor based on diffuse reflectance. Simulations and *in vitro* studies showed that higher intensities can be collected at short separations while long separations showed a higher signal to background ratio. Separations in the 2-6 mm range provided sufficient SBR while maintaining high levels of reflectance which allows the use of less power on the light sources to save battery power. In addition, the effect of wavelengths selection was studied and the 735, 805, and 940 nm wavelengths were found to have a good oxygenation signal, penetration, and performance consistency over a wide range of oxygen saturation levels. In addition, LEDs are commercially available at these wavelengths.

The latter part (Chapters IV-VI) described the testing of the sensor *in vitro*, *ex vivo*, and *in vivo*. Phantoms were designed to mimic the anatomy of the liver vasculature and the optical and mechanical properties of hepatic tissue. These phantoms were used in fluidic circuits that simulate hepatic blood flow. Dye mixtures were designed to mimic the optical properties of blood in the desired wavelength range and eliminate the use of blood in the *in vitro* testing. The sensor detected oxygen saturation changes with a prediction error of 1.3% within a study and 4.6% across studies. These errors are on the same order as the preparation error of the different dye solutions used in the study. In addition, perfusion changes were resolved with a resolution of 0.07 mL/min/g. Similar results were obtained with the *ex vivo* rat liver perfusion studies where the RMSE in detecting perfusion changes was found to be 0.08 mL/min/g of tissue. Finally, the sensor

was tested in a series of *in vivo* porcine studies. In these studies we were able to measure venous oxygenation, arterial oxygenation, and perfusion with an RMSE of 3.93%, 2.82%, and 0.13 mL/min/g respectively.

Future work should focus on miniaturizing the electronics to make the sensor implantable. Different coating and fixation strategies should also be investigated. In particular, photonic textiles can be used to design a probe that is flexible and easy to fix on tissue [145]. Some groups have shown the possibility to fabricate an "electronic patch" that coats the sensor electronics and adheres to skin [146]. In the design of the sensor, the addition of a second detector at a different distance from the source provides a measure of the differential pathlength factor which is needed to calibrate the measurements of the sensor. This feature will be most valuable for long term studies where the calibration factor might change over time due to sensor encapsulation and/or movement. In addition, the use of multiple detectors will increase the collected light intensity and different processing methods can be used to benefit from that. The use of custom made photodetectors can increase the active area of detection without increasing the probe size leading to higher signal levels [61].

In addition, the preliminary results from the PPG waveform analysis are very promising. This part of the signal is very rich in information that is still to be studied and understood. Investigating and quantifying tissue mechanical properties non-invasively has many other potential applications ranging from monitoring wound healing, to fibrosis of various types of tissue.

REFERENCES

[1] Guyton, A. C., and Hall, J. E., [Textbook of medical physiology] Elsevier Saunders, Philadelphia (2006).

[2] Starzl, T. E., Groth, C. G., Brettschneider, L., Penn, I., Fulginiti, V. A. *et al.*, "Orthotopic homotransplantation of the human liver," Ann Surg, 168(3), 392-415 (1968).

[3] Zarrinpar, A., and Busuttil, R. W., "Liver transplantation: past, present and future," Nat Rev Gastroenterol Hepatol, 10(7), 434-40 (2013).

[4] Adam, R., McMaster, P., O'Grady, J. G., Castaing, D., Klempnauer, J. L. *et al.*, "Evolution of liver transplantation in Europe: report of the European Liver Transplant Registry," Liver Transpl, 9(12), 1231-43 (2003).

[5] Organ Procurement and Transplantation Network (OPTN) and Scientific Registry of Transplant Recipients (SRTR). OPTN / SRTR 2011 Annual Data Report. Rockville, MD: Department of Health and Human Services, Health Resources and Services Administration, Healthcare Systems Bureau, Division of Transplantation; 2012.

[6] Varotti, G., Grazi, G. L., Vetrone, G., Ercolani, G., Cescon, M. *et al.*, "Causes of early acute graft failure after liver transplantation: analysis of a 17-year single-centre experience," Clin Transplant, 19(4), 492-500 (2005).

[7] Quiroga, J., Colina, I., Demetris, A. J., Starzl, T. E., and Van Thiel, D. H., "Cause and timing of first allograft failure in orthotopic liver transplantation: a study of 177 consecutive patients," Hepatology, 14(6), 1054-62 (1991).

[8] Eghtesad, B., Miller, C. M., and Fung, J. J., [Cleveland Clinic:Current clinical medicine, 2nd edition, "Post-liver transplantation management"] Elsevier Saunders, Philadelphia, 85, 564-570 (2009).

[9] Ericson, M. N., Wilson, M. A., Coté, G. L., Baba, J. S., Xu, W. *et al.*, "Implantable sensor for blood flow monitoring after transplant surgery," Minim Invasive Ther Allied Technol, 13(2), 87-94 (2004).

[10] Ericson, M. N., Wilson, M., Cote, G., Britton, C. L., Xu, W. *et al.*, "Development of an implantable oximetry-based organ perfusion sensor," Conf Proc IEEE Eng Med Biol Soc, 3, 2235-8 (2004).

[11] Klar, E., Bredt, M., Kraus, T., Angelescu, M., Mehrabi, A. *et al.*, "Early assessment of reperfusion injury by intraoperative quantification of hepatic microcirculation in patients," Transplant Proc, 29(1-2), 362-3 (1997).

[12] Klar, E., Kraus, T., Bredt, M., Osswald, B., Senninger, N. *et al.*, "First clinical realization of continuous monitoring of liver microcirculation after transplantation by thermodiffusion," Transpl Int, 9 Suppl 1, S140-3 (1996).

[13] Takaya, S., Nonami, T., Selby, R., Doyle, H., Murray, G. *et al.*, "The relationship of systemic hemodynamics and oxygen consumption to early allograft failure after liver transplantation," Transpl Int, 6(2), 73-6 (1993).

[14] Humeau, A., Steenbergen, W., Nilsson, H., and Stromberg, T., "Laser Doppler perfusion monitoring and imaging: novel approaches," Med Biol Eng Comput, 45(5), 421-435 (2007).

[15] Laustsen, J., Pedersen, E. M., Terp, K., Steinbruchel, D., Kure, H. H. *et al.*, "Validation of a new transit time ultrasound flowmeter in man," Eur J Vasc Endovasc Surg, 12(1), 91-6 (1996).

[16] Bowman, H. F., and Balasubramaniam, T. A., "A new technique utilizing thermistor probes for the measurement of thermal properties of biomaterials," Cryobiology, 13(5), 572-80 (1976).

[17] Khot, M. B., Maitz, P. K., Phillips, B. R., Bowman, H. F., Pribaz, J. J. *et al.*, "Thermal diffusion probe analysis of perfusion changes in vascular occlusions of rabbit pedicle flaps," Plast Reconstr Surg, 115(4), 1103-9 (2005).

[18] Vajkoczy, P., Roth, H., Horn, P., Lucke, T., Thomé, C. *et al.*, "Continuous monitoring of regional cerebral blood flow: experimental and clinical validation of a novel thermal diffusion microprobe," J Neurosurg, 93(2), 265-274 (2000).

[19] Klar, E., Kraus, T., Bleyl, J., Newman, W. H., Bowman, H. F. *et al.*, "Thermodiffusion for continuous quantification of hepatic microcirculation--validation and potential in liver transplantation," Microvasc Res, 58(2), 156-66 (1999).

[20] Boas, D. A., and Dunn, A. K., "Laser speckle contrast imaging in biomedical optics," J Biomed Opt, 15(1), 011109-011109-12 (2010).

[21] Duncan, D. D., and Kirkpatrick, S. J., "Can laser speckle flowmetry be made a quantitative tool?," J Opt Soc Am A, 25(8), 2088-2094 (2008).

[22] Gagnon, L., Desjardins, M., Jehanne-Lacasse, J., Bherer, L., and Lesage, F., "Investigation of diffuse correlation spectroscopy in multi-layered media including the human head," Opt Express, 16(20), 15514-15530 (2008).

[23] Shang, Y., Zhao, Y., Cheng, R., Dong, L., Irwin, D. *et al.*, "Portable optical tissue flow oximeter based on diffuse correlation spectroscopy," Opt Lett, 34(22), 3556-3558 (2009).

[24] Yu, G., Durduran, T., Lech, G., Zhou, C., Chance, B. *et al.*, "Time-dependent blood flow and oxygenation in human skeletal muscles measured with noninvasive near-infrared diffuse optical spectroscopies," J Biomed Opt, 10(2), 024027-024027 (2005).

[25] Yu, G., Durduran, T., Zhou, C., Wang, H. W., Putt, M. E. *et al.*, "Noninvasive monitoring of murine tumor blood flow during and after photodynamic therapy provides early assessment of therapeutic efficacy," Clin Cancer Res, 11(9), 3543-52 (2005).

[26] Shang, Y., Zhao, Y., Cheng, R., Dong, L., Irwin, D. *et al.*, "Portable optical tissue flow oximeter based on diffuse correlation spectroscopy," Opt Lett, 34(22), 3556-8 (2009).

[27] Materne, R., Smith, A. M., Peeters, F., Dehoux, J. P., Keyeux, A. *et al.*, "Assessment of hepatic perfusion parameters with dynamic MRI," Magn Reson Med, 47(1), 135-42 (2002).

[28] Veit-Haibach, P., Treyer, V., Strobel, K., Soyka, J. D., Husmann, L. *et al.*, "Feasibility of integrated CT-liver perfusion in routine FDG-PET/CT," Abdom Imaging, 35(5), 528-36 (2010).

[29] Faber, D. J., Aalders, M. C. G., Mik, E. G., Hooper, B. A., van Gemert, M. J. C. *et al.*, "Oxygen saturation-dependent absorption and scattering of blood," Phys Rev Lett, 93(2), 028102-028102-4 (2004).

[30] Friebel, M., Helfmann, J., Netz, U., and Meinke, M., "Influence of oxygen saturation on the optical scattering properties of human red blood cells in the spectral range 250 to 2000 nm," J Biomed Opt, 14(3), 034001-034001-6 (2009).

[31] Prahl, S., "Optical absorption of hemoglobin," Oregon Medical Laser Center, http://omlc.ogi.edu/spectra/hemoglobin/, accessed on January 20, 2011, (1999).

[32] Beilman, G. J., Groehler, K. E., Lazaron, V., and Ortner, J. P., "Near-infrared spectroscopy measurement of regional tissue oxyhemoglobin saturation during hemorrhagic shock," Shock, 12(3), 196-200 (1999).

[33] Ferrari, M., and Quaresima, V., "A brief review on the history of human functional near-infrared spectroscopy (fNIRS) development and fields of application," Neuroimage, 63(2), 921-35 (2012).

[34] Kamat, V., "Pulse oximetry," Indian J. Anaesth, 46(4), 261-268 (2002).

[35] Sahni, R., "Noninvasive monitoring by photoplethysmography," Clin Perinatol, 39(3), 573-83 (2012).

[36] Severinghaus, J. W., "Takuo Aoyagi: discovery of pulse oximetry," Anesth Analg, 105(6 Suppl), S1-4 (2007).

[37] Squire, J., "Instrument for measuring quantity of blood and its degree of oxygenation in web of the hand," Clin Sci, 4, 331-339 (1940).

[38] Akl, T. J., Long, R., McShane, M. J., Ericson, M. N., Wilson, M. A. *et al.*, "Optimizing probe design for an implantable perfusion and oxygenation sensor," Biomed Opt Express, 2(8), 2096-109 (2011).

[39] Hickey, M., and Kyriacou, P. A., "Optimal spacing between transmitting and receiving optical fibres in reflectance pulse oximetry," J Phys: Conf Ser, 85(1), 012030 (2007).

[40] Mannheimer, P. D., Fein, M. E., and Casciani, J. R., "Physio-optical considerations in the design of fetal pulse oximetry sensors," Eur J Obstet Gynecol Reprod Biol, 72, S9-S19 (1997).

[41] Reichelt, S., Fiala, J., Werber, A., Forster, K., Heilmann, C. *et al.*, "Development of an implantable pulse oximeter," IEEE Trans Biomed Eng, 55(2 Pt 1), 581-8 (2008).

[42] Zakharov, P., Talary, M. S., and Caduff, A., "A wearable diffuse reflectance sensor for continuous monitoring of cutaneous blood content," Phys Med Biol, 54(17), 5301-5320 (2009).

[43] Akl, T. J., Wilson, M. A., Ericson, M. N., and Cote, G. L., "Intestinal perfusion monitoring using photoplethysmography," J Biomed Opt, 18(8), 87005 (2013).

[44] Allen, J., "Photoplethysmography and its application in clinical physiological measurement," Physiol Meas, 28(3), R1-39 (2007).

[45] Sandberg, M., Zhang, Q., Styf, J., Gerdle, B., and Lindberg, L. G., "Non-invasive monitoring of muscle blood perfusion by photoplethysmography: evaluation of a new application," Acta Physiol Scand, 183(4), 335-43 (2005).

[46] Jobsis, F. F., "Noninvasive, infrared monitoring of cerebral and myocardial oxygen sufficiency and circulatory parameters," Science, 198(4323), 1264-1267 (1977).

[47] Delpy, D. T., and Cope, M., "Quantification in tissue near–infrared spectroscopy," Philos Trans R Soc B, 352(1354), 649-659 (1997).

[48] De Felice, C., Latini, G., Vacca, P., and Kopotic, R. J., "The pulse oximeter perfusion index as a predictor for high illness severity in neonates," Eur J Pediatr, 161(10), 561-562 (2002).

[49] Awad, A. A., Stout, R. G., Ghobashy, M. A., Rezkanna, H. A., Silverman, D. G. *et al.*, "Analysis of the ear pulse oximeter waveform," J Clin Monit Comput, 20(3), 175-84 (2006).

[50] Subramanian, H., Ibey, B. L., Xu, W. J., Wilson, M. A., Ericson, M. N. *et al.*, "Real-time separation of perfusion and oxygenation signals for an implantable sensor using adaptive filtering," IEEE Trans Biomed Eng, 52(12), 2016-2023 (2005).

[51] Sugimoto, H., Okochi, O., Hirota, M., Kanazumi, N., Nomoto, S. *et al.*, "Early detection of liver failure after hepatectomy by indocyanine green elimination rate measured by pulse dye-densitometry," J Hepatobiliary Pancreat Surg, 13(6), 543-8 (2006).

[52] Michalak, G. J., Goodrich, G. P., Schwartz, J. A., James, W. D., and O'Neal, D. P., "Murine photoplethysmography for *in vivo* estimation of vascular gold nanoshell concentration," J Biomed Opt, 15(4), 047007-047007-5 (2010).

[53] Baulig, W., Bernhard, E. O., Bettex, D., Schmidlin, D., and Schmid, E. R., "Cardiac output measurement by pulse dye densitometry in cardiac surgery," Anaesthesia, 60(10), 968-73 (2005).

[54] Cennini, G., Arguel, J., Aksit, K., and van Leest, A., "Heart rate monitoring via remote photoplethysmography with motion artifacts reduction," Opt Express, 18(5), 4867-75 (2010).

[55] Verkruysse, W., Svaasand, L. O., and Nelson, J. S., "Remote plethysmographic imaging using ambient light," Opt Express, 16(26), 21434-21445 (2008).

[56] Kamshilin, A. A., Teplov, V., Nippolainen, E., Miridonov, S., and Giniatullin, R., "Variability of microcirculation detected by blood pulsation imaging," PLoS One, 8(2), e57117 (2013).

[57] Wieringa, F. P., Mastik, F., and van der Steen, A. F., "Contactless multiple wavelength photoplethysmographic imaging: a first step toward "SpO2 camera" technology," Ann Biomed Eng, 33(8), 1034-41 (2005).

[58] Mannheimer, P. D., Casciani, J. R., Fein, M. E., and Nierlich, S. L., "Wavelength selection for low-saturation pulse oximetry," IEEE Trans Biomed Eng, 44(3), 148-158 (1997).

[59] Yamashita, Y., Maki, A., and Koizumi, H., "Wavelength dependence of the precision of noninvasive optical measurement of oxy-, deoxy-, and total-hemoglobin concentration," Med Phys, 28(6), 1108-14 (2001).

[60] Reuss, J., and Siker, D., "The pulse in reflectance pulse oximetry: Modeling and experimental studies," J Clin Monit Comput, 18(4), 289-299 (2004).

[61] Duun, S. B., Haahr, R. G., Birkelund, K., and Thomsen, E. V., "A ring-shaped photodiode designed for use in a reflectance pulse oximetry sensor in wireless health monitoring applications," IEEE Sens J, 10(2), 261-268 (2010).

[62] Ibey, B., Subramanian, H., Ericson, N., Xu, W., Wilson, M. *et al.*, "Processing of pulse oximeter signals using adaptive filtering and autocorrelation to isolate perfusion and oxygenation components," Proc SPIE, 5702, (2005).

[63] Ericson, M., Frank, S., Britton, C., Baba, J., Lee, S. *et al.*, "A custom electronics platform for implantable perfusion sensor development," Future of Instrumentation International Workshop (FIIW), 63-66 (2011).

[64] Kienle, A., and Patterson, M. S., "Improved solutions of the steady-state and the time-resolved diffusion equations for reflectance from a semi-infinite turbid medium," J Opt Soc Am A Opt Image Sci Vis, 14(1), 246-54 (1997).

[65] Schmitt, J. M., Zhou, G. X., Walker, E. C., and Wall, R. T., "Multilayer model of photon diffusion in skin," J Opt Soc Am A, 7(11), 2141-2153 (1990).

[66] Wang, L. H., Jacques, S. L., and Zheng, L. Q., "MCML - Monte-Carlo modeling of light transport in multilayered tissues," Comput Methods Programs Biomed, 47(2), 131-146 (1995).

[67] Guyton, A. C., [Textbook of medical physiology] Saunders, Philadelphia (1991).

[68] Ritz, J. P., Roggan, A., Isbert, C., Müller, G., Buhr, H. J. *et al.*, "Optical properties of native and coagulated porcine liver tissue between 400 and 2400 nm," Lasers Surg Med, 29(3), 205-212 (2001).

[69] Tziafalia, C., Vlychou, M., Tepetes, K., Kelekis, N., and Fezoulidis, I. V., "Echo-Doppler measurements of portal vein and hepatic artery in asymptomatic patients with hepatitis B virus and healthy adults," J Gastrointestin Liver Dis, 15(4), 343-6 (2006).

[70] Wang, P. J., Li, W. C., Xi, G. M., Wang, H. Q., Zhang, Z. H. *et al.*, "Biomechanical study of hepatic portal vein in humans and pigs and its value in liver transplantation," Transplant Proc, 41(5), 1906-10 (2009).

[71] Avolio, A. P., "Multi-branched model of the human arterial system," Med Biol Eng Comput, 18(6), 709-18 (1980).

[72] Wang, L., Jacques, S. L., and Zheng, L., "CONV--convolution for responses to a finite diameter photon beam incident on multi-layered tissues," Comput Methods Programs Biomed, 54(3), 141-50 (1997).

[73] Weiss, G. H., Nossal, R., and Bonner, R. F., "Statistics of penetration depth of photons re-emitted from irradiated tissue," J Mod Opt, 36(3), 349-359 (1989).

[74] Lindh, W. Q., [Delmar's comprehensive medical assisting : administrative and clinical competencie] Delmar Cengage Learning, Clifton Park, NY (2013).

[75] Millasseau, S. C., Ritter, J. M., Takazawa, K., and Chowienczyk, P. J., "Contour analysis of the photoplethysmographic pulse measured at the finger," J Hypertens, 24(8), 1449-1456 (2006).

[76] Boas, D. A., Gaudette, T., Strangman, G., Cheng, X., Marota, J. J. *et al.*, "The accuracy of near infrared spectroscopy and imaging during focal changes in cerebral hemodynamics," Neuroimage, 13(1), 76-90 (2001).

[77] Aoyagi, T., "Pulse oximetry: its invention, theory, and future," J Anesth, 17(4), 259-266 (2003).

[78] Delpy, D. T., Cope, M., Vanderzee, P., Arridge, S., Wray, S. *et al.*, "Estimation of optical pathlength through tissue from direct time of flight measurement," Phys Med Biol, 33(12), 1433-1442 (1988).

[79] Lane, N. J., Thorniley, M. S., Manek, S., Fuller, B. J., and Green, C. J., "Hemoglobin oxygenation kinetics and secondary ischemia in renal transplantation," Transplantation, 61(5), 689-96 (1996).

[80] Pogue, B. W., and Patterson, M. S., "Review of tissue simulating phantoms for optical spectroscopy, imaging and dosimetry," J Biomed Opt, 11(4), 041102-041102-16 (2006).

[81] Casciaro, S., Conversano, F., Musio, S., Casciaro, E., Demitri, C. *et al.*, "Full experimental modelling of a liver tissue mimicking phantom for medical ultrasound studies employing different hydrogels," J Mater Sci-Mater M, 20(4), 983-989 (2009).

[82] Cournane, S., Cannon, L., Browne, J. E., and Fagan, A. J., "Assessment of the accuracy of an ultrasound elastography liver scanning system using a PVA-cryogel phantom with optimal acoustic and mechanical properties," Phys Med Biol, 55(19), 5965-5983 (2010).

[83] Harris, E. J., Miller, N. R., Bamber, J. C., Symonds-Tayler, J. R. N., and Evans, P. M., "Speckle tracking in a phantom and feature-based tracking in liver in the presence of respiratory motion using 4D ultrasound," Phys Med Biol, 55(12), 3363-3380 (2010).

[84] Kim, K. S., Lee, J. M., Kim, S. H., Kim, K. W., Kim, S. J. *et al.*, "Image fusion in dual energy computed tomography for detection of hypervascular liver hepatocellular carcinoma phantom and preliminary studies," Invest Radiol, 45(3), 149-157 (2010).

[85] Kopka, L., He, H. D., Foley, W. D., Hu, H., Jacobson, D. R. *et al.*, "Low-contrast detectability of a new multislice versus a monoslice helical CT in a liver phantom," Radiology, 209P, 284-284 (1998).

[86] Martinsen, A. C. T., Saether, H. K., Olsen, D. R., Skaane, P., and Olerud, H. M., "Reduction in dose from CT examinations of liver lesions with a new postprocessing filter: A ROC phantom study," Acta Radiologica, 49(3), 303-309 (2008).

[87] Olerud, H. M., Olsen, J. B., and Skretting, A., "An anthropomorphic phantom for receiver operating characteristic studies in CT imaging of liver lesions," Brit J Radiol, 72(853), 35-43 (1999).

[88] Prakash, P., Converse, M. C., Mahvi, D. M., and Webster, J. G., "Measurement of the specific heat capacity of liver phantom," Physiol Meas, 27(10), N41-N46 (2006).

[89] Schindera, S. T., Nelson, R. C., Mukundan, S., Paulson, E. K., Jaffe, T. A. *et al.*, "Hypervascular liver tumors: Low tube voltage, high tube current multi-detector row CT for enhanced detection - Phantom study," Radiology, 246(1), 125-132 (2008).

[90] Wang, H. Z., Xu, L. F., Yu, J., Huang, Q. M., Wang, X. Y. *et al.*, "Phantom study of the classification of liver fibrosis based on nuclear magnetic resonance elasto-graphy," Acta Physica Sinica, 59(10), 7463-7471 (2010).

[91] Passos, D., Hebden, J. C., Pinto, P. N., and Guerra, R., "Tissue phantom for optical diagnostics based on a suspension of microspheres with a fractal size distribution," J Biomed Opt, 10(6), 064036-064036-11 (2005).

[92] Sun, P., and Wang, Y., "Measurements of optical parameters of phantom solution and bulk animal tissues *in vitro* at 650 nm," Opt Laser Technol, 42(1), 1-7 (2010).

[93] Puhl, G., Schaser, K. D., Vollmar, B., Menger, M. D., and Settmacher, U., "Noninvasive *in vivo* analysis of the human hepatic microcirculation using orthogonal polarization spectral imaging," Transplantation, 75(6), 756-761 (2003).

[94] Michael, G. J., "Alimentary system," The Barts and The London School of Medicine and Dentistry, https://courses.stu.qmul.ac.uk/smd/kb/microanatomy/d/alimentary/.

[95] Ozcan, M. U., Ocal, S., Basdogan, C., Dogusoy, G., and Tokat, Y., "Characterization of frequency-dependent material properties of human liver and its pathologies using an impact hammer," Med Image Anal, 15(1), 45-52 (2011).

[96] Bolin, F. P., Preuss, L. E., Taylor, R. C., and Ference, R. J., "Refractive-index of some mammalian-tissues using a fiber optic cladding method," Appl Opt, 28(12), 2297-2303 (1989).

[97] Long, R., King, T., Akl, T., Ericson, M. N., Wilson, M. *et al.*, "Optofluidic phantom mimicking optical properties of porcine livers," Biomed Opt Express, 2(7), 1877-92 (2011).

[98] Braet, F., and Wisse, E., "Structural and functional aspects of liver sinusoidal endothelial cell fenestrae: a review," Comp Hepatol, 1(1), 1 (2002).

[99] Hong, H. C., Chen, C. M., Chou, Y. C., and Lin, C. H., "Study of novel electrical routing and integrated packaging on bio-compatible flexible substrates," Microsyst Technol, 16(3), 423-430 (2010).

[100] Wang, P. J., He, F., Liao, D. H., Zhang, J., Li, W. C. *et al.*, "The impact of age on incremental elastic modulus and incremental compliance of pig hepatic portal vein for liver xenotransplantation," Xenotransplantation, 16(1), 5-10 (2009).

[101] Di Ninni, P., Martelli, F., and Zaccanti, G., "The use of India ink in tissue-simulating phantoms," Opt Express, 18(26), 26854-26865 (2010).

[102] Madsen, S. J., Patterson, M. S., and Wilson, B. C., "The use of India ink as an optical absorber in tissue-simulating phantoms," Phys Med Biol, 37(4), 985-993 (1992).

[103] Takatani, S., and Graham, M. D., "Theoretical analysis of diffuse reflectance from a two-layer tissue model," Biomedical Engineering, IEEE Transactions on, BME-26(12), 656-664 (1979).

[104] Akl, T. J., King, T. J., Long, R., Ericson, M. N., Wilson, M. A. *et al.*, "*In vitro* performance of a perfusion and oxygenation optical sensor using a unique liver phantom," Proc SPIE, 8229, (2012).

[105] Akl, T. J., King, T. J., Long, R., McShane, M. J., Nance Ericson, M. *et al.*, "Performance assessment of an opto-fluidic phantom mimicking porcine liver parenchyma," J Biomed Opt, 17(7), 077008-077008-9 (2012).

[106] Lima, A. P., Beelen, P., and Bakker, J., "Use of a peripheral perfusion index derived from the pulse oximetry signal as a noninvasive indicator of perfusion," Crit Care Med, 30(6), 1210-1213 (2002).

[107] Nogawa, M., Tanaka, S., Shibata, M., and Yamakoshi, K., "Development of a tissue oxygen consumption measurement method based on near-infrared photoplethysmography," Conf Proc IEEE Eng Med Biol Soc, 3, 2227-30 (2004).

[108] Wang, L., Lo, B., and Yang, G. Z., "Reflective photoplethysmograph earpiece sensor for ubiquitous heart rate monitoring," 4th International Workshop on Wearable and Implantable Body Sensor Networks (BSN 2007), 13, 179-183 (2007).

[109] Meigas, K., Kattai, R., and Lass, J., "Continuous blood pressure monitoring using pulse wave delay," Proceedings of the 23rd Annual International Conference of the Ieee Engineering in Medicine and Biology Society, Vols 1-4, 23, 3171-3174 (2001).

[110] Gonzalez, R., Manzo, A., Delgado, J., Padilla, J. M., Trenor, B. *et al.*, "A computer based photoplethysmographic vascular analyzer through derivatives," Computers in Cardiology 2008, Vols 1 and 2, 177-180 (2008).

[111] Lax, H., Feinberg, A. W., and Cohen, B. M., "Studies of the arterial pulse wave. I. The normal pulse wave and its modification in the presence of human arteriosclerosis," J Chronic Dis, 3(6), 618-31 (1956).

[112] Wu, H. T., Lin, B. S., Liu, C. C., and Liu, A. B., "A new contour analysis of photoplethysmographic pulse measured at the finger," Atherosclerosis Supplements, 11(2), 190-190 (2010).

[113] Shikata, T., and Sakai, T., "Elastogenesis in the liver," Pathol Int, 24(1), 21-31 (1974).

[114] Pellicoro, A., Aucott, R. L., Ramachandran, P., Robson, A. J., Fallowfield, J. A. *et al.*, "Elastin accumulation is regulated at the level of degradation by macrophage metalloelastase (MMP-12) during experimental liver fibrosis," Hepatology, 55(6), 1965-1975 (2012).

[115] El-Desoky, A. E., Seifalian, A., Cope, M., Delpy, D., and Davidson, B., "Changes in tissue oxygenation of the porcine liver measured by near-infrared spectroscopy," Liver Transpl Surg, 5(3), 219-26 (1999).

[116] Arvidsson, D., Svensson, H., and Haglund, U., "Laser-Doppler flowmetry for estimating liver blood flow," Am J Physiol, 254(4 Pt 1), G471-6 (1988).

[117] Webster, J. G., [Design of pulse oximeters] Institute of Physics Pub., Bristol ; Philadelphia (1997).

[118] Watzman, H. M., Kurth, C. D., Montenegro, L. M., Rome, J., Steven, J. M. *et al.*, "Arterial and venous contributions to near-infrared cerebral oximetry," Anesthesiology, 93(4), 947-53 (2000).

[119] Tortoriello, T. A., Stayer, S. A., Mott, A. R., McKenzie, E. D., Fraser, C. D. *et al.*, "A noninvasive estimation of mixed venous oxygen saturation using near-infrared spectroscopy by cerebral oximetry in pediatric cardiac surgery patients," Paediatr Anaesth, 15(6), 495-503 (2005).

[120] CDC, Injury in the United States: 2007 Chartbook Centers for Disease Control and Prevention, (2013).

[121] WHO, Injuries and violence: the facts. World Health Organization, (2010).

[122] Tisherman, S. A., Barie, P., Bokhari, F., Bonadies, J., Daley, B. *et al.*, "Clinical practice guideline: endpoints of resuscitation," J Trauma, 57(4), 898-912 (2004).

[123] Fries, C. A., and Midwinter, M. J., "Trauma resuscitation and damage control surgery," Surgery (Oxford), 28(11), 563-567 (2010).

[124] Cohn, S. M., Nathens, A. B., Moore, F. A., Rhee, P., Puyana, J. C. *et al.*, "Tissue oxygen saturation predicts the development of organ dysfunction during traumatic shock resuscitation," J Trauma Acute Care Surg, 62(1), 44-55 (2007).

[125] Lanzman, R. S., Wittsack, H. J., Martirosian, P., Zgoura, P., Bilk, P. *et al.*, "Quantification of renal allograft perfusion using arterial spin labeling MRI: initial results," Eur Radiol, 20(6), 1485-91 (2010).

[126] Hamaoka, T., McCully, K. K., Quaresima, V., Yamamoto, K., and Chance, B., "Near-infrared spectroscopy/imaging for monitoring muscle oxygenation and oxidative metabolism in healthy and diseased humans," J Biomed Opt, 12(6), 062105-062105-16 (2007).

[127] Boushel, R., Langberg, H., Olesen, J., Gonzales-Alonzo, J., Bulow, J. *et al.*, "Monitoring tissue oxygen availability with near infrared spectroscopy (NIRS) in health and disease," Scand J Med Sci Sports, 11(4), 213-22 (2001).

[128] Ferrari, M., Mottola, L., and Quaresima, V., "Principles, techniques, and limitations of near infrared spectroscopy," Can J Appl Physiol, 29(4), 463-87 (2004).

[129] Niwayama, M., Lin, L., Shao, J., Kudo, N., and Yamamoto, K., "Quantitative measurement of muscle hemoglobin oxygenation using near-infrared spectroscopy with correction for the influence of a subcutaneous fat layer," Rev Sci Instrum, 71(12), 4571-4575 (2000).

[130] Pujary, C., Savage, M., and Mendelson, Y., "Photodetector size considerations in the design of a noninvasive reflectance pulse oximeter for telemedicine applications," Proceedings of the IEEE 29th Annual Northeast Bioengineering Conference, 148-149 (2003).

[131] Hiltebrand, L. B., Krejci, V., Banic, A., Erni, D., Wheatley, A. M. *et al.*, "Dynamic study of the distribution of microcirculatory blood flow in multiple splanchnic organs in septic shock," Crit Care Med, 28(9), 3233-41 (2000).

[132] Chan, E., Menovsky, T., and Welch, A. J., "Effects of cryogenic grinding on soft-tissue optical properties," Appl Opt, 35(22), 4526-32 (1996).

[133] Johansson, K., Ahn, H., Lindhagen, J., and Lundgren, O., "Tissue penetration and measuring depth of laser Doppler flowmetry in the gastrointestinal application," Scand J Gastroenterol, 22(9), 1081-8 (1987).

[134] Hickey, M., Samuels, N., Randive, N., Langford, R. M., and Kyriacou, P. A., "Measurement of splanchnic photoplethysmographic signals using a new reflectance fiber optic sensor," J Biomed Opt, 15(2), 027012-027012-8 (2010).

[135] Shamir, M. Y., Avramovich, A., and Smaka, T., "The current status of continuous noninvasive measurement of total, carboxy, and methemoglobin concentration," Anesth Analg, 114(5), 972-8 (2012).

[136] Li, H., Lin, L., and Xie, S. S., "Refractive index of human whole blood with different types in the visible and near-infrared ranges," Proc SPIE, 1(8), 517-521 (2000).

[137] Skinner, S. A., and O'Brien, P. E., "The microvascular structure of the normal colon in rats and humans," J Surg Res, 61(2), 482-490 (1996).

[138] Akl, T. J., King, T. J., Long, R., Baba, J. S., McShane, M. J. *et al.*, "Optimizing source detector separation for an implantable perfusion and oxygenation sensor," Proc SPIE, 7906, (2011).

[139] Horn, E. P., Sessler, D. I., Standl, T., Schroeder, F., Bartz, H. J. *et al.*, "Non-thermoregulatory shivering in patients recovering from isoflurane or desflurane anesthesia," Anesthesiology, 89(4), 878-86 (1998).

[140] Pozos, R. S., Israel, D., McCutcheon, R., Wittmers, L. E., Jr., and Sessler, D., "Human studies concerning thermal-induced shivering, postoperative "shivering," and cold-induced vasodilation," Ann Emerg Med, 16(9), 1037-41 (1987).

[141] Castronuovo Jr, J. J., Adera, H. M., Smiell, J. M., and Price, R. M., "Skin perfusion pressure measurement is valuable in the diagnosis of critical limb ischemia," J Vasc Surg, 26(4), 629-637 (1997).

[142] Adera, H. M., James, K., Castronuovo, J. J., Jr., Byrne, M., Deshmukh, R. *et al.*, "Prediction of amputation wound healing with skin perfusion pressure," J Vasc Surg, 21(5), 823-8; discussion 828-9 (1995).

[143] Tew, G. A., Ruddock, A. D., and Saxton, J. M., "Skin blood flow differentially affects near-infrared spectroscopy-derived measures of muscle oxygen saturation and blood volume at rest and during dynamic leg exercise," Eur J Appl Physiol, 110(5), 1083-9 (2010).

[144] Ferrari, M., Muthalib, M., and Quaresima, V., "The use of near-infrared spectroscopy in understanding skeletal muscle physiology: recent developments," Philos T R Soc A, 369(1955), 4577-4590 (2011).

[145] Rothmaier, M., Selm, B., Spichtig, S., Haensse, D., and Wolf, M., "Photonic textiles for pulse oximetry," Opt Express, 16(17), 12973-12986 (2008).

[146] Haahr, R. G., Duun, S., Thomsen, E. V., Hoppe, K., and Branebjerg, J., “A wearable "electronicpPatch" for wireless continuous monitoring of chronically diseased patients,” 2008 5th International Summer School and Symposium on Medical Devices and Biosensors, 196-200 (2008).

APPENDIX A

MONTE CARLO SIMULATION SOFTWARE

```
%%%%%%%%%%%%%%%%%%%%%%%%monte_carlo_6.m%%%%%%%%%%%%%%%%%%%%
%This program was last updated on July 22,2010
%V6 has the added feature of specifying the numerical aperture of the
%light source
%V5 It includes the extra output of penetration depth at different
%detector positions
%The diffuse reflectance is calculated as a function of r and z where r
%is the radial distance from the source and z is the penetration depth
%In previous versions the diffuse reflectance was calculated as a
%function of x and y
clear all
tic
nb_of_photons=1000000;
step_size=0.01;
%size_limit=2;
threshold=0.001;
NA=0.4;     %numerical aperture of the source
nb_of_layers=3;

%%%%%%%%%%Define the optical properties%%%%%%%%%%%
%medium
nf(1)=1;
nf(nb_of_layers+2)=1;
%layer1
mua(1)=1.1594;
mus(1)=63.014;
g(1)=0.925;
g2(1)=g(1)^2;
nf(2)=1.33;
%layer2
%OXY 7400nm
mua(2)=2.4084;
mus(2)=3050;
g(2)=0.9941;
g2(2)=g(2)^2;
nf(3)=1.392;
%layer3
mua(3)=1.1594;
mus(3)=63.014;
g(3)=0.925;
g2(3)=g(1)^2;
nf(4)=1.33;
%%%%%%%%%%Define the boundaries%%%%%%%%%%%%%%%%%%%
bnd(1)=0;
bnd(2)=0.3;
bnd(3)=1.0;
```

```
bnd(4)=1.5;
%%%%%%%%%%%%%%%%%%%%%%%%%%%%%%%%%%%%%%%%%%%%%%%%%%%%%%%%%%%%%%%%%%%%%%%%
size_limit=max(bnd);
r=sqrt(2*(size_limit/2)^2);
% refl_r=zeros(ceil(r/step_size),size_limit/step_size);
% absorbed=zeros(ceil(r/step_size)+1,size_limit/step_size);
refl_r=zeros(5/step_size,size_limit/step_size);
absorbed=zeros(5/step_size,size_limit/step_size);
b=0;
for i=1:(nb_of_layers+1)
alpha_c(i)=asin(min(nf(i:i+1))/max(nf(i:i+1)));
end
for j1=1:100
for i=1:nb_of_photons/100
    pos.x=0;
    pos.y=0;
    pos.z=0;
    max_depth=0;
    alpha_i=asin(NA*rand/nf(1));  % Angle with the z axis, this is
limited by the NA of the source
    alpha_t=asin(nf(1)*sin(alpha_i)/nf(2));
    muz=cos(alpha_t);
    Rxy=muz*tan(alpha_t);
    theta_x=acos(2*(rand-0.5));     %launching angle relative to the x
axis, the ray has an equal opportunity to be launched at any direction
relative to X
    mux=Rxy*cos(theta_x);
    muy=Rxy*sin(theta_x);


    Refl=0.5*((sin(alpha_i-alpha_t)/sin(alpha_i+alpha_t))^2+…
                  (tan(alpha_i-alpha_t)/tan(alpha_i+alpha_t))^2);

    weight=1-Refl;
    layer=1;    %photon enters the first layer
    while (1)
    S=-log(rand)/(mua(layer)+mus(layer));

    if muz<0
        dS=(bnd(layer)-pos.z)/muz;
    else
        dS=-(pos.z-bnd(layer+1))/muz;
    end

    sg=sign(muz);
    %%%%%%%%%%%%%%%%%%Surface reflections%%%%%%%%%%%%%%%%%%
    %%%%%%%%%%%%%%%%%%%%%%%%%%%%%%%%%%%%%%%%%%%%%%%%%%%%%%%%%%%%%%%%%%%%%%%%
        while (S>=dS)
            pos.x=pos.x+dS*mux;
            pos.y=pos.y+dS*muy;
            pos.z=pos.z+dS*muz;
            alpha_i=acos(abs(muz));
```

```
            S=S-dS;
            if
nf(layer+1)>=nf(layer+1+sg)&&(alpha_i>alpha_c(layer+(sg>0)))
                Refl=1;
            else
                alpha_t=asin(nf(layer+1)*sin(alpha_i)/nf(layer+1+sg));
                Refl=0.5*((sin(alpha_i-alpha_t)/sin(alpha_i+alpha_t))^2
                  +(tan(alpha_i-alpha_t)/tan(alpha_i+alpha_t))^2);
            end

            if (rand<=Refl)
                muz=-muz;
            else
                if (muz<0)
                    if layer==1
                        r=sqrt(pos.x^2+pos.y^2);

refl_r(floor(r/step_size+1),floor(max_depth/step_size+1))=…
refl_r(floor(r/step_size+1),floor(max_depth/step_size+1))+weight;
                        b=1;
                        break
                    else
                        layer=layer-1;
                    end
                else
                    if layer==nb_of_layers
                        b=1;
                        break
                    else
                        layer=layer+1;
                    end
                end
                muz=sg*cos(alpha_t);
                mux=mux*nf(layer+1-sg)/nf(layer+1);
                muy=muy*nf(layer+1-sg)/nf(layer+1);
                S=S*(mua(layer-sg)+mus(layer-sg))/…
                              (mua(layer)+mus(layer));
            end
            if muz<0
                    dS=(bnd(layer)-pos.z)/muz;
            else
                    dS=-(pos.z-bnd(layer+1))/muz;
            end
        end
        if (b==1)
            b=0;
            break
        end
%%%%%%%%%%%%%%%%%%%%%%%%%%%%%%%%%%%%%%%%%%%%%%%%%%%%%%%%%%%%%%%%%%%%%%%%%%%%

    pos.x=pos.x+mux*S;
    pos.y=pos.y+muy*S;
    pos.z=pos.z+muz*S;
```

```
    max_depth=max(max_depth,pos.z);
    theta=acos((1+g2(layer)-((1-g2(layer))/…
      (1-g(layer)+2*g(layer)*rand))^2)/(2*g(layer)));
    phi=2*pi*rand;
    albedo=mus(layer)/(mus(layer)+mua(layer));
    %r=ceil(sqrt(pos.x^2+pos.y^2+pos.z^2)/step_size);

%     rx=ceil((size_limit/2+pos.x)/step_size+1); %size_limit/2+1 is an
offset since X and Y can be either negative or positive, the start of
the array corresponds to -size_limit/2
%     ry=ceil((size_limit/2+pos.y)/step_size+1);
    r=floor(sqrt(pos.x^2+pos.y^2)/step_size + 1);
    rz=ceil((pos.z)/step_size);
%     if
(rx<=0)||(rx>size_limit/step_size)||(ry<=0)||(ry>size_limit/step_size)
%         break
%     end


    %if r>size_limit/step_size
     %   break
    %end
    absorbed(r,rz)=absorbed(r,rz)+weight*(1-albedo);
    weight=weight*albedo;
    if (muz>0.9999)
        mux=sin(theta)*cos(phi);
        muy=sin(theta)*sin(phi);
        muz=sign(muz)*cos(theta);
    else
        mux_n=sin(theta)*(mux*muz*cos(phi)-muy*sin(phi))/…
                        (sqrt(1-muz^2))+mux*cos(theta);
        muy_n=sin(theta)*(muy*muz*cos(phi)+mux*sin(phi))/…
                        (sqrt(1-muz^2))+muy*cos(theta);
        muz_n=-sin(theta)*cos(phi)*sqrt(1-muz^2)+muz*cos(theta);
        mux=mux_n;
        muy=muy_n;
        muz=muz_n;
    end
    if (weight<threshold)
       roulette=rand;
        if roulette>0.9
            weight=weight*10;
        else
            break
        end
    end
    end

end
j1
end
```

```
toc
figure,plot([0.05:0.1:0.05+149*0.1],refl_r(2,:)/nb_of_photons)
hold on
plot([0.05:0.1:0.05+149*0.1],refl_r(6,:)/nb_of_photons,'--r')
plot([0.05:0.1:0.05+149*0.1],refl_r(11,:)/nb_of_photons,'-.m')
plot([0.05:0.1:0.05+149*0.1],refl_r(21,:)/nb_of_photons,'.-.g')
legend('d=0.15mm','d=0.55mm','d=1.05mm','d=2.05mm')
axis([0 5 0 max(max(refl_r(2,:)))/nb_of_photons])
xlabel('Penetration Depth(mm)')
ylabel('Energy(a.u.)')
title('Point detector at d_(_m_m_) from source')
hold off
% figure,imagesc([-size_limit/2:step_size:size_limit/2-step_size],[-
size_limit/2:step_size:size_limit/2-step_size],refl);
% xlabel('X(cm)')
% ylabel('Y(cm)')
%
% for i=1:size_limit/step_size
% a(i,:)=absorbed(i,ceil(size(absorbed,2)/2),:);
% end
% z=[0:step_size:size_limit-step_size];
% figure,imagesc(z-size_limit/2,z,a')
% xlabel('X(cm)')
% ylabel('Z(cm)')
% axis([-size_limit/2 size_limit/2 0 size_limit])
```

```
%%%%%%%%%%%%%%%%%%%%conv_gauss%%%%%%%%%%%%%%%%%%%
%This program modifies the output of the monte carlo code to take into
%account the spatial distribution of the source. This is done by
%convolving the output with the spacial distribution of the source

%%%%%%%%%%%%%%%%%%%INPUT%%%%%%%%%%%%%%%%%%%%%
FWHM=2.4;              %Full width half max of the source spatial
ditsribution in mm
source_position=0;  % Source position in mm
s=0.1;               %step size in mm, this should be the same as the
step size used in the MC code
size_limit=100;

x=[s/2:s:(size_limit/s-1)*s+s/2];
sigma=FWHM/(2*sqrt(2*log(2)));
source_dist=gaussmf(x,[sigma source_position]);
figure,plot(x,source_dist)
axis([0 3*sigma 0 1])
xlabel('r(mm)')
ylabel('Normalized Source Intensity(a.u.)')

for i=1:size(refl_r,2)
    refl_r_conv(:,i)=conv(refl_r(:,i),source_dist);
end

figure,plot(x,sum(refl_r_conv(1:size(x,2),:)'))
title('Diffuse Reflectance from a Gaussian distributed source')
```

```
%%%%%%%%%%%%%%%%%%%%detector_size.m%%%%%%%%%%%%%%%%%%%%
%Last modified on June 22, 2011
%Tony Akl
%tja161@gmail.com
%Optical BioSensing Lab (OBSL)

clc, clear Fxy
x=[0.05:0.05:max(r)];
y=[-2.8:0.05:2.8];
rmax=max(r);
%correction_factor=pi*4*0.05*r;%correction_factor=pi*0.1*(2*r+0.1);
%Fr=sum(refl_r(1:500,:)')./(1000000*correction_factor);
Fr=C;
for i=1:size(x,2)
    for j=1:size(y,2)
        rij=round(sqrt(x(i)^2+y(j)^2)/0.1);
        Fxy(i,j)=Fr(rij);
    end
end
refl_xy=Fxy;%*0.0001; %The 0.0001 factor was used to normalize by the
number of photons and convert from mm2 to cm2

% x2=[2:4:ceil(max(r)/4)*4];
% k=1;
% refl_x4mm=zeros(1,size(x2,2));
for i=25:length(x)-28
    refl_4_5X5_5mm(i-24)=mean(mean(refl_xy(i-
24:i+23,round(size(refl_xy,2)/2)-28:round(size(refl_xy,2)/2)+27)));
end
refl_4_5X5_5mm=refl_4_5X5_5mm*2.5*2.4;  %Multiply by the area of the
detector since we used the average to calculate this quantity
display('End')
```

APPENDIX B

DYES PREPARATION

Figure 83 shows the extinction coefficient of the dye mixture mimicking oxygenated hemoglobin on different pH levels. The mixture was found to be pH sensitive and that is why we started preparing the dyes in a high concentration buffer solution.

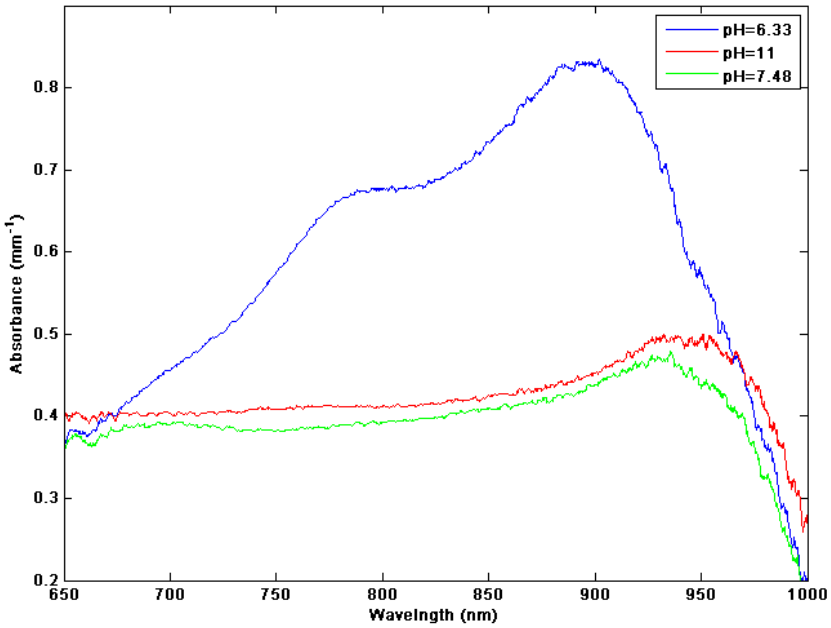

Fig. 83. Absorbance of the oxygenated hemoglobin dye mixture for different pH levels.

The changes in optical properties with pH led to problems with the dyes stability as shown in Figure 84. All these problems were resolved when using a high concentration PBS buffer (100 mM, pH 7.4).

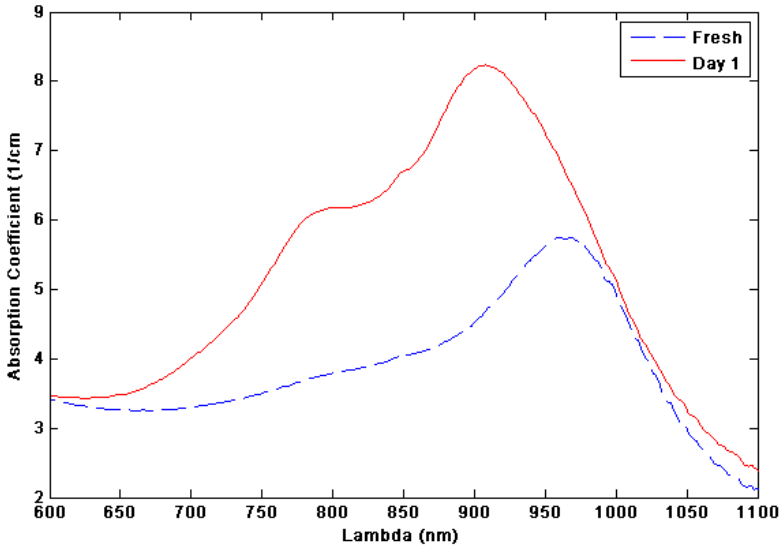

Fig. 84. The change in optical properties of the oxy-hemoglobin dye mixture over 24 hours when prepared in a 10 mM PBS buffer solution.

Another problem that was encountered with the dyes was the clogging of the microfluidic channels. The dye mixtures were forming large aggregates over time and causing the microchannels to clog and eventually rupture under pressure. Figure 85 shows the aggregation of dyes. The use of 100 mM PBS buffer eliminated this problem.

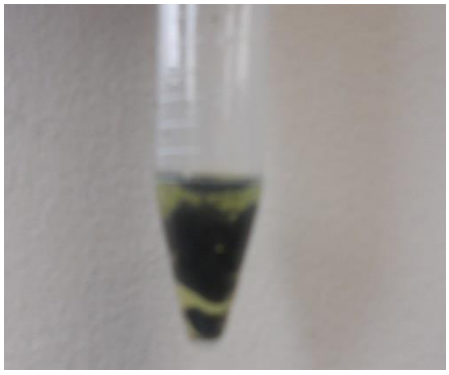

Fig. 85. Picture of the oxy-hemoglobin dye mixture aggregation.

APPENDIX C

PUMP CONTROL SYSTEM

This appendix shows the virtual instrument (VI) designed in LabVIEW to control the pumping circuit and read the values of a thermistor to provide a measure of temperature when needed. This VI was used in the *in vitro* and *ex vivo* studies to control flow and/or monitor temperature.

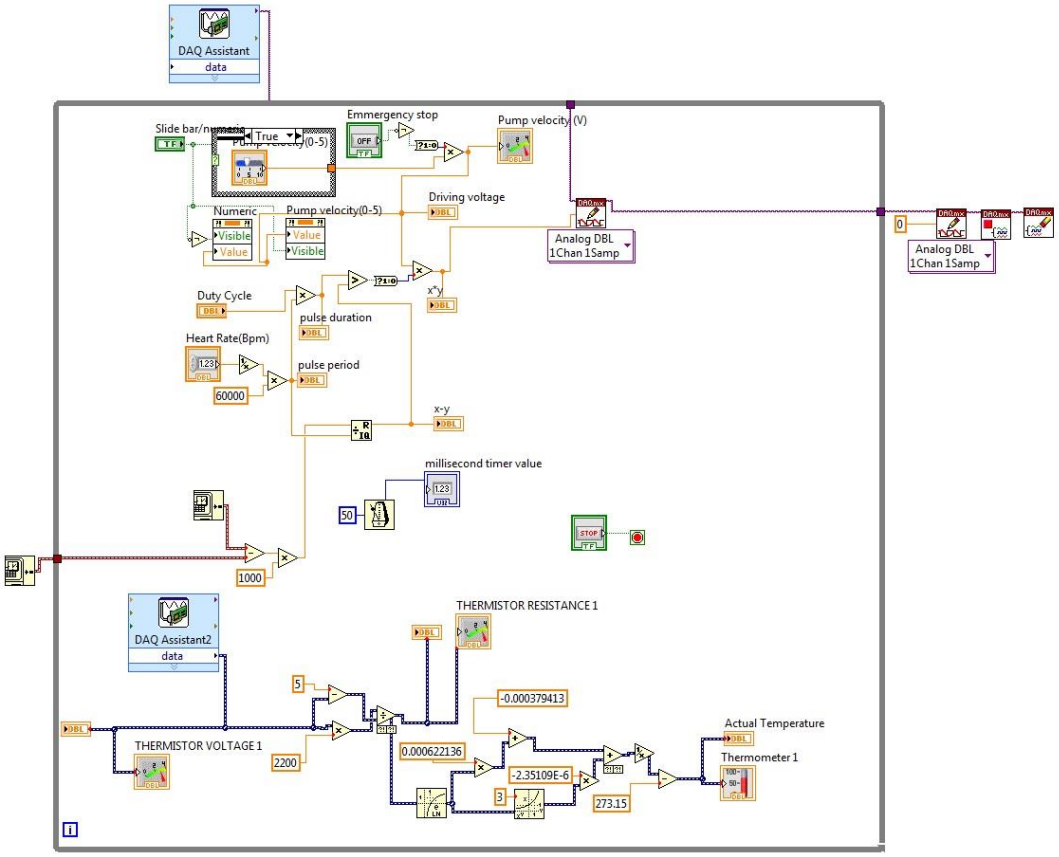

Fig. 86. Block diagram of the LabVIEW virtual instrument (VI) used for the in vitro *studies.*

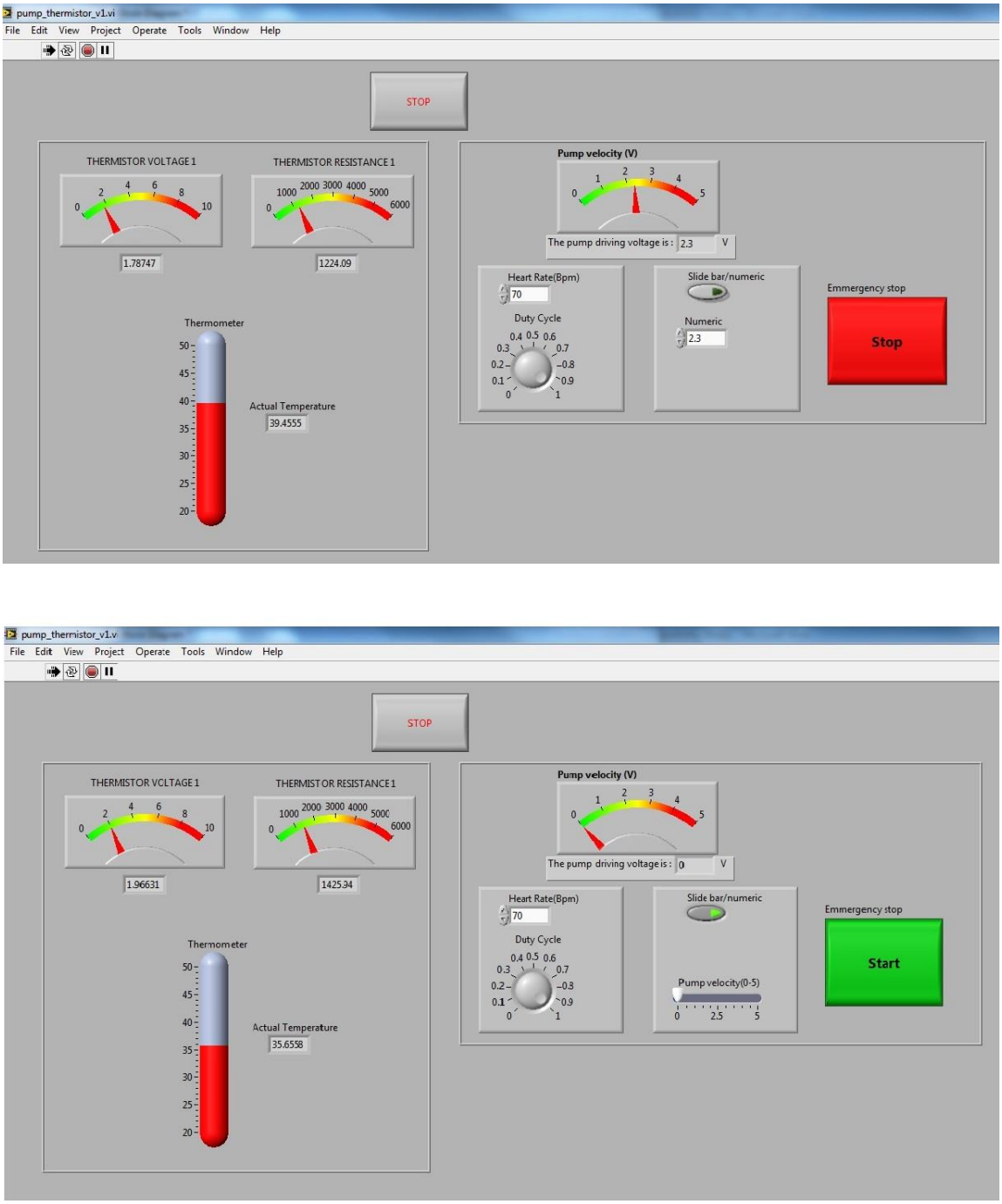

Fig. 87. Pictures of the front panel of the LabVIEW virtual instrument (VI) that controls the pumps and reads data from the thermistor to provide a measure of the temperature.

APPENDIX D

STRESS STRAIN TESTING

```
% This program calculates the Young's Modulus from the stress-strain
data
% obtained by the instron machine
% It was created on 9/18/2011
% Tony Akl
% tja161@gmail.com
% Optical Biosensing laboratory
% Texas A&M University
%
clc
[fname, fpath]=uigetfile({'*.csv','Comma Separated Values
(*.csv)';'*.txt','Text Document (*.txt)';'*.xls','Excel 2003 Worksheet
(*.xls)';'*.xlsx','Excel 2007 Worksheet (*.xslx)';'*.*','All files
(*.*)'}); ;
prompt = {'Length (mm)','Thickness (mm):','Width (mm):'};
dlg_title = 'Input Young''s Modulus calculations';
num_lines = 1;
def = {'15','4.1','3.03'};
answer = inputdlg(prompt,dlg_title,num_lines,def);
len=str2num(char(answer(1)));
thickness=str2num(char(answer(2)));width=str2num(char(answer(3)));
data=importdata(strcat(fpath,fname));
time_s=data.data(:,1);extension_mm=data.data(:,2);
load_N=data.data(:,3);
fig = figure;
plot(extension_mm,load_N)
ylabel('Load (N)'),xlabel('Extension (mm)')
dcm_obj = datacursormode(fig);
set(dcm_obj,'DisplayStyle','datatip',...
'SnapToDataVertex','off','Enable','on')
[X1 Y1]=input_selection(dcm_obj);
[X2 Y2]=input_selection(dcm_obj);
A=width*thickness;
P=(Y2-Y1)/A;
slope=(Y2-Y1)/(X2-X1);
display(strcat('The calculated slope is:  ', num2str(slope),' N/mm'));
YM=P/((X2-X1)/len);
display(strcat('The calculated Young''s Modulus is:  ', num2str(YM),'
MPa'));
msgbox(strcat('The calculated Young''s Modulus is:  ', num2str(YM),'
MPa'));
close(fig)


function [X Y]=input_selection(dcm_obj)
```

```
uiwait(msgbox('Select one point on the linear part of the curve then
press Enter'))
k=0;
while(k==0)
    k=waitforbuttonpress;
end

btn=questdlg('Are you satisfied with your selection?');
while btn(1)=='N'
    uiwait(msgbox('Select one point on the linear part of the curve
then press OK'))
    waitforbuttonpress
    btn=questdlg('Are you satisfied with your selection?');
end
if btn(1)=='C'
    X=0;Y=0;
    return
end
pt = getCursorInfo(dcm_obj);
X=pt.Position(1);
Y=pt.Position(2);
end
```

APPENDIX E

FAST FOURIER TRANSFORM PROCESSING

This section shows two examples of MATLAB code for processing the PPG signals using an FFT based algorithm. The first example processes all data as one segment while the second example splits the data in multiple time windows and the results show the temporal trends.

```
%Last updated 06-26-2012
%Latest updates: Input dialog box and time limits
%                Figures saved automatically
%Tony Akl
%tja161@gmail.com
%%
%%%%%%%%%%%%%%%%%%%%%%%%Data Input%%%%%%%%%%%%%%%%%%%%%%%%%%%%%
data_dir=uigetdir(strcat(dropbox_path,'Research\Perfusion sensor
project\Perfusion Sensor documents\Animal Studies\Porcine\EXP 06-29-
2011(Oxygenation studies)\TAMU 6-28-2011\Exp10\'),'Pick a directory');
base_filename='Run6_Probe';
nb_of_files=1;
first_file=0;
Fs=300;     %sampling frequency in Hz
minf=1.3;
maxf=5;
cut_off=0.2;
nb=1;
start_time=0;   %starting time in seconds
end_time=-1;    %ending time, if set to an invalid number (negative or
bigger than limit) it will read until the end of the data file.
probes=[1,2,3,4];
default_answer={'',num2str(nb_of_files),num2str(first_file),num2str(Fs)
,num2str(minf),num2str(maxf),num2str(cut_off),num2str(start_time),num2s
tr(end_time),num2str(probes)};
answer=inputdlg({'Comments:','Number of files to read:','First file
index:', 'Sampling frequency (Hz):',...
    'Minimum expected frequency (Hz):','Maximum expected frequency
(Hz):', 'Threshold (For peak power calculations,0-1):',...
   'Start time (Set to 0 for invalid answers):','End time (Set to the
end of data file for invalid answers):','Probes to be
processed:'},'Inputs',1,default_answer);
a_num=str2num(char(answer(2:9)));
nb_of_files=a_num(1); first_file=a_num(2); Fs=a_num(3); minf=a_num(4);
maxf=a_num(5); cut_off=a_num(6);start_time=a_num(7);end_time=a_num(8);
probes=str2num(char(answer(10)));comm=answer(1);
```

```
gain=[(3+1)*440/8 (1+1)*440/8 440 440];
%%
%%%%%%%%%%%%%%%%%%%%%%%%%Main Program%%%%%%%%%%%%%%%%%%%%%%%%%%
%% Reading data
cd(data_dir)
if data_dir(length(data_dir)) ~= '\'
    data_dir=strcat(data_dir,'\');
end
start_time=start_time*Fs+1-first_file*60*Fs;
end_time=end_time*Fs+1-first_file*60*Fs;
for p1=1:length(probes)
p=probes(p1);
fname=strcat(data_dir,base_filename,num2str(p),'_');
data_all=importdata(strcat(fname,num2str(first_file),'.txt'));
%data_all=importdata(strcat(base_filename,'.txt'));
file1=first_file;
    for i=1:nb_of_files-1
        if i>nb_of_files-1
            break
        end
        file1=file1+1;
        temp=importdata(strcat(fname,num2str(file1),'.txt'));
        data_all=[data_all; temp];
    end

if (start_time>=length(data_all))||(start_time<=0)
    start_time=1;
    msgbox(strcat('Invalid input. End time set to ',
num2str(data_all(length(data_all),1)),'s'),'Invalid input')
end
if (end_time>length(data_all))||(end_time<=0)||(end_time<=start_time)
    end_time=length(data_all);
    msgbox(strcat('Invalid input. End time set to ',
num2str(data_all(length(data_all),1)),'s'),'Invalid input')
end
data_all=data_all(start_time:end_time,:);


time=data_all(:,1);
%AC
AC735=data_all(:,2);
AC805=data_all(:,3);
AC940=data_all(:,4);
%DC
DC735=data_all(:,5);
DC805=data_all(:,6);
DC940=data_all(:,7);
%Sum
total735=AC735+DC735;
total805=AC805+DC805;
total940=AC940+DC940;
%% Fourrier transforms
n=length(AC735);
```

```
NFFT=n;%2^nextpow2(n);      % If the NFFT is set at 2^next
FFT735=fft(AC735,NFFT)/n;
power735=abs(FFT735).^2;
FFT805=fft(AC805,NFFT)/n;
power805=abs(FFT805).^2;
FFT940=fft(AC940,NFFT)/n;
power940=abs(FFT940).^2;

% Detecting HR
f=Fs/2*linspace(0,1,NFFT/2);
[l kmin]=max(f>=minf);
[l kmax]=max(f>=maxf);
[maxFFT735 l]=max(abs(FFT735(kmin:kmax)));
HR735=f((kmin+l-1))
i=kmin+l-2;
while(abs(FFT735(i))>cut_off*maxFFT735)&&(i>1)
    i=i-1;
end
imin735=i;
fmin735=f(imin735);

i=kmin+l;
while(abs(FFT735(i))>cut_off*maxFFT735)
    i=i+1;
end
imax735=i;
fmax735=f(imax735);

power735=sum(abs(FFT735(imin735:imax735)));

[maxFFT805 l]=max(abs(FFT805(kmin:kmax)));
HR805=f((kmin+l-1))

i=kmin+l-2;
while(abs(FFT805(i))>cut_off*maxFFT805)&&(i>1)
    i=i-1;
end
imin805=i;
fmin805=f(imin805);
i=kmin+l;
while(abs(FFT805(i))>cut_off*maxFFT805)
    i=i+1;
end
imax805=i;
fmax805=f(imax805);
power805=sum(abs(FFT805(imin805:imax805)));

[maxFFT940 l]=max(abs(FFT940(kmin:kmax)));
HR940=f((kmin+l-1))
i=kmin+l-2;
while(abs(FFT940(i))>cut_off*maxFFT940)&&(i>1)
    i=i-1;
```

```
end
imin940=i;
fmin940=f(imin940);

i=kmin+1;
while(abs(FFT940(i))>cut_off*maxFFT940)
    i=i+1;
end
imax940=i;
fmax940=f(imax940);
power940=sum(abs(FFT940(imin940:imax940)));

%% Plotting and data output
figure(p),subplot(3,2,1), plot(f,2*abs(FFT735(1:NFFT/2)))
axis([0 10 0 1.1*max(2*abs(FFT735(kmin:kmax)))]),title(['735 nm';comm])
subplot(3,2,3), plot(f,2*abs(FFT805(1:NFFT/2)))
axis([0 10 0 1.1*max(2*abs(FFT805(kmin:kmax)))]),title(['805 nm';comm])
subplot(3,2,5), plot(f,2*abs(FFT940(1:NFFT/2)))
axis([0 10 0 1.1*max(2*abs(FFT940(kmin:kmax)))]),title(['940 nm';comm])

h(p)=figure(p);
subplot(3,2,1), hold on, plot([fmin735 fmin735],[0 4*maxFFT735],'--r')
plot([fmax735 fmax735],[0 4*maxFFT735],'--r'),hold off
ylabel('|FFT|'),xlabel('f(Hz)')
subplot(3,2,3);
hold on, plot([fmin805 fmin805],[0 4*maxFFT805],'--r')
plot([fmax805 fmax805],[0 4*maxFFT805],'--r'),hold off
ylabel('|FFT|'),xlabel('f(Hz)')
subplot(3,2,5)
hold on, plot([fmin940 fmin940],[0 4*maxFFT940],'--r')
plot([fmax940 fmax940],[0 4*maxFFT940],'--r'),hold off
ylabel('|FFT|'),xlabel('f(Hz)')
set(h(p),'Units','Normalized')
set(h(p),'Position',[0 0 1 1])

flow(nb,1:3)=[abs(maxFFT735) abs(maxFFT805) abs(maxFFT940)];
meanDC(nb,1:3)=[mean(DC735) mean(DC805) mean(DC940)];
FFT_peak=[maxFFT735 maxFFT805 maxFFT940]
FFT_power=[power735 power805 power940]*Fs/(NFFT-2)
DC=[mean(DC735) mean(DC805) mean(DC940)]
R(p)=(flow(:,1)./meanDC(:,1))./(flow(:,3)./meanDC(:,3))

HR(p,:)=[HR735 HR805 HR940]*60, AC=[AC735 AC805 AC940];DCt=[DC735 DC805
DC940];ACDC=AC./DCt;
ch1_ch3=ACDC(:,1)./ACDC(:,3);

R2(p)=
log((((maxFFT735/gain(p))+DC(1))./DC(1)))./log((((maxFFT940/gain(p))+DC
(3))./DC(3)));
PI(p,:)= 100*[maxFFT735/(gain(p)*DC(1)) maxFFT805/(gain(p)*DC(2))
maxFFT940/(gain(p)*DC(3))];
%% Filter and plot waveforms
```

```
maxf1=6;
[b,a]=butter(4,[minf maxf1]/150);
AC7351=filter(b,a,AC735);AC8051=filter(b,a,AC805);AC9401=filter(b,a,AC9
40);
t1=strcat(base_filename,num2str(p));
t1=replace_char(t1,'_','-');
subplot(3,2,2);plot(time,AC7351),xlabel('Time (s)'),ylabel('AC
(V)'),title([t1;comm])
subplot(3,2,4);plot(time,AC8051),xlabel('Time (s)'),ylabel('AC
(V)'),title([t1;comm])
subplot(3,2,6);plot(time,AC9401),xlabel('Time (s)'),ylabel('AC
(V)'),title([t1;comm])

end
%% Saving figures
figure(probes(1))
%data_dir=save_dir;
ButtonName = questdlg('Would you like to save the
images?','Save','Yes','No','Yes');
switch ButtonName,
    case 'Yes',
        save_dir=uigetdir(data_dir,'Save directory');
        cd(save_dir)
        for i=1:length(probes)

saveas(h(probes(i)),strcat('Probe',num2str(probes(i)),'.fig'));
        end
            msgbox('Figures saved successfully','Data saved')
    case 'No',
        msgbox('Figures not saved, you can still save them
manually','Data not saved')
end
excel_out=[R2 PI(1,:) PI(2,:) PI(3,:) PI(4,:) HR(1,:) HR(2,:) HR(3,:)
HR(4,:)];
%excel_out=[flow meanDC flow./meanDC R];
display('END')
```

```
%% Thefollowing program processes the data similar to the previous
%% example with the added feature of splitting the data in multiple
%% segments to look at temporal trends within a dataset.

clear all
dropbox_path=getdropbox;
%% Inputs

processing_interval=25; %processing interval duration in seconds
time_step=10;            %time step in seconds
start_time=0;
t0=0;    %The time stamp on the first file of the experiment
                        %All data will be referenced to this time point
Fs=300;     %sampling frequency in Hz
minf=1.5;
maxf=2.5;
cut_off=0.2;
nb_of_files=21;
first_file=210;
start_index=1;
end_index=18000*nb_of_files;
sheet_name=strcat(num2str(floor(start_index/Fs)),'s-
',num2str(floor(end_index/Fs)),'s');
probes=[2 3];
gain=[20.39849 70.17787 33.66493];

data_dir=uigetdir(strcat(dropbox_path,'Research\Perfusion sensor
project\Perfusion Sensor documents\Animal Studies\Porcine\EXP 06-29-
2011(Oxygenation studies)\TAMU 6-28-2011\Exp10\'),'Pick a directory');
base_filename='Run1_Probe';

%%
dt=processing_interval;

np=length(probes);
%%%%%%%%%%%%%%%%%%%%%%%%%Main Program%%%%%%%%%%%%%%%%%%%%%%%%%
%%

for i1=1:length(probes)
p=probes(i1);
fname=fullfile(data_dir,strcat(base_filename,num2str(p),'_'));

probes_data=importdata(strcat(fname,num2str(first_file),'.txt'));
%data_all=importdata(strcat(base_filename,'.txt'));
file1=first_file;
    for i=1:nb_of_files-1
        if i>nb_of_files-1
            break
        end
        file1=file1+1;
        temp=importdata(strcat(fname,num2str(file1),'.txt'));
        probes_data=[probes_data; temp];
```

```
    end

end_index=min(end_index,length(probes_data));
data_all2=probes_data(start_index:end_index,:);
ts=1;
nmax=end_index-start_index;
jmax=floor((nmax-dt*Fs/2)/(time_step*Fs));
if jmax==0
    jmax=1;
end

for j=1:jmax
tf=min(ts+dt*Fs,nmax);

data_temp=data_all2(ts:tf,:);

% time=[0:1/Fs:(end_index-start_index)/Fs];
%AC
AC735=data_temp(:,2);
AC805=data_temp(:,3);
AC940=data_temp(:,4);
%DC
DC735=data_temp(:,5);
DC805=data_temp(:,6);
DC940=data_temp(:,7);

%% Fourrier transforms
n=length(AC735);
NFFT=n;%2^nextpow2(n);      % If the NFFT is set at 2^next
FFT735=fft(AC735,NFFT)/n;
power735=abs(FFT735).^2;
FFT805=fft(AC805,NFFT)/n;
power805=abs(FFT805).^2;
FFT940=fft(AC940,NFFT)/n;
power940=abs(FFT940).^2;

% Detecting HR
f=Fs/2*linspace(0,1,NFFT/2);
[l kmin]=max(f>=minf);
[l kmax]=max(f>=maxf);
[maxFFT735 l]=max(abs(FFT735(kmin:kmax)));
HR735=f((kmin+l-1));
i=kmin+l-2;
while(abs(FFT735(i))>cut_off*maxFFT735)&&(i>1)
    i=i-1;
end
imin735=i;
fmin735=f(imin735);

i=kmin+l;
while(abs(FFT735(i))>cut_off*maxFFT735)
    i=i+1;
```

```
end
imax735=i;
fmax735=f(imax735);

power735=sum(abs(FFT735(imin735:imax735)));

[maxFFT805 l]=max(abs(FFT805(kmin:kmax)));
HR805=f((kmin+l-1));

i=kmin+l-2;
while(abs(FFT805(i))>cut_off*maxFFT805)&&(i>1)
    i=i-1;
end
imin805=i;
fmin805=f(imin805);
i=kmin+l;
while(abs(FFT805(i))>cut_off*maxFFT805)
    i=i+1;
end
imax805=i;
fmax805=f(imax805);
power805=sum(abs(FFT805(imin805:imax805)));

[maxFFT940 l]=max(abs(FFT940(kmin:kmax)));
HR940=f((kmin+l-1));
i=kmin+l-2;
while(abs(FFT940(i))>cut_off*maxFFT940)&&(i>1)
    i=i-1;
end
imin940=i;
fmin940=f(imin940);

i=kmin+l;
while(abs(FFT940(i))>cut_off*maxFFT940)
    i=i+1;
end
imax940=i;
fmax940=f(imax940);
power940=sum(abs(FFT940(imin940:imax940)));

%% Data output
flow(j,i1,1:3)=[abs(maxFFT735) abs(maxFFT805) abs(maxFFT940)];
meanDC(j,i1,1:3)=[mean(DC735) mean(DC805) mean(DC940)];
% FFT_peak=[maxFFT735 maxFFT805 maxFFT940]
% FFT_power=[power735 power805 power940]*Fs/(NFFT-2)
DC=[mean(DC735) mean(DC805) mean(DC940)];
R(j,i1)=(flow(j,i1,1)./meanDC(j,i1,1))./(flow(j,i1,3)./meanDC(j,i1,3));

HR(j,i1,:)=[HR735 HR805 HR940]*60; %AC=[AC735 AC805 AC940];DCt=[DC735
DC805 DC940];ACDC=AC./DCt;
%ch1_ch3=ACDC(:,1)./ACDC(:,3);
```

```
R2(j,i1)=
log((((maxFFT735/gain(i1))+DC(1))./DC(1))).log((((maxFFT940/gain(i1))+
DC(3))./DC(3)));
PI(j,i1,:)= 100*[maxFFT735/(gain(i1)*DC(1)) maxFFT805/(gain(i1)*DC(2))
maxFFT940/(gain(i1)*DC(3))];

t(j)=start_time-t0+mean(data_temp(:,1));
ts=ts+time_step*Fs;
end
end
%%
output1=zeros(length(t),length(probes)*12+3);
output1=[t' t'/60 (t'-t(1))];
for i=1:length(probes)
    for j=1:3
        output1(:,3+(i-1)*12+j) = flow(:,i,j);
        output1(:,6+(i-1)*12+j) = meanDC(:,i,j);
        output1(:,9+(i-1)*12+j) = flow(:,i,j)./meanDC(:,i,j);
        output1(:,12+(i-1)*12+j) = HR(:,i,j);
    end
end

%% Initializing headers
header2={' ' ' ' ' ' ' 'Probe2' 'Probe2' 'Probe2' 'Probe2' 'Probe2'...
    'Probe2' 'Probe2' 'Probe2' 'Probe2' 'Probe2' 'Probe2' 'Probe2'...
    'Probe3' 'Probe3' 'Probe3' 'Probe3' 'Probe3' 'Probe3' 'Probe3'...
    'Probe3' 'Probe3' 'Probe3' 'Probe3' 'Probe3'...
    };


header1={'Time(s)' 'Time(min)' 'Relative time(s)' ...
 'FFT peak' 'FFT peak' 'FFT peak' 'DC' 'DC' 'DC' 'PI' 'PI' 'PI' 'HR'
'HR' 'HR'...
 'FFT peak' 'FFT peak' 'FFT peak' 'DC' 'DC' 'DC' 'PI' 'PI' 'PI' 'HR'
'HR' 'HR'...
 %'FFT peak' 'FFT peak' 'FFT peak' 'DC' 'DC' 'DC' 'PI' 'PI' 'PI' 'HR'
'HR' 'HR'
 };

header3={' ' ' ' ' ' ' ' 'Ch1' 'Ch2' 'Ch3' 'Ch1' 'Ch2' 'Ch3'...
    'Ch1' 'Ch2' 'Ch3' 'Ch1' 'Ch2' 'Ch3'...
    'Ch1' 'Ch2' 'Ch3' 'Ch1' 'Ch2' 'Ch3'...
    'Ch1' 'Ch2' 'Ch3' 'Ch1' 'Ch2' 'Ch3'...
    %'Ch1' 'Ch2' 'Ch3' 'Ch1' 'Ch2' 'Ch3'...
    %'Ch1' 'Ch2' 'Ch3' 'Ch1' 'Ch2' 'Ch3'...
    };

%% Saving data
excel_out=[header1;header2;header3;num2cell(output1)];
ButtonName = questdlg('Would you like to save the
data?','Save','Yes','No','Yes');
```

```
switch ButtonName,
    case 'Yes',
        [save_name,pname]=uiputfile({'*.xls', 'Excel Worksheet
(*.xls)'},'Saving data');
        save_name=fullfile(pname,save_name);
        [status msg]=xlswrite(save_name,excel_out,sheet_name);
        if status==1
            msgbox('Data saved successfully','Data saved')
        else
            msgbox(msg.message,'Data not saved')
        end
    case 'No',
        msgbox('Data not saved! You can still save them
manually.','Data not saved')
end
%%
display('END')
```

APPENDIX F

PULSE ANALYSIS

```
% This program computes the pulse amplitude and quantifies the rise and
% fall time and slopes for a PPG signal.
%
% V2 added the following features:
%   -The ability to process data from multiple probes at the same time
%   -The ability to save processed data into an excel file
%
% V2.1 Minor update: added a 4th order band-pass butterworth filter
%
% Last updated: 08/14/2013
% Tony J. Akl
% tja161@gmail.com

%%%%%%%%%%%%%%%%%%%%%%%%%Data Input%%%%%%%%%%%%%%%%%%%%%%%%%%%%%
data_dir=uigetdir;
% data_dir='F:\Research\Perfusion sensor\BRP data\Porcine
studies\2011\TAMU 6-28-2011\EXP6';
base_fname='occlusion3_Probe';
nb_of_files=-1;
first_file=0;
Fs=300;     %data sampling frequency in Hz
minf=0.8;
maxf=3.0;
probes=[1 2 3 4];
start_index=2100;
%%
%% Saving data dialog
ButtonName = questdlg('Would you like to save the
data?','Save','Yes','No','Yes');

switch ButtonName
    case 'Yes',
        [save_name,pname]=uiputfile({'*.xls', 'Excel Worksheet
(*.xls)'},'Saving data');
        save_name=fullfile(pname,save_name);
end
%% Constructing filter
[b_filt,a_filt] = butter(4,[minf maxf]/(Fs/2));
%%
%%%%%%%%%%%%%%%%%%%%%%%%%Main Program%%%%%%%%%%%%%%%%%%%%%%%%%%%%
%% Finding the start date from the log file
cd(data_dir);
try
    fn=dir('*.log');
    temp=importdata(fn.name,',','8');
catch
```

```
    msgbox('No log file found, start time is set to the current
timing!')
    temp=datevec(now);
end
start_time=datevec(strcat(temp(2),',',temp(3)));
time_offset=start_time(4)*3600+start_time(5)*60+start_time(6);
%%
for p=1:length(probes)
base_filename = strcat(base_fname,num2str(probes(p)));
data_all = file_read(data_dir, base_filename, nb_of_files, first_file);
% data_all=data_all(start_index:end,:);
time = data_all(start_index:end,1);
%AC
AC735_raw = data_all(:,3); AC805_raw = data_all(:,3); AC940_raw =
data_all(:,4);
% %DC
DC735 = data_all(start_index:end,5); DC805 =
data_all(start_index:end,6); DC940 = data_all(start_index:end,7);
% %Sum
% total735=AC735+DC735; total805=AC805+DC805; total940=AC940+DC940;
%% Filtering signal
AC735 = filter(b_filt,a_filt,AC735_raw);
AC805 = filter(b_filt,a_filt,AC805_raw);
AC940 = filter(b_filt,a_filt,AC940_raw);
AC735 = AC735(start_index:end);
AC805 = AC805(start_index:end);
AC940 = AC940(start_index:end);
%% Fourrier transforms
n=length(AC735);
NFFT=2^nextpow2(n);
NFFT=n;
FFT735=fft(AC735,NFFT)/n;
power735=abs(FFT735).^2;
FFT805=fft(AC805,NFFT)/n;
power805=abs(FFT805).^2;
FFT940=fft(AC940,NFFT)/n;
power940=abs(FFT940).^2;

%% Detecting average HR
f=Fs/2*linspace(0,1,NFFT/2);
[l kmin]=max(f>=minf);
[l kmax]=max(f>=maxf);

[maxFFT735 l]=max(abs(FFT735(kmin:kmax)));
HR735=f((kmin+l-1));
T735=1/HR735;

%% Detecting local maxima and minima and pulse rate
cpt=1;nb=0;
clear maxa mina maxt mint
while cpt<(n-2.0*T735*Fs)
    nb=nb+1;
    [maxa(nb) kmax] = max(AC735(cpt:ceil(cpt+T735*Fs)));
```

```
    maxt(nb)=cpt+kmax-1;
    [mina(nb)  kmin] = min(AC735(maxt(nb):maxt(nb)+ceil(T735*Fs)));
    mint(nb)=maxt(nb)+kmin-1;
%     cpt=maxt(nb)+T735*Fs;
    cpt=mint(nb);
end
%% Temporal heart rate/period and pulse amplitude
Tmax=diff(maxt)/Fs;
Tmin=diff(mint)/Fs;
Amp=maxa-mina;
clear DC_average
for i=1:length(maxt)-1
DC_average(i)=mean(DC735(maxt(i):maxt(i+1)));
end
DC_average(end+1)=mean(DC735(maxt(end):end));
%% Detecting slopes
clear falling_slope rising_slope maxt_thresh maxa_thresh maxt_thresh2
maxa_thresh2
clear mint_thresh mina_thresh mint_thresh2 mina_thresh2
min_thresh=mina+0.1*Amp;    %The slopes are calculated for the section
10% above
max_thresh=maxa-0.2*Amp;    %minimum and 10% below maximum
for i=1:length(maxt)
    temp=AC735(maxt(i):mint(i));
    a=find(temp>=min_thresh(i) & temp<=max_thresh(i));
    dt=time(maxt(i)+a(end)-1)-time(maxt(i)+a(1)-1);
    maxt_thresh(i)=maxt(i)+a(1)-1;  mint_thresh(i)=maxt(i)+a(end)-1;
    maxa_thresh(i)=temp(a(1));mina_thresh(i)=temp(a(end));
    da=mina_thresh(i)-maxa_thresh(i);
    falling_slope(i)=da/dt;
end
Amp2=maxa(2:end)-mina(1:end-1);
min_thresh2=mina(1:end-1)+0.1*Amp2; %The slopes are calculated for the
section 10% above
max_thresh2=maxa(2:end)-0.3*Amp2;   %minimum and 10% below maximum
for i=2:length(maxt)
     temp=AC735(mint(i-1):maxt(i));
     a=find(temp>=min_thresh2(i-1) & temp<=max_thresh2(i-1));
     dt=time(mint(i-1)+a(end)-1)-time(mint(i-1)+a(1)-1);
     maxt_thresh2(i-1)=mint(i-1)+a(end)-1;mint_thresh2(i-1)=mint(i-
1)+a(1)-1;
     maxa_thresh2(i-1)=temp(a(end));mina_thresh2(i-1)=temp(a(1));
     da=maxa_thresh2(i-1)-mina_thresh2(i-1);
     rising_slope(i-1)=da/dt;
end
%% Rise and fall times
rise_time=maxt_thresh2-mint_thresh2;
fall_time=mint_thresh-maxt_thresh;
%% Saving results
temp1=[(time(mint)+time_offset) time(mint) time(maxt) min_thresh' mint'
mint_thresh' maxt' maxt_thresh'...
    maxa_thresh' maxa' mina_thresh' mina' fall_time' Amp'
DC_average'...
```

```
    fall_time' falling_slope'];
temp2=[Tmax' Tmin' min_thresh2' mint_thresh2' maxt_thresh2'
maxa_thresh2' ...
    rise_time' rising_slope' Amp2'];
header1={'time(mint) offset' 'time(mint)' 'time(maxt)' 'min_thresh'
'mint' 'mint_thresh' ...
    'maxt' 'maxt_thresh' 'maxa_thresh' 'maxa' 'mina_thresh' 'mina' ...
    'fall_time' 'Amp' 'DC_average' 'fall_time' 'falling_slope'
'Tmax'...
    'Tmin' 'min_thresh2' 'mint_thresh2' 'maxt_thresh2'
'maxa_thresh2'...
    'rise_time' 'rising_slope' 'Amp2'};

switch ButtonName
    case 'Yes'
        excel_out=[num2cell(temp1) [num2cell(temp2); {' ' ' ' ' ' ' ' ' '
' ' ' ' ' ' ' ' ' '}]];
        excel_out=[header1;excel_out];
        sheet_name=['Probe ' num2str(probes(p))];
        [status msg]=xlswrite(save_name,excel_out,sheet_name);
        if status==0
            if msg.message=='Excel returned: Error: Object returned
error code: 0x800A03EC.'
                for f_nb=1:ceil(length(excel_out)/50000)
                    [status, msg]=xlswrite(save_name,excel_out((f_nb-
1)*50000+1:min(f_nb*50000,length(excel_out)),:),...
                        [sheet_name '-' num2str(f_nb)]);%, ['A'
num2str((f_nb-1)*10000+1) ':AD'
num2str(min(f_nb*10000,length(excel_out)))]);
                end
            end
            msgbox(msg.message,'Saving Data');
        end
end
```

```
%FILE_READ reads a sequence of data files
% This function takes three inputs and returns two outputs
% Inputs:
%     data_dir: directory where the file is located
%     base_filename: the base filename without the numbering at the
%           end
%     nb_of_files: number of files in the sequence, if a negative
%           number  is given in that field, the function will read all
%           files that start with the base_filename in the specified
%           folder
%    first_file: the numbder/id of the first file
% For example to read the files "C:\Tony_1.txt" until "C:\Tony_4.txt"
% the inputs would be: file_read('C:\','Tony',4,1);
%
% Last updated on 10/06/2011
% Tony J. Akl
% tja161@gmail.com

function [data_all] = file_read(data_dir, base_filename, nb_of_files,
first_file)
if nargin < 2
   error('Not enough input arguments.');
   return
end
if (nargin==2)
    nb_of_files=1;
    first_file=0;
elseif (nargin==3)
    first_file=0;
end
if nb_of_files<0
    myFiles=dir(strcat(fullfile(data_dir,base_filename),'*'));
    nb_of_files=length(myFiles);
end
if nb_of_files==0
    return
end
cd(data_dir)
if data_dir(length(data_dir)) ~= '\'
    data_dir=strcat(data_dir,'\');
end
fname=strcat(data_dir,base_filename,'_');
data_all=importdata(strcat(fname,num2str(first_file),'.txt'));

    for i=1:nb_of_files-1
        if i>nb_of_files-1
            break
        end
        first_file=first_file+1;
        temp=importdata(strcat(fname,num2str(first_file),'.txt'));
        data_all=[data_all; temp];
    end
end
```

```
% This program combines different excel files from the same experiment
% into a single excel file to make data analysis easier. The user the
% inputs name of the sheet in the excel files that he wants to combine
% and selects all the files to merge and the saving location.
%
% V1.1 works for files that has the extra column for adjusted timing
%
% Tony J. Akl
% tja161@gmail.com

%%
[fname1, pname] = uigetfile({'*.xls','Excel files (*.xls)'},'Pick all
data file','MultiSelect','on');
prompt={'Sheet name:'};
name='User Input';
numlines=1;
defaultanswer={'Probe 1'};
sheet_name = char(inputdlg(prompt,name,numlines,defaultanswer));

%% Initializing headers
header1={'time(mint) offset' 'time(mint)' 'time(maxt)' 'min_thresh'
'mint' 'mint_thresh' ...
    'maxt' 'maxt_thresh' 'maxa_thresh' 'maxa' 'mina_thresh' 'mina' ...
    'fall_time' 'Amp' 'DC_average' 'fall_time' 'falling_slope'
'Tmax'...
    'Tmin' 'min_thresh2' 'mint_thresh2' 'maxt_thresh2'
'maxa_thresh2'...
    'rise_time' 'rising_slope' 'Amp2'};
%%
nb_files=0;
fname1=sort(fname1);
excel_out=[header1];
for nf=1:length(fname1)
    fname=char(fname1(nf));
    filename=fullfile(pname,fname);
    [status,sheets1]= xlsfinfo(filename);

    if max(strcmp(sheets1,sheet_name))~=1
        nb_files=nb_files+1;
        files(nb_files)={fname};
        continue
    end
     a=xlsread(filename,sheet_name);
     excel_out=[excel_out; num2cell(a)];
end
[fname, pname]=uiputfile({'*.xls', 'Excel Worksheet (*.xls)'},'Saving
data','Summary.xls');

xlswrite(fullfile(pname,fname),excel_out,sheet_name);
display([num2str(length(fname1)-nb_files) ' files added to ' fname ...
    ' and ' num2str(nb_files) ' files could not be added']);
```

APPENDIX G

TELEMETRY SYSTEM SUPPLEMENTARY DATA

I. Probe fabrication & sensor encapsulation:

All sensor probes were coated with Polydimethylsiloxane (PDMS) to avoid water leakage into the electronics. To do that, the Printed Circuit Board (PCB) with the Light Emitting Diodes (LEDs) and photodetector was secured in a 3D printed mold and PDMS was poured on it. The mold was then placed in an oven for roughly 1 hour at 65°C to cure the PDMS. The PDMS coated electronics were placed in a different mold containing one of three 3D printed suture-holders designed to secure the probes in place (Figure 88). PDMS was poured into this mold and placed again in the oven for an extra hour at 65°C. The probes were left overnight at room temperature before any testing was performed. All PDMS was mixed with a curing agent at a volumetric ration of 10:1 and degassed for 60 minutes to avoid air pockets. The PDMS was degassed again after being poured in the mold to make sure no air bubbles were introduced in the process. The probes were coated with an additional thin layer of electronic grade silicone to avoid any leakage. Prior to the animal studies, all probes were placed in a water bath overnight to test for leakage.

Figure 88-a shows CAD models of the three different suture holders used in the parenchymal (left) and vascular probes (middle and right). The vascular probes were made in two different sizes to be secured around the hepatic artery and portal vein that differ in diameter (HA ~ 5 mm and PV ~ 8-10 mm).

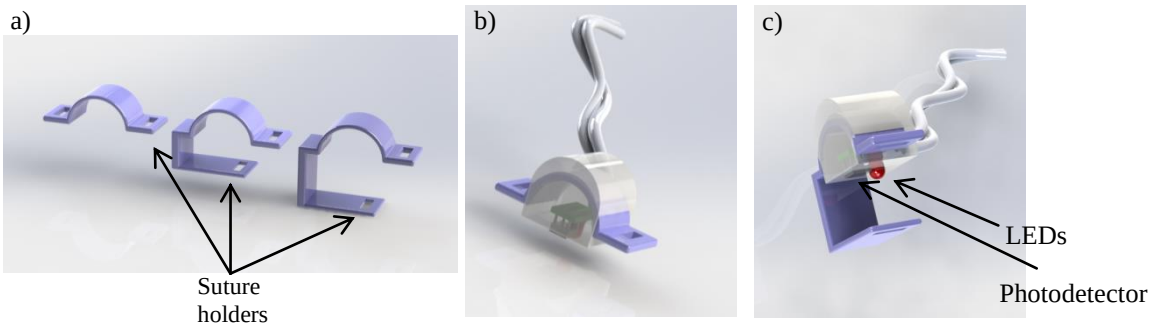

Fig. 88. a-Suture holders for the parenchymal, HA, and PV probes (left to right). b & c-CAD drawing of a parenchymal and a vascular probe respectively.

All sensor electronics were enclosed in a 3D printed box (Figure 89). The box was coated with a thin layer of electronic grade silicone.

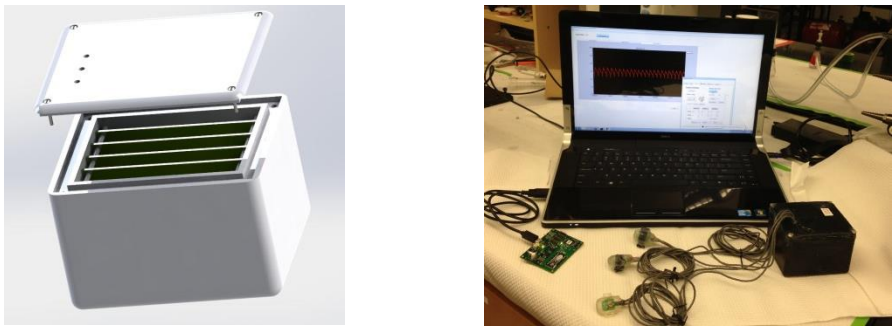

Fig. 89. (Left) CAD drawing of the electronics box showing the PCBs inside. (Right) Picture of the telemetry system showing the sensor, probes, and data acquisition software.

II. Reference Measurements:

The data from the Laser Doppler (LD) Perfusion monitor did not correlate well with tissue perfusion changes. In both studies we had two LD monitors placed on the hepatic tissue: a surface probe and a needle probe. The probes were adjusted and moved to various spots on the tissue to be able to pick up a Doppler signal. We were not able to get a signal with the needle probe. The surface probe gave a good Doppler signal. However, further analysis showed that the signal by that probe correlated well with the hepatic artery flow but not with the portal venous flow. We believe that the LD was probing a branch of the hepatic artery embedded in tissue. The data from the LD was not used as a reference, and instead we used the total hepatic flow obtained by the two Transit-Time Ultrasound flowmeters. Figure 90 shows the correlation between the LD output and the HA and PV flow measured by the Transit-Time flowmeters. As mentioned, the LD signal correlates with the HA flow with a coefficient of determination (R^2) of 0.8 while the correlation with PV flow showed an R^2 of 0.1. The time pattern of the measured signals is shown in Figure 91. Note that during the PV occlusion studies (Figure 91, blue segments), the HA occluders were open (not inflated). All changes in HA flow during these segments are due to a systemic response.

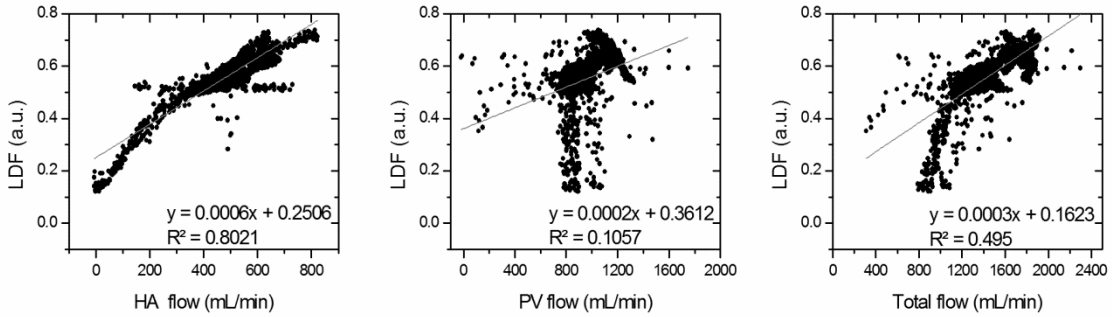

Fig. 90. Scatter plots of the Laser Doppler data versus HA flow (left), PV flow (middle), and total hepatic flow (right). The data shows that the LD data correlates best with the HA flow suggesting that the system was probing a branch of the HA.

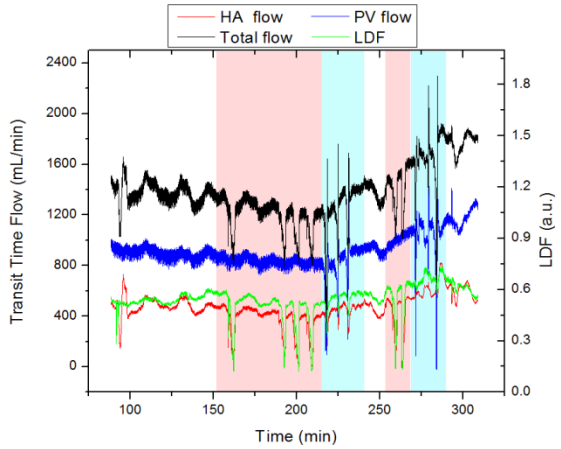

Fig. 91. Reference flow measurements by the transit time flowmeters (left axis) and Laser Doppler flowmeter (right axis). The time segments highlighted in red correspond to HA occlusion studies while the blue segments correspond to PV occlusion studies.

Figure 92 shows the raw data from the arterial and venous oxygenation catheters from both studies described in the manuscript. The catheters used do not measure oxygenation levels above 97.5% and that is why some data for the arterial catheter is missing from the graph below.

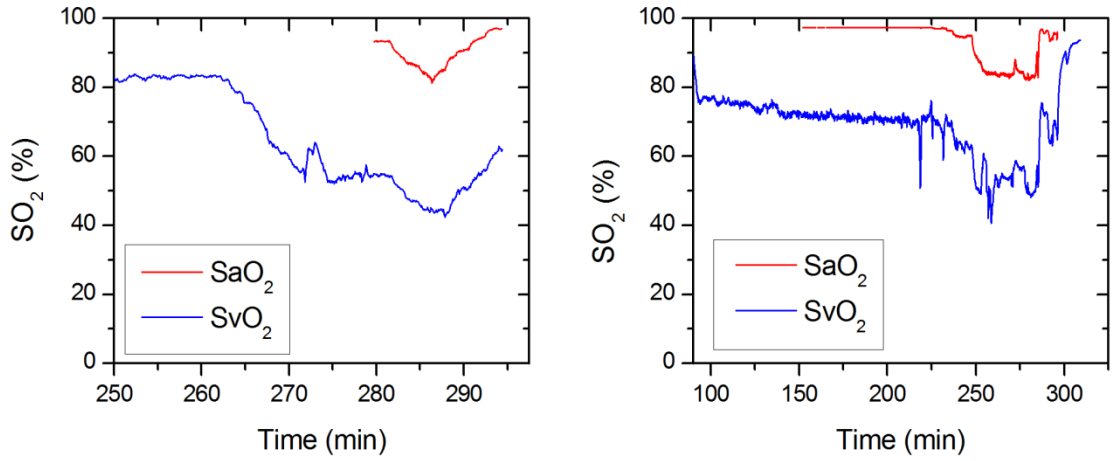

Fig. 92. Data from the arterial and venous oxygenation catheters collected from experiment 1 (left) and 2 (right)

III. Data processing:

Figure 93 shows the correlation between the measured hemoglobin oxygenation index and the different reference oxygenation measurements (MOS and SvO_2). The data show that ΔHbD correlates best with a combination of the two which is expected since the collected light probe both the venous and arterial blood.

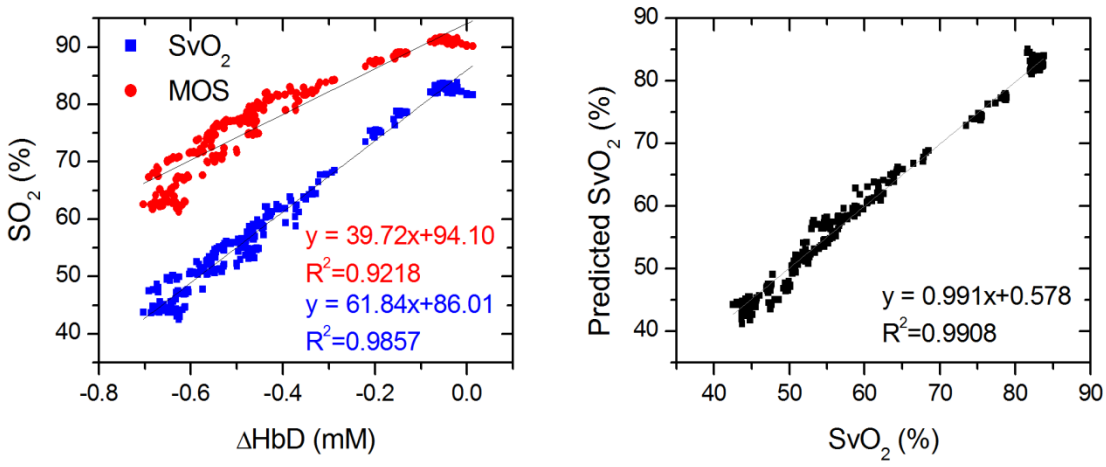

Fig. 93. (Left) Correlation between the measured hemoglobin oxygenation index (ΔHbD) and the measured oxygenation levels. (Right) Calibrated ΔHbD can predict SvO_2 with a higher degree of confidence (R^2=0.99) when using a multiple linear regression taking account for both supply and venous oxygenation.

APPENDIX H

INTESTINAL PERFUSION: SUPPLEMENTARY DATA

According to the Beer-Lambert law, the collected intensity on the surface of the tissue can be expressed in a simplified case by the following equation.

$$I = I_0.\exp(-\varepsilon.C.\ell)$$

Diffuse reflectance is the ratio of the collected light at the surface of the tissue (I) to the light from the light source (I_0):

$$R_\lambda = {}^{I}\!/_{I_0} = \exp(-\varepsilon.C.\ell)$$

In which $$\varepsilon.C.\ell = \varepsilon_{blood}.C_{blood}.\ell_{blood} + \varepsilon_{tissue}.C_{tissue}.\ell_{tissue}$$

A. Oxygenation Signal:

To look at the oxygenation signal, the ratio of the diffuse reflectance is considered in the cases where tissue is perfused with oxygenated and deoxygenated blood. These two cases represent the extreme in oxygenation changes and can be used to study the dynamic range to oxygenation changes which correlates to the sensitivity of the sensor.

$$S_\lambda = \log\left(\frac{R_{HbO_2}}{R_{Hb}}\right) = \varepsilon_{Hb}.C_{blood}.\ell_{blood} - \varepsilon_{HbO_2}.C_{blood}.\ell_{blood}$$

$$S_\lambda \propto \varepsilon_{Hb,\lambda} - \varepsilon_{HbO_2,\lambda}$$

This quantity can be positive or negative depending on the wavelength used. The oxygenation signal is defined as the absolute value of this quantity in order to have a comparison of the sensitivity across the spectrum without being affected by the direction of change in the signal.

$$S_\lambda = \left|\varepsilon_{Hb,\lambda} - \varepsilon_{HbO_2,\lambda}\right|$$ (This corresponds to equation (VI.1))

This equation makes the assumption that the optical pathlength does not change between the cases of oxygenated and deoxygenated blood perfusion. Although this is not exactly true, it can be used as a simplified theory to guide the more accurate Monte Carlo models.

B. <u>Perfusion Signal:</u>

Similar to the derivation of the oxygenation signal, the diffuse reflectance ratio of the ischemic tissue ($C_{blood} = 0$) to the normally perfused tissue can be defined.

In ischemic tissue, there is no blood and $C_{Ischemic} = C_{tissue}$

In normally perfused tissue, blood constitutes 12% of the total volume and thus, $C_{Perfused} = 0.12\ C_{blood} + 0.88\ C_{tissue}$ and the signal to background is,

$$SBR = \log\left(\frac{R_{Ischemic}}{R_{Perfused}}\right) = \varepsilon_{Perfused}.C_{Perfused}.\ell - \varepsilon_{Ischemic}.C_{Ischemic}.\ell$$

Assuming that the product of the chromophores concentration and the pathlength stays the same, the SBR can be reduced to:

$$SBR = \left(0.12\varepsilon_{blood} + 0.88\varepsilon_{tissue} - \varepsilon_{tissue}\right).C.\ell$$

$$SBR \propto 0.12\left(\varepsilon_{blood} - \varepsilon_{tissue}\right)$$

Although these equations have many assumptions, for this paper they were adequate to build hypotheses that were verified through the more accurate Monte Carlo simulations and *in vivo* data.

C. Mean Penetration Depth:

In Chapter VI, the change in the mean penetration depth was shown as a function of wavelength for multiple source to detector separations (Figure 77). Below (Fig. 94) the mean penetration depth versus source to detector separation for multiple wavelengths is shown. Data in this figure were generated using equation (VI.3) based on the work of Weiss *et al.* [73].

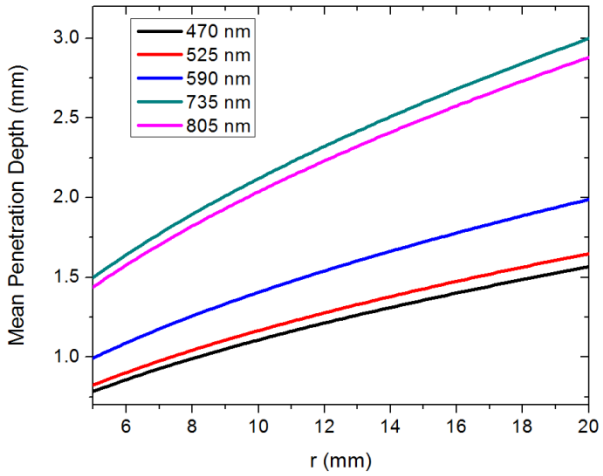

Fig. 94. Mean penetration depth as a function of source to detector separation for multiple wavelengths of interest.

D. *In Vivo* Data:

The modulation ratio (R) was calculated using the equation below. This ratio is typically used in pulse oximetry to measure oxygen saturation changes. In this study, the

inhaled oxygen levels were maintained constant and we did not expect any significant changes in oxygen saturation levels. The modulation ratio was measured to see how stable the signal was. Figure 95 shows the modulation ratio as a function of time and the detected heart rate for the two wavelengths (470, and 525 nm). The modulation ratio shows a stable level during baseline indicating stable oxygenation levels. During the occlusions, the modulation ratio shows an increase which can indicate an increase in oxygenation. However, the pulse almost disappeared during these occlusions which sometimes leads to erroneous oxygenation and heart rate data.

$$R = \frac{\left(AC_{525} / DC_{525} \right)}{\left(AC_{470} / DC_{470} \right)}$$

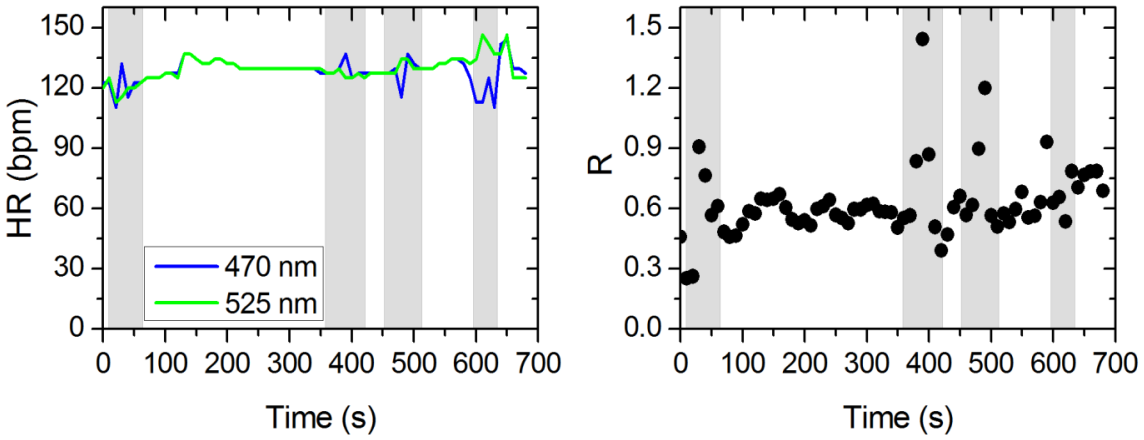

Fig. 95. Heart rate (left panel) and modulation ratio (right panel) measured from the visible wavelengths data. The grey segments indicate the occlusion periods during which the monitored section of the intestine was clamped.

Due to the high amplitude of the noise peak on the NIR wavelengths, it is difficult to visualize the cardiac cycle peak and the high frequency motion in the spectra of Figure 80. Figure 96 shows the 1 to 5 Hz range of the spectra for comparison of the signal peaks. It can be seen that the cardiac cycle peak is 4 to 5 times higher on the visible wavelengths (470 and 525 nm) compared to the NIR wavelengths.

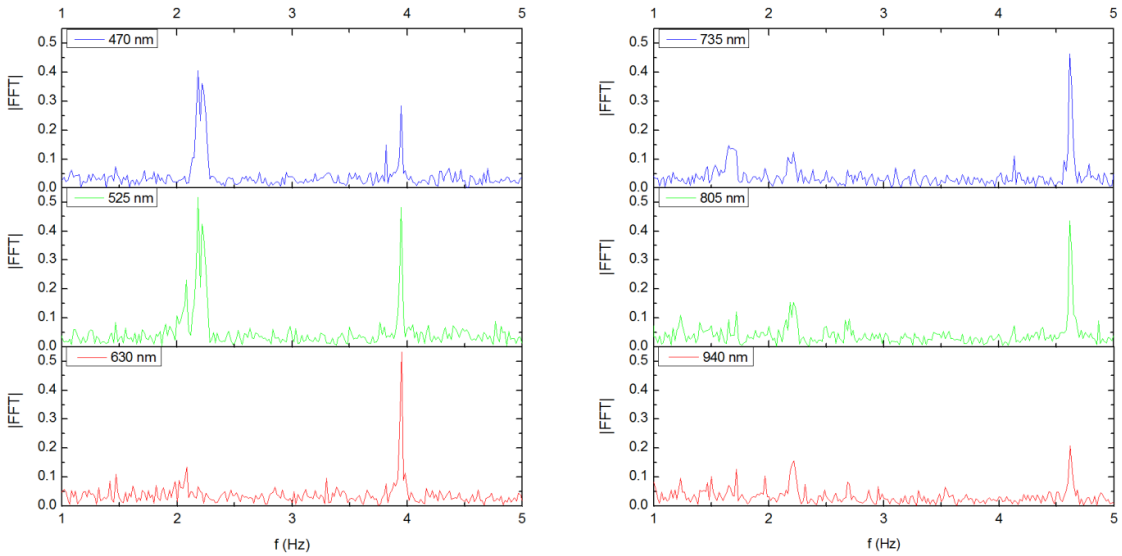

Fig. 96. Zoom-in for the 1 to 5 Hz range in the FFT of the AC signal for all six wavelengths. The cardiac cycle peak is 4 to 5 times higher for the 470 and 525 nm wavelengths compared to the NIR wavelengths.

APPENDIX I

TELEMETRY SENSOR PROCESSING SOFTWARE

This appendix has all the data processing software used with the telemetry sensor.

This first program is used for the FFT processing of the telemetry data:

```
clear all
dropbox_path=getdropbox;
%% Inputs

processing_interval=25; %processing interval duration in seconds
time_step=10;            %time step in seconds
start_time=0;
t0=0;    %The time stamp on the first file of the experiment
                        %All data will be referenced to this time point
Fs=300;     %sampling frequency in Hz
minf=1.5;
maxf=2.5;
cut_off=0.2;
nb_of_files=21;
first_file=210;
start_index=1;
end_index=18000*nb_of_files;
sheet_name=strcat(num2str(floor(start_index/Fs)),'s-
',num2str(floor(end_index/Fs)),'s');
probes=[2 3];
gain=[20.39849 70.17787 33.66493];

data_dir=uigetdir(strcat(dropbox_path,'Research\Perfusion sensor
project\Perfusion Sensor documents\Animal Studies\Porcine\EXP 06-29-
2011(Oxygenation studies)\TAMU 6-28-2011\Exp10\'),'Pick a directory');
base_filename='Run1_Probe';

%%
dt=processing_interval;
np=length(probes);
%%%%%%%%%%%%%%%%%%%%%%%%%%Main Program%%%%%%%%%%%%%%%%%%%%%%%%%%
%%
```

```
for i1=1:length(probes)
p=probes(i1);
fname=fullfile(data_dir,strcat(base_filename,num2str(p),'_'));

probes_data=importdata(strcat(fname,num2str(first_file),'.txt'));
%data_all=importdata(strcat(base_filename,'.txt'));
file1=first_file;
    for i=1:nb_of_files-1
        if i>nb_of_files-1
            break
        end
        file1=file1+1;
        temp=importdata(strcat(fname,num2str(file1),'.txt'));
        probes_data=[probes_data; temp];
    end

end_index=min(end_index,length(probes_data));
data_all2=probes_data(start_index:end_index,:);
ts=1;
nmax=end_index-start_index;
jmax=floor((nmax-dt*Fs/2)/(time_step*Fs));
if jmax==0
    jmax=1;
end

for j=1:jmax
tf=min(ts+dt*Fs,nmax);

data_temp=data_all2(ts:tf,:);

% time=[0:1/Fs:(end_index-start_index)/Fs];
%AC
AC735=data_temp(:,2);
AC805=data_temp(:,3);
AC940=data_temp(:,4);
%DC
DC735=data_temp(:,5);
DC805=data_temp(:,6);
DC940=data_temp(:,7);

%% Fourrier transforms
n=length(AC735);
NFFT=n;%2^nextpow2(n);      % If the NFFT is set at 2^next
FFT735=fft(AC735,NFFT)/n;
power735=abs(FFT735).^2;
FFT805=fft(AC805,NFFT)/n;
power805=abs(FFT805).^2;
FFT940=fft(AC940,NFFT)/n;
power940=abs(FFT940).^2;
```

```
% Detecting HR
f=Fs/2*linspace(0,1,NFFT/2);
[l kmin]=max(f>=minf);
[l kmax]=max(f>=maxf);
[maxFFT735 l]=max(abs(FFT735(kmin:kmax)));
HR735=f((kmin+l-1));
i=kmin+l-2;
while(abs(FFT735(i))>cut_off*maxFFT735)&&(i>1)
    i=i-1;
end
imin735=i;
fmin735=f(imin735);

i=kmin+l;
while(abs(FFT735(i))>cut_off*maxFFT735)
    i=i+1;
end
imax735=i;
fmax735=f(imax735);

power735=sum(abs(FFT735(imin735:imax735)));

[maxFFT805 l]=max(abs(FFT805(kmin:kmax)));
HR805=f((kmin+l-1));

i=kmin+l-2;
while(abs(FFT805(i))>cut_off*maxFFT805)&&(i>1)
    i=i-1;
end
imin805=i;
fmin805=f(imin805);
i=kmin+l;
while(abs(FFT805(i))>cut_off*maxFFT805)
    i=i+1;
end
imax805=i;
fmax805=f(imax805);
power805=sum(abs(FFT805(imin805:imax805)));

[maxFFT940 l]=max(abs(FFT940(kmin:kmax)));
HR940=f((kmin+l-1));
i=kmin+l-2;
while(abs(FFT940(i))>cut_off*maxFFT940)&&(i>1)
    i=i-1;
end
imin940=i;
fmin940=f(imin940);

i=kmin+l;
while(abs(FFT940(i))>cut_off*maxFFT940)
    i=i+1;
end
```

```
imax940=i;
fmax940=f(imax940);
power940=sum(abs(FFT940(imin940:imax940)));


%% Data output
flow(j,i1,1:3)=[abs(maxFFT735) abs(maxFFT805) abs(maxFFT940)];
meanDC(j,i1,1:3)=[mean(DC735) mean(DC805) mean(DC940)];
% FFT_peak=[maxFFT735 maxFFT805 maxFFT940]
% FFT_power=[power735 power805 power940]*Fs/(NFFT-2)
DC=[mean(DC735) mean(DC805) mean(DC940)];
R(j,i1)=(flow(j,i1,1)./meanDC(j,i1,1))./(flow(j,i1,3)./meanDC(j,i1,3));

HR(j,i1,:)=[HR735 HR805 HR940]*60; %AC=[AC735 AC805 AC940];DCt=[DC735
DC805 DC940];ACDC=AC./DCt;
%ch1_ch3=ACDC(:,1)./ACDC(:,3);

R2(j,i1)=
log((((maxFFT735/gain(i1))+DC(1))./DC(1)))./log((((maxFFT940/gain(i1))+
DC(3))./DC(3)));
PI(j,i1,:)= 100*[maxFFT735/(gain(i1)*DC(1)) maxFFT805/(gain(i1)*DC(2))
maxFFT940/(gain(i1)*DC(3))];

t(j)=start_time-t0+mean(data_temp(:,1));
ts=ts+time_step*Fs;
end
end
%%

output1=zeros(length(t),length(probes)*12+3);
output1=[t' t'/60 (t'-t(1))];
for i=1:length(probes)
    for j=1:3
        output1(:,3+(i-1)*12+j) = flow(:,i,j);
        output1(:,6+(i-1)*12+j) = meanDC(:,i,j);
        output1(:,9+(i-1)*12+j) = flow(:,i,j)./meanDC(:,i,j);
        output1(:,12+(i-1)*12+j) = HR(:,i,j);
    end
end



%% Initializing headers
header2={' ' ' ' ' ' ' ' 'Probe2' 'Probe2' 'Probe2' 'Probe2' 'Probe2'...
    'Probe2' 'Probe2' 'Probe2' 'Probe2' 'Probe2' 'Probe2' 'Probe2'...
    'Probe3' 'Probe3' 'Probe3' 'Probe3' 'Probe3' 'Probe3' 'Probe3'...
    'Probe3' 'Probe3' 'Probe3' 'Probe3' 'Probe3'...
    };


header1={'Time(s)' 'Time(min)' 'Relative time(s)' ...
```

```
 'FFT peak' 'FFT peak' 'FFT peak' 'DC' 'DC' 'DC' 'PI' 'PI' 'PI' 'HR'
'HR' 'HR'...
 'FFT peak' 'FFT peak' 'FFT peak' 'DC' 'DC' 'DC' 'PI' 'PI' 'PI' 'HR'
'HR' 'HR'...
 %'FFT peak' 'FFT peak' 'FFT peak' 'DC' 'DC' 'DC' 'PI' 'PI' 'PI' 'HR'
'HR' 'HR'
 };

header3={' ' ' ' ' ' '  'Ch1' 'Ch2' 'Ch3' 'Ch1' 'Ch2' 'Ch3'...
    'Ch1' 'Ch2' 'Ch3' 'Ch1' 'Ch2' 'Ch3'...
    'Ch1' 'Ch2' 'Ch3' 'Ch1' 'Ch2' 'Ch3'...
    'Ch1' 'Ch2' 'Ch3' 'Ch1' 'Ch2' 'Ch3'...
    %'Ch1' 'Ch2' 'Ch3' 'Ch1' 'Ch2' 'Ch3'...
    %'Ch1' 'Ch2' 'Ch3' 'Ch1' 'Ch2' 'Ch3'...
    };

%% Saving data
excel_out=[header1;header2;header3;num2cell(output1)];
ButtonName = questdlg('Would you like to save the
data?','Save','Yes','No','Yes');

switch ButtonName,
    case 'Yes',
        [save_name,pname]=uiputfile({'*.xls', 'Excel Worksheet
(*.xls)'},'Saving data');
        save_name=fullfile(pname,save_name);
        [status msg]=xlswrite(save_name,excel_out,sheet_name);
        if status==1
            msgbox('Data saved successfully','Data saved')
        else
            msgbox(msg.message,'Data not saved')
        end
    case 'No',
        msgbox('Data not saved! You can still save them
manually.','Data not saved')
end
%%
display('END')
```

The following programs are used for the NIRS processing of the telemetry data:

```
% NIRS_v2_1.m
% This program reads and process data from the telemetry system
% The data is processed using NIRS algorithm
% The data is first truncated and the first few seconds are eliminated
% All data is saved in excel files and plotted at the end
%
% v2 (Major update) allows the processing of previously saved matlab
% files which is faster than reading the raw data. The matlab file
% should contain the parameters probes_data, start_time, status_data,
% and comments.
% However, only the probes_data and start_time are required, the rest
% is optional.
%
% This program also runs the updated automated_NIRS_v2 (Major update)
% which fixed some formulas from previous version that caused
% miscalculation of DHbO2 on some wavelengths combinations
%
% v2_1 (Minor changes) allows for selecting multiple preprocessed
% matlab files for processing
%
% Tony J. Akl
% tja161@gmail.com
% Last updated 7/25/2013

%%
FileTypeButton = questdlg('Where is the data?', 'Select Data', ...
    'Raw data file', 'Preprocessed matlab file','Raw data file');
switch FileTypeButton,
    case 'Raw data file'
        process_data; nb_files=1;
    case 'Preprocessed matlab file'
        [fname1 pname1]=uigetfile('*.mat','Select data
file(s)','MultiSelect','on');
        if ischar(fname1)
            nb_files=1;
            fname=fname1;
            load(fullfile(pname1,fname));
            multiple_files = false;
        else
            nb_files=length(fname1);
            fname=char(fname1(1));
            load(fullfile(pname1,fname));
            multiple_files = true;
        end
end
%%
for ifile=1:nb_files
automatic_truncation;
btn = questdlg('Are you content with your selection?','Data
truncation','Yes','No','Yes');
while (1)
```

```
switch btn
    case 'No',
        automatic_truncation;
        btn = questdlg('Are you content with your selection?','Data
truncation','Yes','No','Yes');
    case 'Yes'
        break;
end
end
close all
display(['Starting NIRS processing for :"' fname '"'])
automated_NIRS_inputs_v2;
% automated_NIRS_v2;
%% Close all message boxes
allHandle = allchild(0);
allTag = get(allHandle, 'Tag');
isMsgbox = strncmp(allTag, 'Msgbox_', 7);
delete(allHandle(isMsgbox));

%% Redaing next file for processing
if multiple_files && ifile<nb_files
    fname=char(fname1(ifile+1));
    load(fullfile(pname1,fname));
end
end
```

```
% automated_NIRS_inputs_v2.m
%%
clear DHb* C*

ext_deoxy_l1=1.29559;    %Extinction coefficient of deoxy hemoglobin
for wavelength 1
ext_oxy_l1=0.46448;        %Extinction coefficient of oxy hemoglobin
for wavelength 1
ext_cyt_l1=1.80054;%1.624;
ext_deoxy_l2=0.81439;    %Extinction coefficient of deoxy hemoglobin
for wavelength 2
ext_oxy_l2=0.89708;        %Extinction coefficient of oxy hemoglobin
for wavelength 2
ext_cyt_l2=2.28643;%4.633;
ext_deoxy_l3=0.7872;     %Extinction coefficient of deoxy hemoglobin
for wavelength 3
ext_oxy_l3=1.35165;         %Extinction coefficient of oxy hemoglobin
for wavelength 3
ext_cyt_l3=1.28616;%0.93;

t0=(17-6)*3600+46*60+05;        %Start time for experiment 1-30-13
data_all2=probes_data;
probes=[1 2 3];
np=length(probes);
% DHbO2=zeros(1,length(probes));
% DHb=zeros(1,length(probes));
Ib1=[2.52212524414063,2.63717651367188,2.73635864257813];
Ib2=[3.31726074218750,2.51586914062500,2.43194580078125];
Ib3=[1.79542541503906,1.76239013671875,1.85424804687500];
%%
prompt={'Averaging period (s):'; 'Interoptode separation (cm):'};
name='User Input';
numlines=1;
defaultanswer={'1';'0.7'};
user_inputs=str2num(char(inputdlg(prompt,name,numlines,defaultanswer)))
;
averaging_period =user_inputs(1);
L=user_inputs(2);
averaging_samples=averaging_period*Fs;
averaging_samples=floor(averaging_samples/2);
%%%%%%%%%%%%%%%%%%%%%%%%%Main Program%%%%%%%%%%%%%%%%%%%%%%%%%%%
ButtonName = questdlg('Would you like to save the
data?','Save','Yes','No','Yes');

switch ButtonName
    case 'Yes',
        [save_name,pname]=uiputfile({'*.xls', 'Excel Worksheet
(*.xls)'},'Saving data');
        save_name=fullfile(pname,save_name);
end
clear tf DHbf DHbO2f
for kk=1:length(mx)
    start_index=mx(kk);
```

```
    end_index=mn(kk);
    automated_NIRS_v2;
    display([num2str(kk), ' done and ',num2str(length(mx)-kk),' left'])
end

%% Saving data
trf=tf+start_time-t0;
output1=[tf' tf'/60 trf' DHbf_l12 DHbO2f_l12 DHbf_l12+DHbO2f_l12
DHbf_l13 DHbO2f_l13 DHbf_l13+DHbO2f_l13 DHbf_l23 DHbO2f_l23
DHbf_l23+DHbO2f_l23 Cdeoxyf Coxyf Coxyf+Cdeoxyf Ccytf];
output1=output1(2:end,:);
excel_out=[header1;header2;header3;num2cell(output1)];

switch ButtonName
    case 'Yes'
        [status msg]=xlswrite(save_name,excel_out,['Combined '
num2str(averaging_period) 's']);
        if status==0
            if msg.message == 'Excel returned: Error: Object returned
error code: 0x800A03EC.'
                sname=['Combined ' num2str(averaging_period) 's'];
                for f_nb=1:ceil(length(excel_out)/50000)
                [status, msg]=xlswrite(save_name,...
                  excel_out((f_nb-
1)*50000+1:min(f_nb*50000,length(excel_out)),:),...
                    [sname '-' num2str(f_nb)]);
                end
            end

            msgbox(msg.message,'Saving Data')
        end
end

%% Plotting data
figure,set(gcf, 'Position', get(0,'Screensize')); % Maximize figure.
for i=1:np
    subplot(np,1,i);plot(tf(2:end),DHbf_l13(2:end,i))
    hold on, plot(tf(2:end),DHbO2f_l13(2:end,i),'r')
    plot(tf(2:end),DHbO2f_l13(2:end,i)+DHbf_l13(2:end,i),'g')
    hold off
end
xlabel('Time (s)')
subplot(np,1,1),legend('Hb','HbO_2','tHb',...
    'Location','Best','Orientation','Horizontal')
```

```
% automated_NIRS_v2.m
% V2 includes corrections of the DHbO2 equations
% This program measures changes in Oxy and Deoxy hemoglobin
concentrations
% using the DC levels of a PPG sensor.
%%
sheet_name=strcat(num2str(floor(start_index/Fs)),'s-
',num2str(floor(end_index/Fs)),'s');
data_temp=data_all2(start_index:end_index,:);
clear DHbO2_l* DHb_l* C_*
t=[0:1/Fs:(end_index-start_index)/Fs]+data_temp(1,1);
tr=t+start_time-t0;
for p1=1:np
p=probes(p1);
% time=[0:1/Fs:(end_index-start_index)/Fs];

%DC
DC735=data_temp(:,7*(p-1)+3)*5/2^16;
DC805=data_temp(:,7*(p-1)+5)*5/2^16;
DC940=data_temp(:,7*(p-1)+7)*5/2^16;

Is1=DC735;          %Signal intesity for wavelength 1
Is2=DC805;          %Signal intesity for wavelength 2
Is3=DC940;          %Signal intesity for wavelength 3

mups=[0.3*2.53+0.7*4.76 0.3*2.54+0.7*4.11 0.3*2.71+0.7*3.41];
mua0=[0.3*2.21+0.7*1.19 0.3*4.50+0.7*0.81 0.3*6.5+0.7*0.57];
PF=pathlength_factor(L,mups,mua0,mups);
DA_l1=log(Ib1(p1)./Is1)/PF(1);
DA_l2=log(Ib2(p1)./Is2)/PF(2);
DA_l3=log(Ib3(p1)./Is3)/PF(3);
%Change in oxy hemoglobin concentration
DHbO2_l12(:,p1)=(ext_deoxy_l2*DA_l1-
ext_deoxy_l1*DA_l2)/((ext_oxy_l1*ext_deoxy_l2-
ext_oxy_l2*ext_deoxy_l1)*L);
DHbO2_l13(:,p1)=(ext_deoxy_l3*DA_l1-
ext_deoxy_l1*DA_l3)/((ext_oxy_l1*ext_deoxy_l3-
ext_oxy_l3*ext_deoxy_l1)*L);
DHbO2_l23(:,p1)=(ext_deoxy_l3*DA_l2-
ext_deoxy_l2*DA_l3)/((ext_oxy_l2*ext_deoxy_l3-
ext_oxy_l3*ext_deoxy_l2)*L);
%Change in deoxy hemoglobin concentration
DHb_l12(:,p1)=(ext_oxy_l2*DA_l1-
ext_oxy_l1*DA_l2)/((ext_deoxy_l1*ext_oxy_l2-
ext_deoxy_l2*ext_oxy_l1)*L);
DHb_l13(:,p1)=(ext_oxy_l3*DA_l1-
ext_oxy_l1*DA_l3)/((ext_deoxy_l1*ext_oxy_l3-
ext_deoxy_l3*ext_oxy_l1)*L);
DHb_l23(:,p1)=(ext_oxy_l3*DA_l2-
ext_oxy_l2*DA_l3)/((ext_deoxy_l2*ext_oxy_l3-
ext_deoxy_l3*ext_oxy_l2)*L);
%Change in total hemoglobin concentration
%DHbt(p1,:)=DHbO2(p1,:)+DHb(p1,:);
```

```
% Multi wavelengths processing
multi_wavelength_NIRS;
%% Averaging dta
[ta DHbO2_l12a(:,p1)]=smoothing(t,DHbO2_l12(:,p1),averaging_samples);
[ta DHbO2_l13a(:,p1)]=smoothing(t,DHbO2_l13(:,p1),averaging_samples);
[ta DHbO2_l23a(:,p1)]=smoothing(t,DHbO2_l23(:,p1),averaging_samples);
[ta DHb_l12a(:,p1)]=smoothing(t,DHb_l12(:,p1),averaging_samples);
[ta DHb_l13a(:,p1)]=smoothing(t,DHb_l13(:,p1),averaging_samples);
[ta DHb_l23a(:,p1)]=smoothing(t,DHb_l23(:,p1),averaging_samples);
%%
end
try
    tt=length(tf);
catch
    tt=0;
end
l_ta=length(ta);
tf(tt+1:tt+l_ta) = ta;
DHbf_l12(tt+1:tt+l_ta,:) = DHb_l12a;
DHbf_l13(tt+1:tt+l_ta,:) = DHb_l13a;
DHbf_l23(tt+1:tt+l_ta,:) = DHb_l23a;
DHbO2f_l12(tt+1:tt+l_ta,:) = DHbO2_l12a;
DHbO2f_l13(tt+1:tt+l_ta,:) = DHbO2_l13a;
DHbO2f_l23(tt+1:tt+l_ta,:) = DHbO2_l23a;
Coxyf(tt+1:tt+l_ta,:) = C_oxya;
Cdeoxyf(tt+1:tt+l_ta,:) = C_deoxya;
Ccytf(tt+1:tt+l_ta,:) = C_cyta;
%%
output1=[t' t'/60 tr' DHb_l12 DHbO2_l12 DHb_l12+DHbO2_l12 DHb_l13
DHbO2_l13 DHb_l13+DHbO2_l13 DHb_l23 DHbO2_l23 DHb_l23+DHbO2_l23 C_deoxy
C_oxy C_oxy+C_deoxy C_cyt];

%% Initializing headers
header1={' ' ' ' ' ' 'Wavelengths 1-2' ' ' ' ' ' ' ' ' ' ' ' ' ' ' ' '
'...
   'Wavelengths 1-3' ' ' ' ' ' ' ' ' ' ' ' ' ' ' ' ' ' '...
   'Wavelengths 2-3' ' ' ' ' ' ' ' ' ' ' ' ' ' ' ' ' ' '...
   'All wavelengths' ' ' ' ' ' ' ' ' ' ' ' ' ' ' ' ' ' ' ' ' ' ' ' ' ' ' '};
header2={' ' ' ' ' ' 'Probe1' 'Probe2' 'Probe3' 'Probe1' 'Probe2'
'Probe3'...
    'Probe1' 'Probe2' 'Probe3' 'Probe1' 'Probe2' 'Probe3' 'Probe1'
'Probe2' 'Probe3'...
    'Probe1' 'Probe2' 'Probe3' 'Probe1' 'Probe2' 'Probe3' 'Probe1'
'Probe2' 'Probe3'...
    'Probe1' 'Probe2' 'Probe3' 'Probe1' 'Probe2' 'Probe3' 'Probe1'
'Probe2' 'Probe3'...
    'Probe1' 'Probe2' 'Probe3' 'Probe1' 'Probe2' 'Probe3'};
header3={'Time(s)' 'Time(min)' 'Relative time(s)' ...
    'DHb' 'DHb' 'DHb' 'DHbO2' 'DHbO2' 'DHbO2' 'DHbt' 'DHbt' 'DHbt'...
    'DHb' 'DHb' 'DHb' 'DHbO2' 'DHbO2' 'DHbO2' 'DHbt' 'DHbt' 'DHbt'...
    'DHb' 'DHb' 'DHb' 'DHbO2' 'DHbO2' 'DHbO2' 'DHbt' 'DHbt' 'DHbt'...
    'DHb' 'DHb' 'DHb' 'DHbO2' 'DHbO2' 'DHbO2' 'DHbt' 'DHbt' 'DHbt'
'Cytaa3' 'Cytaa3' 'Cytaa3'};
```

```
%% Saving data
excel_out=[header1;header2;header3;num2cell(output1)];

switch ButtonName
    case 'Yes'
        [status msg]=xlswrite(save_name,excel_out,sheet_name);
        if status==0
            if msg.message=='Excel returned: Error: Object returned
error code: 0x800A03EC.'
                for f_nb=1:ceil(length(excel_out)/50000)
                    [status, msg]=xlswrite(save_name,excel_out((f_nb-
1)*50000+1:min(f_nb*50000,length(excel_out)),:),...
                        [sheet_name '-' num2str(f_nb)]);%, ['A'
num2str((f_nb-1)*10000+1) ':AD'
num2str(min(f_nb*10000,length(excel_out)))]);
                end
            end
            msgbox(msg.message,'Saving Data');
        end
end
%%
```

```
% multi_wavelength_NIRS.m
A=[DA_l1';DA_l2';DA_l3'];
E=[ext_oxy_l1 ext_deoxy_l1 ext_cyt_l1;ext_oxy_l2 ext_deoxy_l2
ext_cyt_l2;ext_oxy_l3 ext_deoxy_l3 ext_cyt_l3];
C=inv(E)*A/L;

C_oxy(:,p1)=C(1,:)';
C_deoxy(:,p1)=C(2,:)';
C_cyt(:,p1)=C(3,:)';

%Data averaging
[ta C_oxya(:,p1)]=smoothing(t,C_oxy(:,p1),averaging_samples);
[ta C_deoxya(:,p1)]=smoothing(t,C_deoxy(:,p1),averaging_samples);
[ta C_cyta(:,p1)]=smoothing(t,C_cyt(:,p1),averaging_samples);
```

```
% process_data.m
%%
%%%%%%%%%%%%%%%%%%%%%%%%%Data Input%%%%%%%%%%%%%%%%%%%%%%%%%%%%%
%data_dir='C:\Tony\Dropbox\Research\Perfusion sensor project\Perfusion
Sensor documents\in vitro data\Implantable system\PV phantom';
clear probes_data status_data comments
[fname,pname]=uigetfile({'*.dat','Data files (*.dat)';'*.*',  'All
Files (*.*)'},'Pick a data file');
full_name=fullfile(pname,fname);
cd(pname)
header_length=58;

%%
%%%%%%%%%%%%%%%%%%%%%%%%%Main Program%%%%%%%%%%%%%%%%%%%%%%%%%%%%%
data_all=importdata(full_name,',');
%%
s=1;d=1;c=1;
for i=header_length+1:length(data_all)
    A=cell2mat(data_all(i));
    [l k]=max((A=='>'));
    data_type=char(A(2:k-1));
    num_data=str2num(A(k+1:length(A)-k-1));
    switch data_type
        case 'Status'
            status_data(s,:)=num_data;s=s+1;
        case 'Data'
            probes_data(d,:)=num_data;d=d+1;
        case 'Comment'
            comments(c)=cellstr(A(k+1:end));c=c+1;
        otherwise
            comments(c-1)=cellstr(strcat(comments(c-1), '___',A));
    end
end
t=char(data_all(4));
t=datevec(t(8:end-7));
start_time=(t(4)-6)*3600+t(5)*60+t(6); %convert time to CT and then to
seconds
clear data_all
```

```
% automatic_truncation.m
%%
clear y mx mn
response_time=2;    %response time in seconds.
dt=1;               %Time to cut out at the deginning of the dataset
Fs=300;
test_data=probes_data(:,2)-mean(probes_data(:,2));
figure,plot(test_data)
uiwait(msgbox('Select the threshold for cutoff and press enter when you
are satisfied with your selection','Threshold'))
[x,y,k]=ginput;
threshold=y(length(y));
y=abs(test_data)<threshold;
response_time=response_time*Fs-1;
for i=1:length(y)-response_time
    y(i)=min(y(i:i+response_time));
end
diffy=diff(y);
hold on,plot(10000*diffy,'r')
data_length=length(test_data);
mx=find(diffy>0);
mn=find(diffy<0);
mx=mx+dt*Fs;
mn=mn+response_time-50;
mn(length(mn)+1)=data_length;
if length(mx)==length(mn)
    msgbox(strcat(num2str(length(mx)),' datasets found.'),'Data
truncation');
else
    msgbox('Error! Retry by selecting a different threshold.','Error!')
end

hold on,plot(mx,test_data(mx),'xg')
plot(mn,test_data(mn),'og')
```

```
% summary_file_v2.m
% This program combines different excel files from the same experiment
% into a single excel file to make data analysis easier. The user the
% inputs name of the sheet in the excel files that he wants to combine
% and selects all the files to merge and the saving location.
%
% Tony J. Akl
% tja161@gmail.com

%%
[fname1, pname] = uigetfile({'*.xls','Excel files (*.xls)'},'Pick all
data file','MultiSelect','on');
prompt={'Sheet name:'};
name='User Input';
numlines=1;
defaultanswer={'Combined 5s'};
sheet_name = char(inputdlg(prompt,name,numlines,defaultanswer));

%% Initializing headers
header1={' ' ' ' ' ' ' 'Wavelengths 1-2' ' ' ' ' ' ' ' ' ' ' ' ' ' ' '
'...
   'Wavelengths 1-3' ' ' ' ' ' ' ' ' ' ' ' ' ' ' ' ' ' ' '...
   'Wavelengths 2-3' ' ' ' ' ' ' ' ' ' ' ' ' ' ' ' ' ' ' '...
   'All wavelengths' ' ' ' ' ' ' ' ' ' ' ' ' ' ' ' ' ' ' ' ' ' ' ' ' '};
header2={' ' ' ' ' ' 'Probe1' 'Probe2' 'Probe3' 'Probe1' 'Probe2'
'Probe3'...
    'Probe1' 'Probe2' 'Probe3' 'Probe1' 'Probe2' 'Probe3' 'Probe1'
'Probe2' 'Probe3'...
    'Probe1' 'Probe2' 'Probe3' 'Probe1' 'Probe2' 'Probe3' 'Probe1'
'Probe2' 'Probe3'...
    'Probe1' 'Probe2' 'Probe3' 'Probe1' 'Probe2' 'Probe3' 'Probe1'
'Probe2' 'Probe3'...
    'Probe1' 'Probe2' 'Probe3' 'Probe1' 'Probe2' 'Probe3'};
header3={'Time(s)' 'Time(min)' 'Relative time(s)' ...
    'DHb' 'DHb' 'DHb' 'DHbO2' 'DHbO2' 'DHbO2' 'DHbt' 'DHbt' 'DHbt'...
    'DHb' 'DHb' 'DHb' 'DHbO2' 'DHbO2' 'DHbO2' 'DHbt' 'DHbt' 'DHbt'...
    'DHb' 'DHb' 'DHb' 'DHbO2' 'DHbO2' 'DHbO2' 'DHbt' 'DHbt' 'DHbt'...
    'DHb' 'DHb' 'DHb' 'DHbO2' 'DHbO2' 'DHbO2' 'DHbt' 'DHbt' 'DHbt'
'Cytaa3' 'Cytaa3' 'Cytaa3'};
%%
nb_files=0;
fname1=sort(fname1);
excel_out=[header1;header2;header3];
for nf=1:length(fname1)
    fname=char(fname1(nf));
    filename=fullfile(pname,fname);
    [status,sheets1]= xlsfinfo(filename);

    if max(strcmp(sheets1,sheet_name))~=1
        nb_files=nb_files+1;
        files(nb_files)={fname};
        continue
    end
```

```
     a=xlsread(filename,sheet_name);
     excel_out=[excel_out; num2cell(a)];
end
[fname, pname]=uiputfile({'*.xls', 'Excel Worksheet (*.xls)'},'Saving
data','Summary.xls');

xlswrite(fullfile(pname,fname),excel_out,sheet_name);
display([num2str(length(fname1)-nb_files) ' files added to ' fname ...
    ' and ' num2str(nb_files) ' files could not be added']);
%%
```

```
% process_fft.m
clear PI R2 HR
Fs=300;     %sampling frequency in Hz
minf=1.1;
maxf=2.7;
cut_off=0.2;
start_index=294000;
end_index=312700;
probes=[1 2 3];

gain=[20.39849 38.69856 96.28571];
%%
%%%%%%%%%%%%%%%%%%%%%%%%%Main Program%%%%%%%%%%%%%%%%%%%%%%%%%%
for i=1:length(probes)
p=probes(i);
%% Input
time=[0:1/Fs:(end_index-start_index)/Fs];
%AC
AC735=probes_data(start_index:end_index,7*(p-1)+2)*5/2^16;
AC805=probes_data(start_index:end_index,7*(p-1)+4)*5/2^16;
AC940=probes_data(start_index:end_index,7*(p-1)+6)*5/2^16;
%DC
DC735=probes_data(start_index:end_index,7*(p-1)+3)*5/2^16;
DC805=probes_data(start_index:end_index,7*(p-1)+5)*5/2^16;
DC940=probes_data(start_index:end_index,7*(p-1)+7)*5/2^16;
%Sum
total735=AC735+DC735;
total805=AC805+DC805;
total940=AC940+DC940;
%% Fourrier transforms
n=length(AC735);
NFFT=n;%2^nextpow2(n);      % If the NFFT is set at 2^next
FFT735=fft(AC735,NFFT)/n;
power735=abs(FFT735).^2;
FFT805=fft(AC805,NFFT)/n;
power805=abs(FFT805).^2;
FFT940=fft(AC940,NFFT)/n;
power940=abs(FFT940).^2;

% Detecting HR
f=Fs/2*linspace(0,1,NFFT/2);
[l kmin]=max(f>=minf);
[l kmax]=max(f>=maxf);
[maxFFT735 l]=max(abs(FFT735(kmin:kmax)));
HR735=f((kmin+l-1))
i=kmin+l-2;
while(abs(FFT735(i))>cut_off*maxFFT735)&&(i>1)
    i=i-1;
end
imin735=i;
fmin735=f(imin735);

i=kmin+l;
```

```
while(abs(FFT735(i))>cut_off*maxFFT735)
    i=i+1;
end
imax735=i;
fmax735=f(imax735);

power735=sum(abs(FFT735(imin735:imax735)));

[maxFFT805 l]=max(abs(FFT805(kmin:kmax)));
HR805=f((kmin+l-1))

i=kmin+l-2;
while(abs(FFT805(i))>cut_off*maxFFT805)&&(i>1)
    i=i-1;
end
imin805=i;
fmin805=f(imin805);
i=kmin+l;
while(abs(FFT805(i))>cut_off*maxFFT805)
    i=i+1;
end
imax805=i;
fmax805=f(imax805);
power805=sum(abs(FFT805(imin805:imax805)));

[maxFFT940 l]=max(abs(FFT940(kmin:kmax)));
HR940=f((kmin+l-1))
i=kmin+l-2;
while(abs(FFT940(i))>cut_off*maxFFT940)&&(i>1)
    i=i-1;
end
imin940=i;
fmin940=f(imin940);

i=kmin+l;
while(abs(FFT940(i))>cut_off*maxFFT940)
    i=i+1;
end
imax940=i;
fmax940=f(imax940);
power940=sum(abs(FFT940(imin940:imax940)));

%% Plotting and data output
figure(p),subplot(3,2,1), plot(f,2*abs(FFT735(1:NFFT/2)))
axis([0 10 0 1.1*max(2*abs(FFT735(kmin:kmax)))]),title('735 nm')
subplot(3,2,3), plot(f,2*abs(FFT805(1:NFFT/2)))
axis([0 10 0 1.1*max(2*abs(FFT805(kmin:kmax)))]),title('805 nm')
subplot(3,2,5), plot(f,2*abs(FFT940(1:NFFT/2)))
axis([0 10 0 1.1*max(2*abs(FFT940(kmin:kmax)))]),title('940 nm')

h(p)=figure(p);
subplot(3,2,1), hold on, plot([fmin735 fmin735],[0 4*maxFFT735],'--r')
```

```
plot([fmax735 fmax735],[0 4*maxFFT735],'--r'),hold off
ylabel('|FFT|'),xlabel('f(Hz)')
subplot(3,2,3);
hold on, plot([fmin805 fmin805],[0 4*maxFFT805],'--r')
plot([fmax805 fmax805],[0 4*maxFFT805],'--r'),hold off
ylabel('|FFT|'),xlabel('f(Hz)')
subplot(3,2,5)
hold on, plot([fmin940 fmin940],[0 4*maxFFT940],'--r')
plot([fmax940 fmax940],[0 4*maxFFT940],'--r'),hold off
ylabel('|FFT|'),xlabel('f(Hz)')
set(h(p),'Units','Normalized')
set(h(p),'Position',[0 0 1 1])

flow(p,1:3)=[abs(maxFFT735) abs(maxFFT805) abs(maxFFT940)];
meanDC(p,1:3)=[mean(DC735) mean(DC805) mean(DC940)];
FFT_peak=[maxFFT735 maxFFT805 maxFFT940]
FFT_power=[power735 power805 power940]*Fs/(NFFT-2)
DC=[mean(DC735) mean(DC805) mean(DC940)]
R(p)=(flow(p,1)./meanDC(p,1))./(flow(p,3)./meanDC(p,3))

HR(p,:)=[HR735 HR805 HR940]*60, AC=[AC735 AC805 AC940];DCt=[DC735 DC805
DC940];ACDC=AC./DCt;
ch1_ch3=ACDC(:,1)./ACDC(:,3);

R2(p)=
log((((maxFFT735/gain(p))+DC(1))./DC(1)))./log((((maxFFT940/gain(p))+DC
(3))./DC(3)));
PI(p,:)= 100*[maxFFT735/(gain(p)*DC(1)) maxFFT805/(gain(p)*DC(2))
maxFFT940/(gain(p)*DC(3))];
%% Filter and plot waveforms
maxf1=10;
[b,a]=butter(4,[minf maxf1]/150);
AC7351=filter(b,a,AC735);AC8051=filter(b,a,AC805);AC9401=filter(b,a,AC9
40);
subplot(3,2,2);plot(time,AC7351),xlabel('Time (s)'),ylabel('AC (V)')
title(strcat( strrep(fname, '_', '-'), 'from
:',num2str(probes_data(start_index)),' s
to',num2str(probes_data(end_index)),' s'));
subplot(3,2,4);plot(time,AC8051),xlabel('Time (s)'),ylabel('AC (V)')
subplot(3,2,6);plot(time,AC9401),xlabel('Time (s)'),ylabel('AC (V)')

end
%% Saving figures
figure(probes(1))
%data_dir=save_dir;
ButtonName = questdlg('Would you like to save the
images?','Save','Yes','No','Yes');
switch ButtonName,
    case 'Yes',
        save_dir=uigetdir(pname,'Save directory');
        cd(save_dir)
        for i=1:length(probes)
```

```
saveas(h(probes(i)),strcat('Probe',num2str(probes(i)),'.fig'));
        end
            msgbox('Figures saved successfully','Data saved')
    case 'No',
        msgbox('Figures not saved, you can still save them
manually','Data not saved')
end
PI=PI';HR=HR';meanDC=meanDC';flow=flow';
excel_out=[cellstr(fname) num2cell([probes_data(start_index,1)
probes_data(end_index,1) R2 flow(1:end) meanDC(1:end) PI(1:end)
HR(1:end)])];
% excel_out=[flow meanDC flow./meanDC];
display('END')
```